UNIVERSITY OF OKLAHOMA
GRADUATE COLLEGE

North Atlantic Winter Surface Extratropical Cyclone Track Variability on Interannual-to-Decadal Time-Scales

A Dissertation
SUBMITTED TO THE GRADUATE FACULTY
in partial fulfillment of the requirements for the
degree of
Doctor of Philosophy

By
MOSTAFA EL HAMLY
Norman, Oklahoma
2004

Downloaded from SHAREOK. Persistent Handle URL: https://hdl.handle.net/11244/734

UMI Number: 3127800

INFORMATION TO USERS

The quality of this reproduction is dependent upon the quality of the copy submitted. Broken or indistinct print, colored or poor quality illustrations and photographs, print bleed-through, substandard margins, and improper alignment can adversely affect reproduction.

In the unlikely event that the author did not send a complete manuscript and there are missing pages, these will be noted. Also, if unauthorized copyright material had to be removed, a note will indicate the deletion.

UMI®

UMI Microform 3127800

Copyright 2004 by ProQuest Information and Learning Company.

All rights reserved. This microform edition is protected against unauthorized copying under Title 17, United States Code.

ProQuest Information and Learning Company
300 North Zeeb Road
P.O. Box 1346
Ann Arbor, MI 48106-1346

© Copyright by Mostafa El Hamly 2004
All Rights Reserved.

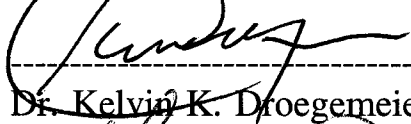
North Atlantic Winter Surface Extratropical Cyclone Track Variability on Interannual-to-Decadal Time-Scales

A Dissertation APPROVED FOR THE
SCHOOL OF METEOROLOGY

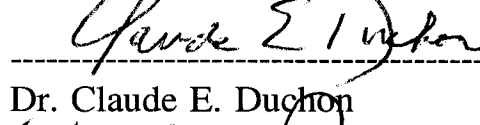
BY



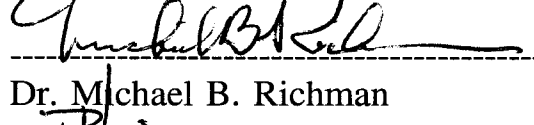
Dr. Peter J. Lamb (Committee Chair)



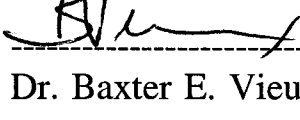
Dr. Kelvin K. Droegemeier



Dr. Claude E. Duchon



Dr. Michael B. Richman



Dr. Baxter E. Vieux

ACKNOWLEDGMENTS

In the name of God All Mighty, the most Gracious, the most Merciful, the Lord of Noah, Abraham, Moses, Jesus, and Muhammad, may the blessing and the peace of God be upon them,

Praise be to God, Lord of the worlds, who made this research work possible. I praise Him for His uncountable great bounties He bestowed on me and ask Him to increase His grace and generosity.

I would like to express my sincere gratitude to my chair advisor Professor Peter J. Lamb, for his generous and unlimited advice, fruitful guidance, understanding, time and unending assistance throughout this work. Indeed, words are inadequate to express my deep gratitude and appreciation to him for being a constant source of encouragement and patience throughout my Ph.D. program. I am also grateful to him for the valuable edition of this manuscript, as well as for the financial support provided through CIMMS.

Additionally, a special acknowledgment is in order for Professors Kelvin K. Droegemeier, Claude E. Duchon, Michael B. Richman, and Baxter E. Vieux (OU/CEES) for their willingness to serve on my doctoral committee, the time, assistance, and continuous supportive statements throughout the development of this work. I learned a lot from their courses they taught me at OU. It is not possible for me to fully express my appreciation and sincere gratitude to them. In particular, I would like to extend my sincere appreciation to Dr. Richman for his valuable input, constructive comments, and discussions for the last 10 years.

Many people whom I have dealt with gave very useful pointers and provided additional encouragement. For this, I am also indebted to Diane H. Portis (Univ. of IL) who never stopped her unlimited assistance and highly valuable suggestions and

discussions. I sincerely appreciate her tremendous help and time during the decade we have worked together more than she will ever know.

The NCEP/NCAR Reanalysis data were obtained from the NOAA-CIRES Climate Diagnostics Center (CDC). We are indebted to Dr. Mark Serreze (Univ. of Colorado) for providing us with his cyclone detection and tracking algorithm and for helpful discussions, and Mike Timlin (NOAA-CIRES CDC) for a correction in the code. I thank Dr. Jeff C. Rogers (Ohio State Univ.) and Dr. J. W. Hurrell (NCAR/CGD) for the use of their NAO indices, and Dr. David W. J. Thompson (Colorado State Univ.) for the use of his Arctic Oscillation (AO) index. I also acknowledge T. M. Smith and R. W. Reynolds (CDC) in the use of the NOAA Extended Reconstructed SST. The 2-D graphics were produced with the GrADS software package developed by Brian E. Doty (COLA-IGES) and his collaborators.

Very special thanks are in order for my dear friend Mohamed Allali (Chapman Univ., Math Dept). His kindness and support during 1994-2000 in Norman have made the years here even more memorable. A word of thanks also is due to all my friends who helped me in one way or another: Dr. Mohamed A. Eissa, Dr. Samir A. Alwazzi, Br. Essam F. Tawfik, David Jahn, Lotfi H., and many others.

I am ever grateful to my father Abdelkader, my mother Halima, my brother and sisters, and all my relatives and friends back home, especially Omar Baddour and DMN colleagues. Without their continuous love, understanding, support and spiritual encouragement, and prayers throughout the decade I spent at OU, I would never have made it this far.

I would also like to express my sincere gratitude to my dear and beloved wife, Salima H. Umm-Nour, for her moral support, understanding, taking care of our kids, her patience that has exceeded far beyond any reasonable expectation, and for her

commitment that can only be a testimony of true and unconditional love, during the course of my stay at OU, and for giving me the strength to accomplish my Ph.D. I would also like to extend my acknowledgement to my so beloved kids, Nour-Eddine and Mohamed A.

Last and not least, I have been praying to all those who helped and supported, whose names were missed unintentionally, asking them for their forgiveness. May God All Mighty, give them the best in this life and the hereafter.

Mostafa El Hamly, March 23, 2004

Table of Contents

CHAPTER 1: INTRODUCTION 1
1.1 BACKGROUND 1
1.2 ADDITIONAL MOTIVATION FOR INVESTIGATION OF THIS TOPIC 3
1.3 SCOPE OF THIS DISSERTATION (OBJECTIVES) 6

CHAPTER 2: DEVELOPMENT OF A HYBRID SPACE- AND TIME-SMOOTHED SURFACE CYCLONE TRACK DENSITY FUNCTION (CDF)
2.1 INTRODUCTION 12
2.2 CYCLONE IDENTIFICATION AND TRACKING METHODS 15
2.2.1 Manual (Traditional) Methods for Cyclone Detection & Tracking 15
2.2.2 Proxy Methods for Cyclone Detection and Tracking 20
2.2.3 Automated Methods for Cyclone Detection and Tracking 21
2.2.4 Construction of a Hybrid Space- and Time-Smoothed Cyclone Track Density Function (CDF) 25
a. Step 1: Application of Serreze's Cyclone Detection & Tracking Algorithm 29
b. Step 2: Application of Akima Interpolation Scheme 32
c. Step 3: Application of Objective Analysis Scheme 35
d. Step 4: Application of Bessel Function 40
2.3 CORRELATION LENGTH OF CDF ANOMALIES 41
2.4 SIGNIFICANCE OF CDF AND RELATED TOPICS 45

CHAPTER 3: LONG-TERM CLIMATOLOGICAL FEATURES OF CYCLONE ACTIVITY **46**
3.1 INTRODUCTION 46
3.2 CLIMATOLOGICAL FEATURES OF CYCLONE ACTIVITY 51
3.2.1 Long-Term Mean and Standard Deviation of Cyclone Characteristics 51
3.2.2 Seasonal Variations of Mean Behavior of CDF 58
3.3 PERSISTENCE OF CYCLONE ACTIVITY 66
3.3.1 Month-to-Month Correlation of CDF Anomalies 67
3.3.2 Autocorrelation Function of Cyclone Parameters 70
3.4 RELATIONSHIPS BETWEEN CYCLONE CHARACTERISTICS 71
3.5 WAVELET ENERGY-BASED ANALYSIS OF CDF 76
3.5.1 Methodology 77
3.5.2 Results 81
3.6 SUMMARY AND CONCLUSIONS 86

CHAPTER 4: INTERANNUAL VARIABILITY OF CYCLONE TRACKS AND ASSOCIATIONS WITH REGIONAL CLIMATE VARIATIONS

4.1 INTRODUCTION 88
4.2 PREVIOUS RELEVANT WORK 91
4.3 DATA AND METHODOLOGY 92
4.3.1 Data 92
a. Grid-Point Time Series 93
b. Non-Grid-Point Time Series 93
4.3.2 Methodology 94
4.4 CLASSIFICATION OF CYCLONE BEHAVIOR INTO MAJOR REGIMES
4.4.1 Spatial VRPC Loadings/Associated Score Time Series 95
a. VRPC1 Pattern 99
b. VRPC2 Pattern 101
c. VRPC3 Pattern 102
d. Trends and Persistence of CDF VRPC Scores 103
4.4.2 Matching Pursuit Transform Time-Frequency Decomposition of CDF Scores 107
4.4.3 Associated Raw Cyclone Tracks 113
a. VRPC1-based Raw Cyclone Track Pattern 113
b. VRPC2-based Raw Cyclone Track Pattern 115
c. VRPC3-based Raw Cyclone Track Pattern 116
4.4.4 Associated Atmospheric and Oceanic Circulation Anomalies 122
4.5 RELATIONSHIPS OF CYCLONE BEHAVIOR WITH OTHER VARIABLES
4.5.1 NAO Impact on Storm Characteristics 134
4.5.2 ENSO Impact on Cyclone Tracks and Atmospheric/Oceanic Circulation 137
4.6 RELATION OF CDF & MOROCCAN PRECIPITATION PATTERNS WITH NAO
4.6.1 Background 141
4.6.2 Relationship of CDF Patterns with Moroccan Precipitation 145
4.6.3 Relationship of Cyclone Tracks and Moroccan Precipitation with NAO
a. Methodology 150
b. Results 153
4.6.4 Predictability of Moroccan Regional Precipitation Index 159
4.7 SUMMARY AND CONCLUSIONS 167

CHAPTER 5: DECADAL-TO-MULTIDECADAL VARIABILITY OF CYCLONE TRACKS INVOLVING OCEAN-ATMOSPHERE INTERACTIONS
5.1 BACKGROUND AND MOTIVATION 172
5.2 DATA AND METHODOLOGY 176
5.3 LF BEHAVIOR OF CDF AND ASSOCIATIONS WITH OTHER ATMOSPHERIC & OCEANIC FIELDS/INDICES 178
5.3.1 Leading Mode (UPC1) of LF Cyclone Track Variability 178
5.3.2 Relationship of LF CDF Behavior to LF Atmospheric/Oceanic Anomalies 185
5.3.3 Removal of Linear Dependence of LF CDF on NAO/SOI 189
5.4 OCEAN-ATMOSPHERE INTERACTIONS 200
5.4.1 Literature Review 200
5.4.2 New Lead/Lag CCA-Based Procedure 204
a. First Application: CCA of LF CDF/SST 205
b. Second Application: CCA of LF SLP/SST 208
5.5 SUMMARY AND CONCLUSIONS 208

CHAPTER 6: ENSEMBLE SIMULATION OF LF NAO FOR 21st CENTURY CLIMATE CHANGES USING GLOBAL COUPLED OCEAN-ATMOSPHERE GCMs 217
6.1 INTRODUCTION 217
6.2 SIMULATIONS OF PRESENT NAO IN COUPLED GCMs 219
6.3 DATA 221
6.4 BRIEF DESCRIPTION OF COUPLED GCMs 222
6.5 NUMERICAL PROCEDURE USED TO COMPUTE NAO INDICES 224
6.6 RESULTS 226
6.7 SUMMARY AND CONCLUSIONS 230

CHAPTER 7: SUMMARY AND CONCLUSIONS/DISCUSSION 235
7.1 SUMMARY AND CONCLUSIONS 235
7.1.1 Introduction 235
7.1.2 CDF and Related Cyclone Characteristics 235
7.1.3 Long-Term Climatological Features of Cyclone Activity 236
7.1.4 Interannual Variability of Cyclone Tracks & Associations with Regional Climate Variations 238
7.1.5 Decadal-to-Multidecadal Variability of CDF Involving Ocean-Atmosphere Interactions 242
7.1.6 Ensemble Simulation of LF NAO for 21st Century Climate Changes Using Global Coupled Ocean-Atmosphere GCMs 247
7.2 NEW CONTRIBUTIONS 249
7.3 FUTURE WORK 251

Appendix: Matching Pursuit Transform (MPT) 253

References 264

ABSTRACT

North Atlantic Winter Surface Extratropical Cyclone Track Variability on Interannual-to-Decadal Time-Scales

Most recent automated methods for detecting and tracking cyclones suffer mainly from spatio-temporal inhomogeneities. To overcome these weaknesses, a new approach was developed to construct a hybrid space- and time-smoothed surface Cyclone track Density Function (CDF) over the North Atlantic Basin on a 2° x 2° grid with 1-day time resolution (Oct-Mar, 1948/49-1998/99). The CDF field is designed to provide a better description of storm tracks rather than tracking individual storms. Development of other related fields of cyclone characteristics (e.g., intensity, moving speed, duration) is enlightening because of additional physical insight/consistency provided. Thus, the aim of this analysis is to give new insight into the North Atlantic winter cyclone track organization and behavior. State-of-the-art techniques, models, and data sets were used to achieve this goal.

The CDF and related cyclone attributes are used to compile a new climatology (including persistence) of cyclone activity. This climatology will be arguably the most accurate and representative set yet compiled. Moreover, use of a novel aspect of wavelet analysis of CDF permitted (1) separation of the high-frequency and low-frequency (LF) components of cyclone activity; and (2) full 2-D grid analyses that document spatial heterogeneity of cyclone behavior, rather than areal averaging.

The variability of cyclone activity at interannual and decadal-to-multidecadal time-scales is examined. First, interannual cyclone variability is classified into three major

modes based on a VARIMAX Rotated Principal Component Analysis (VRPC) of CDF anomalies. Differences between the new CDF modes are emphasized in several respects (e.g., time-frequency decomposition of VRPC scores). Relationships of these unique modes to various atmospheric/oceanic circulation anomalies (in addition to NAO and ENSO) are then documented; the different physical mechanisms involved are elucidated. Further, decadal ocean-atmosphere interactions are explored via a new lead/lag CCA-based procedure. CDF also is used to re-examine the predictability of Moroccan precipitation anomalies by accounting for VRPC scores (besides NAO). Finally, new ensemble simulation of trends in LF NAO for 21st century climate changes using coupled ocean-atmosphere GCMs is analyzed.

CHAPTER 1: INTRODUCTION

1.1 BACKGROUND

In April 1994, a comprehensive proposal entitled "Cooperative Research on 'Al Moubarak' (i.e., the North Atlantic Oscillation, NAO) and Moroccan Precipitation" was submitted to the U.S. Agency for International Development (USAID)-Morocco and the Moroccan Direction de la Météorologie Nationale (DMN). This proposal (Lamb 1994) outlined a substantial (5-8 year) program of cooperative research, development, and training involving DMN and the Cooperative Institute for Mesoscale Meteorological Studies (CIMMS) at The University of Oklahoma (OU). The proposal was jointly funded by DMN, USAID-Morocco, and OU for a three-year period that started in August 1994. The main research components of Lamb's 1994 proposal were:

a. Characterization and Seasonal Behavior of NAO;

b. Relation of Atlantic Weather Systems and Moroccan Precipitation Patterns to NAO; and

c. NAO Variations: Fundamental Causes and Past and Future Patterns.

The original proposal contains the relevant background information and research planning details on each of the above topics.

The NAO is the dominant mode of winter climate variability in the North Atlantic region, influencing central North America, Europe, and Northern Asia. The NAO is a large-scale seesaw in atmospheric mass between the subtropical high and the subpolar low (e.g., Walker and Bliss 1932; van Loon and Rogers 1978; Lamb and Peppler 1987; and many others). The monograph edited by Hurrell et al. (2003) is the most detailed

reference to date on NAO. This book evolved from an American Geophysical Union (AGU) Chapman Conference on the NAO organized in late 2000, in which CIMMS contributed substantially with three presentations. Further information on the NAO is available on the NAO thematic website maintained by D. B. Stephenson (URL=www.met.rdg.ac.uk/cag/NAO/index.html), which was started in August 1997. It aims to collect together useful information about this important climatic phenomenon. The website has many useful links with NAO-related information.

Concerning component (a) of Lamb's (1994) proposal above, substantial progress already has been made on almost all of the research work originally proposed. A paper on NAO seasonality was recently published (Portis et al. 2001), which presents a seasonally and geographically varying mobile index of the North Atlantic Oscillation (henceforth referred to as NAO_m). The present author was a co-author of that paper and will make extensive use of this newly developed NAO_m index in this Dissertation, along with other NAO indices such as those due to Rogers (1984) and Hurrell (1995a). Lamb and his collaborators now are finalizing that work, further disseminating its results within Morocco, and publishing them internationally. In this regard, a comprehensive journal article on the temporal and time-scale behavior of the NAO, expanding on El Hamly et al. (2000), is being prepared for submission to the *Journal of Climate* in late 2004. The findings of this research component are not included in this manuscript.

Substantial progress already has been made on one half of component (b) above – that involving the analysis of Moroccan precipitation patterns and the association of those patterns with the NAO. In combination with the activities proposed for component

(a), Lamb and his collaborators brought this effort to completion and publication as a chapter (Ward et al. 1999) in an important book entitled *"Beyond El Niño: Decadal and Interdecadal Climate Variability"* that had worldwide dissemination. Again, the bulk of this research component is not incorporated in this Dissertation, with the major exception being the utilization here of a Moroccan precipitation regionalization produced in that work. In contrast, investigation of the other half of project component (b) above – that dealing with the North Atlantic weather system linkage between the large-scale NAO and Moroccan precipitation – therefore is a major component of this Dissertation. In this regard, the research embodied in this manuscript is very consistent with Lamb's (1994) proposal.

As for component (c) above, some key findings to date are: (1) the empirical identification (under component (a)) of a pronounced August-November-January NAO oscillation that produces the extreme positive January-February NAO values that induce moderate-to-severe Moroccan drought (El Hamly et al. 1998; Lamb et al. 2000); and (2) the replication of some of that August-January NAO evolution in a 34-year simulation by the ECHAM4 Global Climate Model (GCM) of the Max-Planck-Institut für Meteorologie (Ward et al. 1999). As a new contribution to this component (c), the present study uses existing global coupled ocean-atmosphere GCM runs to investigate the possible changes in the low-frequency behavior of the NAO during the 21st century.

1.2 ADDITIONAL MOTIVATION FOR INVESTIGATION OF THIS TOPIC

Besides Lamb's (1994) proposal mentioned above, this section provides additional motivation for this Dissertation investigating North Atlantic winter surface cyclonic

activity, including its relations with the NAO and Moroccan precipitation patterns.

• It is well known that the climate of the Planet Earth exhibits natural variability on a very broad range of frequencies. In particular, climate variability on decadal and longer time-scales is a subject of increasing interest and relevance (e.g., Deser and Blackmon 1993). Concern over anthropogenic impacts on global climate is a strong catalyst to describe and understand the natural modes of climate system variability. Interaction between the oceans and overlying atmosphere is fundamental to the dynamical processes governing climate and its interannual, decadal, and longer time-scale variability. The detection of trends in climatological time series has become central to discussion of climate change due to the enhanced greenhouse effect. It has been speculated that future global warming will change the frequency and severity of tropical and extratropical storms (e.g., Zhang et al. 2000 and references therein).

• The North Atlantic is a region of critical importance in the global climate system (Deser and Blackmon 1993; Marshall et al. 2001). This basin is one of the most frequent cyclone occurrence regions in the Northern Hemisphere (e.g., Serreze 1995; Geng and Sugi 2001). Cyclones in the North Atlantic Basin may strongly influence the weather and climate of surrounding areas such as eastern United States, eastern Canada, southern Greenland, Iceland, western Europe, Mediterranean Basin, and Northwest Africa (Geng and Sugi 2001). Changes in cyclone tracks play a significant role in shaping anomalous seasonal climate patterns over the North Atlantic (Hurrell and van Loon 1997). With their strong connection to local weather, storm tracks play a prominent part in midlatitude climate dynamics (Chang et al. 2002). Furthermore, long-term variability in extratropical cyclone activity is an aspect of climate of particular interest to society (Paciorek et al.

2002). This Dissertation focuses on the North Atlantic during the winter semester (October-March), as it is during this season that synoptic-scale storm track activity is greatest (e.g., Chang et al. 2002) and the oceanic mixed layer is deepest (e.g., Sutton and Allen 1997).

- The geographical distribution of the primary areas of extratropical cyclogenesis and the principal tracks followed by cyclones are of paramount importance to both the meteorologist and climate scientist (e.g., Whittaker and Horn 1984). Furthermore, knowledge of the preferred locations of real-world cyclone tracks is very useful in assessing the quality of climate simulations (Whittaker and Horn 1984; Chang et al. 2002).

- Damaging ocean waves and storm surges along the United States Atlantic coast are largely due to extratropical cyclones. Changes in the cyclone tracks relative to the mid-Atlantic coast give rise to variations in the frequency of extreme wave and storm surge conditions along the coast, and the consequences are highly significant in terms of human impact (Resio and Hayden 1975; Hirsch et al. 2001 and references therein). Along most of this coast, shorelines are receding (Hayden et al. 1979; Dolan et al. 1979) due to several factors – rise in sea level, lower average cyclone central pressure, reduced coastal sand supply, human activities, and secular variations in cyclone frequency, intensity, and duration.

- Studies of North Atlantic climate variability have become a central focal point of climate research in the post 2000-period (Marshall et al. 2001). However, the North Atlantic climate variability associated with changes in the location and intensity of surface

cyclone tracks has not been studied to as great an extent as that associated with low-frequency components of the atmospheric circulation, such as standing waves, blocking events, and atmospheric teleconnections patterns (e.g., NAO and Arctic Oscillation, AO). In particular, classification of North Atlantic cyclone behavior into major circulation regimes is crucial for investigating relationships of cyclone variability with regional climate variations at different time-scales. Another fundamental issue regarding such variability is how cyclone behavior may be changing with time. Moreover, investigating the El Niño/Southern Oscillation (ENSO) impact on cyclone tracks over the North Atlantic is an important subject as well (e.g., Merkel and Latif 2001; Chang et al. 2002).

1.3 SCOPE OF THIS DISSERTATION (OBJECTIVES)

Using Lamb's (1994) original Proposal components (b) and (c) mentioned in Section 1.1 as a broad framework, the research activities pursued for this Dissertation are outlined below as chapters. Each chapter has a background/motivation section to justify the work in question and also identifies its significance and relationships to other chapters and topics.

The present Chapter 1 (Introduction) provides the overall background and motivation for this Dissertation, and outlines its scope. Chapter 2 presents the methodology adopted and developed to construct a hybrid space- and time-smoothed surface cyclone track density function (CDF) defined on a grid over the North Atlantic. As background information, this chapter first reviews different cyclone identification and tracking methods, such as manual (traditional) methods and their weaknesses, "proxy" methods and their related problems, and automatic ("objective") methods and their pitfalls. This chapter then addresses two main questions: (1) the need for such a hybrid

CDF technique; and (2) how such a CDF function was constructed to provide a better description of storm tracks rather than to track individual storms. This new "CDF approach" involved applications of: (1) an enhanced automated algorithm for detecting and tracking surface cyclones (Serreze 1995; Serreze et al. 1997; McCabe et al. 2001); (2) the Akima (1978) scheme to quantify cyclone characteristics (e.g., intensity, moving speed, duration); (3) a CDF objective analysis scheme (Anderson and Gyakum 1989) as a space/time filter yielding "CDF tracks"; and (4) a Bessel function, spatial interpolation technique to provide a finer spatial resolution for the CDF fields. To date, no cyclone study for the North Atlantic Basin has applied such a CDF approach. Instead, other investigators (e.g., Geng and Sugi 2001) have focused on cyclone counts (i.e., frequencies) that yielded standard individual spatially- and temporally-discontinuous cyclone tracks. Therefore, the CDF function, that yields the first ever winter semester (October-March) surface extratropical cyclone track data set over the North Atlantic Ocean on a 2° latitude x 2° longitude grid for 1948/49-1998/99, is the basis for much of this Dissertation. The NCEP/NCAR Reanalyses employed to construct the CDF fields are regarded as one of the best representations of Northern Hemisphere atmosphere (e.g., Simmonds and Keay 2000a); use of these reanalyses at 6-hourly intervals means that uncertainties associated with identifying and tracking cyclones are greatly reduced. Furthermore, development of the Akima-based fields of cyclone characteristics is enlightening because of the additional physical insight provided; they also demonstrate the physical consistency among the different variables (e.g., CDF tracks are compared to cyclone intensity).

Chapter 3 uses the newly constructed daily CDF data set to document previously unavailable long-term average climatological features (including persistence) of North

Atlantic winter surface extratropical cyclone activity over 51 years (1948/49-1998/99). Additionally, this chapter presents long-term climatologies of related cyclone characteristics generated by application of the Akima scheme to yield a rich picture of the climatological structure of cyclone behavior. The significance of this chapter lies in a number of factors. First, the North Atlantic cyclone climatological features and persistence are derived from fifty-one years of analysis, a period longer than any considered heretofore. With CDF tracks and related cyclone parameters, one can examine different aspects of cyclone activity and assess the interrelations and hence the robustness of the results. Therefore, the resulting climatology of cyclone activity will be arguably the most accurate and representative yet compiled. Finally, use of a novel aspect of wavelet analysis of CDF tracks permits (1) separation of the high-frequency (Chapter 4) and low-frequency (Chapter 5) components of cyclone activity; and (2) establishes the need for full 2-dimensional grid analyses that document the spatial heterogeneity of cyclone behavior, rather than dependence on the areal (e.g., zonal) averaging.

Chapter 4 examines the interannual variability of North Atlantic winter cyclone activity and its associations with regional climate variations. The CDF and related Akima-based cyclone variables are used in this analysis to yield a rich picture of cyclone variability. First, this chapter classifies cyclone behavior into three major circulation regimes based on a VARIMAX Rotated Principal Component Analysis (VRPC) of CDF anomalies. This work adds to previous efforts in several new ways and differences between the present analysis and previous work are discussed in detail in Chapter 4. The present VRPC-based regime classification is the first ever conducted for the North Atlantic Ocean. In this regard, Chapter 4 emphasizes differences between the three distinctly different CDF track modes in several respects. In addition, short-term

variability in cyclone activity is related to short-term variability in regional teleconnections patterns (e.g., NAO, SOI) (e.g., Paciorek et al. 2002). Relationships of ENSO with atmospheric (e.g., SLP) and oceanic (e.g., SST) circulation anomalies within this basin are examined as well. Finally, Chapter 4 utilizes the above cyclone analysis results, that were obtained initially for the entire North Atlantic Basin, for immediate application to the interannual variability of Moroccan precipitation. The key issues here are how much of North Atlantic cyclone activity is NAO-related and how much is not, and the extent to which this separation influences Moroccan precipitation. Predictability of Moroccan regional precipitation indices also is revisited by taking into account the additional new CDF track modes (besides NAO). The results are expected to enhance substantially our existing NAO-based statistical framework for Moroccan precipitation prediction (El Hamly et al. 1998; Ward et al. 1999).

Chapter 5 examines North Atlantic winter cyclone activity at decadal and longer time-scales; a Lanczos filter (Duchon 1979) is applied to grid-point time series and indices to retain only low-frequencies (periods greater than 10 years). This chapter has two main components. The first documents decadal-to-multidecadal variability of low-frequency (LF) winter CDF anomalies, and analyzes associations of the LF behavior of CDF tracks with other LF atmospheric and oceanic fields/indices (NAO, ENSO). In particular, this chapter examines trends in cyclone activity through spatial distribution patterns (not previously published) and assesses whether the historically unprecedented trends in the wintertime NAO circulation patterns over the past three decades have been imprinted upon the North Atlantic cyclone behavior. The second component of this chapter diagnoses ocean-atmosphere interactions over the North Atlantic Basin on decadal and longer time-scales. This part investigates some controversial and important questions

concerning such ocean-atmosphere interactions. On decadal-to-multidecadal time-scales, there may be a mutual coupling between the two fluids (e.g., Deser and Blackmon 1993; Sutton and Allen 1997; Grötzner et al. 1998; Marshall et al. 2001). Given the possible existence of such a coupled mode, ocean-atmosphere interactions are investigated using a new Canonical Correlation Analysis (CCA)-based procedure between components of dominant CDF and SST modes, with a variable lead/lag applied to either score time series. This analysis may help identify the role of the ocean in the North Atlantic decadal climate variability. This will contribute to our understanding of how the North Atlantic atmospheric circulation could respond to ocean forcing on decadal time-scales, and to determine the extent to which SST anomalies feedback on the atmospheric circulation.

Chapter 6 analyses the LF component of NAO simulations of 21st century climate changes from global coupled ocean-atmosphere GCMs (NCAR-PCM, CGCM2, HadCM3, and CSIRO/Mk2). Since the NAO is highly correlated with the leading mode of interannual CDF anomalies, this analysis builds on work reported in Chapter 4. Specifically, as a new contribution to climate change studies, this analysis highlights the impact of using different greenhouse gas forcing scenarios (e.g., Houghton et al. 2001) on NAO trends in fully coupled models. A prerequisite for such NAO prediction is a realistic simulation of the present NAO variability in coupled models; many recent studies (e.g., Meehl et al. 2000) already have explored this issue and shown that these coupled models in general perform reasonably well in this regard. In this chapter, trends in LF NAO/nodes are computed and compared and contrasted between different NAO indices, between coupled models, and between forcing scenarios. However, since ensemble averaging reduces the noise level in model-simulated climate changes (e.g., Dai et al. 2001), this study performs ensemble averaging of NAO behavior under different forcing

scenarios. Moreover, a complete picture of the seasonal variations of predicted trends in LF NAO/nodes under different scenarios is provided.

Finally, Chapter 7 summarizes the new contributions of this Dissertation to research in the field of climate variability, and then proceeds to discuss their implications for the global climate trends (in addition to Morocco) and offers suggestions for future research work.

CHAPTER 2: DEVELOPMENT OF A HYBRID SPACE- AND TIME-SMOOTHED SURFACE CYCLONE TRACK DENSITY FUNCTION (CDF)

2.1 INTRODUCTION

The North Atlantic Ocean is one of the most frequent regions of extratropical cyclone occurrence in the Northern Hemisphere (Serreze 1995; Geng and Sugi 2001). Cyclones in the North Atlantic Basin can strongly influence the weather and climate of surrounding areas such as eastern United States, eastern Canada, southern Greenland, Iceland, western Europe, the Mediterranean Basin, and Northwest Africa (Geng and Sugi 2001). Changes in intensity and position of cyclone tracks play a significant role in shaping atmospheric circulation anomalies over the North Atlantic (Hurrell and van Loon 1997). With their strong connection to local weather, storm tracks play a prominent role in midlatitude climate dynamics (Chang et al. 2002). Furthermore, long-term variability in extratropical cyclone activity is an aspect of climate of particular interest to society (Paciorek et al. 2002).

The geographical distribution of the primary areas of extratropical cyclogenesis and the principal tracks followed by cyclones are of great importance to both the operational meteorologist and climate scientist (Whittaker and Horn 1984). Because of their association with day-to-day weather events, cyclones very much are part of the purview of the operational meteorologist. Likewise, the climate scientist is interested in the spatial distribution and temporal variation of cyclogenesis and cyclone tracks to analyze the Earth's pattern of climates and, especially, to investigate shifts/trends in these

parameters from one climate episode to another over a broad range of time-scales. Consequently, studies concerning the geographical distribution of cyclogenesis and main cyclone tracks have long appeared in the meteorological and climatological literature (Whittaker and Horn 1981). Furthermore, researchers engaged in modeling the atmospheric general circulation to simulate climate variations, not only simulate the mean flow, but also cyclone development, movement, and decay. To these modelers, knowledge of the observed preferred locations of cyclogenesis, cyclone tracks, and cyclolysis is very useful in assessing the performance of their climate simulations (Whittaker and Horn 1984; Chang et al. 2002).

Damaging ocean waves and storm surges along the United States (U.S.) Atlantic coast are largely due to extratropical cyclones. Resio and Hayden (1975) found that an increase in storm damage along the U.S. East Coast coincided with secular variations of the general circulation. They suggested that a significant trend had occurred in the large-scale circulation, particularly an increase in the frequency of high-latitude blocking. Dickson and Namias (1976) also attributed increased frequency of cyclones off the U.S. Atlantic coast between the 1940s and 1960s to blocking in the Greenland area and negative temperature anomalies in the U.S. Southeast. Changes in the cyclone tracks relative to the mid-Atlantic coast give rise to variations in the frequency of extreme wave and storm surge conditions along the coast, and the consequences are highly significant in terms of human impact (Resio and Hayden 1975; Hirsch et al. 2001 and references therein). Along most of this coast, shorelines are receding (Hayden et al. 1979; Dolan et al. 1979) due to several factors – rise in sea level, lower average cyclone central pressure, reduced coastal sand supply, human activities, and secular variations in cyclone frequency, intensity, and duration.

Conducting the above studies or other related investigations requires analysis of cyclone track variability and its associations with regional climate variations at different time-scales, assessment or intercomparison of the performance of numerical models, study of the cyclone response to natural or simulated climate variability, understanding of the climatological behavior of surface cyclones, and quantification of the consequences of any trend/shift in storm tracks in terms of human impact. These challenges, in turn, require, *a priori*, a reliable procedure to adequately identify and track cyclones over the region of interest. Building a high-quality data set of cyclone activity is hence of paramount importance before conducting research into cyclone behavior. Thus, the first step in the present study was to create a high-quality surface extratropical cyclone data set for the North Atlantic Basin.

Therefore, this chapter describes the methodology adopted to construct a hybrid space- and time-smoothed cyclone track density function (henceforth referred to as CDF) defined on a grid over the North Atlantic. But, before proceeding to the CDF description, this chapter first reviews the different cyclone identification and tracking methods found in the literature, such as manual (traditional) methods and their weaknesses (Section 2.2.1), "proxy" methods and their related problems (Section 2.2.2), and automatic ("objective") methods and their pitfalls (Section 2.2.3). Then, Section 2.2.4 describes why and how a new CDF was constructed to provide a better description of characteristic storm tracks, rather than to track individual storms. This new "CDF approach" involved: (1) enhancement of an existing automated algorithm for identifying and tracking surface cyclones (Serreze 1995; Serreze et al. 1997; McCabe et al. 2001); (2) application of the Akima (1978) scheme to quantify cyclone characteristics (e.g., intensity, moving speed,

duration); (3) application of an objective analysis scheme (Anderson and Gyakum 1989) as a space/time filter yielding "CDF tracks"; and (4) use of a Bessel function, an appropriate spatial interpolation technique to yield finer spatial resolution for the daily CDF fields.

This CDF function yields the first ever winter semester (October-March) surface extratropical cyclone track data set over the North Atlantic Ocean for a 50+ year period (1948-99). To date, no cyclone study for the North Atlantic Basin has applied such a CDF approach. To document the variability of winter storm track structures over this basin the resultant gridded CDF data set is used extensively, across a broad range of time-scales, in subsequent chapters. To examine the correlation length of the cyclone tracks over the North Atlantic, Section 2.3 presents the correlation field and associated correlogram for the CDF anomalies. Finally, Section 2.4 outlines the significance of CDF and related topics.

2.2 CYCLONE IDENTIFICATION AND TRACKING METHODS

2.2.1 Manual (Traditional) Methods for Cyclone Detection and Tracking

Early studies of cyclone climatology and long-term variations over North America and the North Atlantic were performed by identifying cyclone features on synoptic charts and tracking the features manually owing to the lack of adequate computational power to automate the process. General characteristics of extratropical cyclones (and anticyclones) and their relationships to the larger-scale circulation were revealed through climatological analyses of their spatial distributions and temporal variations. Examples of the most often cited studies of this type are Petterssen (1950, 1956), Hosler and Gamage (1956), Klein (1957, 1958), Reitan (1974, 1979), Colucci (1976), Zishka and

Smith (1980), Hayden (1981a), and Whittaker and Horn (1981, 1982, 1984). Of particular relevance in the present context was Rogers (1990), who found that during positive North Atlantic Oscillation (NAO) months the main cyclone track has a pronounced northeastward orientation, remaining parallel to the North American East Coast and crossing Newfoundland with a cyclone frequency maximum in mid-ocean southeast of Greenland. In the negative polarity NAO mode, cyclones crossing the western Atlantic move eastward, tracking along latitude 45°N on average, in proximity to the Gulf Stream.

The main weaknesses associated with the above manually-based studies include:

• *Missing data/various data sources/sampling problems*

Data in some areas could be missing (e.g., Whittaker and Horn 1984, Fig. 1). Furthermore, several data sources were sometimes used in the same study (e.g., Whittaker and Horn 1984; Changnon et al. 1995); care was needed to eliminate duplication and to ensure consistency in the cyclone tracking procedure. However, this may have resulted in some spatial-temporal inhomogeneity in the data. Moreover, observing networks that provided the basic cyclone data for such studies varied over the study domain. Reitan (1974) noted that low-latitude oceans off the major shipping routes were poorly sampled and the high-latitudes had observing networks inferior to those of midlatitude land masses.

• *Inconsistency in counting a cyclone center*

In some studies (e.g., Hayden 1981a; Whittaker and Horn 1984), a low-pressure center was counted only once in a grid-box; repeated entries by the same cyclone into the same grid-box were not tabulated. Thus, the counting procedure was independent of time,

so that the time of entrance and length of time in a box were not considered. This differs from Petterssen's (1956) or Klein's (1957) method that used counts at specific synoptic times (1230 GMT); this method can be thought of as measuring the duration of cyclonic activity, since it may not count fast-moving systems that could cross a grid area in less than a specified period (e.g., 24 hours) or may lead to multiple counts of slow-moving systems in an area. Reitan (1974) noted that differences that result from counting cyclone centers at a specific map-time as opposed to counting cyclone tracks would have accounted for some differences in patterns of cyclone activity between early studies.

• *Inconsistency in defining cyclogenesis*

Cyclogenesis traditionally was defined as the initial point of formation of a low-pressure center with at least one closed 4 hPa interval isobar for 24 hours or more (e.g., Whittaker and Horn 1981, 1984). However, in the period prior to 1964, isobar intervals of 5 hPa were standard on the charts used to complete the cyclone census outside North America. This could have introduced some bias in the cyclone tracking procedure.

• *Area correction problem*

Since the area enclosed by a latitude/longitude quadrangle decreases with increasing latitude, schemes for adjusting quadrangle areas were introduced. Hence, raw grid-cell cyclone frequencies were adjusted in some studies (e.g., Reitan 1974, 1979; Brennan and Smith 1978) to compensate for the smaller boxes at higher latitudes. However, Zishka and Smith (1980) reported that an area correction scheme may unrealistically distort the cyclone frequency distribution. Thus, they decided to retain the actual cyclone counts without adjustments. Other investigators (e.g., Hayden 1981a; Rogers 1990) followed Zishka and Smith (1980) in using raw grid-cell cyclone

frequencies rather than area-normalized frequencies, avoiding a latitude-dependent bias that can occur as a result of area normalization (Ballenzweig 1959). Hayden (1981b) also discussed this "area correction" problem and showed that adjusting for latitude may bias the results at higher latitudes (raw frequency means were generally larger than area-normalized frequency means). To overcome this problem, Changnon et al. (1995) designed a methodology that incorporated use of 5° latitude diameter equal-area circles located in a grid over North America; such a grid of equal-area circles eliminated two related problems associated with conventional grid systems, area-inequality and area-normalization, and thus allowed for comparison of cyclone frequency counts among circles. Furthermore, a S-mode Principal Component Analysis (PCA) is sensitive to changes in the differences in the density of stations or grid points on a given region. This problem can be overcome by interpolating the data to an equal-area grid (e.g., Karl et al. 1982), by using a fairly uniform distribution of stations (e.g., Richman and Lamb 1985), or by designing a spatially uniform density grid by means of the criteria of a constant density of points in each latitude circle (e.g., Araneo and Compagnucci 2004). Moreover, Taylor (1986) showed that traditional methods also are biased in that they preferentially weight certain storm track directions over others; the problem is that the frequency depends not only on how many storm tracks are found in a region, but also on the direction that the storms are traveling.

- *Inconsistency in defining grid size*

The grid size was subjectively chosen (e.g., Reitan 1974). The use of a larger area would result in loss of resolution while a much smaller area would give an unrealistically small value for the frequency of cyclones. Both Petterssen (1950) and Klein (1957) used

a 5° latitude x 5° longitude grid. Reitan (1974) used a larger grid size with 550 km as average radius. Colucci's (1976) results were presented for 1° x 1° quadrangles while other investigators used a 2° x 2° grid (e.g., Brennan and Smith 1978; Zishka and Smith 1980). Hayden (1981a,b) used a 2.5° x 5° grid while Whittaker and Horn (1984) and Rogers (1990) used 5° x 5° grid. Note the grid size still is subjectively chosen in "objective" (modern) cyclone identification and tracking methods (Section 2.2.3).

• *Failure in estimating cyclone strength*

Once a cyclone had been identified and tracked, central sea level pressure (SLP) or central vorticity were generally used to gauge cyclone intensity. Unfortunately, these point measures often fail to represent the true strength of a cyclonic circulation or its variation with time, as illustrated in Figs 3-4 of Sinclair (1997). Although cyclogenesis is commonly associated with falling central pressure, this is not always the case; conversely, rapidly falling pressure does not always indicate cyclogenesis. Two cyclones having similar central vorticity do not necessarily have the same intensity; a major cyclogenesis event could happen despite the absence of any central vorticity change.

Therefore, it was very difficult in most cases to make objective comparisons between early cyclone studies due to the above weaknesses. Qualitative comparisons were all that could be made, in general (Reitan 1974). Furthermore, manual methods were generally inconclusive as to how to assess clear long-term changes of cyclone activity in a given region (e.g., North America, North Atlantic Ocean).

2.2.2 Proxy Methods for Cyclone Detection and Tracking

As opposed to the above labor-intensive traditional methods, "proxy methods" are based on a "proxy" variable employed to define and compute cyclone tracks. In general, the term "storm tracks" in proxy methods refers to regions of maximum variance of SLP (or of other parameters such as 500-hPa geopotential height, transient eddy poleward heat flux) arising from disturbances with periods of less than about one week (effects of synoptic time-scale transients), rather than the trajectories of individual cyclones as in manual methods. The rationale for this definition of "storm tracks" is given in Blackmon et al. (1984) and Cai and van den Dool (1991). Examples of such studies include Lau (1988), Trenberth and Hurrell (1994), Hurrell (1995b), Hurrell and van Loon (1997), and Rogers (1997). Note that proxy methods represent a relatively simple way to evaluate storm tracks, involving fewer arbitrary decisions than the traditional trajectory methods, but create approximations of the cyclone tracks that do not identify individual cyclone centers as would be required when diagnosing instantaneous weather conditions.

The relationship of a proxy variable to traditional synoptic storm tracks was assessed by some investigators. Wallace et al. (1988) found the relationship exhibited *positional biases* from synoptically determined cyclone tracks, although they observed no major changes in overall structure. They concluded that "it is not generally possible to infer the tracks of individual highs and lows from a knowledge of the high-pass-filtered anomalies, together with the climatology, because all frequency bands contribute to the patterns observed on individual synoptic maps." Furthermore, Anderson and Gyakum (1989) found that the differences between their analysis of actual cyclone positions and results from Lau's (1988) proxy of band-pass variance fields were "substantial". Because

of these limitations, most recent approaches explicitly have considered the weather systems that cause the variability, using the automated methods described in next section (Blender et al. 1997). Moreover, despite the fact that the Eulerian storm track approach (i.e., proxy method) has dominated until recently due to its ease of application and provision of a general storm track activity measure, Eulerian methods do not tell us everything about the types of systems that constitute storm track activity, and most storm attributes can only be speculated from such statistics (Hoskins and Hodges 2002; Anderson et al. 2003). Thus, the present study chose not to use a proxy variable for cyclone tracks; rather, it adopted a feature-tracking (Lagrangian) approach based on an enhanced automated cyclone detection and tracking algorithm (Section 2.2.3 below) followed by substantial improvements of the output of that algorithm (Section 2.2.4).

2.2.3 Automated Methods for Cyclone Detection and Tracking

Besides the need to remedy the weaknesses inherent in manual methods (Section 2.2.1), there are many additional circumstances where it is imperative to objectively identify and track individual cyclones, especially in long time series of numerical analyses (e.g., NCEP/NCAR and ECMWF Reanalysis products, GCM simulations). In numerous applications, where relatively large sample sizes spanning many years are highly desirable for statistically significant results, labor-intensive manual tracking methods are much less feasible and less reliable (Sinclair 1997). Furthermore, automated procedures always yield consistent, repeatable results, and avoid the dependence on subjective decisions for which outcomes may vary over the period of study and between analysts.

A typical automatic method has two major components: (1) ***Cyclone Detection*** from a series of search patterns, testing whether a grid-point SLP (or surface geopotential height) value is surrounded by grid-point values higher than the central point being tested. The detection threshold determines how many systems are tracked (e.g., a threshold of 1 hPa will identify more systems than if a 2 hPa threshold is used); and (2) ***Cyclone Tracking***, based on a "nearest-neighbor" search procedure. A cyclone's trajectory is determined by computing the distance to cyclones detected in the previous chart and assuming the cyclone has taken the path of minimum distance. If the nearest neighbor in the previous chart is not within an area determined by imposing a maximum cyclone velocity in each direction, then cyclogenesis is assumed to have occurred. These thresholds are determined empirically for each specific region. Examples of such studies are Murray and Simmonds (1991a,b), König et al. (1993), Sinclair (1994, 1997), Serreze (1995), Blender et al. (1997), Serreze et al. (1997), and Geng and Sugi (2001).

Among the most important weaknesses of automated methods are:

• *Disadvantage of using near-surface geopotential height*

Blender et al (1997) noted one disadvantage of using this variable to identify and track surface cyclones: disconnected height contours may occur due to a large pressure gradient superimposed by the large-scale flow (e.g., Sinclair 1994, Fig. 1), although a vorticity maximum is present. The present author used NCEP/NCAR Reanalysis SLP data (Kalnay et al. 1996; Kistler et al. 2001) to objectively identify and track surface cyclones and so avoid this problem (Subsection 2.2.4a below).

• *Edge effect problem*

Serreze (1995) noted that, for a relatively small study domain, it was often impossible to determine whether an observed system formed (decayed) within or migrated into (out of) the data field, hence biasing cyclogenesis, cyclolysis, and SLP tendency statistics near the map edge. Therefore, the present study started with the entire Northern Hemisphere as initial data field and then confined subsequent analyses to the North Atlantic Basin, hence avoiding any risk of this "edge effect" problem.

• *Possible biases in algorithm output*

Owing to the 2-hPa cyclone detection threshold and relatively coarse grids used (e.g., NMC), Serreze et al. (1997) reported that cyclone central pressures will tend to be overestimated with this effect increasing poleward. Because of the tendency for greater overestimation of central pressures as systems deepen, SLP tendency also will tend to be underestimated, with this effect greater for intense systems with strong pressure gradients near their center. Thus, it can be argued that the algorithm will tend to depict cyclogenesis (cyclolysis) as occurring after (before) its "true" occurrence, hence possibly biasing where these events are observed. To remedy these possible biases, an enhanced version of Serreze's algorithm was used here. The algorithm is essentially that described by Serreze (1995) and Serreze et al. (1997), except (1) it was modified (by Serreze and Lo, Personal Communication, January 1998) for application to the more temporally consistent 6-hr NCEP/NCAR SLP fields, (2) a 1-hPa cyclone detection threshold was used (following McCabe et al. (2001) in which Serreze is a co-author), and (3) other "bugs" in the code were fixed (see Subsection 2.2.4a below for more details).

• *Spatial and temporal inhomogeneities*

Some ambiguities remain for these automated cyclone detection and tracking methods about what is treated as a "surface cyclone". This limitation is closely related to the spatial resolution of the analysis. Paciorek et al. (2002), who developed six indices of Northern Hemisphere cyclone activity (winters 1949-99) to estimate time trends, admitted that these cyclone count indices have two drawbacks despite their intuitive match to the idea of cyclone activity. First, the cyclone counts do not lend themselves to robust statistical analysis because they are discrete indices with small values in many locations, particularly the intense cyclone counts over land. Second, the definition of such indices involves several arbitrary choices. In addition to the spatial inhomogeneity, possible temporal inhomogeneities also may exist in cyclone data sets produced by automated methods (Trenberth and Olson 1988; Serreze et al. 1997). Some of these temporal discontinuities may arise where a new secondary development divides a cyclone into two circulation centers (e.g., Sinclair 1997, Fig. 6). To remedy the above weaknesses, the present author went one step further (next section) by applying a CDF objective analysis scheme to the cyclone counts produced by the above enhanced version of Serreze's algorithm. This CDF scheme reduces spatial and temporal inhomogeneities via a weighting function that controls both the space and time extent of the smoothing used to create the "CDF tracks".

• *Definition of thresholds*

Several input parameters (thresholds) have to be set for any automated cyclone detection and tracking method (Trigo et al. 1999). For instance, the most important adjustable parameters in Serreze's algorithm are:

- Pressure threshold for identifying cyclones (1 hPa); a possible bias in algorithm output related to this threshold was discussed above.

- Maximum search distance for tracking cyclones between time steps (800 km; hence, a maximum displacement velocity of about 130 km/h restricts the range of motion). Any possible bias due to inadequate specification of this threshold is alleviated by use of the CDF described below.

- Limit on allowable absolute pressure tendency between time steps (20 hPa).

- Limit on permissible northward/southward and westward migration between time steps (600 km). Again, any eventual bias resulting from an improper choice of this threshold is minimized by the CDF procedure.

- A possible additional constraint on cyclone intensity – that the averaged pressure difference between the central grid-point and the eight surrounding grid-points is larger than a certain threshold (e.g., Blender et al. 1997; Geng and Sugi 2001) – was not imposed in the present use of Serreze's algorithm.

2.2.4 Construction of a Hybrid Space- and Time-Smoothed Cyclone Track Density Function (CDF)

It is crucial that the cyclone data set developed here not be unwittingly degraded by the above limitations inherent in automatic methods. These feature-based analysis methods all have their deficiencies, but they have an intuitive match to the phenomena being studied (Paciorek et al. 2002). Confidence in the present cyclone data set was increased through use of the CDF. A Flow Diagram of this unique CDF technique is given in Fig. 2.1 and basic details appear in Table 2.1. The CDF approach involves successive applications of:

(1) an enhanced automated cyclone identification and tracking algorithm (Subsection ***a*** below/Step 1 in Fig. 2.1 and Table 2.1);

(2) the Akima (1978) scheme that converts non-uniform latitude-longitude grid to uniform latitude-longitude grid (Subsection ***b*** below/Step 2 in Fig. 2.1 and Table 2.1);

(3) a CDF objective analysis scheme (Subsection ***c*** below/Step 3 in Fig. 2.1 and Table 2.1); and

(4) a Bessel function, an appropriate spatial interpolation technique (Subsection ***d*** below/Step 4 in Fig. 2.1 and Table 2.1) to yield finer spatial resolution for CDF fields.

Hence, the previous automated algorithm-based studies (e.g., Geng and Sugi 2001) differ from this CDF-based cyclone study at least in two major respects: first, they suffer mainly from spatial and temporal inhomogeneities (Section 2.2.3 above); and second, they lack the several advantages related to the application of the CDF objective analysis scheme.

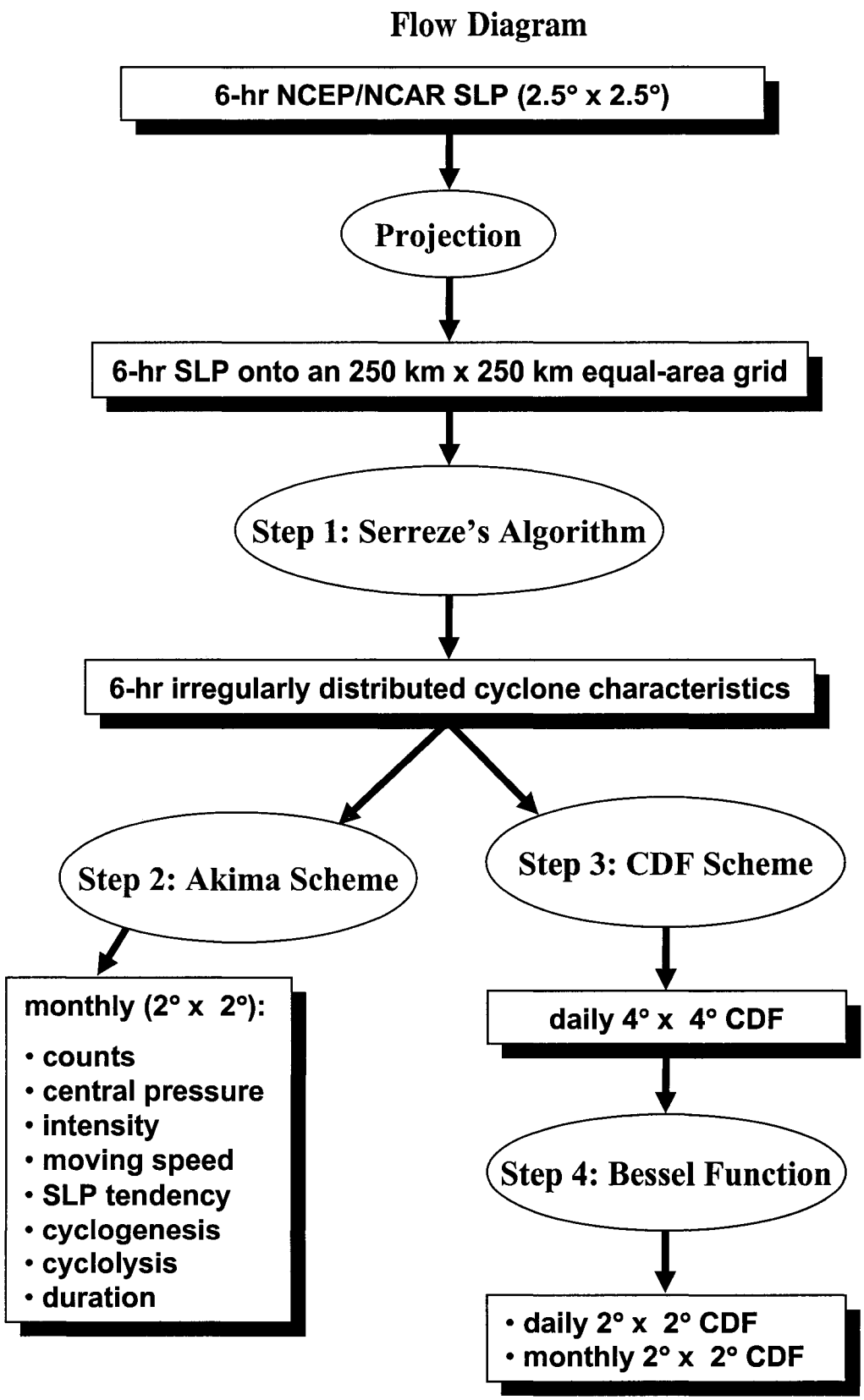


Fig. 2.1. Flow diagram of cyclone identification and tracking procedure incorporating CDF approach.

Table 2.1. Details of cyclone detection and tracking procedure incorporating CDF approach.

Step #	Application	Numerical Tool	Input	Output	Comments
Step 1	Cyclone Detection & Tracking Algorithm	An enhanced automated cyclone identification and tracking algorithm (Serreze 1995; Serreze et al. 1997; McCabe et al. 2001) using a 1-hPa cyclone detection threshold (e.g., McCabe et al. 2001).	6-hr NCEP/NCAR SLP (Kalnay et al. 1996; Kistler et al. 2001). SLP data were provided on a 2.5° x 2.5° grid and were first projected onto a 250 km x 250 km equal-area grid (Armstrong and Brodzik 1995) prior to identification of cyclones.	A 51-year (1948/49-1998/99) Oct-Mar compilation of North Atlantic 6-hr surface extratropical cyclone counts (i.e., frequencies) and related cyclone characteristics (e.g., intensity).	The algorithm was first run over the entire NH for each calendar month to avoid any risk of the edge effect problem (Serreze 1995). Final study domain= 20°N-72°N/ 80°W-0°.
Step 2	Akima Scheme	Akima (1978) scheme, a numerical method of bivariate interpolation and smooth surface fitting for irregularly-distributed data points.	The above North Atlantic 6-hr surface extratropical cyclone counts and related cyclone variables (e.g., intensity).	2° x 2° monthly anomalies of: counts, central pressure, intensity, moving speed, pressure tendency, cyclogenesis and cyclolysis events, and duration.	The input domain for Akima scheme was set to (10°N-90°N/ 100°W-0°) – a domain larger than the final one to reduce the edge effect problem due to Akima scheme.
Step 3	Objective Analysis Scheme	A hybrid space- and time- objective analysis scheme (Anderson and Gyakum 1989) that controls the scale, time, and the number of disturbances admitted as cyclones.	North Atlantic Oct-Mar 6-hr surface cyclone counts for 1948-99 (i.e., output of Step 1).	A hybrid space- and time-smoothed surface cyclone track density function (CDF) for the North Atlantic, on a 4° x 4° grid with 1-day time resolution.	The resulting CDF field has had the smaller time (<7 days) and space (< 3.5°) scales filtered out.
Step 4	Bessel Function	A spatial interpolation technique (bilinear interpolation as a first guess, then a higher order fit) to yield finer spatial resolution for the CDF fields.	The above daily CDF fields on 4° x 4° grid for 1948-99.	Daily CDF fields on a 2° x 2° grid for 1948-99; monthly (from Oct to Mar) CDF anomalies.	The daily and monthly CDF anomalies are in units of cyclones/day/ (250 km x 250 km area).

a. Step 1: Application of Serreze's Cyclone Detection & Tracking Algorithm

Six-hourly surface cyclone counts and other related cyclone characteristics (central pressure, intensity, translation velocity, pressure tendency, and cyclogenesis and cyclolysis events) over the entire Northern Hemisphere for each individual calendar month during 1948-99 were produced using an enhanced version of Serreze's cyclone detection and tracking algorithm (Serreze 1995; Serreze et al. 1997; McCabe et al. 2001) applied to 6-hourly NCEP/NCAR Reanalysis SLP fields. The logic of this algorithm is fully described in Serreze (1995) and Serreze et al. (1997). Subsequent analyses were confined to the North Atlantic Basin and for winter semesters only. Therefore, the cyclone data set produced by this step is a 51-year (1948/49-1998/99) winter semester (October-March) compilation of North Atlantic 6-hourly surface extratropical cyclone variables (9294 study days). The (final) study domain extends from 20°N to 72°N, and from 80°W to 0°. The total number of the 6-hourly cyclones identified over this domain throughout the period of coverage is 98,294, an average of 2.64 cyclones for each 6-hour interval.

In the present study, a 1-hPa cyclone detection threshold was used following Deser et al. (2000) and McCabe et al. (2001). A cyclone is defined as surface-pressure low and therefore identified as a local minimum in the SLP field. This local minimum should occur within an area covering 3 x 3 grid-points. By inspecting a series of 3 x 3 search shells of grid-points, the algorithm can identify systems with essentially any shape (Serreze 1995). From a one-month comparison with manual analyses, Serreze (1995) reported that this nearest-neighbor approach (cf., algorithms of Murray and Simmonds 1991a, and Sinclair 1994) tracked systems correctly better than 98% of the time. Other investigators used the 1-hPa cyclone detection threshold (e.g., Deser et al. 2000; McCabe et al. 2001 in which Serreze is a co-author) with the 6-hourly NCEP/NCAR Reanalysis

SLP data, whereas Serreze (1995) and Serreze et al. (1997) previously used a 2-hPa threshold with the 12-hourly NMC SLP fields.

The newer version of Serreze's algorithm has been one of his main projects over the last few years (Personal Communication, October 1997). Hence, many of the possible "bugs" in the code have been worked out. According to his 1997 paper, Serreze has "tinkered" with it since his 1995 paper when he tracked cyclones over the Arctic. For instance, he fixed a "bug" in the local Laplacian calculation that defines cyclone intensity. In February 1998, a revised version of Serreze's algorithm was written by the present author after fixing the following two bugs: (1) the first one found by the author had to do with marking the end of months; i.e., the starting and stop dates for the charts; and (2) leap versus non-leap years (found by D. H. Portis, CIMMS, OU). Furthermore, in December 2000 this author incorporated in the above version a correction by Mike Timlin (NOAA-CIRES Climate Diagnostics Center (CDC), University of Colorado, Personal Communication, May 2000) for computing distances across the prime meridian. In summary, this study used the latest version of Serreze's algorithm (essentially that described in McCabe et al. 2001) in addition to incorporating the above corrections in the code. Note that Serreze's algorithm (using 1-hPa threshold) now is run on a daily basis by CDC; see http://www.cdc.noaa.gov/map/clim/storm.shtml that shows tracked cyclones through their life cycle for the most recent 30 days (cyclones are categorized by intensity or week).

The 2.5° x 2.5° input SLP data were first projected (within Serreze's newer algorithm) onto an Equal-Area Scalable Earth (EASE) 250 km x 250 km equal-area grid (Armstrong and Brodzik 1995) via a Cressman (1959) interpolation scheme, prior to

identification of cyclone centers. Hence, the resulting cyclone counts represent the number of cyclone occurrences per 250 km x 250 km area. Use of such an equal-area grid has the advantage of obviating the need to use an "area correction" scheme (Section 2.2.1; see Changnon et al. 1995 for an overview). However, the resulting raw irregularly-distributed cyclone counts (and other related attributes such as intensity) suffer mainly from spatial and temporal inhomogeneities. A standard way to surmount this problem is to average grid values over time and/or over a certain region (e.g., latitudinal bands), as has been done by most investigators (e.g., Geng and Sugi 2001 and McCabe et al. 2001, who used December-February and November-March as winter seasons, respectively). Deser et al. (2000), who used primarily the same Serreze (1997) algorithm in documenting Arctic sea ice variability in the context of recent atmospheric trends, summed the number of cyclones for each winter (January-March) season during 1958-97 and, unlike the previous cyclone studies, did not apply any areal averaging. Instead, they smoothed the cyclone totals with a three-point binomial filter in the zonal and meridional directions, and so maintained the 2-dimensional (2D) structure of their cyclone data set.

However, all previous cyclone studies treated the space and time dimensions separately, whereas in nature these two dimensions are closely related, particularly in the context of cyclone track variability. Therefore, the principles followed in this present analysis are: (1) to adopt a full 2D grid analysis (2° x 2°) instead of areal averaging; (2) to maintain a much finer time resolution (e.g., one day for cyclone tracks and one month for other cyclone characteristics); and (3) to account for space and time *concurrently* in developing cyclone tracks (Step 3 below).

b. Step 2: Application of Akima Interpolation Scheme

The 6-hourly cyclone counts were summed for each individual winter month (from October to March) instead of overall winter *seasons* during 1948-99. The resulting monthly cyclone totals were then interpolated onto a 2° x 2° grid using the Akima (1978) scheme – a numerical method of bivariate interpolation and smooth surface fitting for z values given at irregularly-distributed data points in the x-y plane. The interpolating function is a fifth-degree polynomial in x and y defined in each triangular cell that has projections of three data points in the x-y plane as its vertexes. Each polynomial is determined by the given values of z and estimated values of partial derivatives at the vertexes of the triangle. Procedures for dividing the x-y plane into a number of triangles, for estimating partial derivatives at each data point, and for determining the polynomial in each triangle are described in Akima (1978).

Application of the Akima scheme yielded a monthly regularly-distributed "cyclone counts" variable, henceforth referred to as CCS (in cyclones/month/250 km x 250 km). Note that Akima scheme was applied over a domain (10°N-90°N/100°W-0°) larger than the final study domain (20°N-72°N/80°W-0°) to minimize the edge effect problem due to Akima interpolation scheme. Similarly, the same Akima procedure was applied to the 6-hourly cyclogenesis and cyclolysis events to generate monthly cyclogenesis (GEN) and cyclolysis (LYS) totals in cyclones/month/250 km x 250 km. Removal of the climatological seasonal cycle from the individual monthly mean fields of any cyclone parameter in this study was accomplished by subtracting the long-term averaged values for a given grid-cell and calendar month from corresponding values for the same grid-cell and calendar month in individual years.

Figs. 2.2a,d present two representative cases showing monthly cyclone totals (CCS) for October 1997 and March 1993, respectively. Spatial inhomogeneities are particularly noticeable in such fields primarily because the time dimension is not accounted for in the Akima scheme. To maintain a much finer time resolution (e.g., day or month) with no spatial inhomogeneities at the same time, a space/time filter (i.e., CDF; next step) will be applied to cyclone counts.

Other cyclone variables such as Cyclone Central Pressure (CCP, hPa), Cyclone Intensity (CIN, local Laplacian of SLP, 10^5 hPa/m^2), Cyclone Translation Velocity (CTV, km/h), and Cyclone Pressure Tendency (CPT, hPa/6 hr), were computed using the following steps: (1) for each individual winter month, the Akima scheme was applied to the 6-hourly cyclone data to yield daily grid-cell data within that month; (2) daily grid-cell anomalies were computed by subtracting from all daily data in a given winter month the monthly mean values for that grid-cell and calendar month (e.g., Lau 1988); (3) monthly means of the daily anomalies were computed next; and (4) monthly gridded anomaly fields finally were generated. Following several authors (e.g., Roebber 1984; Serreze et al. 1997), the SLP tendency values were adjusted geostrophically to a reference latitude (46°), in order to take into account the fact that cyclones at different latitudes with similar pressure gradients would produce different geostrophic winds.

Another important variable, cyclone average lifetime (CLT, days) was quantified. This parameter was not directly generated by the enhanced cyclone detection and tracking algorithm (Step 1), but was developed as follows: (1) for each winter month, the total number of individual systems detected over the entire Northern Hemisphere was determined from the 6-hourly cyclone data set; (2) the duration of each system identified

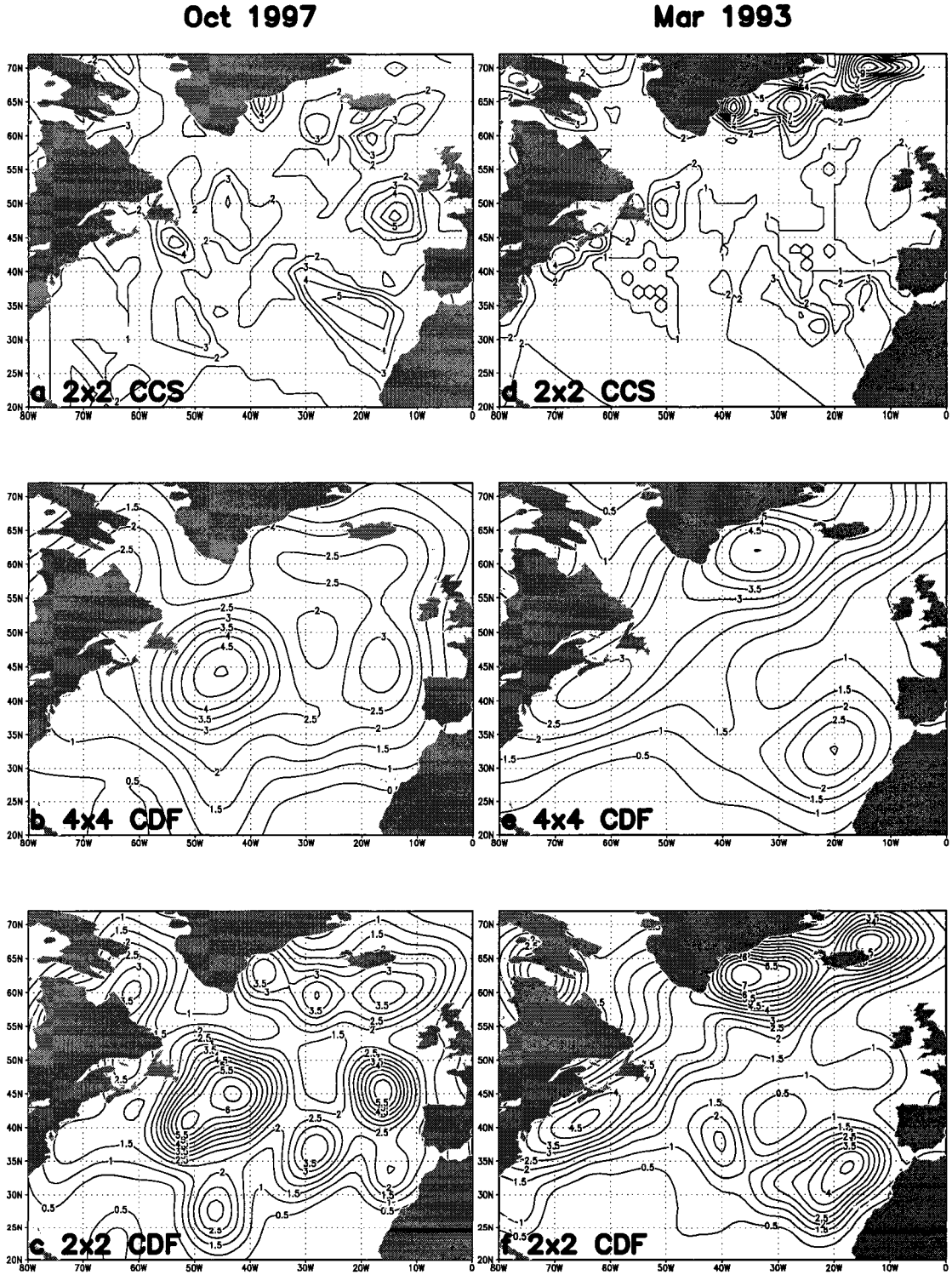


Fig. 2.2. Illustration of results of analysis stages for two representative months. Maps present distributions for October 1997 in left panels (a-c) of North Atlantic: (a) surface cyclone counts (CCS), number of cyclones per month per 250 km x 250 km area, interpolated onto a 2° x 2° grid via Akima scheme (Step 2 in Fig. 2.1 and Table 2.1); (b) surface cyclone track density field (CDF) computed as monthly mean of daily CDF fields that were calculated on a 4° x 4° grid (Step 3) prior to application of Bessel function; and (c) as in (b) but after interpolating the daily 4° x 4° CDF fields onto a 2° x 2° grid using the Bessel function (Step 4). Right panels (d-f): as in panels (a-c) but for March 1993.

during that month was then calculated; (3) the resulting CLT data set was confined to the North Atlantic Basin. The initial treatment of the entire Northern Hemisphere permitted identification of systems that formed outside the North Atlantic and eventually lost their identities within this basin. The CLT variable was assigned to the final position where the system lost its identity; (4) the Akima scheme was then applied to yield a 2° x 2° gridded CLT field; and (5) monthly CLT anomalies finally were derived.

As will be shown in subsequent chapters, the development of such Akima-based cyclone fields is enlightening because of the additional physical insights they provide by revealing the physical consistency among the independent variables; e.g., CDF tracks (that will be constructed in Step 3 below) are compared to cyclone intensity patterns. Additionally, the wide range of Akima-based gridded variables will be used in subsequent chapters to obtain a rich picture of North Atlantic cyclonic activity.

c. Step 3: Application of Objective Analysis Scheme

To date, all North Atlantic cyclone studies based on automated cyclone detection and tracking algorithms (Section 2.2.3) determined a "storm track" by identifying successive latitudes and longitudes of cyclone centers with the same system identification number. Because of the above weaknesses inherent in such a standard (raw) "cyclone track" definition, the investigation went a step further to construct hybrid space- and time-smoothed surface cyclone track density function (CDF) fields for the study domain based on the objective analysis scheme of Anderson and Gyakum (1989). The CDF approach is designed to provide a better description of modal "storm tracks", rather than to describe the movement of individual cyclones. The constraint of having to track individual cyclones, which is inherent in all automated and manual methods, is relaxed in the CDF

approach.

The North Atlantic 6-hourly surface extratropical cyclone counts for the winter semesters (October-March) of 1948-99, outputted from Step 1 (Fig. 2.1, Table 2.1) were used as input for the objective analysis scheme to yield "*CDF tracks*". Note that the same 6-hourly surface cyclone counts were used (in Step 2) as input for the Akima scheme to yield a different gridded variable (CCS) that represents cyclone *counts*. The CDF construction was accomplished by evaluating Eq. 1a below on a 4° x 4° grid with 1-day time resolution,

$$C(\mathbf{r},t) = \sum_{j=1}^{N} W(\mathbf{r}-\mathbf{r}_j, t-t_j) \qquad (2.1a)$$

$$W(d\mathbf{r},dt) = \cos^2\frac{d\mathbf{r}}{S_r}\cos^2\frac{dt}{S_t} \qquad (2.1b)$$

when $|\frac{d\mathbf{r}}{S_r}|$ and $|\frac{dt}{S_t}|$ are less than $\pi/2$, otherwise W=0 (Anderson and Gyakum 1989). Here, $\mathbf{r}$ and t denote the position vector of the CDF variable and corresponding time, respectively, with $\mathbf{r}_j$ being the position vector of the j^{th} cyclone identified at time t_j. The summation in Eq. 1a is taken over all of the 6-hourly identified cyclones (N=98,294) in the data set. Owing to this huge total number of cyclones, computational requirements became prohibitive if the CDF space and time resolutions were less than 4° latitude/longitude grid and 1-day, respectively.

The W(d$\mathbf{r}$,dt) is a weighting function that defines the space and time extent of the smoothing used to create the function C($\mathbf{r}$,t). Following Anderson and Gyakum (1989), the space and time resolutions of the analysis are determined by the parameters S_r and S_t, which are set to $14/\pi$ degree of latitude (or longitude) and $28/\pi$ days, respectively. The

weighting function (Fig. 2.3) gives more (less) weight to nearby (distant) identified cyclones *in space and time simultaneously*. Hence, to define "cyclone tracks", the CDF technique accounts for all surrounding identified ("observed") cyclones (in all directions) at a given time, as well as for all observed cyclones in the near past and future of the observation of a given cyclone location. Thus, the CDF tracks are *not* "quantized", which is the essence/uniqueness of this CDF approach, but instead should be thought of as spatially/temporally continuous cyclone tracks as opposed to the standard (raw) individual (fragmented) cyclone tracks. Note that the CDF function controls – through its weighting function W(**dr**,dt) – the scale, time, and the number of disturbances admitted as cyclones.

The above approach contrasts with the methodology of previous studies in several important respects. Geng and Sugi (2001) developed their cyclone data set over the North Atlantic on a 4.5° x 4.5° grid with a 3-month (December-February) time resolution for 1958-98. McCabe et al. (2001) analyzed trends in Northern Hemisphere surface cyclone frequency and intensity for 5° latitudinal bands with a 5-month (November-March) time resolution for 1959-97. It should be noted that, to date, *no* previous cyclone study over the North Atlantic Basin considered application of such a CDF approach or any similar objective analysis scheme; rather, all investigators have contented themselves just with using cyclone counts. Further, note that the above CDF fields will be interpolated further via a Bessel technique (Step 4 below), onto a 2° x 2° grid with a 1-day time resolution. Note that the Step 4 could be avoided if appropriate computer resources were available at the time the computation of the 4° x 4° CDF fields was performed.

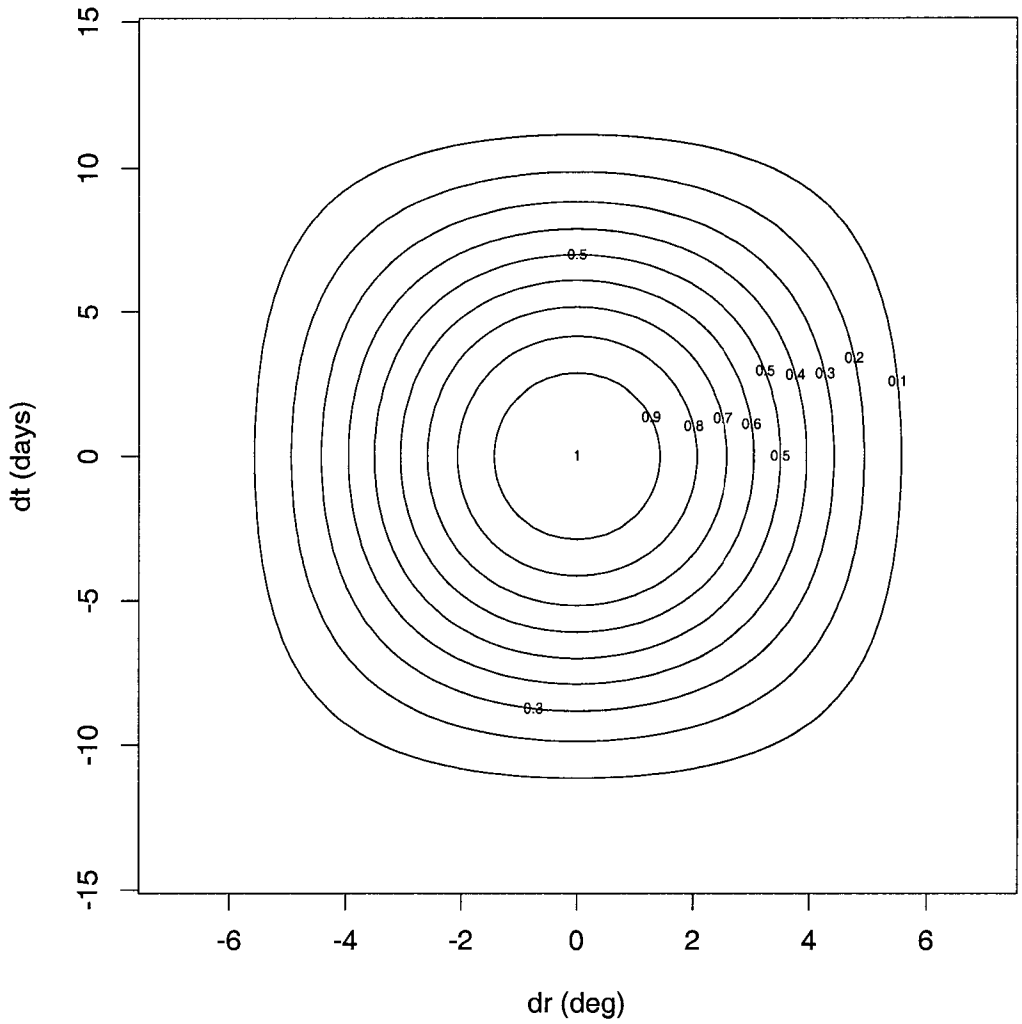


Fig. 2.3. Weighting function W(**dr**,dt) (dimensionless) for the hybrid space- and time-smoothed surface cyclone track density function (CDF) applied over the North Atlantic Basin. Abscissa **dr** (in degrees) denotes the Euclidean distance between the vector position of the CDF variable and the vector position of a cyclone identified via an automated cyclone detection and tracking algorithm. Ordinate dt denotes the corresponding difference (in days) between the CDF variable time and the time at which the identified cyclone was detected. See text for statement of characteristics of CDF fields produced by this weighting function.

Figs. 2.2b,e present the CDF fields computed as monthly mean of the above daily 4° x 4° CDF grid-point values for October 1997 and March 1993, respectively. Compared to the 2° x 2° cyclone frequency field for the same month (Figs. 2.2a,d), the noise in the data clearly is suppressed by applying the CDF scheme. Note that the key

features of Fig. 2.2a (i.e., cyclone count maxima northwest of Portugal, mid-Atlantic, northwest of Newfoundland) are retained in Fig. 2.2b. However, the cyclone track maximum off the Atlantic coast of Morocco is not identified at this coarser spatial resolution of 4° x 4°. Similarly, in March 1993, the cyclone frequency maximum over the Greenland Sea (Fig. 2.2d) is very poorly represented by the 4° x 4° resolution (Fig. 2.2e). This resolution-related problem will be resolved via application of a Bessel function (next step).

In summary, the construction of such CDF fields has several advantages, such as:
(1) assigning irregularly-distributed cyclone counts to points on a regular grid in space at each time step;
(2) suppression of noise in the data to accentuate the synoptic-scale disturbances with characteristic periods of several days, which is accomplished without applying the medium-pass filter (i.e., "proxy" method; Section 2.2.2) described in Blackmon (1976);
(3) better suppression of high-frequency spatial and temporal fluctuations via the CDF weighting function (Fig. 2.3) – which is approximately equivalent in resolution to a bin counting procedure using a $\mp 3.5°$ box with ∓ 7 day time resolution – so that this resulting CDF field on a 4° x 4° grid has had the smaller time (<7 days) and space (< 3.5°) scales filtered out;
(4) relaxation of the constraint of tracking individual cyclones; and
(5) additionally and importantly, these uniform CDF fields should minimize the potential errors that can affect eigenvectorial patterns extracted from irregularly-spaced data (e.g., Karl et al. 1982).

d. Step 4: Application of Bessel Function

Equations 1a and 1b allow computation of cyclone track density fields for any space and time resolution. As stated before, the space and time resolutions of the present CDF calculations were set in the previous step to 4° x 4° and 1-day, respectively. This spatial-temporal resolution was the finest practicable from the standpoint of computer resources available at the time the computations were performed, as the CDF scheme is computationally very expensive. Therefore, a subsequent and final step (Step 4) was needed in the analysis – the spatial interpolation of the above daily 4° x 4° CDF fields onto a 2° x 2° grid using a Bessel function, to provide finer spatial resolution for the CDF fields.

The Bessel technique used here was first developed at the U.S. Navy's Fleet Numerical Meteorology and Oceanography Center (by D. Hensen, http://tenkimap.com/grads/udf/), and operates as follows. First, at each time step, bilinear interpolation is performed at all points to produce a "first guess" or background field. Then, improvements to the bilinear "first guess" field are made using higher-order terms in the Bessel interpolator. Generally, it is recommended to employ a Bessel technique when interpolating because its use of higher-order terms in the polynomial interpolation function produces a closer fit to the original data in regions of rapid changes (e.g., large gradients around low-pressure centers). Bessel functions have been used in numerous applications in climate science in recent years (e.g., Winkler et al. 1997; Palutikof et al. 1997; Palutikof et al. 2002).

Figs. 2.2c,f present the CDF fields computed as monthly mean of the above daily 2° x 2° CDF grid-point values for October 1997 and March 1993, respectively.

Compared to the 4° x 4° CDF pattern for the same month (Figs. 2.2b,e), we can clearly see that the cyclone tracks can be identified much more definitively at the finer spatial resolution. Fig. 2.2 further reveals that high-resolution analyses using the CDF scheme may resolve many additional weaker disturbances while coarse-resolution analyses may fuse or even eradicate smaller features that are actually important circulation centers. Also, this figure shows that a single large CDF feature at coarser resolution may break up into several smaller features at finer resolution.

Once the daily CDF fields were created from the above Bessel technique, daily and then monthly CDF anomalies were computed as in Step 2.

2.3 CORRELATION LENGTH OF CDF ANOMALIES

Fig. 2.4 presents a correlation R_{lk} for the CDF anomalies over the North Atlantic Basin. R_{lk} is the temporal correlation of the CDF anomalies between a given grid point at location l and a grid point at location k. That is, k is fixed, and R_{lk} is calculated for all other grid points in the study domain. In this figure, k varies from 1 to 6, corresponding to different grid points centered over the Labrador Sea, southeast of Greenland, southwest of Newfoundland, East of Iceland, storm-formation region (Sutton and Allen 1997), and to the west of the Strait of Gibraltar, respectively. The importance of these oceanic regions will be discussed in subsequent chapters. Fig. 2.4 reveals that the correlations at short distances from the centers are very near one. Note in particular that the correlation for the southeast of Greenland displays a simple south-north dipole structure. This figure also indicates a substantial anisotropy with elliptical contours in most regions of the Basin. This shows that the CDF function is not homogeneous.

The isotropic component of the correlation field (Fig. 2.4) can be determined by first plotting the above correlation R_{lk} of each grid point pair (l,k) on a scatter diagram as a function of the absolute distance r between the two grid points l and k (Daley 1991, p. 112). Fig. 2.5 is an example of such a scatter diagram for a grid point centered over the storm-formation region. Each point in this figure represents the correlation of a single grid point pair. Then, one can fit a curve through all the points using an appropriate fitting procedure to produce a single curve R(r) for this particular region. Such fitted curves can be used for forecast background field (Daley 1991). Also, one has to know the correlogram R(r) (Fig. 2.5) (or the variogram) to use either generalized least-squares or kriging (Venables and Ripley 1994, p. 389). It should be noted that the correlogram for CDF depends upon each region (plots not shown).

In general, calculation of background error correlations can be made considerably more efficient if the above correlation functions are specified as analytic functions. Thus, a functional form for CDF can be proposed. These functional forms are sometimes called correlation models or candidate correlation models (see Daley 1991 for more details), and they are very useful in objective analysis/atmospheric data assimilation.

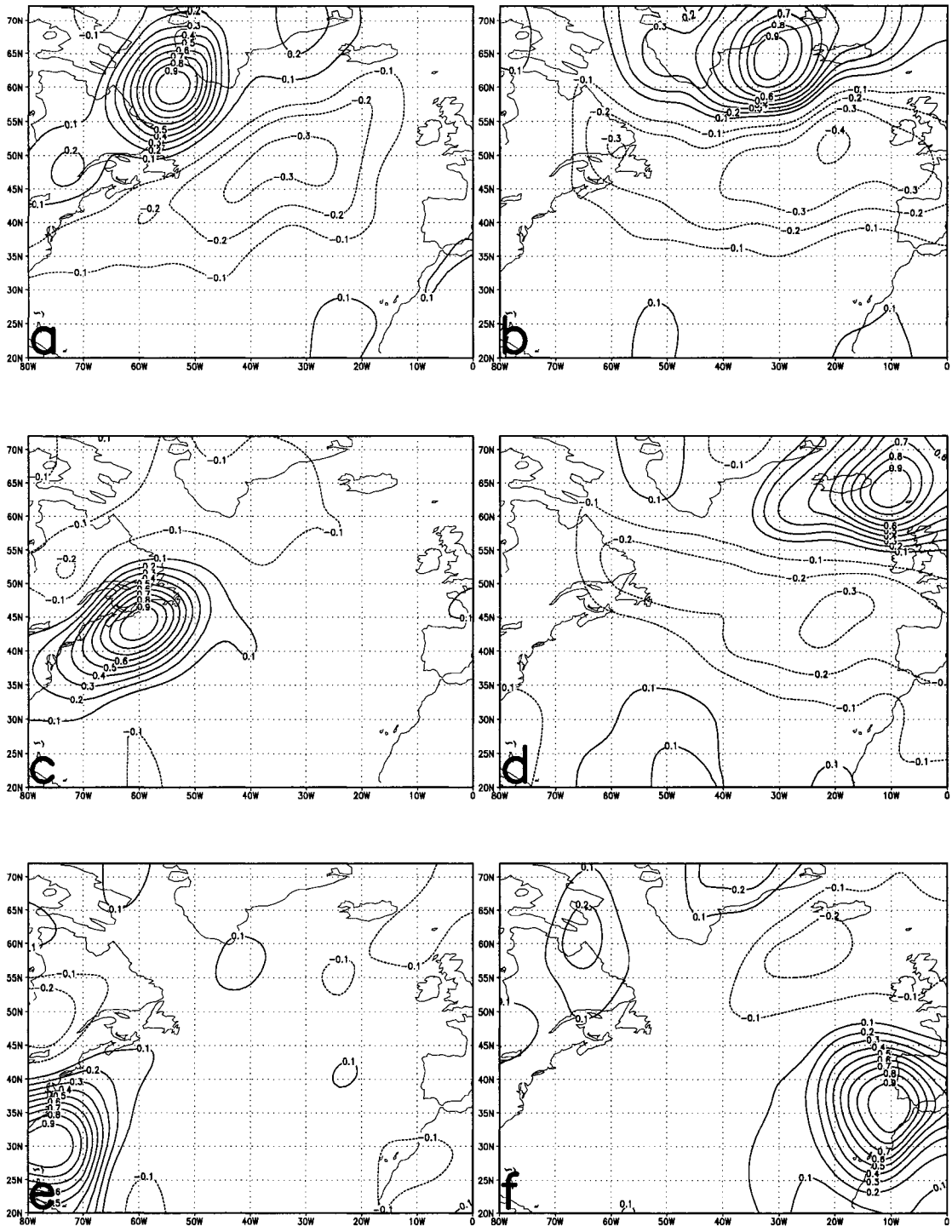


Fig. 2.4. Correlation field for the CDF anomalies. All correlations are with respect to a fixed grid point centered over the Labrador Sea (Panel a), southeast of Greenland (Panel b), southwest of Newfoundland (Panel c), east of Iceland (Panel d), storm-formation region (Panel e), and to the west of the Strait of Gibraltar (Panel f). See text for more details.

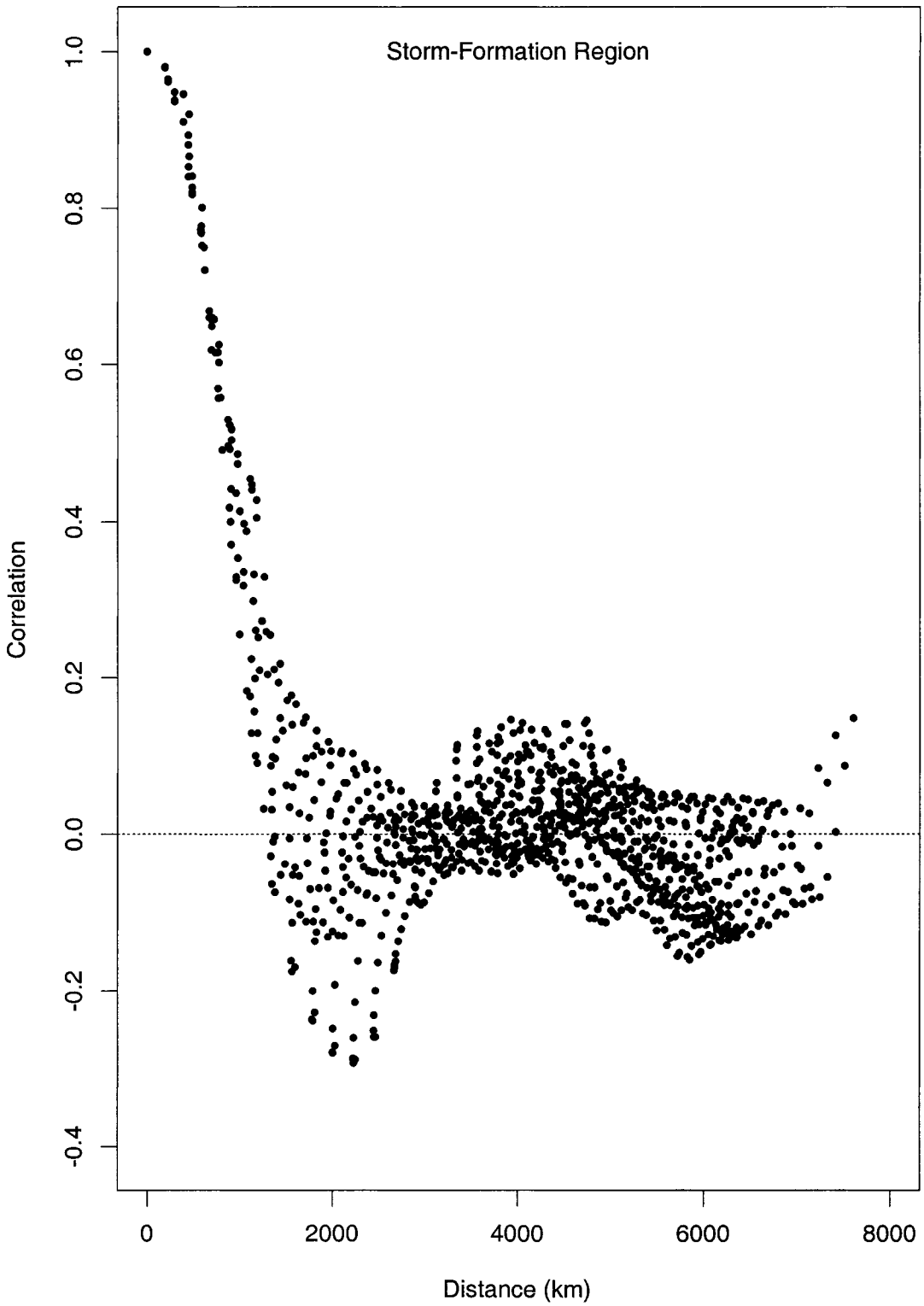


Fig. 2.5. Correlogram for the CDF anomalies with respect to the grid point (30°N, 76°W) centered over the storm-formation region (Sutton and Allen 1997). The correlation field of CDF anomalies with respect to this point is shown in Fig. 2.4.

2.4 SIGNIFICANCE OF CDF AND RELATED TOPICS

The above construction of the hybrid space- and time-smoothed surface CDF fields over the North Atlantic for the winter semesters (October-March) of 1948-99 provided the foundation for this investigation. The NCEP/NCAR reanalyses employed to develop these CDF fields are regarded as one of the best representations of the Northern Hemisphere atmosphere (e.g., Simmonds and Keay 2000a); use of these reanalyses at 6-hourly intervals means that uncertainties with identifying and tracking individual cyclones are greatly reduced. The aim of this unique CDF approach is to give new insight into storm track organization and behavior over the North Atlantic. These CDF fields are used extensively in subsequent chapters – for a comprehensive and more accurate long-term climatological description of North Atlantic winter surface extratropical cyclone activity (Chapter 3); for a new classification of North Atlantic cyclone behavior into major modes of variability on interannual time-scale and associations with regional climate variations (Chapter 4), which provides better understanding of the dynamics of the atmosphere; for analyzing the decadal-to-multidecadal variability of cyclone activity, involving ocean-atmosphere interactions (Chapter 5); as well as for possible projections of 21st century cyclone behavior under increasing atmospheric greenhouse gases, and their implications for regional and local weather conditions (Chapter 6). Encouraging preliminary results concerning mainly Chapters 4-5 appear in El Hamly et al. (2001a,b).

CHAPTER 3: LONG-TERM CLIMATOLOGICAL FEATURES OF CYCLONE ACTIVITY

3.1 INTRODUCTION

It long has been appreciated that mobile, O-scale (1000 km) high and low pressure systems generate much of the day-to-day weather variability in midlatitudes. Accordingly, it is natural that the geographical distribution and characteristics of these transients – whether in terms of their preferred paths of travel (i.e., storm tracks), relative frequency of occurrence, or range of intensity – have been and remain a topic of extreme relevance to the science and practice of weather forecasting (Chang et al. 2002). Consequently, studies concerning the spatial distribution of cyclogenesis and main storm tracks have long appeared in the meteorological and climatological literature (Whittaker and Horn 1981). Furthermore, researchers engaged in modeling the large-scale atmospheric circulation to understand climate variability, not only simulate the mean flow, but also cyclone development, movement, and decay. To these modelers, knowledge of the observed preferred locations and typical characteristics of storm tracks is very useful in assessing the quality of their climate simulations (Whittaker and Horn 1984; Chang et al. 2002).

To date, no published study has presented a comprehensive basic climatology (mean and variability) of observed North Atlantic winter surface extratropical cyclone characteristics. Previous work included a few papers that dealt with very limited sectors of the North Atlantic Basin – e.g., Serreze et al. (1997) examined climatological features of Icelandic Low cyclone activity using Serreze's automated algorithm for identifying and

tracking surface cyclones (described in Chapter 2 above), and Hirsch et al. (2001) developed a climatology of the U.S. East Coast winter storms using another automated procedure. Other research treated the North Atlantic within the entire Northern Hemisphere – e.g., Lambert (1988) extracted a winter cyclone event climatology from a five-year simulation by the Canadian Climate Centre GCM, and Paciorek et al. (2002) examined Northern Hemisphere extratropical storm activity for the winters 1949-99 using six indices derived from the NCEP/NCAR Reanalysis data.

To date, the only paper that has dealt, even indirectly and partially, with basic climatological aspects of cyclone activity within the North Atlantic Ocean is Geng and Sugi (2001). They performed a Principal Component Analysis of cyclone frequency over the North Atlantic and then regressed cyclone parameters (i.e., cyclone frequency, central pressure gradient, deepening rate, moving speed) upon the first principal component of cyclone frequency to examine trends in cyclone activity. Superimposed on the resulting regression patterns (depicted in their Fig. 2) are single isopleths of climatological cyclone frequency of 7.0 cyclones/4.5° latitude x 4.5° longitude grid cell/season (December-February), central pressure gradient of 16 hPa/1000 km, deepening rate of 0.3 hPa h^{-1}, and moving speed of 13 m s^{-1}. This presentation of only a single isopleth for each individual cyclone parameter thus failed to provide a complete 2-dimensional geographical distribution of these cyclone variables.

The main difficulty in compiling a thorough basic climatology of North Atlantic cyclone characteristics lies in the spatial and temporal inhomogeneities ("spikiness", see Chapter 2) present in previous cyclone data sets. For instance, Paciorek et al. (2002) developed six indices of Northern Hemisphere cyclone activity (winters 1949-99) from

the NCEP/NCAR Reanalysis data to estimate time trends. They admitted that their cyclone count indices have drawbacks despite being intuitively matched to the idea of cyclone activity for two reasons: (1) they do not lend themselves to robust statistical analysis because they are discrete indices with small counts in many locations, particularly the intense cyclone counts over land; and (2) their definition involves several arbitrary choices. This may explain why such climatologies are seldom derived using automated cyclone detection and tracking methods. Hence, producing objectively analyzed data sets of cyclone parameters on regularly-spaced grids expedites development of a basic cyclone climatology and affords at the same time the opportunity to explore some of the most important characteristics of these cyclones such as persistence.

The development in Chapter 2 of the hybrid space- and time-smoothed cyclone track density function (CDF) provides a unique quantitative measure of winter surface extratropical storm tracks on a grid for the North Atlantic Basin. Therefore, one purpose of this chapter (Section 3.2) is to use the carefully constructed daily CDF data set to develop a previously unavailable long-term basic climatology (mean and standard deviation) of North Atlantic cold-season (October-March) surface extratropical cyclone occurrence over 51 years (1948/49-1998/99) for a 2° latitude x 2° longitude grid. Additionally, this section presents long-term climatologies of other related cyclone characteristics (e.g., intensity, moving speed, pressure tendency) generated by application of the Akima scheme described in Chapter 2 to yield a rich picture of the climatological features of cyclone behavior. The availability of these cyclone fields is enlightening because they permit us to demonstrate physical consistency among the cyclone variables (e.g., CDF is compared to cyclone intensity).

The present geographical domain is sufficiently large, and the 51-year winter semester study period is sufficiently long, that this study can treat a large number of cyclone systems that both formed and eventually lost their identities over the North Atlantic Ocean. Further, Zishka and Smith (1980) stated that, although cyclones (and anticyclones) exhibit short-term variations, they also possess a high degree of continuity over longer time-scales dictated by the long-term radiation balance, land/water distributions, and orographic features. Hence, the present large gridded cyclone data base for this basin also provides the opportunity to examine one of the distinctive and unique characteristics of these cyclones – climatological persistence, on which research has not been published previously. Such persistence of cyclone activity will be examined in Section 3.3, through documentation of geographical distribution patterns of both month-to-month correlation analysis and the autocorrelation function at different lag months. Paciorek et al. (2002) noted that there is no standard measure of cyclone activity, because cyclones are complicated phenomena that may exhibit changes in intensity, duration, location, and frequency. Section 3.4 examines relationships between cyclone variables themselves (e.g., CDF versus intensity) through temporal correlations between pairs of cyclone parameters at each grid point to assess how these cyclone attributes vary jointly over the North Atlantic Basin.

Climate scientists increasingly are devoting attention to understanding the modes and mechanisms of natural variability in the climate system (e.g., Simmonds and Keay 2000b). Therefore, after documenting the *mean* behavior of various characteristics of North Atlantic winter cyclones over five decade period (Sections 3.2, 3.3, and 3.4), the data set developed in Chapter 2 also allows us to consider several aspects of the

variability of these features in subsequent chapters. Chang et al. (2002) noted that midlatitude storm track variability of the Northern Hemisphere cool season spans a broad range of time-scales. It is becoming common in climate science to focus on either the short-term/high-frequency (e.g., Lau 1988) or longer-term/low-frequency (e.g., Chang and Fu 2002) variability of the process being studied.

Thus, given the availability of the North Atlantic CDF fields, it was possible to address the following two questions – first, is it legitimate to separate the high-frequency (HF) and low-frequency (LF) components of the CDF signal and, second, how does this distinction vary over the North Atlantic Basin? This second issue raises the question of the efficacy of producing regional averages of the 2-D gridded fields of the CDF and related cyclone characteristics that readily would yield time series. This spatial averaging approach is widely used in climate science (e.g., Simmonds and Keay 2000b; Geng and Sugi 2001; McCabe et al. 2001; Paciorek et al. 2002), but can obscure important details (Paciorek et al. 2002). The advantage of applying such spatial averaging to 2-D gridded fields makes computations much faster and subsequent analyses much easier, since it yields time series that allow one to appreciate detailed temporal variations of cyclone parameters. One way to address this important issue is to perform both a full grid and regional analyses (e.g., Paciorek et al. 2002). However, one original way to address both issues raised above (i.e., HF versus LF components; full grid analysis versus regional averaging), *without* necessarily performing both full grid and regional analyses, is to use Wavelet Analysis. Thus, Section 3.5 examines spatial distribution patterns of Percentage Wavelet Energy Concentration (PEC) of CDF anomalies over the North Atlantic obtained using the Discrete Wavelet Transform (DWT) technique. This section will address the

following three issues – the utility of performing such a wavelet transform, the selection of DWT and not other wavelet transforms, and how this PEC approach separates the CDF signal into HF and LF components and addresses the "full grid analysis versus regional averaging" issue as well. Finally, Section 3.6 recapitulates the key points and outlines the significance of the work presented in this chapter.

3.2 CLIMATOLOGICAL FEATURES OF CYCLONE ACTIVITY

This section examines the long-term basic climatological patterns of cyclone behavior (CDF and related cyclone characteristics) on seasonal and monthly time-scales.

3.2.1 Long-Term Mean and Standard Deviation of Cyclone Characteristics

Fig. 3.1 presents geographical patterns of long-term mean cyclone activity in terms of the CDF, pressure tendency, translation velocity, and intensity. A total of 306 winter months were used for each individual cyclone parameter. The mean CDF pattern (Fig. 3.1a) has a southwest-to-northeast axis of maximum values with three extrema southeast of Greenland (absolute maximum), over the Labrador Sea (relative maximum), and southwest of Newfoundland (relative maximum). The absolute maximum cyclone activity exceeding 4.5 cyclones/day/(250 km x 250 km area) dominates the 60°-65°N zonal band. Redevelopment of extratropical cyclone systems migrating from the southwest, which is common between Greenland and Iceland (e.g., U.K. Meteorological Office 1964; Whittaker and Horn 1982, 1984), may explain in part the absolute maximum southeast of Greenland. Furthermore, note that this absolute maximum is near the Greenland Sea, a main site – besides the Labrador Sea and the Sargasso Sea (20°-35°N, 70°-30°W) – where the deep ventilation of the North Atlantic takes place (Dickson 1996). The names and locations of these seas mentioned in this Dissertation are indicated in Fig. 3.7f.

Moreover, it is worth noting that Sinclair (1997) found that southeast of Greenland is one of the two principal Northern Hemisphere "cyclone graveyards" (besides the Gulf of Alaska); such a cyclone graveyard ultimately contributes to that CDF peak, as was confirmed further by the long-term mean of cyclone counts (not shown).

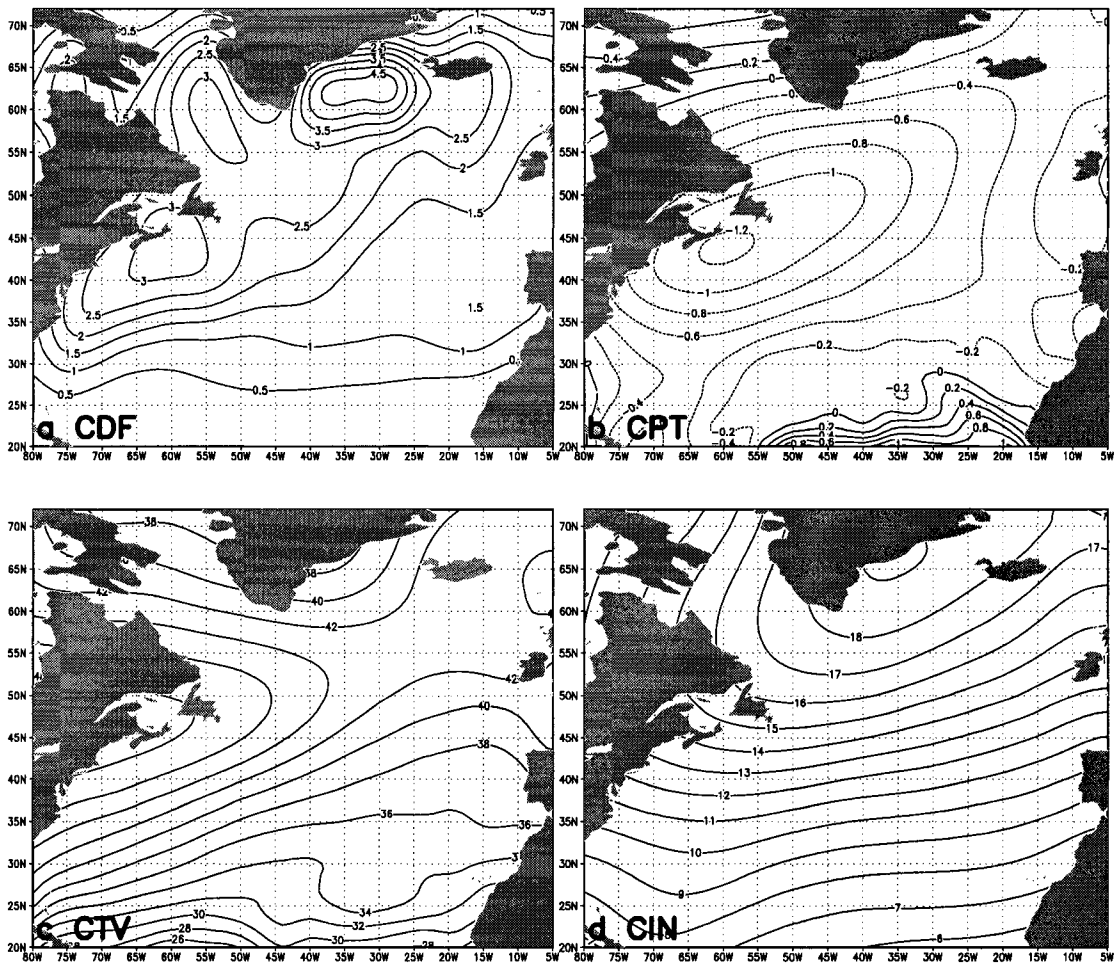


Fig. 3.1. Long-term mean patterns of the following North Atlantic winter semester (October-March) fields for 1948-99: (a) surface extratropical cyclone track density function (CDF, cyclones/day/250 km x 250 km area); (b) cyclone pressure tendency (CPT, hPa/6 h); (c) cyclone translation velocity (CTV, km/h); and (d) cyclone intensity (CIN, defined as local Laplacian of SLP, 10^5 hPa/m^2). Positive/negative isopleths in (b) are solid/broken lines.

The first relative maximum of cyclone activity exceeding 3 cyclones/day/(250 km x 250 km area) occurs over the Labrador Sea (Fig. 3.1a) that is another site of major oceanic convection. The intensity of ocean convection here was observed to covary

(positively) with the North Atlantic Oscillation (NAO) (Dickson et al. 1996; Lab Sea Group 1998; Marshall et al. 2001); note that Chapter 4 shows the NAO is highly correlated with the leading mode of CDF anomalies. For instance, Dickson et al. (1996) showed that, during the NAO minimum of the 1960s, with an extreme Greenland ridge feeding record amounts of fresh water into the northern gyre in the form of the Great Salinity Anomaly, and its partner cell over the Southeast U.S. causing a southwestward retraction of storm activity, the surface freshening and postwar minimum in storm activity in the intervening area of the Labrador Sea also brought a progressive reduction, and ultimately a cessation, of wintertime convection there. This was attributed to "a direct impact of the shifting atmospheric circulation on the ocean; while this certainly does not rule out either feedbacks from anomalous ice and SST conditions on the atmosphere, or autonomous oscillations of the ocean's overturning circulation, it does tend to minimize them." The link between propagating SST anomalies and the properties of water mixed at the end of winter (McCartney et al. 1996) shows that the end-product of the transformation process, Labrador Sea Water (LSW), underwent extended warming and cooling trends consistent with the phase of the NAO (e.g., Fig. 5 in Marshall et al. 2001). The second relative maximum of cyclone activity (Fig. 3.1a), also exceeding 3 cyclones/day/(250 km x 250 km area), is downstream of the Sargasso Sea and to the south of Nova Scotia and Newfoundland. This storminess maximum also is aligned along the Gulf Stream. Regions of strong SST gradients are conducive, in a climatological sense, to the development of maritime cyclones (Colucci 1976; Whittaker and Horn 1984; Roebber 1984; Sinclair 1997).

Fig. 3.1 also reveals that the geographical patterns of the long-term mean of CDF, deepening rate, moving speed, and intensity are physically consistent with each other, with absolute maxima in the CDF (Fig. 3.1a) and intensity (Fig. 3.1d) southeast of Greenland, whereas cyclone deepening rate (Fig. 3.1b) and moving speed (Fig. 3.1c) maximize upstream near Nova Scotia and Newfoundland. This is consistent with the fact that cyclones usually reach their maximum intensity a little downstream areas of maximum cyclone deepening rate and moving speed. This finding was also reported by Geng and Sugi (2001) who regressed tracked cyclone variables upon the first principal component of cyclone frequency over the North Atlantic. Additionally, the moving speed of cyclones with non-zero translation velocities (i.e., exclusion of stationary cyclones from Fig. 3.1c) was found to maximize (exceeding 58 km/h) along the southeast of Canada near Nova Scotia and Newfoundland (not shown). The long-term mean pattern of cyclone central pressure is very similar to that of the cyclone intensity, with an absolute minimum central pressure around Iceland (not shown). There is a noticeable tendency for the absolute maximum of cyclone duration to occur over the 55°-65°N latitudinal band, extending from the Labrador Sea to the east of Iceland (not shown).

The CDF pattern confirms the strong tendency for cyclones to form and intensify near the eastern seaboard of North America, with activity focused on the regions of strongest SST gradient or strong wintertime land/sea temperature contrast (Whittaker and Horn 1984; Sinclair 1997; Sutton and Allen 1997). In the most recent review paper on storm track dynamics, Chang et al. (2002) showed that the structure of the transient eddy fluxes of heat and momentum strongly implicates baroclinic instability as the ultimate mechanism generating the transients that constitute the storm tracks. Strong baroclinic conversion of the available potential energy from the time-mean flow to the transients

coincides with the rapid growth in transient variance in the downstream (eastward) direction. This baroclinic growth peaks where the baroclinicity of the flow is largest, as measured, e.g., by the Eady parameter (Lindzen and Farrell 1980). Chang et al. (2002) found that this Eady parameter has its maximal value at the core of the tropospheric jet (300-hPa zonal wind shown in their Fig. 3b) that also lies just off the east coast of North America where CDF exhibits its second relative maximum (Fig. 3.1a).

Fig. 3.2 presents geographical patterns of the long-term standard deviations of cyclone characteristics in terms of the CDF, pressure tendency, translation velocity, and intensity. The same 306 winter months were used for each individual cyclone parameter, as in Fig. 3.1. The spatial pattern of the standard deviation of CDF (Fig. 3.2a) does not share the southwest-to-northeast orientation of the mean CDF pattern (Fig. 3.1a). Instead, it has broader basin-wide variability with a clear absolute maximum southeast of Greenland. This absolute maximum variability southeast of Greenland, exceeding 2 cyclones/day/(250 km x 250 km area), coincides with the absolute maximum cyclone activity displayed in the mean CDF pattern. The same coincidence with cyclone activity maxima characterizes the two relative maxima of cyclone variability over the Labrador Sea and southwest of Newfoundland (Fig. 3.2a), exceeding 1.4 and 1.2 cyclones/day/(250 km x 250 km area), respectively. The 1.2 relative variability maximum off the east coast of North America may be explained in part by the eastward displacement of storm tracks that parallel the coast and to cyclogenesis along the U.S. mid-Atlantic portion (Hayden 1981a). However, note the existence of two other relative maxima of cyclone variability (exceeding 1.4 cyclones/day/250 km x 250 km area), one just south of Iceland and the second farther west of Strait of Gibraltar (Fig. 3.2a). These two relative maxima do not appear directly linked to any maximum storminess (Fig. 3.1a). The above results can be

interpreted in the light of the fact that the variance of a random variable **x** can be expressed as the difference between two terms: $\mathrm{var}(\mathbf{x}) = \langle \mathbf{x}^2 \rangle - \langle \mathbf{x} \rangle^2$ where $\langle\ \rangle$ is the expectation operator. The $\langle \mathbf{x} \rangle$ term was displayed in Fig. 3.1. In other words, two terms are involved in expressing the variability of a random variable.

The variability of cyclone pressure tendency is minimized over the Labrador Sea (Fig. 3.2b). The pattern of such variability has a simple northwest-to-southeast gradient, with a maximum off West Africa. In contrast, variability patterns of both cyclone intensity (Fig. 3.2d) and central pressure (not shown) share the same southwest-to-northeast orientation north of ~35°N, with increasing variability towards Iceland and the Greenland Sea. The variability of cyclone moving speed also increases southward over the storm-formation region (82°-69°W, 25°-35°N) defined in Sutton and Allen (1997), with a minimum over the Labrador Sea (Fig. 3.2c) apparently associated with the minimum of cyclone pressure tendency (Fig. 3.2b). The maximum variability in the cyclone moving speed probably is linked to the storm-formation region. The relative maximum variability over the Strait of Gibraltar can be explained in part by the Bernoulli effect. The same pattern of moving speed variability was found when stationary cyclones were excluded from Fig. 3.2c (not shown). Finally, the variability of cyclone average lifetime peaks over the 40°-45°N latitudinal band (west of Portugal) and east of Iceland (not shown). The latter maximum of duration variability does not appear directly linked to the absolute maximum cyclone duration, which occurs from the Labrador Sea towards east of Iceland (not shown). Finally, the coefficient of variation (normalized standard deviation) of CDF increases southward, south of 30°N, reflecting more variability in CDF than expected (plot now shown).

The present long-term climatological mean differs from Geng and Sugi (2001, Fig. 2) in several respects: (1) Fig. 3.1 presents a *full* spatial distribution (instead of a single isopleth) for each individual cyclone parameter; (2) the cyclone intensity is better defined here as the local Laplacian of SLP (Fig. 3.1d) rather than the cyclone central pressure gradient; (3) for the definition of cyclone moving speed, the present study differentiates between (i) all tracked cyclones and (ii) cyclones with non-zero velocities to exclude stationary features; (4) the spatial patterns of CDF, cyclogenesis and cyclolysis events (not shown), and cyclone average lifetime (not shown) were examined for the first time; and (5) the standard deviation fields of all cyclone variables (Fig. 3.2) are new products.

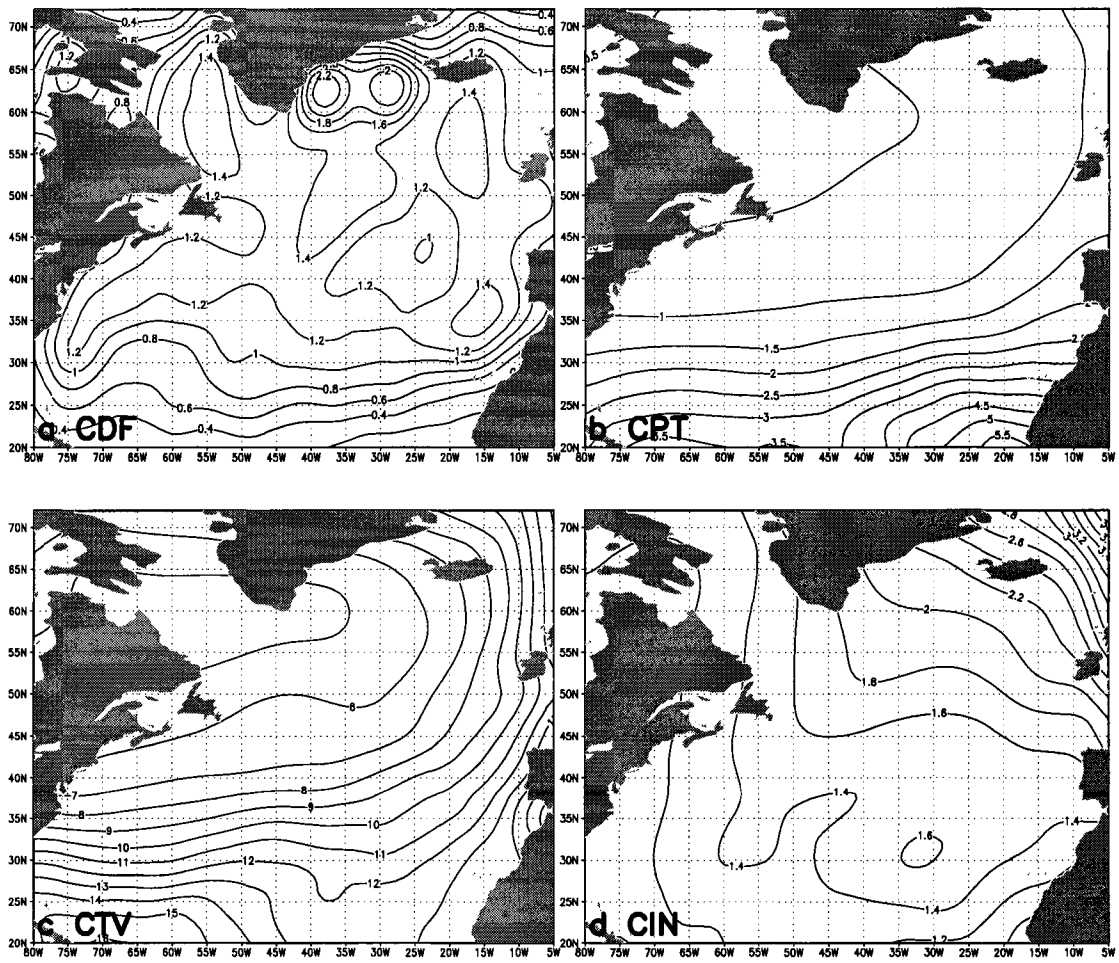


Fig. 3.2. As in Fig. 3.1 except for standard deviation.

3.2.2 Seasonal Variations of Mean Behavior of CDF

Fig. 3.3 presents geographical patterns of the mean CDF for each winter month from October through March. A total of 51 individual monthly CDF fields were used to produce the pattern for each month. This figure clearly reveals a significant intraseasonal variability in cyclone activity over the North Atlantic for the winters 1948-99. Thus, in later sections it was necessary to remove the climatological seasonal cycle from the individual monthly mean fields of each cyclone parameter. This was accomplished by subtracting the long-term averaged values for a given calendar month from corresponding values of the same calendar month in individual years.

A strong feature of all 6 months in Fig. 3.3 is the constancy of the CDF maximum between southeast of Greenland and Iceland. With respect to the seasonal mean CDF (Fig. 3.1a), October is marked by decreased cyclone activity southwest of Newfoundland (especially) and over the Labrador Sea. Relative to October, there is a marked tendency for November cyclone activity to increase both over the Labrador Sea and southwest of Newfoundland, and to decrease slightly southeast of Greenland. The storminess in December and January tends to increase clearly from November both southeast of Greenland and southwest of Newfoundland, while a decline from November levels is characteristic of cyclone activity from west of the Iberia Peninsula northward to Scotland (December) and over the Labrador Sea (January). Then, the cyclone activity southwest of Newfoundland tends to increase remarkably in February. Finally, March is characterized particularly by substantial decreased cyclone activity southeast of Greenland/Labrador Sea (i.e., over the northern part of the basin) and an increase in storminess west of the Strait of Gibraltar and also over the Atlas Mountains (not shown). In their objective climatology of cyclones over the Mediterranean region, Trigo et al.

(1999) noted that Saharan cyclones seem to be the dominant feature of the Mediterranean spring, as the area south of the Atlas Mountains becomes a major source of cyclones.

The association of storm tracks with midlatitude baroclinic zones suggests that storm tracks, like the mean pole-to-equator temperature gradient in various longitudinal sectors, will experience a pronounced annual cycle (Chang et al. 2002). Nakamura (1992) provided the most complete proxy picture of the seasonal variations of Northern Hemisphere storm tracks. In particular, he documented seasonal variations of North Atlantic storm tracks by constructing a latitude-month section showing the seasonal march of 300-hPa bandpass meridional velocity variance averaged over the 60°-20°W longitude sector. To complement Nakamura (1992), Fig. 3.4 presents a latitude-month CDF section averaged over the present wider longitude domain (i.e., 80°W-0°). This indicates a latitudinal distribution of cyclone activity that is largely invariant from month-to-month, particularly south of ~40°N (i.e., to the south of the southern maximum in the long-term mean CDF, Figs. 3.1a and 3.3) and north of ~65°N (north of the northern maximum in CDF). Most importantly, Fig. 3.4 shows that the maximum North Atlantic cyclone activity occurs in a relatively narrow latitude zone centered on 60°N throughout the winter semester, due to the predominance of the two CDF maxima southeast of Greenland and over the Labrador Sea noted earlier (Figs. 3.1a, 3.3a-f). This latitudinal zone experiences slightly decreased storminess in February, because of some CDF weakening southeast of Greenland (Fig. 3.3e), and a significant decline in March as the cyclone activity tends to diminish substantially both southeast of Greenland and over the Labrador Sea (Fig. 3.3f). In contrast, Nakamura (1992) found the above Atlantic (longitude band 60°-20°W) proxy storm track attained maximum intensity only in midwinter (November-January) and further south (centered on ~50°N).

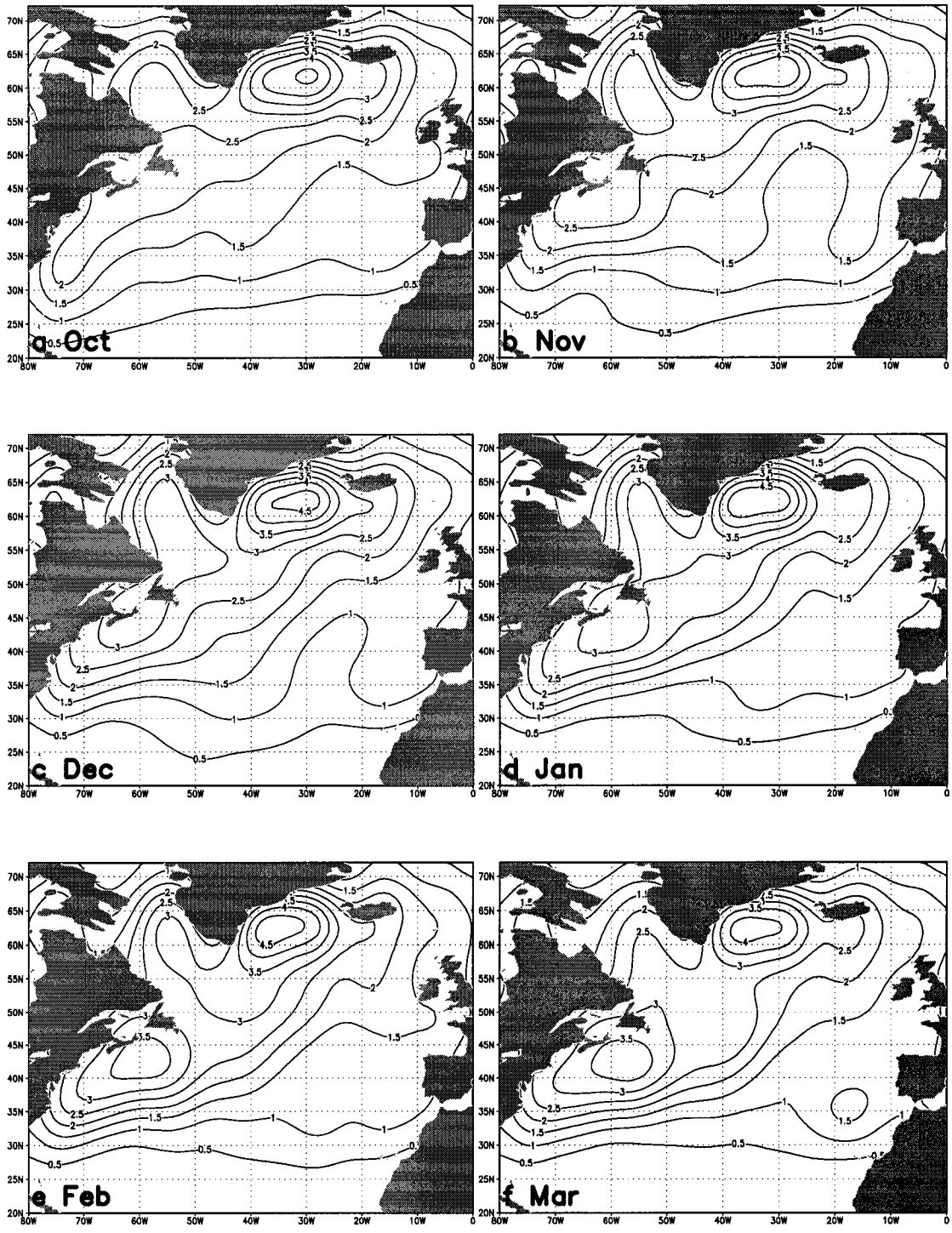


Fig. 3.3. Long-term mean patterns of North Atlantic surface extratropical cyclone track density function (CDF, cyclones/day/250 km x 250 km area) for each winter calendar month for 1948-99.

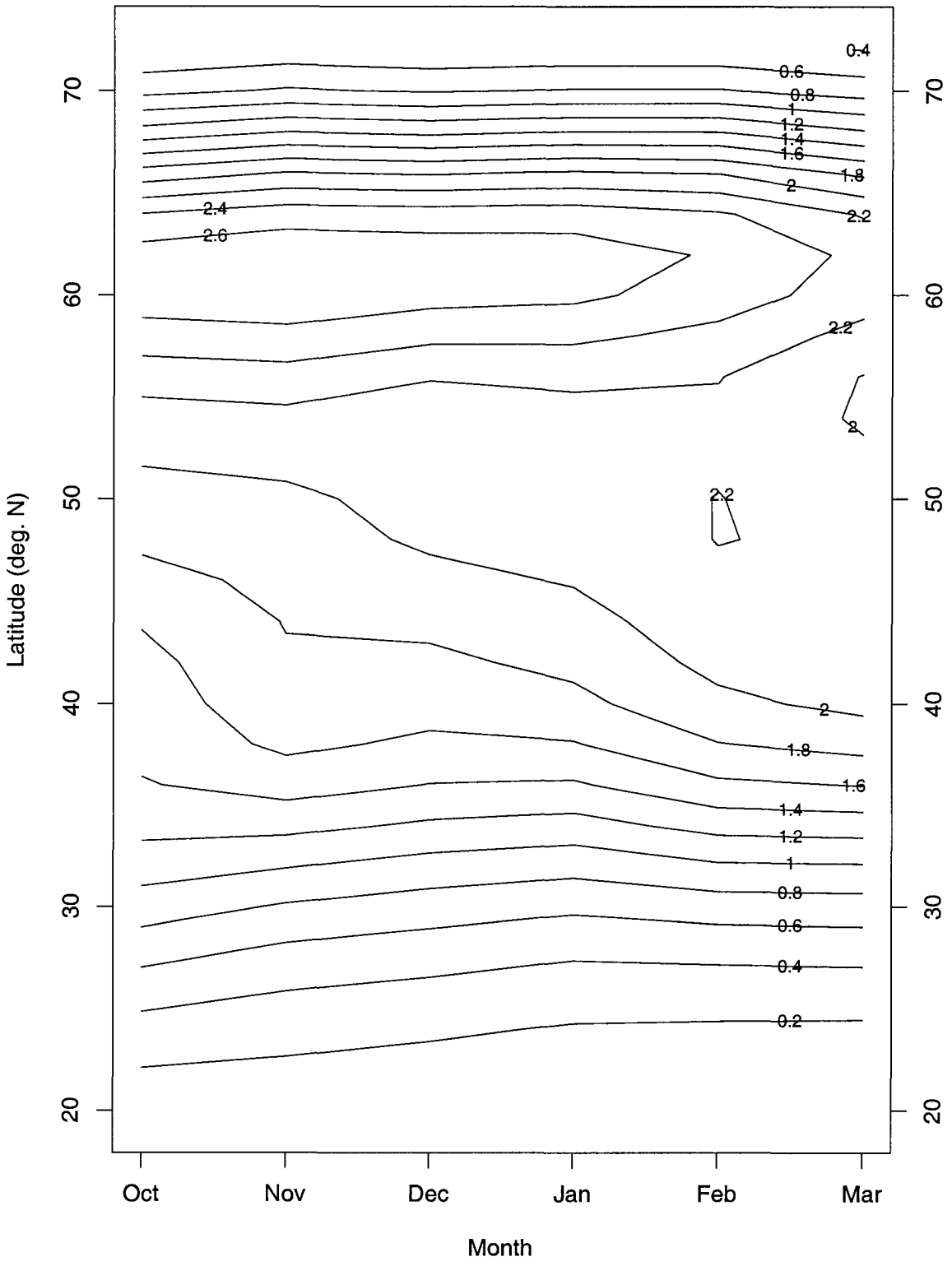


Fig. 3.4. Latitude-month section showing the seasonal march of North Atlantic winter semester (October-March) surface extratropical cyclone track density function (CDF) during 1948-99 (cyclones/day/250 km x 250 km area). The CDF field has been averaged over the longitude band 80°W-0° for 2° latitude zones.

Fig. 3.5 expands on Figs. 3.3 and 3.4 by depicting the seasonal march of standardized area-averaged CDF anomalies for the areas of CDF maxima (Fig. 3.1a) southeast of Greenland (60°-65°N, 40°-25°W), over the Labrador Sea (55°-65°N, 60°-50°W), and southwest of Newfoundland (40°-50°N, 65°-55°W). The first principal feature of Fig. 3.5 is the coherent tendency among the months of the winter core (December-January-February) to experience above-average cyclone activity over the three oceanic regions. It is interesting to note that the month of maximum storminess varies regionally from December (Labrador Sea) to January (southeast of Greenland) to February (southwest of Newfoundland). Second, October is unique among the winter semester months in its below-average cyclone activity over all the three regions, especially southwest of Newfoundland. Third, March stands out as having the lowest storminess for the two northern regions, southeast of Greenland and the Labrador Sea, which is reflected in the latitude-time CDF section in Fig. 3.4.

Finally, the time series of CDF anomalies for the above three regions were found to be uncorrelated with each other. Furthermore, of all of the winter semester months, February (October) has an overall highest (lowest) storminess integrated over the entire North Atlantic Basin (not shown).

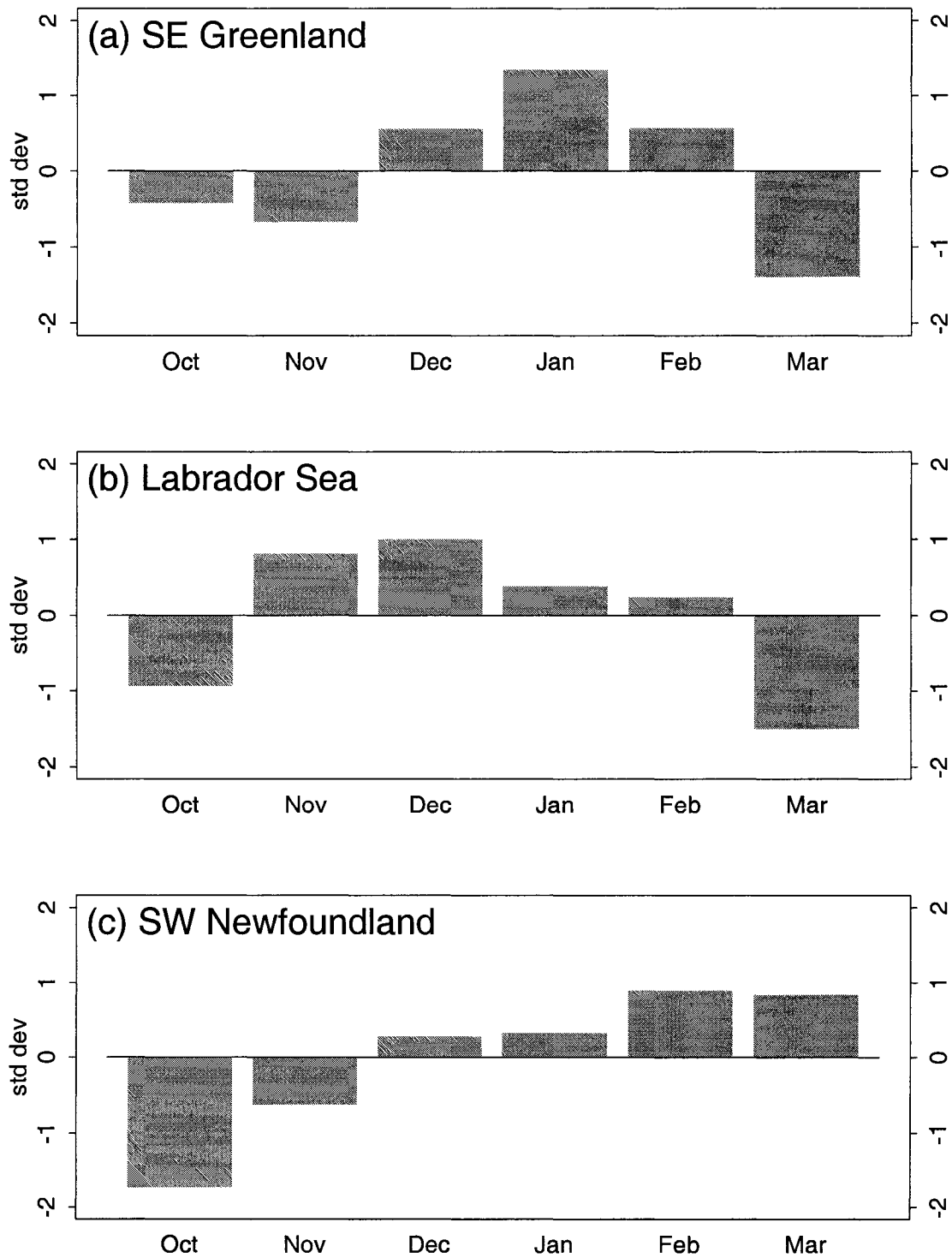


Fig. 3.5. Seasonal march of standardized area-averaged anomalies (std devs) of North Atlantic surface extratropical cyclone track density function (CDF, cyclones/day/250 km x 250 km area) during 1948-99 for major regions of cyclone activity. (a) southeast of Greenland (60°-65°N, 40°-25°W); (b) Labrador Sea (55°-65°N, 60°-50°W); and (c) southwest of Newfoundland (40°-50°N, 65°-55°W). These regions are delineated by dotted boxes in Fig. 3.7d. The CDF field was first averaged over the above regions. Then, the standardized departures were computed for each region by subtracting the respective October-March mean from each calendar monthly value and dividing by the respective October-March standard deviation. Hence, all the resulting time series have zero mean and unit variance.

Fig. 3.6 presents spatial distribution patterns of the long-term standard deviation of CDF for each winter calendar month from October through March. As in Fig. 3.3, each monthly pattern was produced from 51 individual calendar months. Fig. 3.6 reveals strong spatial differences in cyclone variability for each winter month, and also considerable variations in the patterns and magnitude of CDF variability from month-to-month. In particular, note that most of the absolute maxima in CDF variability (Fig. 3.6) do not appear directly linked to the three maxima in the mean CDF pattern (Fig. 3.3). A particular exception is the absolute maximum in CDF variability off Morocco in March (Fig. 3.6f), which appears directly related to the relative maximum in the mean CDF there (Fig. 3.3f). Another exception is the absolute maximum in CDF variability west of Iceland in February (Fig. 3.6e), which may be explained in part by the absolute maximum in cyclone activity southeast of Greenland (Fig. 3.3e).

As opposed to the long-term mean patterns of CDF for each calendar month (Fig. 3.3), there are no common oceanic regions occupied by the CDF variability maxima in Fig. 3.6. This is due to the changing location of variability maxima from month-to-month. Also, note where areas of maximum variability do coincide with low CDF values, relatively few events produce that variability. The most prominent example is the 6.5 maximum south of the domain in January (Fig. 3.6d). Two other examples are the 2.5 south of the domain (February) and 4.5 in the central domain (November). Finally, there is a clear northeastward propagation in the northern part of the basin of the absolute maximum in CDF variability from October to December, and somewhat eastward propagation in the southern part from January to March.

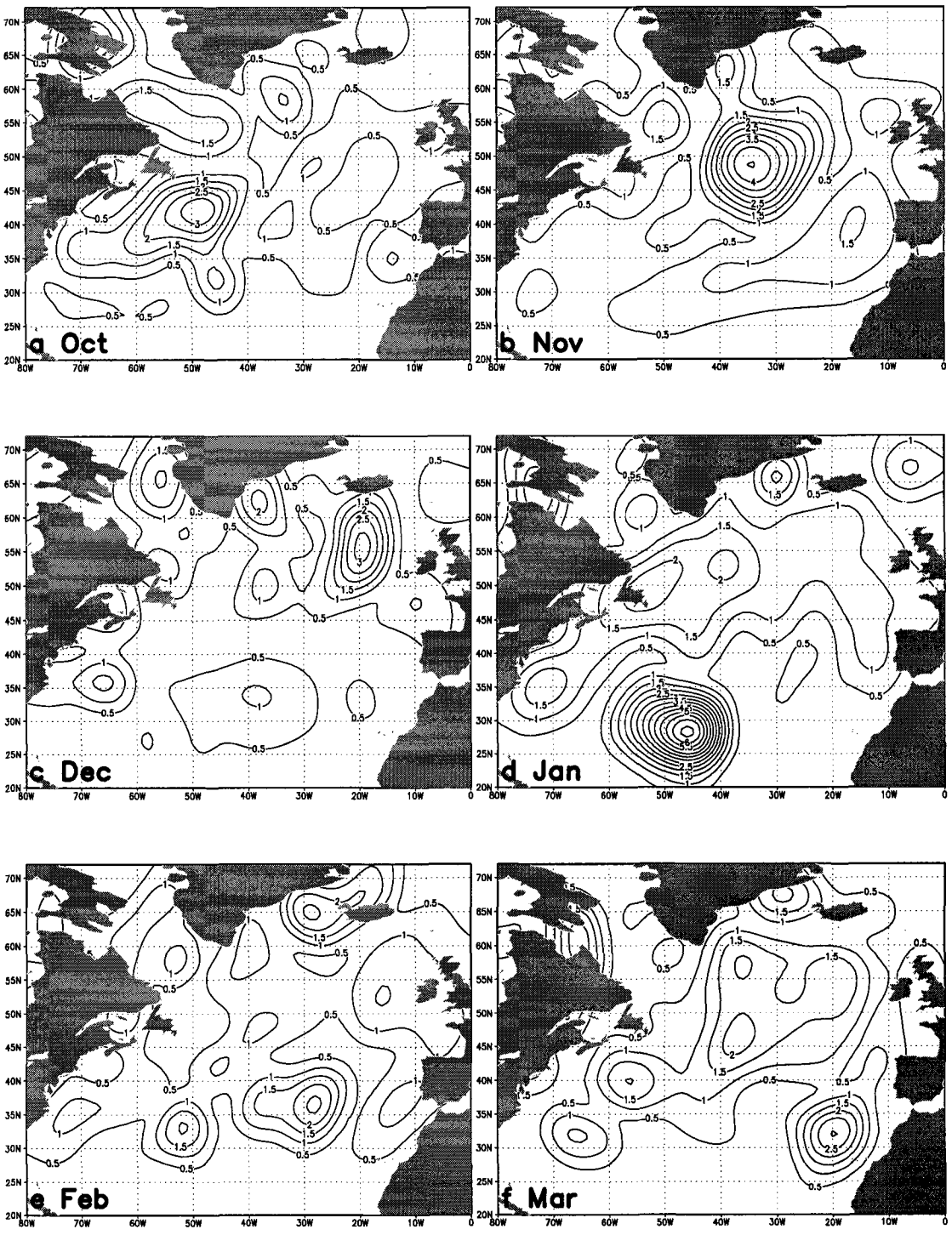


Fig. 3.6. As in Fig. 3.3 except for standard deviation.

Therefore, the entire North Atlantic Basin is used herein as the region over which areal averages of the standard deviation of CDF were computed. Of all of the winter semester months, January (December) has the highest (lowest) variability in cyclone activity over the entire North Atlantic. Specifically, the standardized area-averaged CDF variability extremes for the entire basin (computed as in Fig. 3.5) are +1.60 (January) and -1.52 std devs (December). Hence, the winter core exhibits both the highest cyclone activity in February and highest cyclone variability in January over the entire basin. Because of this strong intraseasonal variability in some areas, it was decided to normalize the CDF anomalies at each grid point for a given winter month (i.e., zero mean and unit variance) by the temporal standard deviation of the calendar month in question depicted in Fig. 3.6. The resulting standardized CDF anomaly fields are used in subsequent chapters.

3.3 PERSISTENCE OF CYCLONE ACTIVITY

In addition to the mean and variability characteristics of North Atlantic cold-season surface cyclones documented above on a seasonal and monthly basis, cyclone persistence throughout the winter semester now is quantified in terms of month-to-month correlation and autocorrelation function analyses. This inquiry was motivated by Zishka and Smith's (1980) statement that, "although cyclones and anticyclones exhibit short-term variations, they also possess a high degree of continuity over longer time-scales dictated by the long-term radiation balance, land/water distributions, and orographic features." Such reasoning led Hayden and Smith (1982) to develop a persistence-based multivariate statistical (EOF) method for season-in-advance cyclone frequency prediction for eastern North America and the western North Atlantic for 1885-1980.

3.3.1 Month-to-Month Correlation of CDF Anomalies

Fig. 3.7 presents month-to-month correlation patterns of North Atlantic winter semester (October-March) CDF anomalies. This figure shows that month-to-month correlation of cyclone activity is generally weak and largely positive. For the Labrador Sea and off the U.S. East Coast (Fig. 3.7a), October/November is the only pairing of consecutive months with notable persistence ($r > 0.5$). This relatively strong persistence is associated with CDF maxima over the Labrador Sea and southwest of Newfoundland, depicted in both the seasonal and monthly mean CDF patterns (Figs. 3.1a, 3.3a,b). Note that October/November persistence is relatively weaker ($r > 0.3$) to the southeast of Greenland where CDF maximizes (Figs. 3.1a, 3.3a,b). In contrast, the November/December transition (Fig. 3.7b) is characterized by a relatively strong persistence ($r > 0.4$) in the southwestern part of the study domain. Early winter (December/January) stands out as having strong persistence ($r > 0.5$) over the central-southern portion of the basin (Fig. 3.7c) and to the west of western Europe and the U.K. ($r > 0.4$). The latter feature persists more strongly ($r > 0.5$) from January/February (Fig. 3.7d) and weakens into February/March. The strongest February/March persistence ($r > 0.5$) occurs over the central-southern portion of the domain as characterized December/January.

Table 3.1 focuses on the three regions delineated in Fig. 3.7d where cyclonic activity is greatest (Figs. 3.1a, 3.3). It shows that these regions manifest their highest month-to-month CDF persistence in both February/March ($r=0.27$ at 94%) and December/January ($r=0.22$ at 81%) for the southeast of Greenland, and in October/November ($r=0.38$ at 99%) for the Labrador Sea. The entire basin has its highest persistence in December/January ($r=0.34$ at 98%). Therefore, the above results

conclusively reveal that the month-to-month correlation of CDF anomalies is generally weak over the basin, with significant spatial and intraseasonal variations. This may be explained in part by the strong spatial and intraseasonal variations in both CDF mean (Fig. 3.3) and variability (Fig. 3.6).

Note that the month-to-month CDF persistence is weak even for the three regions of greatest cyclone activity (Table 3.1) due mainly to the strong local CDF variability. For instance, for the southeast of Greenland region that exhibits the lowest month-to-month correlation in January/February (r = 0.05), the respective time series are *not* necessarily significantly correlated even though the CDF mean is very high in both months. The area-averaged CDF mean for this region is 4.66 (4.47) cyclones/day/(250 km x 250 km area) in January (February). The weakest persistence was confirmed by the detailed yearly variations of the area-averaged CDF mean in these two months. The corresponding plots (not shown) reveal that the two time series, indeed, show no interrelationship. This is probably due to the considerable variability in the two time series; i.e., the standard deviation of CDF for this region is 2.89 (3.20) cyclones/day/(250 km x 250 km area) in January (February).

Table 3.1. Month-to-month correlations of the area-averaged CDF anomalies for the regions of CDF maxima in Fig. 3.1a (delineated in Fig. 3.7d) and the entire North Atlantic Basin. The CDF anomalies were first averaged over the 4 regions, then month-to-month correlations of the resulting time series of areal averages were computed. Values next to the correlations indicate statistical significance levels (%) according to a two-sided Student's t-test that factors in the effective sampling size of the time series (Wilks 1995; p. 127).

Area/pairing	O/N	N/D	D/J	J/F	F/M
SE of Greenland	0.06 (29.97)	0.11 (47.27)	0.22 (80.81)	0.05 (27.56)	0.27 (93.54)
Labrador Sea	0.38 (98.53)	0.15 (64.50)	0.17 (73.48)	0.19 (80.71)	0.20 (82.50)
SW of Newfoundland	0.10 (49.15)	0.08 (43.30)	-0.02 (10.09)	-0.06 (27.59)	0.10 (49.26)
Entire Basin	0.27 (91.05)	0.25 (91.23)	0.34 (98.17)	0.26 (93.30)	0.31 (96.61)

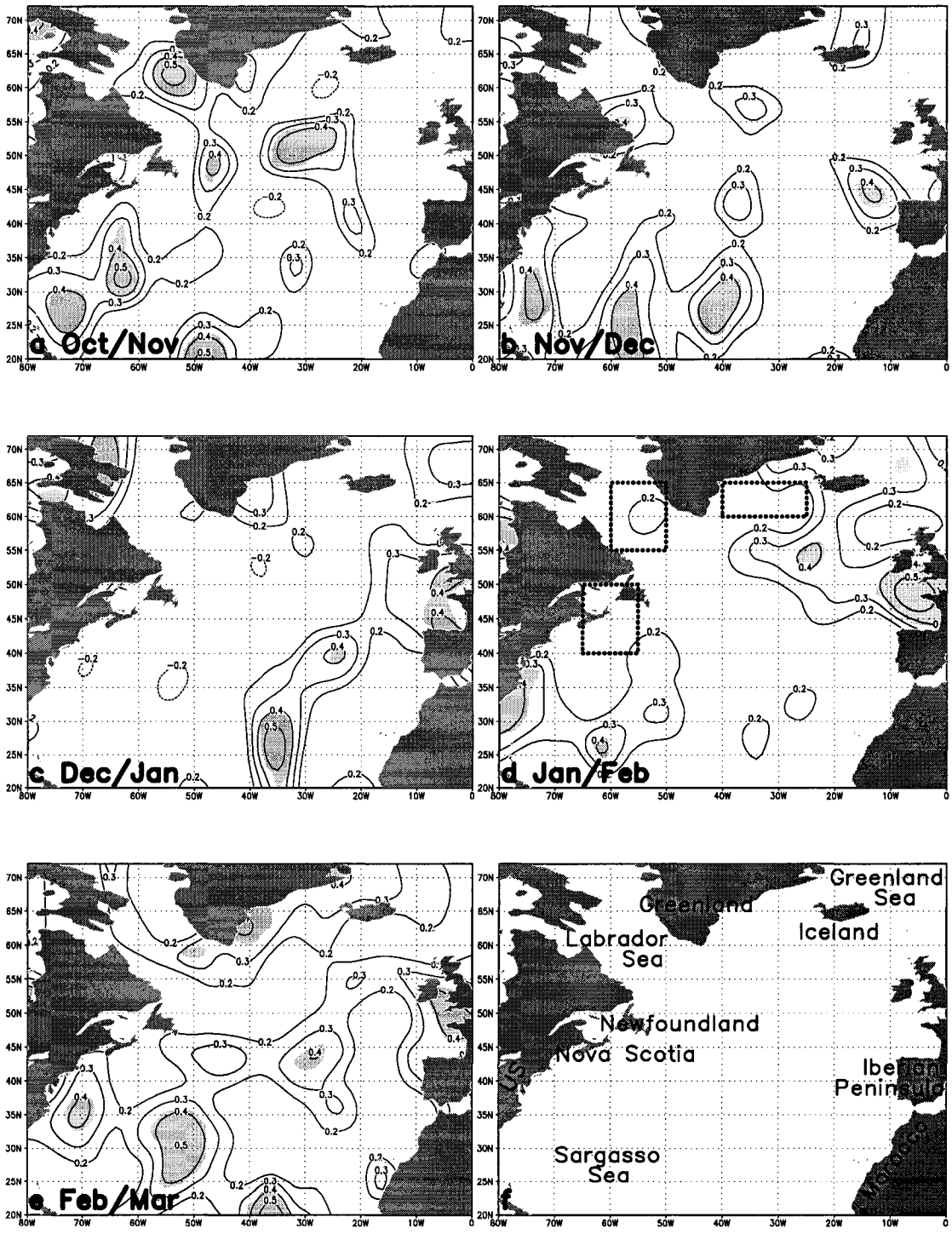


Fig. 3.7. Isopleths of month-to-month correlation of North Atlantic winter semester surface extratropical cyclone track density function (CDF) anomalies for 1948-99 (panels a-e). The dotted boxes in panel (d) indicate the regions of CDF maxima (in Fig. 3.1a) over which the areal averaging was applied in previous sections. The names and locations of the seas mentioned in this Dissertation are indicated in panel (f). Light shading covers areas where those month-to-month correlations are statistically significant at the 99% confidence level according to a two-sided Student's t-test that factors in the effective sampling size of the time series at each grid point (Wilks 1995, p. 127). Only correlation coefficients greater than 0.2 in magnitude are contoured.

3.3.2 Autocorrelation Function of Cyclone Parameters

To further investigate the persistence of North Atlantic cyclonic activity, Fig. 3.8 presents spatial distribution patterns of the 1-month lag autocorrelation function (ACF1) for several cyclone anomaly fields (CDF, central pressure, intensity, moving speed, pressure tendency). This figure shows that the ACF1 values for these fields are generally weak, though statistically significant.

Within this overall result, Fig. 3.8 suggests month-to-month CDF persistence is strongest over both the northern and southern parts of the basin. Fig. 3.8a displays an absolute maximum month-to-month persistence in CDF, exceeding 0.30, near the central-southern edge of the basin and a relative maximum over the storm-formation region off the U.S. East Coast ($r > 0.24$). An absolute maximum persistence in cyclone counts also affects this storm-formation region (not shown). Further, the CDF ACF1 field contains relative maxima ($r > 0.21$) southeast of Greenland and over the Labrador and Greenland Seas. The cyclone central pressure persists moderately over and around the same Labrador Sea ($r > 0.24$) and Iceland/Greenland Sea ($r > 0.21$) regions (Fig. 3.8b). The latter relative maximum is consistent with the absolute minimum in the long-term mean of cyclone central pressure over Iceland (not shown). Note that the cyclone central pressure displays persistence mainly over the northern North Atlantic. Fig. 3.8c shows strongest month-to-month persistence in cyclone intensity over the northern part of the basin, particularly southeast of Iceland towards U.K. ($r > 0.30$) and over the central North Atlantic ($r > 0.25$). This is somewhat consistent with the maximum in the long-term mean of cyclone intensity (depicted in Fig. 3.1d), which occurs farther north to the southeast of Greenland. Finally, ACF1 of the cyclone moving speed maximizes ($r > 0.18$) over Nova Scotia (Fig. 3.8d) and in a similar region when stationary cyclones are

excluded (plot not shown), whereas the ACF1 of the cyclone pressure tendency peaks ($r > 0.21$) further northeast over the central North Atlantic, south of Greenland (Fig. 3.8e).

Fig. 3.8 also reveals that the geographical distributions of the autocorrelation function of CDF, deepening rate, moving speed, and intensity/central pressure are physically consistent with each other. Maxima in the CDF and intensity/central pressure occur in the vicinity of southeast of Greenland/Greenland Sea, whereas persistence of cyclone moving speed and deepening rate maximize upstream over Nova Scotia/northeast of Newfoundland. This is consistent with the fact that cyclones usually reach their maximum intensity a little downstream of the maximum cyclone deepening rate and moving speed (Fig. 3.1). The ACF of the CDF field at longer lags (lag = 2, 3,..., 6 months) was found to decay rapidly, and so the plots are not shown.

3.4 RELATIONSHIPS BETWEEN CYCLONE CHARACTERISTICS

This section examines local relationships between cyclone variables (e.g., CDF versus intensity). Paciorek et al. (2002) noted that there is no standard measure of cyclone activity because cyclones are complicated phenomena that may exhibit changes in intensity, duration, location, and frequency. They also stated that "a given index of cyclone activity may be closely related to some, but not all, of these aspects of cyclone behavior." Such relationships can be examined through temporal correlations between pairs of cyclone parameters at each grid point to assess how these cyclone attributes vary jointly over the North Atlantic Basin. Fig. 3.9 presents spatial correlation patterns between all pairs of the following cyclone characteristics: CDF, pressure tendency (CPT), translation velocity (CTV), and intensity (CIN). These maps of correlations between cyclone attributes highlight regions in which pairs of cyclone variables are closely related.

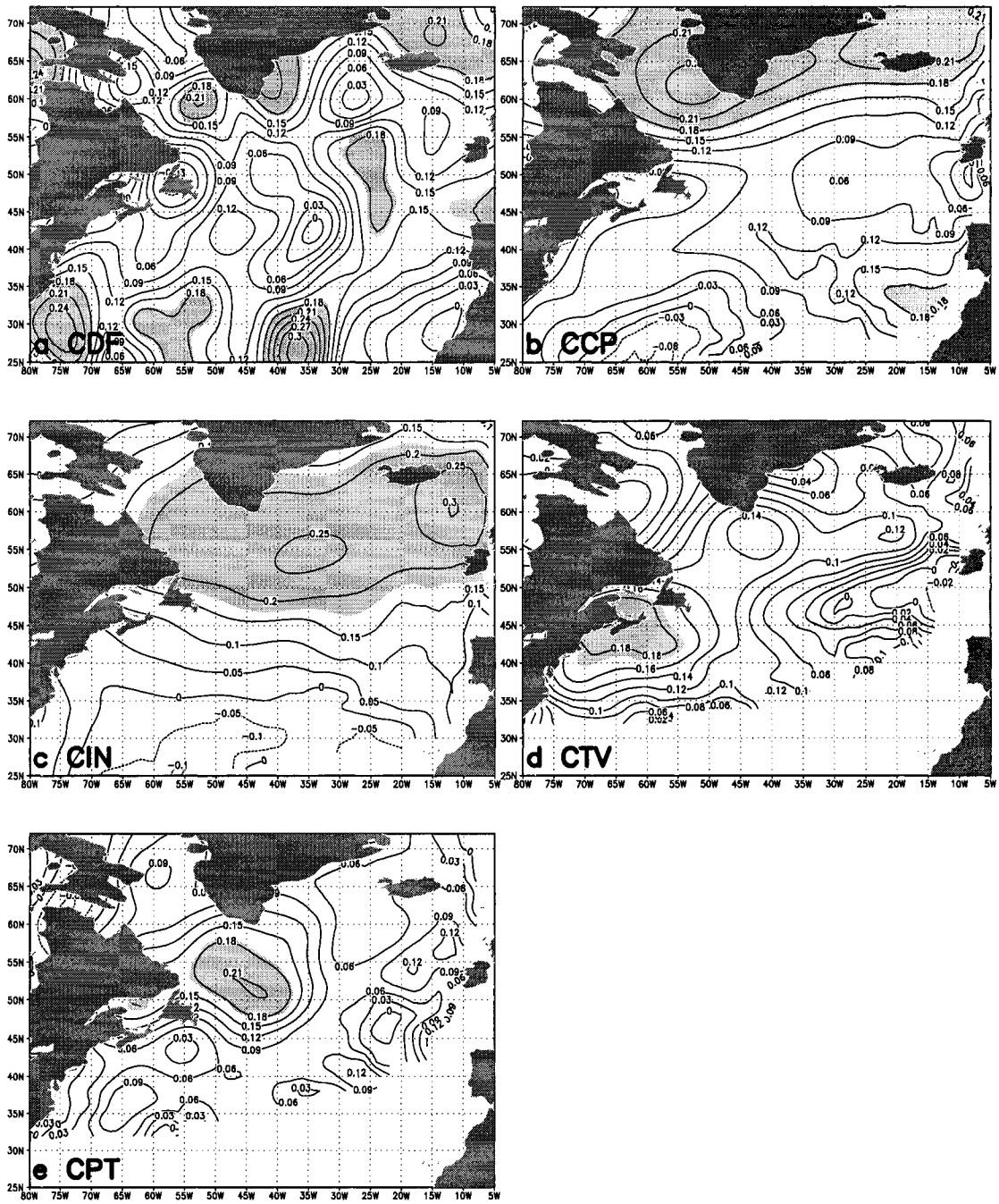


Fig. 3.8. Spatial patterns of autocorrelation function at lag = 1 month (ACF1) of the following North Atlantic winter semester (October-March) surface extratropical cyclone anomaly fields for 1948-99: (a) cyclone track density function (CDF); (b) central pressure; (c) intensity; (d) cyclone translation velocity; and (e) pressure tendency. Light shading represents areas where ACF1 is statistically significant at the 99% confidence level according to a local two-sided Student's t-test that factors in the effective sampling size of each field at a given grid point (Wilks 1995, p. 127). Regions with insufficient data coverage (number of missing values greater than 10% of the total number of records (306) at any individual grid point) are not contoured in (b) through (f) (i.e., cyclone fields obtained from application of the Akima scheme in Subsection 2.2.4b); these edge effects are due to the Akima interpolation.

As background for these spatial correlations, the long-term mean geographical patterns of these cyclone parameters were presented in Fig. 3.1.

Fig. 3.9 reveals that, over the entire North Atlantic Basin, both cyclone pressure tendency (Fig. 3.9a) and moving speed (Fig. 3.9b) are very weakly dependent on the contemporary CDF. Therefore, with respect to CDF, both cyclone pressure tendency and moving speed can be regarded as independent variables and are used as such in this Dissertation; this is enlightening because of the additional physical insight and robustness of results that is provided (e.g., Subsections 3.2.1 and 3.3.2, Chapter 4). In contrast, CDF is markedly linked (positively) to the cyclone intensity over the northern part of the basin, with significant correlations exceeding +0.5 largely confined to the southeast of Greenland (Fig. 3.9c), where both cyclone parameters display absolute maxima in their long-term means (Figs. 3.1a,d). This suggests that cyclones are most intense when they are most active/prevalent over this region. Among all of the above cyclone characteristics, the pressure tendency has overall strongest interrelations ($|r| \geq 0.6$) with the cyclone moving speed (Fig. 3.9d) and intensity (Fig. 3.9e) over the central-western North Atlantic. Following Serreze et al. (1997), the 6-h SLP tendency was analyzed through the life history of each system from the central pressure (P) values as $P_t - P_{t-1}$, where t is time. The location of each SLP tendency observation is taken as that at time t. Use of this sign convention accounts for the negative correlations in Figs. 3.9d,e. Those correlation patterns suggest that, over the central-western part of the basin, there is a marked tendency for cyclone systems to move faster as they deepen, with this effect greater for intense systems. The simple monopole structure in both the CPT/CTV and CPT/CIN pairings is physically consistent with the predominance of the monopole structure in CTV/CIN that is centered slightly further east (Fig. 3.9f).

Fig. 3.10 expands on Fig. 3.9 by showing the temporal variations of standardized winter (October-March) area-averaged anomalies of the above cyclone pairings for key regions delineated in Figs. 3.9c-f. The regions chosen are those with relatively large correlations in this figure, which are confirmed by Fig. 3.10. Of the cyclone relations presented in Fig. 3.10, moving speed stands out as having the strongest relationship with cyclone pressure tendency (r=-0.76) and the weakest link with the intensity (r=+0.54). The cyclone intensity has very similar correlation magnitudes with both CDF (r=+0.64) and cyclone pressure tendency (r=-0.62). The time series of area averages in Fig. 3.10 also reveal strong interannual variability in the above cyclone characteristics and clearly contain long-term components and noticeable imprints of decadal variability.

Fig. 3.10a displays prominent year-to-year fluctuations in cyclone activity/intensity southeast of Greenland, with a significant downward trend in the 1960s, followed by a considerable upward trend afterwards. Chapter 4 examines the interannual variability of cyclone activity over the North Atlantic Basin. Further, by examining Fig. 3.10a, we can identify a sharp transition in the evolution of these two cyclone attributes (i.e., CDF and intensity) around 1970. This transition (along with the decadal-to multidecadal variability of CDF) is further investigated in Chapter 5 for the entire basin. This transition also is apparent for both cyclone pressure tendency (CPT) (Fig. 3.10b,c) and cyclone translation velocity (CTV) (Fig. 3.10b,d) over the central-western North Atlantic where CPT (CTV) exhibits a significant negative (positive) trend in 1970s-early 1990s. Although we have tried to indicate some of the important features of Fig. 3.10 regarding the interannual-to-decadal variability of the above cyclone attributes over different regions, a detailed regional analysis of such variability is out of the scope of this chapter.

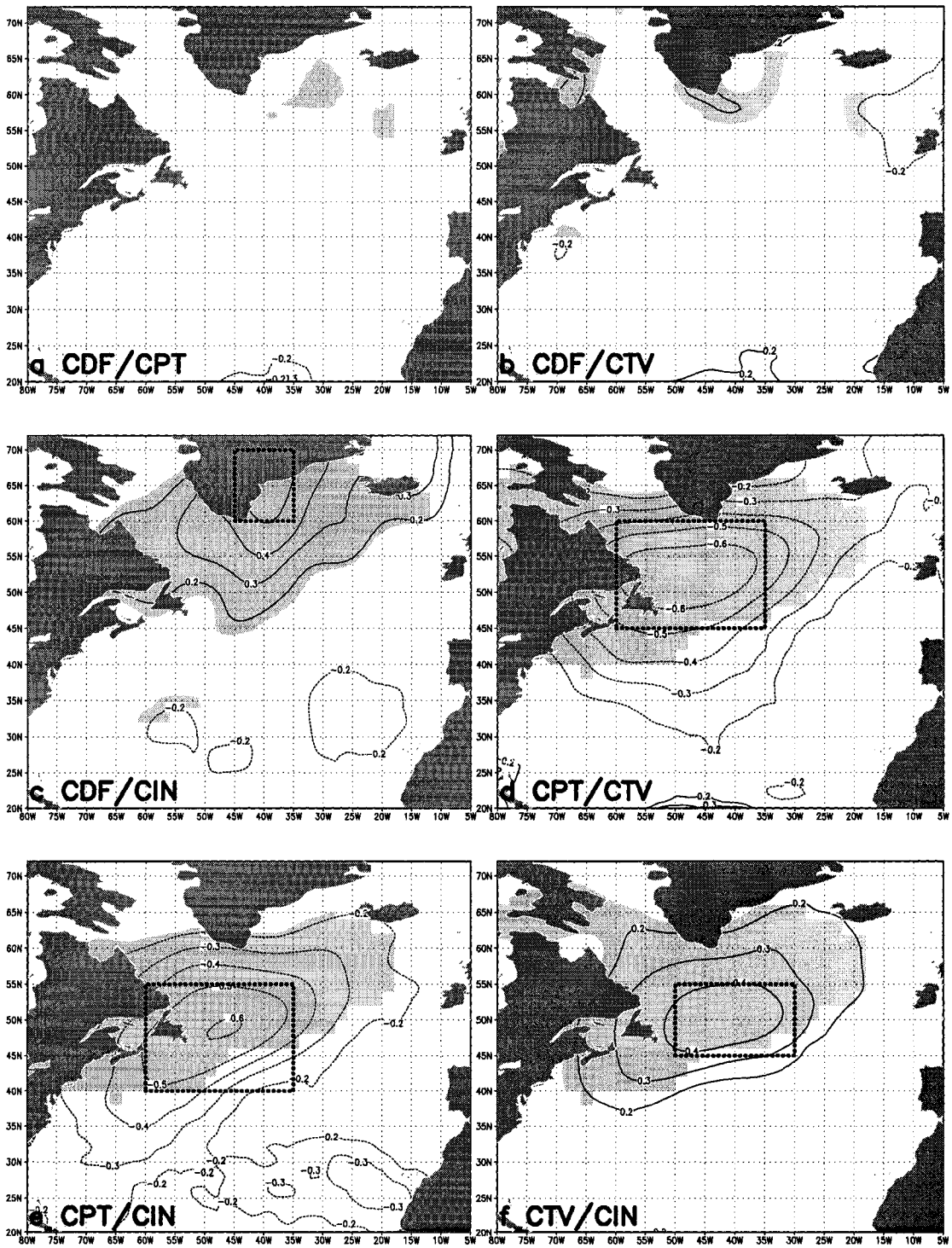


Fig. 3.9. Spatial correlation patterns between pairs of North Atlantic winter semester (October-March, 1948-99) cyclone characteristics. CDF, CPT, CTV, and CIN denote cyclone track density function, cyclone pressure tendency, cyclone translation velocity, and cyclone intensity, respectively. The dotted boxes in panels (c-f) indicate the regions of relatively large correlations over which areal averaging was applied to generate the standardized area-averaged CDF anomalies depicted in Fig. 3.10. Solid (dashed) contours indicate positive (negative) correlation coefficients. Light shading covers areas where correlations are statistically significant at the 99% confidence level according to a two-sided Student's t-test that factors in the effective sampling size of the time series at each grid point (Wilks 1995, p. 127). Only correlation coefficients greater than 0.2 in magnitude are contoured.

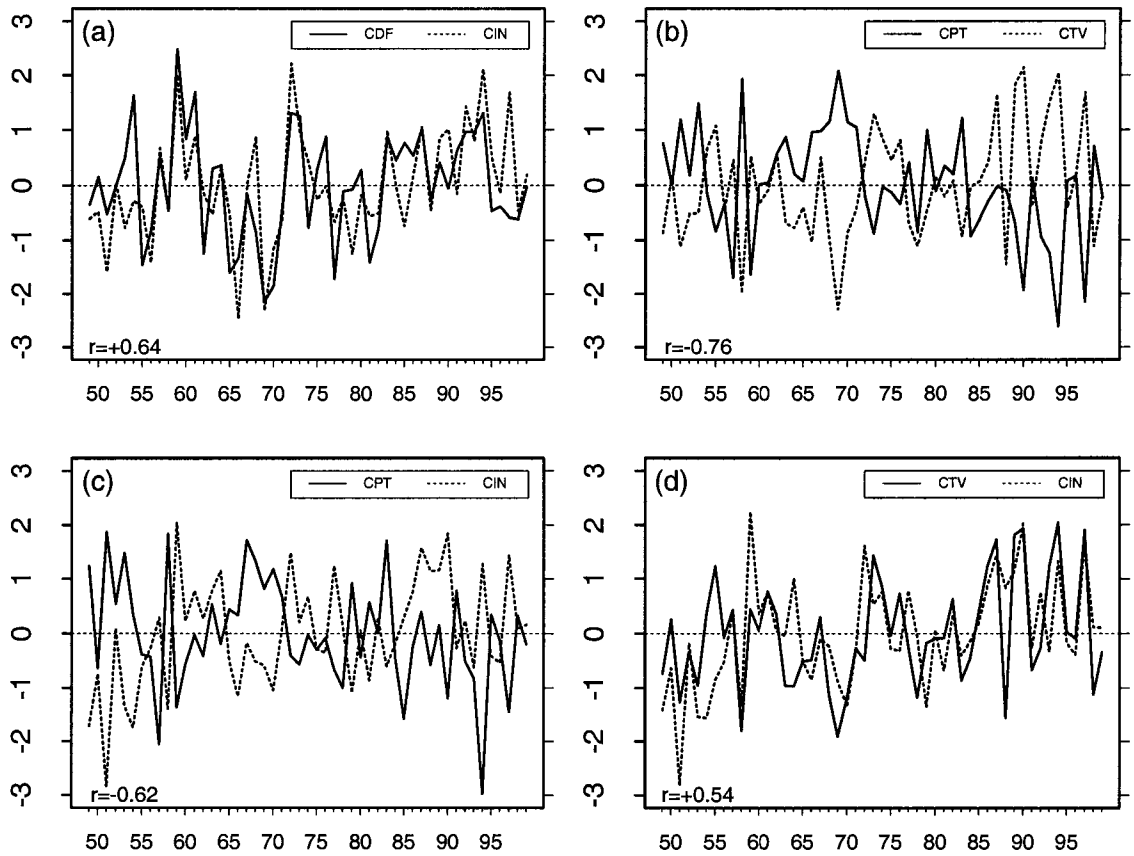


Fig. 3.10. 1949-99 time series of standardized winter (October-March) mean (1 value/semester) anomalies of cyclone parameters for key regions in North Atlantic (delineated in Figs. 3.9c-f). Panel (a) relates CDF and CIN (defined in Fig. 3.9 caption) for 60°-70°N/45°-35°W region; Panel (b) relates CPT and CTV for 45°-60°N/60°-35°W region; Panel (c) relates CPT and CIN for 40°-55°N/60°-35°W region; and Panel (d) relates CTV and CIN for 45°-55°N/50°-30°W region. Correlation coefficients appear in bottom left-hand corners of each panel. The year (minus 1900) labeled on the horizontal axis corresponds to the year in which January occurs. All cyclone variables shown in this figure have zero mean and unit variance.

3.5 WAVELET ENERGY-BASED ANALYSIS OF CDF

Previous sections used a full grid, 2-dimensional approach to examine the long-term climatological features and persistence of cyclone activity. This approach will be adopted in subsequent chapters as well. The purposes of this section are (1) to support this use of the full 2-D grid approach as opposed to more extensive use of regional averaging and (2) separate interannual versus longer time-scales of the CDF signal. A wavelet transform (described next) was used to carry out this task; results are discussed in Subsection 3.5.2.

3.5.1 Methodology

Wavelet transform is an analysis tool well suited to the study of multi-scale, nonstationary geophysical processes occurring over finite spatial and temporal domains (e.g., Daubechies 1990; Lau and Weng 1995; Torrence and Compo 1998; Mallat 1999). It can be used to analyze time series that contain nonstationary power at many different frequencies. An excellent mathematical introduction to the theory of wavelets is available in Daubechies (1992). The power of wavelet analyses is that frequency *and* time decompositions of time series data are possible. In contrast, traditional Fourier analysis produces only frequency decomposition. A wavelet transform uses generalized local base functions (wavelets) that can be stretched and translated with a flexible resolution in both frequency and time, whereas a Fourier transform uses sine and cosine base functions that have infinite spans and are globally uniform in time (e.g., Lau and Weng 1995). Wavelet transforms are *localized* in time and are good building block functions for a variety of signals, including signals with features that change over time and signals that have jumps and other non-smooth features. Conversely, a traditional Fourier series approximation is not well suited to these types of signals (e.g., Bruce and Gao 1996). For instance, the examples provided in Fournier (2000), whether from images, explicit functions, or observed geopotential height, illustrate the greater efficiency of (orthonormal) wavelet analysis over Fourier analysis.

Wavelet transforms have been used in numerous studies in geophysics (see review by Torrence and Compo 1998). Atmospheric science studies not included in this review are wide-ranging, having dealt with field forecast verification (Briggs and Levine 1997), removing ground and intermittent clutter contamination from wind profiler signals (Jordan et al. 1997), temporal variability of the energy balance of thick Arctic pack ice (Lindsay

1998), atmospheric pollution modeling (Ekstrom and Hales 2000), convective momentum transport observed during the TOGA COARE intense observing period (Tung and Yanai 2002), turbulent patch identification in microstructure profiles (Piera et al. 2002), ensemble experiments on numerical weather prediction error and uncertainty for a North Pacific forecast failure (Hacker et al. 2003), and interannual variability in southern Québec streamflow (Anctil and Coulibaly 2004), among others.

This section introduces the terminology used in performing a wavelet transform, but will not provide detailed mathematical theory and justification. For more specifics, see Daubechies (1992), the special issue of the *IEEE Proceedings* (1996) edited by Kovačević and Daubechies, or Mallat (1999). The present study uses Discrete Wavelet Transform (DWT) as opposed to Continuous Wavelet Transform (e.g., Ouergli 2002) because of the orthogonality property of the former. For orthogonal wavelets, (1) the sum of the wavelet variances over all scales is equal to the variance of the observations (e.g., Lindsay 1998), and (2) DWT additionally is energy-preserving so that energy of the detailed spectrum and smooth spectrum sum to the total energy of the signal (e.g., Bruce and Gao 1996).

Here, the DWT wavelet transform uses orthogonally constructed wavelets of the symmlets type ("s8") after Daubechies (1992), with the symmlets being constructed to be as nearly symmetric as possible. The symmlets have mother ($\psi(t)$) and father ($\phi(t)$) wavelets. Over time, the mother (father) wavelet integrates to zero (one). The mother wavelet is used to estimate the high-frequency details, whereas the father wavelet is used to estimate the smoother, low-frequency characteristics of the time series. The wavelet approximation to a time series, f(t), is the sum of the contribution of the father wavelet

translated k times over the time series for the largest time-scale or dilation, J, and the sum of the contribution of the mother wavelet translated k times over the time series for each of the time-scales j where j=1,2,...,J. The contribution of the wavelet localized in time (via the translation factor, k) and scale (via the dilation factor, j) is the product of the wavelet coefficient and the wavelet function.

Mathematically, the wavelet approximation to a time series f(t) can be expressed as:

$$f(t) = \sum_k S_{J,k}\ \phi_{J,k}(t) + \sum_k d_{J,k}\ \psi_{J,k}(t) + \sum_k d_{J-1,k}\ \psi_{J-1,k}(t) + \ldots + \sum_k d_{1,k}\ \psi_{1,k}(t) \qquad (3.1)$$

where

- j=1,2,...,J defines the scale factor for the 2^j time-scale;
- k=1,2,...,$n/2^j$ where n is the length of the time series;
- t is located at the k^{th} translation of the 2^j time-scale: k * 2^j;
- $S_{J,k}$ represents the smooth part of the time series and is the wavelet coefficient for the father wavelet, $\phi_{J,k}(t)$, where $S_{J,k} = \int \phi_{J,k}(t)\ f(t)\ dt$;
- $d_{j,k}$ represents the "details" part of the time series and is the wavelet coefficient for the mother wavelet, $\psi_{j,k}(t)$, where $d_{j,k} = \int \psi_{j,k}(t)\ f(t)\ dt$ for j=1,2,...,J. The detail coefficients $d_{J,k}$, $d_{J-1,k}$, ..., $d_{1,k}$ represent progressively finer "corrections" to the smooth trend, capturing the high-frequency oscillations in the signal, f(t).

The energy (E_j) of the wavelet spectrum at the time-scale, 2^j, is defined as the summation of the square of the wavelet coefficients for that time-scale. Since DWT is energy-preserving, the total energy (E) of the time series is the sum of the energy at each of the time-scales, such that

$$E = E_S + E_d = \sum_{i=1}^{n} f_i^2 \qquad (3.2)$$

where

$E_S = \sum_{k=1}^{n/2^J} |S_{J,k}|^2$ is the energy of the smooth spectrum at the time-scale 2^J;

$E_d = \sum_{j=1}^{J} \sum_{k=1}^{n/2^j} |d_{j,k}|^2$ is the energy of the detailed spectrum at the time-scales 2^j, for j=1,2...,J; and

f_i is the discrete signal (i=1,2,...,n).

In this analysis, DWT was applied to pseudo-continuous time series of monthly CDF anomalies for the winter semesters (October-March) of 1951-99; hence, the total number of records (n) was 288. Note that the CDF field was originally constructed for October-March to focus on wintertime because (1) the synoptic-scale storm track activity is largest (Nakamura 1992; Chang et al. 2002) and (2) the oceanic mixed layer over the North Atlantic is at its deepest in winter (e.g., Sutton and Allen 1997); i.e., SST anomalies are most likely to express deeper subsurface anomalies. Therefore, the input time series for DWT are not completely continuous, though "physically homogeneous". The total number of scale levels (J) was set to 5 for a maximum time-scale of 2^J or about 5 winter semesters ($n/2^J = 9$ must be an integer). Hence, other time-scales resolved here were 2^1, 2^2, ..., 2^{J-1} winter months. E_s/E and E_d/E were computed at each individual grid point yielding spatial patterns of Percentage Wavelet Energy Concentration (PEC) of CDF anomalies over the North Atlantic Basin.

To justify the application of a Wavelet Transform to the above pseudo-continuous time series, the sensitivity of the PEC analysis to using different lengths of the winter season was investigated. The 5-month, 4-month, ..., and 2-month winter seasons yielded

the same key results (Figs. 3.12 and 3.13 for the respective detailed and smooth parts of the signal) as for the full winter semester (Fig. 3.11). Other investigators also have applied wavelet techniques to pseudo-continuous time series – Fournier (2003) employed 53 years of December, January, and February 6-hourly data in his analysis of observed atmospheric blocking for 1948-2000.

3.5.2 Results

Fig. 3.11 shows the Percentage DWT Energy Concentration of both the "details" part (periods less than ~ 5 years) and the remaining smooth part of the CDF signal, for which both parts sum to 100% at each grid point. This figure displays clear *spatial discontinuities* in the energy concentration of CDF fields over the North Atlantic in both the high-frequency (upper panel) and low-frequency (lower panel) bands. Thus, any areal averaging (e.g., zonal-averaging) at a given frequency band over a particular region (e.g., latitudinal band) may obscure important details. Therefore, this Dissertation will continue to analyze mainly 2-dimensional gridded cyclone fields rather than 1-D time series for latitude zones or smaller regions, unless there is a need to analyze/visualize detailed temporal variations of a particular cyclone parameter for a spatially coherent region.

Further, Fig. 3.11a shows that most regions of the North Atlantic have more than 95% of the total energy concentration in the detailed spectrum of cyclone activity. This is not surprising, considering the high-frequency nature of the atmosphere over the North Atlantic. In particular, it is worth noting that the percentage energy concentration in the detailed spectrum exceeds 99% of total CDF energy over a region in the Labrador Sea – which is the site of a major oceanic gyre for oceanic convection (Dickson et al. 1996); see Subsection 3.2.1 for more details – and near Newfoundland where the Labrador

Current interfaces with the Gulf Stream. The extratropical atmosphere over this area is very dynamically and thermodynamically active (Palmer and Sun 1985). A more elongated area with "details" PEC exceeding 99% of total energy has a southwest-northeastward orientation in mid-ocean southeast of Greenland; it is near a region of maximum cyclone track activity (Fig. 3.1a) and variability (Fig. 3.2a). Moreover, note that the area where the smooth PEC exceeds 5% (Fig. 3.11b) in the central-southern North Atlantic Basin is over a region with a previously demonstrated link to low-frequency variations in the SST field (Sutton and Allen 1997). In addition to spatial inhomogeneity in the energy of cyclone tracks, this PEC Analysis also revealed a clear distinction between the high- and low-frequency components of cyclone activity. Therefore, it was decided to discriminate between these two frequency bands, and hence forth separately examine North Atlantic cyclone variability at interannual time-scale (Chapter 4) and decadal-to-multidecadal time-scales (Chapter 5). Note that this PEC Analysis also was applied to the Akima-based cyclone fields (in addition to CDF) and yielded the same results and conclusions (not presented). Finally, as for the PEC Analysis based on different lengths of the winter season, the corresponding DWT parameters are given in Table 3.2.

Table 3.2. DWT parameters for different lengths of the winter season. n is the maximum sampling size of the time series. J is the maximum number of scale levels ($n/2^J$ must be an integer) for a maximum time-scale of 2^J winters. The cutoff period (yr) is given by 2^J/length.

Length	n	J	$n/2^J$	2^J (winters)	Cutoff Period (yr)
6 (ONDJFM)	288	5	9	32	5.33
5 (NDJFM)	224	5	7	32	6.40
4 (NDJF)	192	5	6	32	8.00

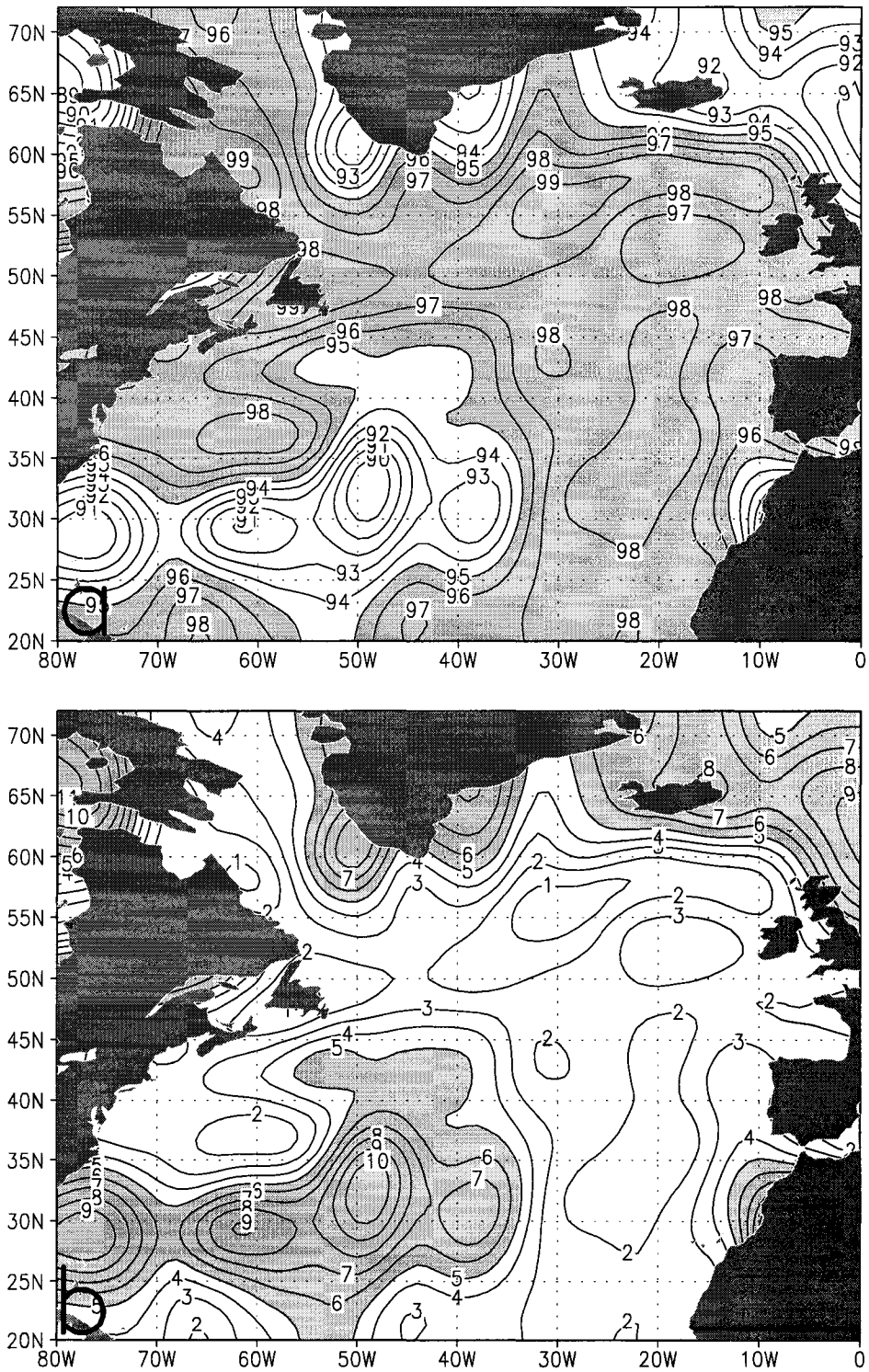


Fig. 3.11. Spatial patterns of Percentage Wavelet Energy Concentration (PEC) from a Discrete Wavelet Transform (DWT) analysis of North Atlantic winter semester (October-March) surface extratropical cyclone track density function (CDF) anomalies for 1951-99 (n = 288). Contours are in percent. Total number of scale levels (J) is set to 5 for a maximum time-scale of $2^J \sim 5$ winters ($n/2^J = 9$ must be an integer). Panel (a) presents detailed spectrum (periodicities < ~ 5 years) of the CDF signal; panel (b) presents the remaining smooth spectrum of the signal (periodicities > ~ 5 years). For orthogonal wavelets (i.e., "s8" after Daubechies 1992), DWT is energy-preserving so that, at each grid point, energy of the detailed spectrum (a) and smooth spectrum (b) sum to 100%. Light shading denotes areas where PEC is greater than 95% in (a) and 5% in (b).

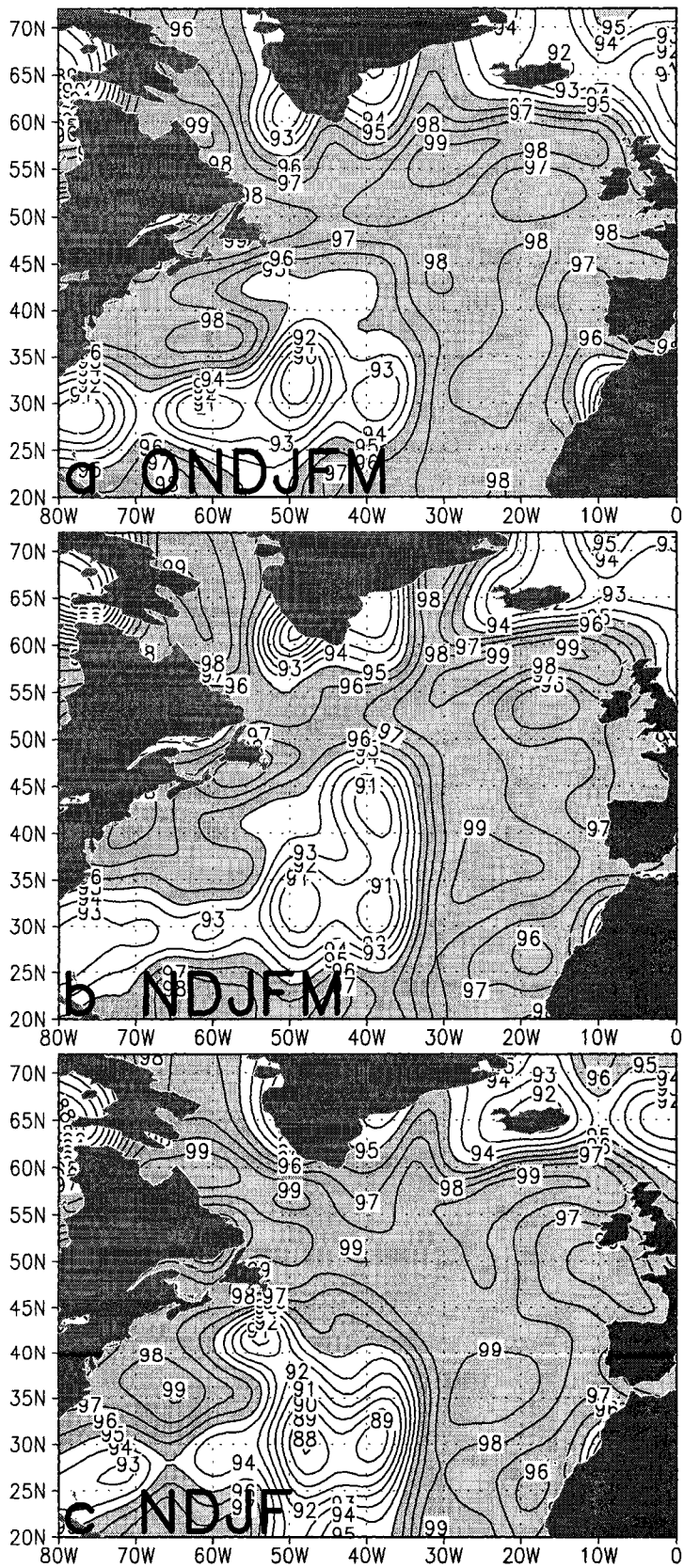


Fig. 3.12. As in Fig. 3.11a (detailed spectrum) but for different lengths of the winter semester. Panel (a) reproduces Fig. 3.11a (full winter semester) for comparison purpose. Panels b-c correspond to November-March (5 months) and November-February (4 months), respectively.

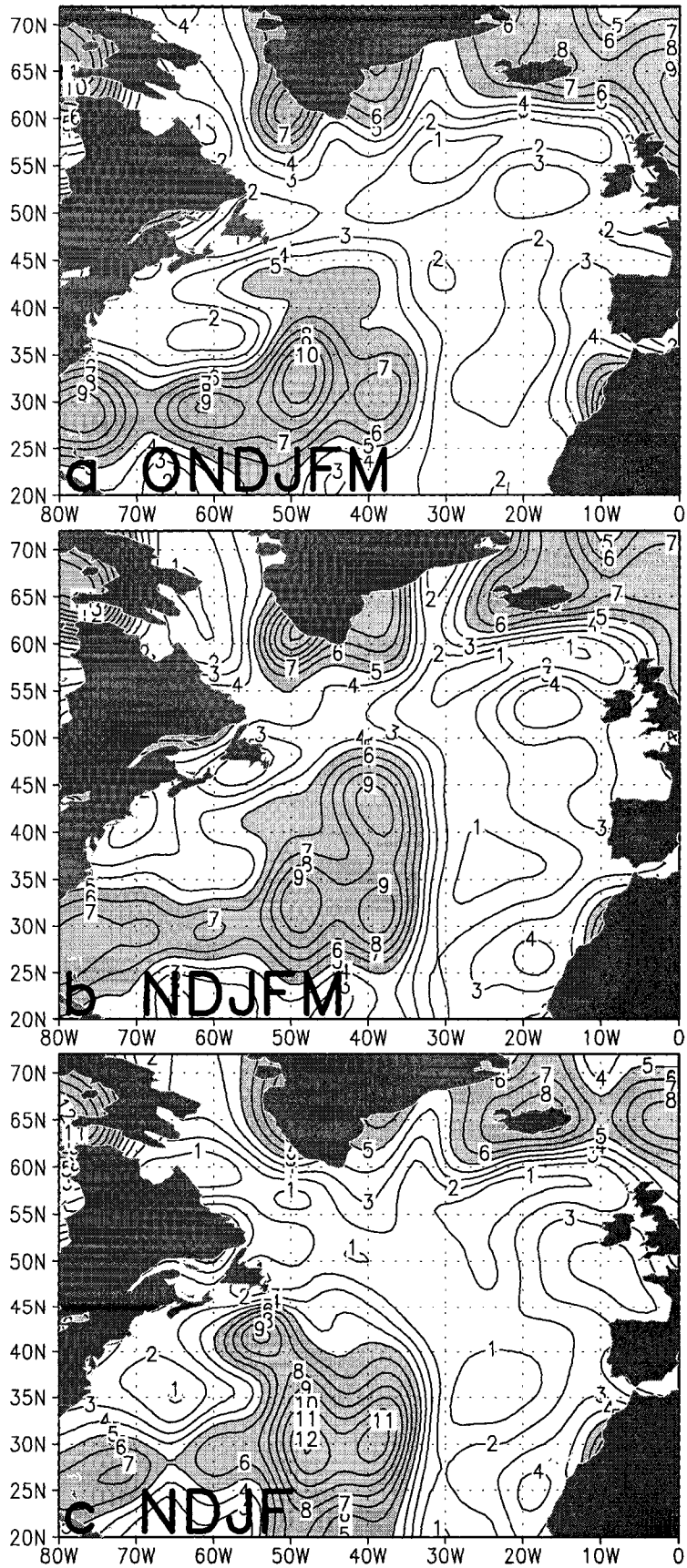


Fig. 3.13. As in Fig. 3.12 but for the remaining smooth spectrum of the signal in each winter season.

3.6 SUMMARY AND CONCLUSIONS

The key results obtained from this investigation of the long-term (1948-99) climatology of North Atlantic cold-season (October-March) surface extratropical cyclone activity and characteristics are as follows:

- Although the cyclone characteristics display different spatial patterns of variability, the spatial patterns of the long-term mean of the cyclone track density function (CDF), deepening rate, moving speed, and intensity are physically consistent with each other.
- The spatial patterns of CDF mean and standard deviation both exhibit strong intraseasonal variability.
- Month-to-month persistence of cyclone activity is generally weak, with significant spatial and intraseasonal variability. Further, the 1-month lag autocorrelation function (ACF1) of the cyclone parameters is, in general, also weak, though the ACF1 fields are physically consistent with each other. This weakness in cyclone persistence may be explained in part by the above bullet key point.
- Both cyclone pressure tendency and moving speed are very weakly dependent on the contemporary CDF over most of the basin. In contrast, CDF is more closely related to the cyclone intensity southeast of Greenland. Over the central-western North Atlantic, there is a marked tendency for cyclone systems to move faster as they deepen, with this effect greater for intense systems.

The significance of the work presented in this chapter lies in number of factors. First, the North Atlantic cyclone climatology has been derived from 51 years (1948/49-1998/99) of data, a period longer than any considered heretofore. For the CDF and other related cyclone parameters, different aspects of cyclone activity were examined and their

interrelations and hence the robustness of the results were assessed. Also, this climatology has been compiled using the CDF, one of the most reliable automated methods of analysis of surface cyclone activity available to date. The NCEP/NCAR reanalyses employed to construct CDF are regarded as one of the best long-term representations of the Northern Hemisphere atmosphere (e.g., Simmonds and Keay 2000a). Additionally, the Reanalysis SLP used in this present study to identify and track cyclones is in the most reliable class of reanalysis variables (Kalnay et al. 1996). Use of these reanalyses at short (6-hourly) intervals greatly reduced uncertainties involved in identifying and tracking cyclones. Hence, this climatology of North Atlantic winter cyclone activity is arguably the most accurate and representative yet produced. Finally, use of the unique PEC Analysis of CDF supported (1) separation of the high-frequency (treated in Chapter 4) and low-frequency (Chapter 5) components of cyclone activity; and (2) use of full 2-dimensional grid analyses that document the spatial heterogeneity of cyclone behavior, rather than zonal- or other area-averaging approaches.

CHAPTER 4: INTERANNUAL VARIABILITY OF CYCLONE TRACKS AND ASSOCIATIONS WITH REGIONAL CLIMATE VARIATIONS

4.1 INTRODUCTION

As stated previously, it long has been recognized that mobile, O-scale (1000 km) high and low pressure systems cause much of the day-to-day weather variability in midlatitudes. The introduction to the previous chapter summarized the high contemporary relevance of these systems for the weather forecasting and climate science communities. Climate scientists increasingly are devoting attention to understanding the modes and mechanisms of natural variability in the climate system (e.g., Simmonds and Keay 2000b). Therefore, after documenting the long-term mean behavior of various characteristics of North Atlantic winter semester (October-March) surface extratropical cyclone activity for 1948-99 in the preceding chapter, the cyclone data set developed in Chapter 2 also allows us to consider many aspects of the variability of these features in subsequent chapters.

Chang et al. (2002) noted that the variability of midlatitude storm track structures during the Northern Hemisphere cool season spans a broad range of time-scales. Given this wide range of frequencies, it is becoming common in climate science to focus upon either the short-term (e.g., Lau 1988) or longer-term (e.g., Chang and Fu 2002) variability of the process being studied (e.g., storm activity). Such a discrimination between the high-frequency and low-frequency components of North Atlantic winter cyclone variability was supported in the preceding chapter via application of a novel Discrete

Wavelet Transform-based analysis technique to cyclone track density function (CDF) anomalies (Section 3.5/Figs. 3.11, 3.12, 3.13). This analysis suggested a cutoff frequency of ~5 years. Therefore, the purpose of this chapter is to examine the interannual variability of North Atlantic winter cyclone activity and its associations with regional climate variations, including one sensitive bordering region (Morocco). Lower frequency variability will be dealt with in next chapter. Several analysis methods are applied to the CDF data set and other related cyclone parameters (e.g., intensity, moving speed, duration) to illuminate the variability of winter cyclone track structures over the North Atlantic Basin.

The present chapter is organized as follows. Previous relevant work is reviewed in Section 4.2. The data and methodology used are presented in Section 4.3. Next, the principal modes of North Atlantic winter surface extratropical cyclone track variability are identified from a VARIMAX Rotated Principal Component (VRPC) Analysis of CDF anomalies (Section 4.4). This section emphasizes fundamental differences between the leading modes (i.e., VRPC1, VRPC2, VRPC3) of CDF in several respects, yielding a new classification of North Atlantic winter cyclone behavior into three major circulation regimes. Relationships of atmospheric and oceanic anomalies to the CDF modes also are documented and some suggestions are offered concerning the different physical mechanisms involved.

In addition, short-term cyclone variability can be related to global and regional teleconnection patterns, such as the El Niño/Southern Oscillation (ENSO) and North Atlantic Oscillation (NAO) phenomena (e.g., Paciorek et al. 2002). Subsection 4.5.1 documents the regional NAO impact on North Atlantic storm characteristics.

Additionally, the possibility of a more remote ENSO influence on North Atlantic winter storm tracks and atmospheric/oceanic circulation is explored in Subsection 4.5.2. Diverse studies, both observational and modeling, have investigated connections between ENSO-related tropical Pacific SST anomalies and global atmospheric circulation variations (reviewed in Trenberth et al. 1998). While the ENSO impact on regional atmospheric circulation is well established in some regions of the world (e.g., Australia), the response in the North Atlantic sector is much less clear. However, Fraedrich (1994) concluded from observational studies that a weak response may exist in some atmospheric variables (SLP, temperature, precipitation) during winter seasons (DJF) of El Niño or La Niña events. Furthermore, Merkel and Latif (2001) conducted high-resolution atmospheric GCM experiments to assess the ENSO impact on the North Atlantic/European sector and found a southward shift of the North Atlantic low-pressure systems in El Niño winters (DJF). These Fraedrich (1994) and Merkel and Latif (2001) results prompted analysis of the present CDF and related cyclone data sets in the ENSO teleconnection context.

Finally, Section 4.6 utilizes the above cyclone analysis work that was initially performed for the entire North Atlantic Basin, for immediate application to Moroccan precipitation variability. This analysis follows directly from Lamb's (1994) proposal that stressed the need for enhanced understanding of the relations between: (a) the NAO and the eastern North Atlantic low-pressure weather systems that provide Moroccan precipitation; and (b) those weather systems and the spatial/temporal patterns of Moroccan precipitation. The key issues are how much of the cyclone activity is NAO-related, and how much is not, and the implications this has for the predictability of Moroccan precipitation (El Hamly et al. 1998; Ward et al. 1999).

4.2 PREVIOUS RELEVANT WORK

Geng and Sugi (2001) investigated the variability of North Atlantic cyclone activity for the winter "core" (December-February, 1958-98) through an Unrotated Principal Component Analysis of cyclone frequency. Their presentation and discussion was limited to the first Principal Component (PC1) that represented only 16.2% of the total variance. Several fields (cyclone deepening rate, cyclone central pressure gradient, cyclone moving speed, SST) were then regressed upon the PC1 of cyclone frequency. The investigation reported below, on the other hand, does not limit the cyclone analysis to the first unrotated PC1. Instead, this investigation used the three CDF VRPC modes to classify North Atlantic winter storm behavior into three major circulation regimes (Section 4.4).

Also, the present study differs from Geng and Sugi (2001) in several other major respects: (1) it uses space/time objectively analyzed (spatially and temporally) continuous CDF fields instead of depending on standard cyclone counts; (2) the CDF data set has a 2° latitude x 2° longitude grid with 1-month (instead of season) time resolution for 1948-99, whereas Geng and Sugi developed their cyclone data set on a 4.5° x 4.5° grid with 3-month (December-February) time resolution for 1958-98; (3) Section 3.2 presented complete spatial patterns for the basic climatology of cyclone characteristics, while Section 3.3 documented the spatial distribution of cyclone persistence via month-to-month correlation and autocorrelation function analysis, neither of which was treated by Geng and Sugi; (4) the next chapter examines the geographical distribution of trend in cyclone activity, whereas Geng and Sugi's trend analysis used 1-dimensional time series obtained after areal averaging that can bias results; and (5) adopting a broader perspective, the present study relates the CDF field to various atmospheric and oceanic anomalies

(Subsection 4.4.4), ENSO (Subsection 4.5.2), and Moroccan regional precipitation patterns (Section 4.6).

Also relevant is Blender et al.'s (1997) delineation of winter (November-March) cyclone tracks in the North Atlantic/European region (80°W-30°E/30°N-80°N) for 1990-94 using ECMWF analyses data set of 1000-hPa geopotential height. They first developed an algorithm to identify midlatitude cyclones and cyclone paths with as few constraints as possible. Then, they applied a Cluster Analysis to relative trajectories of the cyclones, which yielded a classification of three distinctly different groups of cyclone tracks characterizing stationary, northeastward- and zonally-traveling storms. Therefore, the present analysis differs from Blender et al. (1997) by having a much longer observational basis, employing a somewhat different cyclone detection and tracking procedure followed by application of the CDF objective analysis scheme, and analyzing the cyclone data using alternative statistics. Differences between the present results and Blender et al.'s ones are discussed in Subsection 4.4.3. The VRPC-based cyclone regime classification developed here is the first available for the North Atlantic Ocean.

4.3 DATA AND METHODOLOGY

4.3.1 Data

This chapter uses raw data only, with no prior low-pass filtering being applied, to document interannual variability. Filtered time series (gridded or otherwise) are employed in next chapter to investigate longer-term variability. The time period treated is 1948-99 for all data sets. Winter is taken to be the 6-month semester from October to March. Hence, there are 306 individual winter calendar months in all data sets. As now explained, two types of data sets are used in this analysis: grid-point time series

(Subsection ***a*** below) and non-grid-point time series (Subsection ***b*** below).

a. Grid-Point Time Series

• *Cyclone data sets*: CDF (El Hamly et al. 2001a) and other related cyclone fields (e.g., intensity, moving speed, duration) whose construction was fully described in Chapter 2.

• *Atmospheric and oceanic data sets*: SLP, surface wind vector and wind speed, surface air temperature, sensible and latent heat net fluxes, precipitation rate, and 500-hPa geopotential height (Z500) from the NCEP/NCAR Reanalysis Project (Kalnay et al. 1996; Kistler et al. 2001); and NOAA extended reconstructed SST from the NOAA-CIRES CDC website (URL=http://www.cdc.noaa.gov/cdc/reanalysis/reanalysis.shtml) (Smith and Reynolds 2003).

b. Non-Grid-Point Time Series

• *Regional teleconnection indices*: (1) NAO indices: Rogers' NAO (NAO_r, Rogers 1984); Hurrell's NAO (NAO_h, Hurrell 1995a); and Mobile NAO (NAO_m, Portis et al. 2001); and (2) ENSO indices: Southern Oscillation Index (SOI) and various SST indices (e.g., Niño 3.4 SST) available online at the NOAA Climate Prediction Center (CPC) website (URL=http://www.cpc.ncep.noaa.gov/data/indices/index.html); other indices were used as well, such as Montroy et al.'s (1998) tropical Pacific SST modes.

• *Moroccan Regional Precipitation (MRR) indices* – regionally-averaged standardized departures (z-scores) (El Hamly et al. 1997a; Ward et al. 1999).

4.3.2 Methodology

The various methods applied in this chapter now are listed or briefly described. More details on some methods are provided in the corresponding sections indicated.

• *VARIMAX Rotated Principal Component Analysis* (VRPC; Subsection 4.4.1): This well known technique is described fully in Richman (1986), Gong and Richman (1995), and Montroy et al. (1998).

• *Matching Pursuit Transform* (MPT; Subsection 4.4.2): As explained in Mallat and Zhang (1993), Bruce and Gao (1996), and Vincent and Bengio (2002), MPT, a cutting edge wavelet technique, is an iterative procedure whereby successive waveforms are found to estimate a signal within a time series f(t) (e.g., CDF VRPC scores). These waveforms are drawn from a waveform dictionary that usually contains a redundant set of functions that permits more versatility in matching the signal structures in f(t). This versatility in matching signal structures is a main reason for its development in the signal-processing and wavelets community. More details on MPT procedure are given in the Appendix provided at the end of this Dissertation.

• *Point-correlation maps* (Subsection 4.6.2): These display spatial correlation patterns.

• *Compositing Analysis*: It provides high-minus-low composite difference fields of gridded anomalies (e.g., SST) based upon either one time series (Subsection 4.4.4, Section 4.5) or two time series simultaneously with additional constraints on the two time series in question as in Subsection 4.6.3a that deals with relationship of CDF and Moroccan precipitation with NAO.

• *Multiple Regression Method* (Subsection 4.6.4): This involves choosing the "Best Model" (e.g., for prediction of Moroccan regional precipitation indices) using Stepwise Selection (e.g., Weisberg 1980).

4.4 CLASSIFICATION OF CYCLONE BEHAVIOR INTO MAJOR REGIMES

The phenomenology of North Atlantic winter surface extratropical cyclone tracks is examined here. This section first uses VARIMAX Rotated Principal Component (VRPC) Analysis to identify the major modes (i.e., VRPC1, VRPC2, VRPC3) of CDF variability, and then proceeds to emphasize fundamental differences between these leading modes in several respects. Specifically, these differences are documented in terms of: (1) spatial VRPC loading patterns and associated score time series (Subsection 4.4.1); (2) a wavelet (Matching Pursuit Transform) time-frequency decomposition of the CDF VRPC scores (Subsection 4.4.2); (3) raw surface extratropical cyclone tracks associated with positive and negative extreme CDF VRPC monthly scores for each cyclone track mode (Subsection 4.4.3); and (4) compositing analysis of relationships of the cyclone modes with various atmospheric and oceanic circulation anomalies (Subsection 4.4.4).

4.4.1 Spatial VRPC Loadings/Associated Score Time Series

To identify coherent modes of variability in North Atlantic winter cyclone tracks, a Principal Component (PC) Analysis was applied to individual monthly CDF anomaly fields for 1948-99. Unrotated PCs (UPCs) first were derived from the inter-grid-cell correlation matrix, yielding a set of spatial loading patterns (Figs. 4.1a-c) and their associated time series of PC scores. However, in general, the unrotated solutions seldom show the simple, unique, statistically robust patterns of spatial variability existing in data sets (Richman 1986). Further, when physical interpretation is a primary goal of PCA, rather than simply data compression, it often is desirable to rotate a subset of the initial eigenvectors to a second set of new coordinate vectors (e.g., Wilks 1995, p. 393). Thus, in order to obtain statistically robust patterns, VARIMAX rotation was performed on a certain number of the unrotated patterns. Based on a scree test of the eigenvalues

(Richman 1986, not shown), three PCs were retained for the orthogonal rotation.

The resulting spatial loading patterns for these three VARIMAX-rotated PCs (VRPCs) and their associated score time series are depicted in Figs. 4.1d-f and 4.2, respectively. Fig. 4.1 shows that the UPC and VRPC patterns are quite similar, which confirms that the CDF modes are robust. However, the rotated PCs conform more to the idea of simple structure, since each VRPC pattern emphasizes more uniquely a particular feature of the variability of CDF anomalies. The 0.1+ weaker extremum south of the domain in VRPC1 pattern (Fig. 4.1d) is much weaker than its UPC1 counterpart (0.3) (Fig. 4.1a), thus emphasizing the dipole structure of VRPC1. The two centers of action in VRPC2 are stronger in magnitude (0.6) than their UPC2 analogues (0.5), showing that VRPC2 has stronger dipole structure than UPC2. The southern extremum in VRPC3 is stronger in magnitude (0.6) than its UPC3 counterpart (0.5). The 0.1 extremum west of the Strait of Gibraltar in VRPC3 is much weaker than its UPC3 counterpart (0.3). This demonstrates that VRPC3 conforms more to the idea of simple and stronger structure. Thus, the VARIMAX rotation has better isolated the patterns of variability.

Therefore, only the three VRPC modes are retained and treated further in this analysis, with the UPC modes being discarded. These three VARIMAX PCs (i.e., VRPC1, VRPC2, VRPC3), whose patterns are described below, collectively account for approximately 26.4% of total CDF variance depicted in Fig. 3.2a. Consistent with the design of the VARIMAX algorithm, each of these VRPCs explains similar fractions of the total variance.

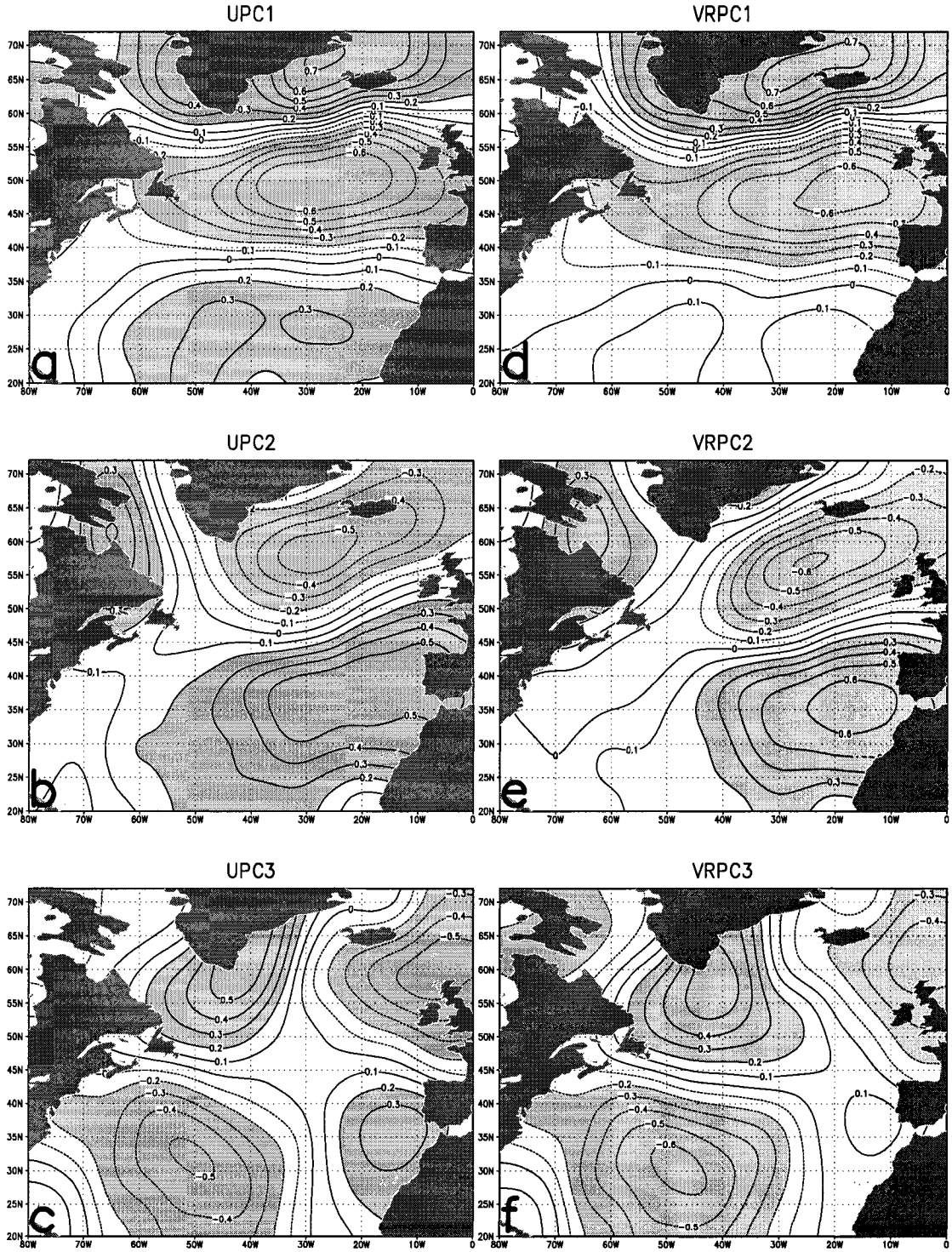


Fig. 4.1. Spatial loading patterns for leading modes of North Atlantic winter semester (October-March) surface extratropical cyclone track density function (CDF) anomalies for 1948-99. Panels (a)-(c) depict Unrotated Principal Component (UPC) modes (i.e., UPC1, UPC2, UPC3) that explain 10.3%, 8.9%, and 7.1% of total CDF variance, respectively. Panels (d)-(f) depict VARIMAX Rotated Principal Component (VRPC) modes (i.e., VRPC1, VRPC2, VRPC3) that explain 10.1%, 8.8%, and 7.5% of the total variance, respectively. Solid (dashed) contours indicate positive (negative) spatial loadings. Shading: a hyperplane cutoff is set to ±0.2 following Richman and Gong (1999).

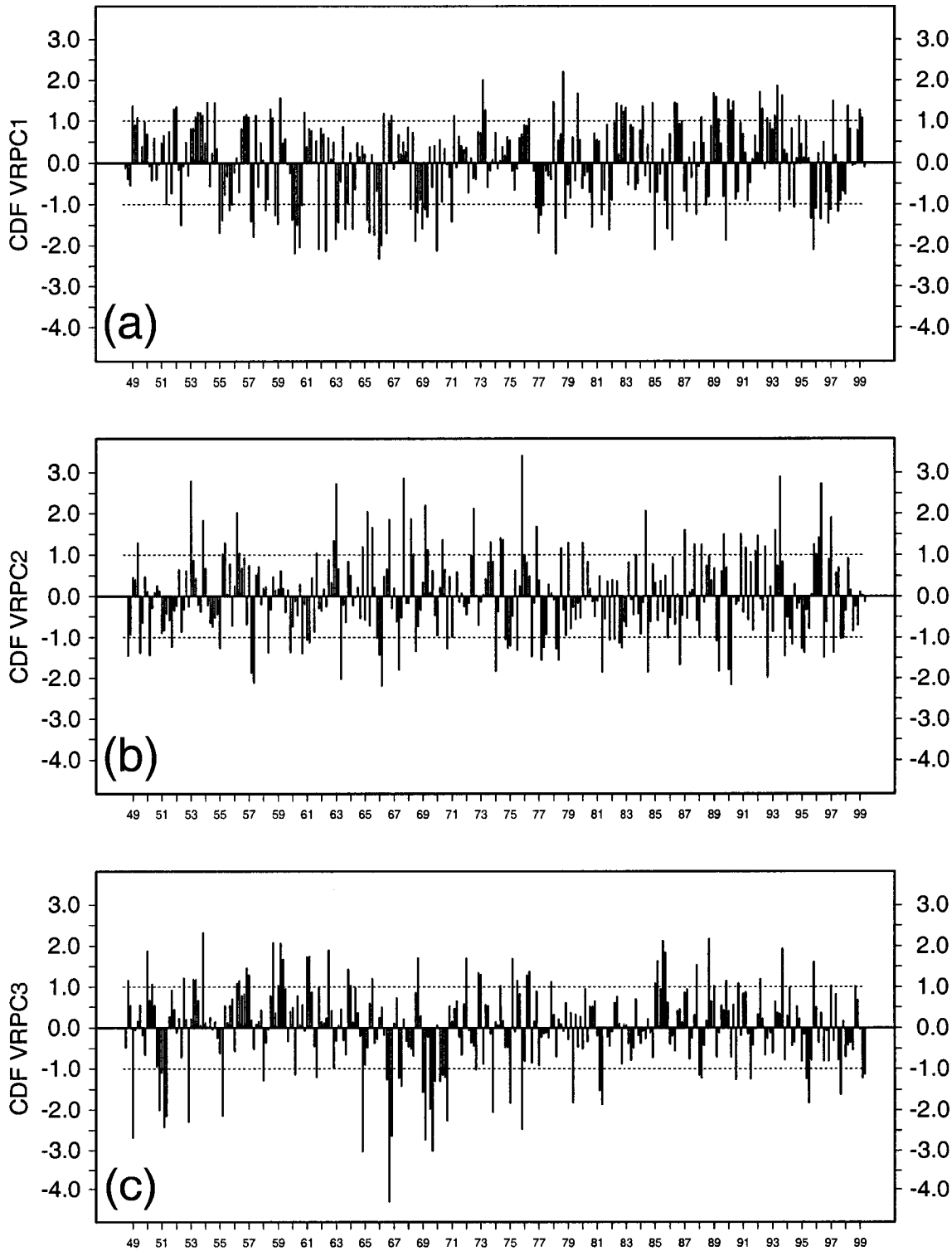


Fig. 4.2. Standardized time series of scores associated with the three VARIMAX Rotated Principal Component (VRPC) modes (given in Figs. 4.1d-f) of North Atlantic winter semester (October-March) surface extratropical cyclone track density function (CDF) anomalies for 1948-99. Panels (a), (b), and (c) present the VRPC1, VRPC2, and VRPC3 score time series, respectively. The year (minus 1900) labeled on the horizontal axis corresponds to the year in which January occurs. Each CDF VRPC score time series has zero mean and unit variance and is collectively uncorrelated with the other time series. Horizontal dashed lines in each panel indicate the cutoff score thresholds (±1) used in subsequent compositing analysis.

a. VRPC1 Pattern

This first mode of the cyclone track density function (Fig. 4.1d), which explains 10.1% of total CDF variance, is characterized by a simple south-north dipole structure. The northern center of action is maximized over the Greenland/Iceland corridor. The southern center of action is located over the central-eastern North Atlantic to the southwest of Ireland. These extrema straddle the climatological cyclone track in the raw CDF field depicted in Fig. 3.1a, with their polarity depending upon the sign of the CDF VRPC1 score time series (Fig. 4.2a). For instance, in its positive (negative) phase, this mode is associated with above (below)-normal cyclone activity over the Greenland/Iceland corridor, contrasting with below (above)-normal storminess over the central-eastern North Atlantic. This CDF mode thus reflects predominant northward or southward displacements of the primary storm track from its time-mean position in Fig. 3.1a. Note that the elongated sharp transition between the two centers of action, where the sign of the spatial loadings for CDF VRPC1 changes, has a dominant southwest-northeast orientation.

Further, it is worth noting that this pattern is strongly reminiscent of the positive polarity of the NAO, although it is shifted north relative to the locations of the traditional NAO nodes (van Loon and Rogers 1978; Lamb and Peppler 1987). In fact, CDF VRPC1 score and NAO_r (NAO_h) time series are highly correlated at r=+0.83 (r=+0.81) (Table 4.1). VRPC1 shows less relationship with NAO_m (r=+0.47), mainly due to the fact that the winter mobile (non-station) subtropical high nodes (computed for 1948-99) are shifted farther south of the southern node of VRPC1 mode. The mobile subpolar and subtropical nodes undergo nearly "parallel" month-to-month winter displacements, so the latitudinal separation between the two nodes generally remains constant (Portis et al. 2001, Fig. 1).

Table 4.1. Correlation coefficients between the three North Atlantic winter semester (October-March, 1948-99) monthly CDF VRPC score time series (Fig. 4.2) and monthly time series of three NAO indices due to Rogers (1984) (NAO_r), Hurrell (1995a) (NAO_h), and Portis et al. (2001) (NAO_m). Total number of months in each individual VRPC/NAO time series is 306. Values next to the correlations indicate statistical significance levels (%) according to a two-sided Student's t-test that factors in the effective sampling size of the time series (Wilks 1995, p. 127). Pairwise scatter plots of the above time series are given in Fig. 4.22.

	NAO_r	NAO_h	NAO_m
CDF VRPC1	0.83 (99.99)	0.81 (99.99)	0.47 (99.99)
CDF VRPC2	-0.31 (99.99)	-0.35 (99.99)	-0.49 (99.99)
CDF VRPC3	-0.05 (53.66)	-0.01 (14.70)	0.31 (99.99)

- ***NAO vs the Arctic Oscillation (AO)***

Thompson and Wallace (1998, 2000) and Thompson et al. (2000) presented evidence for the significance of the pattern of variability they referred to as the AO (following the earlier studies of Lorenz (1950) and Kutzbach (1970)). Although the two AO and NAO modes are highly correlated (e.g., Deser 2000), Wallace (2000) indicated that the NAO and AO are different interpretations of the same entity (i.e., NAO/AO: two paradigms – one phenomenon). That is, the NAO paradigm envisions this phenomenon as involving a unique teleconnection pattern in the Atlantic sector that varies on interannual and longer time-scales in association with large-scale atmosphere-ocean interaction. In contrast, the AO paradigm posits the existence of independent, fundamentally zonally symmetric (or "annular") modes of variability in the northern and the southern hemispheres, both of which fluctuate on intraseasonal as well as interannual time-scales. However, Deser (2000) reported that the "annular" character of the AO is more a reflection of the dominance of its Arctic center of action than any coordinated behavior of the Atlantic and Pacific centers of action in the SLP field. She found that the AO is nearly indistinguishable from the NAO ($r = 0.95$ for monthly data). Ambaum et

al. (2001) suggested that the NAO paradigm may be more physically relevant and robust for Northern Hemisphere variability than is the AO paradigm. However, they noted that this does not disqualify many of the physical mechanisms associated with the annular modes (e.g., AO) for explaining the existence of the NAO. Rogers (2001) reported a winter inseparability. The area of influence of the AO is the entire polar cap, whereas the NAO is limited to the North Atlantic and surrounding coastal areas (Magnusdottir et al. 2004). Therefore, only the NAO mode is retained and treated further in this Dissertation. For the present winter semester (October-March, 1948-99), the AO and the NAO are significantly correlated ($r = 0.70$ for NAO_r, 0.71 for NAO_h, and 0.58 for NAO_m).

b. VRPC2 Pattern

This second mode of the CDF anomaly field (Fig. 4.1e), which explains 8.8% of the total variance, also has a dipole structure, but with key changes from VRPC1. Relative to VRPC1 (Fig. 4.1d), the VRPC2 pattern has the opposite polarity and nodes shifted farther south. Further, compared to the positive phase of VRPC1 mode, the VRPC2, in its negative phase, reflects less cyclone activity over its northern node (centered southwest of Iceland). The southern center of action is located immediately west of the Strait of Gibraltar. This mode depicts northward or southward migration of a storm track from its long-term mean location. For instance, in its positive phase, this mode is associated with below-normal cyclone activity southwest of Iceland, contrasting with above-normal storminess west of the Strait of Gibraltar. The elongated sharp transition between these two CDF extrema also has a prevailing southwest-northeast orientation.

As opposed to the first mode, the VRPC2 is much less a NAO-like pattern than VRPC1, since it is shifted south with respect to the locations of the traditional NAO nodes and has a relatively weaker third center of action over the Labrador Sea. In fact, the CDF VRPC2 score and NAO_r (NAO_h) time series are negatively correlated at r=-0.31 (r=-0.35) (Table 4.1). This weaker correlation is important because it indicates that the CDF VRPC2 mode departs from the traditional and well known NAO. VRPC2 displays a little higher negative correlation magnitude with NAO_m (r=-0.49) due in part to the characteristic location of the mobile subtropical high node in January (eastern Atlantic in the vicinity of the southern node of VRPC2 mode) (Portis et al. 2001, their Fig. 1). The regional relevance of this pattern will become evident in Section 4.6, which shows that the positive phase of VRPC2 mode is associated with wet conditions over the northwestern Atlantic coastal areas of Morocco.

c. VRPC3 Pattern

This third mode of the CDF anomalies (Fig. 4.1f), which explains 7.5% of the total variance, also has a dipole but in the central North Atlantic Basin. The northern center of action is maximized over the southern tip of Greenland, bounded to the west and east by weaker extrema of opposite sign. The southern node affects the central-southern part of the basin. This VRPC3 pattern is suggestive of wave-like modulation of eddy activity, with above and below normal eddy amplitudes occurring at preferred sites. It is similar in polarity to VRPC1 (Fig. 4.1d), but the pattern is shifted farther to the southwest and is associated with fewer cyclones south of Greenland in its positive phase. The possible intrusion of tropical cyclones from the south into the North Atlantic Basin, is accounted for by this third mode (during its negative phase).

Note that in this pattern, as opposed to the first and second CDF modes, the elongated transition between the two main extrema that affect most of the basin has a prevailing west northwest-east southeast orientation from Nova Scotia to the Iberian Peninsula. The time series of VRPC3 scores and the NAO_r/NAO_h indices are very poorly correlated (Table 4.1). This is not surprising since the centers of action of this mode are not near the locations that NAO_r and NAO_h are sampling. However, there is some link between the VRPC3 mode and the NAO_m (r=+0.31) resulting from the southwestward excursions of the mobile subtropical high nodes in February-March and especially November (Portis et al. 2001, their Fig. 1).

d. Trends and Persistence of CDF VRPC Scores

Linear trends (via least-squares fit) in the CDF VRPC scores (Fig. 4.2) were found to be not statistically significant and so are not shown. The autocorrelation Function (ACF) of each score time series is displayed in Fig. 4.3. At 1-month lag, the three score time series exhibit autocorrelations of +0.18, +0.11, and +0.29, respectively. Hence, of all three modes, VRPC3 (affects mid-Atlantic) is the most persistent at 1-month lag; whereas VRPC1 and VRPC2 (influence eastern North Atlantic) are less persistent. As for NAO (not shown), the persistence between winter months is weak for VRPC1; the 1-month lag ACF of $NAO_r/NAO_h/NAO_m$ is +0.17/+0.20/+0.18, respectively. In contrast, the strong persistence of the Southern Oscillation Index (SOI) is reflected in a 1-month lag ACF of +0.60. Fig. 4.3 shows that ACF of the CDF VRPC scores at longer lags ($\geq$ 2 months) plunges rapidly, with the ACF values being statistically insignificant.

Bar plots of the month-to-month persistence of CDF VRPC scores are shown in Fig. 4.4. February/March emerges as the only pairing of consecutive winter months with

significant persistence for all three modes (r=+0.32, +0.31, and +0.43 significant at 96.21%, 94.89%, and 99.71% levels, respectively). For VRPC1, this persistence steadily increases (though statistically insignificant) from the beginning of the winter semester to its end. VRPC2 persistence is more variable, but with an additional relatively significant value in December/January (r=+0.27 at 92.24%). VRPC3 persistence seems to fit a quadratic (convex) function, with maxima at the ends of the winter season and the minimum at the midpoint (i.e., in December/January). VRPC3 features significant persistence in both January/February (r=+0.29 at 92.87%) and October/November (r=0.50 at 99.92%). Note that, of all the modes and pairings of consecutive winter months, October/November has the highest month-to-month persistence for VRPC3. In contrast, as for NAO, November/December was found to be the only pair of consecutive months with significant persistence for both NAO_r and NAO_m during 1948-2001. Specifically, in this pair, VRPC1 (NAO_r) manifests a persistence of 0.21 (0.28). Finally, the correlation averages over all pairings of consecutive winter months for the three modes are +0.234, +0.144, and +0.316, respectively, which is consistent with the ordering of the 1-month lag VRPC ACFs in Fig. 4.3. Thus, VRPC3 (VRPC2) is the most (least) persistent mode at 1-month lag.

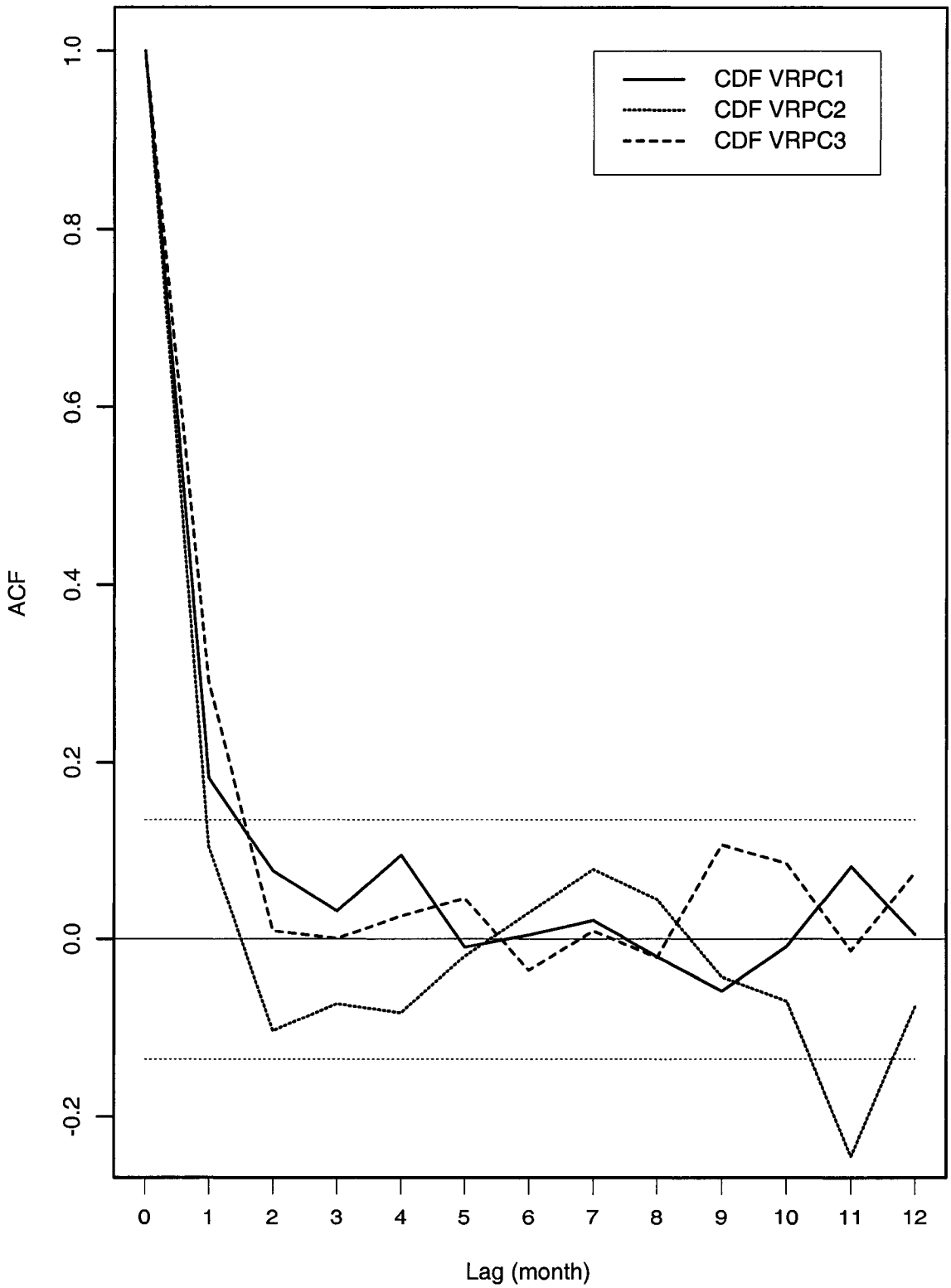


Fig. 4.3. Autocorrelation function (ACF) as function of lag (month) of North Atlantic winter semester (October-March, 1948-99) CDF VRPC score time series (given in Fig. 4.2). Total number of records in each individual VRPC time series is 306 months. The correlation coefficient magnitude of 0.136 (0.178) is statistically significant at the 95% (99%) confidence level according to a two-sided Student's t-test that factors in the average effective sampling size of the three time series (Wilks 1995, p. 127). Horizontal dashed lines indicate the 95% confidence limits.

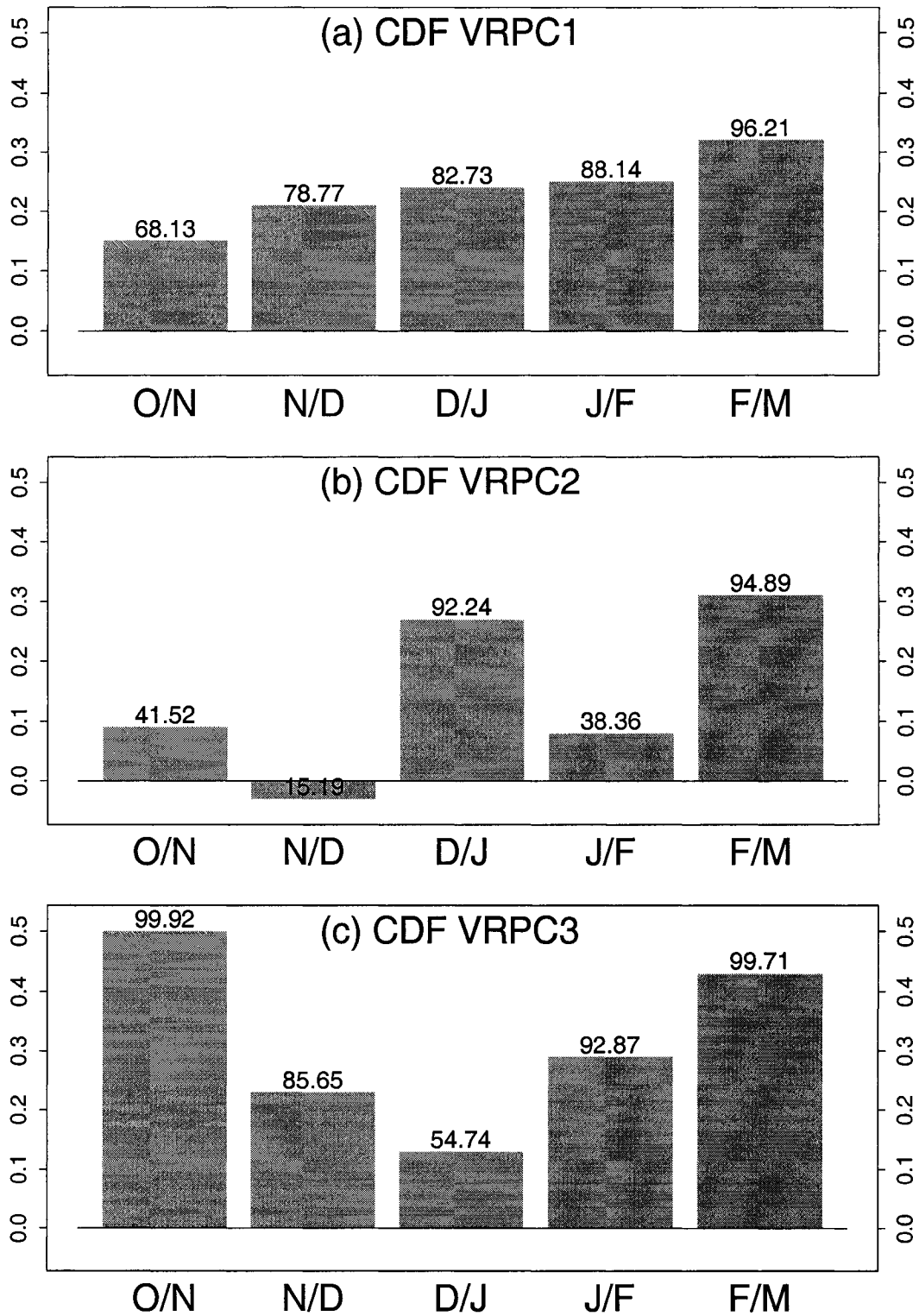


Fig. 4.4. Month-to-month persistence of North Atlantic winter semester (October-March, 1948-99) CDF VRPC score time series (given in Fig. 4.2). Panels (a), (b), and (c) present month-to-month correlations of VRPC1, VRPC2, and VRPC3, respectively. Total number of records in each monthly VRPC time series is 51. Values on top of bars indicate statistical significance levels (in percent) of those correlations according to a two-sided Student's t-test that factors in the effective sampling size of each time series (Wilks 1995, p. 127).

4.4.2 Matching Pursuit Transform Time-Frequency Decomposition of CDF Scores

One key finding from the preceding section is that the persistence of CDF VRPC score time series (via both 1-month lag autocorrelation function and month-to-month correlation analyses) is generally weak. This suggests that the CDF signal may be nonstationary. Therefore, the purpose of the present investigation is to address the following two questions:

(a) Is there any changing nature of each CDF "track" mode with time? and

(b) Singularities in time and frequency of each CDF VRPC score time series?

To address the above questions, wavelet analysis was applied to the CDF signal. Wavelet Analysis is the topic of much contemporary enthusiasm in mathematics, engineering, and scientific circles. As noted by Bruce and Gao (1996), wavelet theory has unified and extended ideas from several domains, such as sub-band filtering, approximation theory, signal processing, image processing, nonparametric estimation. Matching Pursuit Transform (MPT) was selected here among other wavelet techniques (e.g., DWT, Section 3.5) in order to best match the signal structures. Mallat and Zhang (1993) showed that matching pursuits provide extremely flexible signal representations. Following El Hamly et al. (2000), who first applied the MPT procedure to the mobile NAO_m index (URL=http://xtide.ldeo.columbia.edu/~visbeck/nao/figure/figure.html), this wavelet technique also is applied herein to each CDF VRPC score time series separately. A detailed description of the MPT algorithm is given in Appendix. Note that the MPT-based approach applied herein is the first ever conducted in the specific context of cyclone track variability.

In this matching pursuit application, CDF study period was restrained to October 1951-March 1999, yielding a sampling size, n, of 288 (as in Section 3.5). The total number of scale levels, J (i.e., the total number of multi-resolution components), is set to 5 ($n/2^J = 9$ must be an integer). Fig. 4.5 depicts the MPT time-frequency plane plot for each CDF score time series, showing the 50 most energetic wavelet atoms of the signal in each mode. In the time-frequency plane plot, each wavelet coefficient occupies a box having a constant area. This relationship is a version of the known "*Heisenberg uncertainty principle*" and states that a signal cannot simultaneously be concentrated in arbitrarily small time and frequency regions (see Appendix for more details). Fine-scale coefficients occupy tall thin boxes, whereas coarser-scale coefficients occupy flat wide boxes. In Fig. 4.5, the color-scale of each box corresponds to the absolute value of a wavelet packet coefficient $w_{j,b,k}$, where the index j corresponds to the scale level (or resolution level, j=1,2,...,J), the index k denotes the translation shift ($k=1,2,...,n/2^j$), and b is the oscillation parameter ($b=0,1,...,2^j-1$). The horizontal/vertical center of a box in Fig. 4.5 is located at the time/frequency center of the associated wavelet packet function. It is worth noting that a significant difference between the DWT (Section 3.5) and MPT transforms is that DWT is characterized by two parameters (frequency, time) whereas MPT is based on three parameters (frequency, time, oscillation). Recall that, for comparison, Fourier Transform involves one parameter (frequency) only; i.e., the time information is completely lost.

Fig. 4.5 shows that the changing nature of the CDF signal is very well reflected in the Matching Pursuit Transform time-frequency decomposition. Also, this figure clearly reveals that each individual CDF mode displays different patterns of cyclone activity at a given point in time for a particular frequency band.

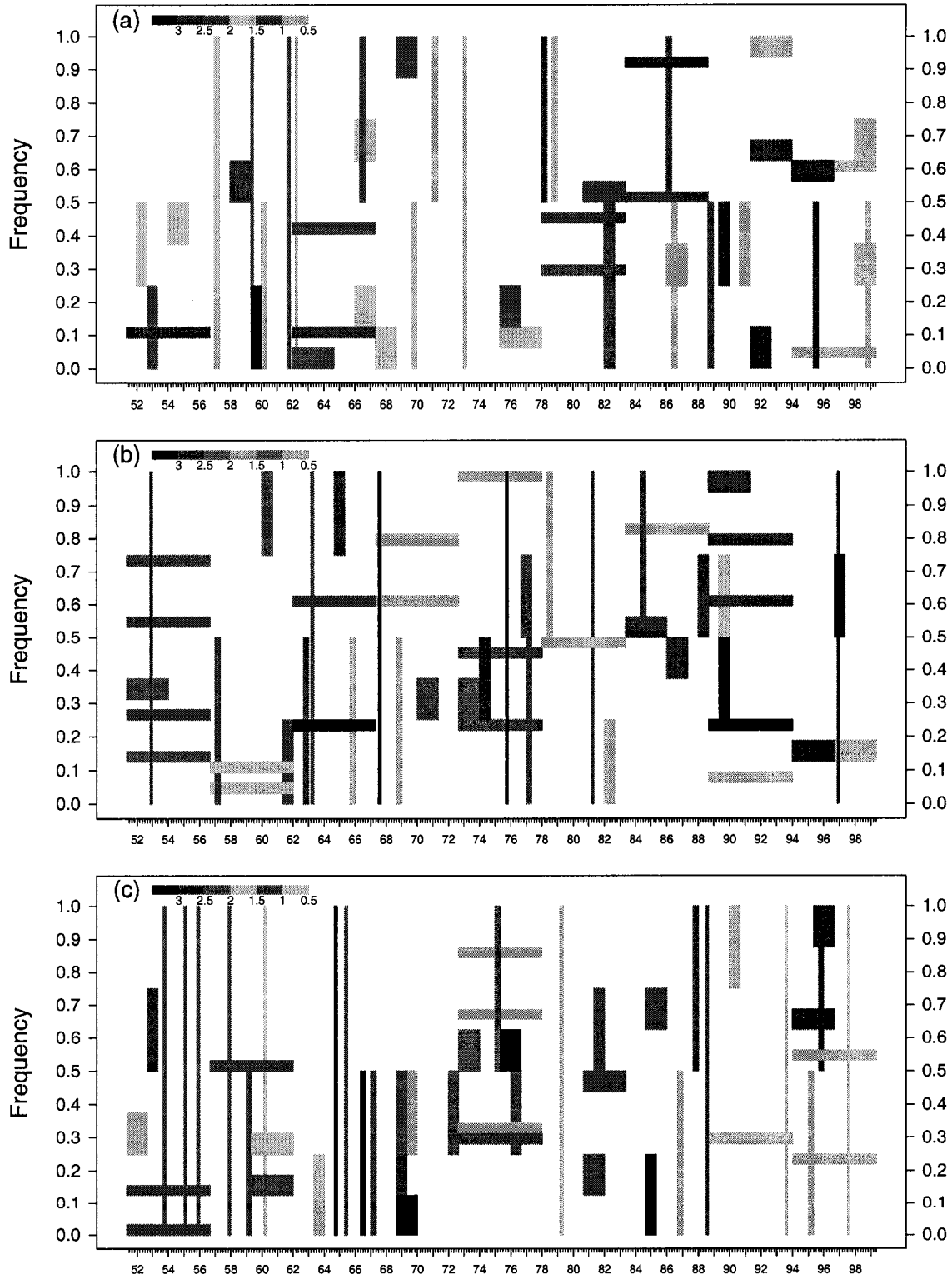


Fig. 4.5. Matching Pursuit Transform (MPT) time-frequency plane plots for CDF modes VRPC1 (Panel a), VRPC2 (Panel b), and VRPC3 (Panel c) for winter semesters (October-March) of 1951-99 (n = 288). As in Fig. 3.11, total number of scale levels (J) is set to 5 (so that $n/2^J = 9$ is an integer); total number of MPT atoms used is 50. The year (minus 1900) labeled on the horizontal axis corresponds to the year in which January occurs. See text and Appendix for more details.

Singularities in time ("jumps" or Dirac-like signals) are very well localized in time and very poorly localized in frequency (they span the whole frequency spectrum). The Appendix shows that these time singularities correspond exactly to the most extreme fine-scale features of the signal as defined by MPT (i.e., j=0; b=0). They represent the "details" part of the signal. Fig. 4.5 includes six of these time singularities for CDF VRPC1 (November 1961, January 1973, February 1957, February 1962, January 1957, and March 1959; sorted by decreasing atom magnitude), all of which occur in the first half of the study period (before March 1975). In contrast, while VRPC2 also has six time singularities (November 1975, October 1967, December 1952, December 1996, February 1963, and February 1981), they are dispersed over the whole study period, with two pronounced singularities occurring around mid-period (black thin vertical boxes). As opposed to the previous two modes, CDF VRPC3 has time singularities that are most prevalent in the first half of the study period (one of which is of substantial power), with 7/11 (4/11) occurring before (after) March 1975. Thus, the three CDF modes exhibit different time-based singularity characters.

In contrast, singularities in frequency are relatively well localized in frequency (low and high frequencies in general) and poorly localized in time by virtue of the "*Heisenberg uncertainty principle*". The Appendix shows that these frequency singularities correspond exactly to the most extreme coarse-scale features of the signal as revealed by the Matching Pursuit Transform (i.e., j=J). They represent the "smooth" part of the signal. CDF VRPC1 is characterized by more frequency singularities in the second half of the study period, with 6/9 occurring after March 1975. In contrast, CDF VRPC2 stands out as having 19 frequency singularities spread relatively uniformly over most of the period, with two considerable strength (black flat wide boxes). As opposed to the

first two modes, CDF VRPC3 displays 10 frequency singularities, primarily concentrated in the beginning, middle, and end of the period, with 4/10 of relatively notable strength around the mid-period. Thus, the three CDF VRPC modes are of quite different frequency-based singularity nature.

Therefore, another key finding is that the Matching Pursuit Transform is very efficient in identifying singularities in both time and frequency. This is perhaps not surprising, given the fact that the MPT is a "greedy" algorithm as was discussed by Davis et al. (1997) in their adaptive greedy approximations. Further, the existence of the above singularities in both time and frequency shows that the CDF signal is indeed characterized by non-stationarity.

Also, Fig. 4.5a shows that there was a substantial decrease in time singularities, contrasting with an increase in frequency singularities for CDF VRPC1 over the study period. Consistent with this is Hurrell and van Loon's (1997) reported tendency for the NAO power spectrum for the winter (December-March) to become redder with time in recent decades; their result was indicated clearly by an increase in running 60-year lag one autocorrelations of the NAO for 1865-1994. Recall that the NAO_h is correlated quite highly with the present leading mode of CDF anomalies (Table 4.1). Further, El Hamly et al. (2000) reported that the changing nature of the NAO_m signal was reflected in its MPT time-frequency decomposition – coarser-scale features in the lower frequency range have been more dominant in recent years and finer-scale features were more dominant in the 1960s and 1970s.

Moreover, the time singularity of CDF VRPC1 that occurred in January 1973 will be examined further in Chapter 5. It is shown that low-frequency winter CDF UPC1 score time series displays a clear transition in 1971/72, from an earlier period when the main cyclone track was generally zonal across the North Atlantic Basin, to the more recent era when the main cyclone track had a pronounced northeastward orientation, resulting in above-normal cyclone activity southeast of Greenland and over the Greenland Sea. Chang and Fu (2002, 2003), who examined upper-tropospheric eddy variance/covariance statistics over the Northern Hemisphere using NCEP/NCAR Reanalysis data (DJF, 1948/49-1998/99), also found a transition during the early 1970s from a weak storm track state prior to 1972/73 to a strong storm track state subsequently. They have chosen to denote storm track intensity primarily using high-pass-filtered 300-hPa meridional velocity variance. The leading EOF of this "proxy" variable corresponds to the simultaneous strengthening/weakening of both the Pacific and Atlantic storm tracks.

Finally, as for the DWT (Section 3.5), the sensitivity of the MPT technique to using different lengths of the winter season was investigated. The 5-month, 4-month, ..., and 2-month seasons yielded essentially the same key findings (plots not shown). As opposed to the Fourier Transform that analyses the whole signal (*global* support), Wavelet Transform provides localized time-frequency analysis (*local* support). That is, the bases in Fourier Transform have a global support; i.e., each basis (sinusoid) extends across the entire signal, whereas in Wavelet Transform, the bases (wavelets) are localized in time and frequency. This "localization" property justifies in part the application of a Wavelet Transform to the present pseudo-continuous time series.

4.4.3 Associated Raw Cyclone Tracks

To further document and confirm the efficacy of the three CDF VRPC modes in Fig. 4.1, Figs. 4.6-4.8 present the North Atlantic *raw* surface extratropical cyclone tracks associated with each individual mode. A raw cyclone track is determined by identifying successive latitudes and longitudes of cyclone centers with the same system identification number (e.g., Serreze et al. 1997; Geng and Sugi 2001). Differences between raw individual (fragmented) cyclone tracks and spatially/temporally continuous CDF "tracks" were discussed in Subsection 2.2.4c.

Some authors constrain the cyclone lifetime scale to filter out short-lived centers, most of which correspond either to weak troughs with little weather activity, or to secondary minima within complex systems, that are not deep enough to last more than a few hours or to develop into individual lows. For instance, Blender et al. (1997) identified cyclone track regimes in the North Atlantic using cyclones with lifetimes of 3 days and longer. Trigo et al. (1999) considered only cyclones that last a minimum of 12 hours. McCabe et al. (2001) used only cyclones that existed for two or more consecutive observation periods (i.e., at least 12 hours). Geng and Sugi (2001) analyzed only cyclones that last a minimum of 24 hours. Following Anderson and Gyakum (1989), no constraint was applied on the lifetime scale of the cyclones in this present study because the cyclone counts were subject to the CDF objective analysis scheme that is a space and time filter (Subsection 2.2.4c).

a. VRPC1-based Raw Cyclone Track Pattern

The raw cyclone track pattern for the winter semester month with the most positive CDF VRPC1 score (November 1978 with 66 different cyclone systems, Fig. 4.2a)

is displayed in Fig. 4.6a. The track is oriented southwest-to-northeast stretching from the U.S. East Coast to extreme Northwestern Europe. Thus, for this regime, a very well-defined southwest-to-northeast cyclone track maximum across mainly the entire northern part of the basin leads to the accumulation of occluded cyclones over Iceland and surrounding regions. Very few of these cyclone tracks successfully reach Great Britain and Western Europe. This cyclone track pattern here is termed the "type 1+ regime". It is substantiated further by the pattern in Fig. 4.6c for the second positive extreme month (February 1973 with 56 cyclone systems, Fig. 4.2a), which features a cyclone maximum over the Greenland/Iceland corridor that is the culmination of a well defined cyclone track from the southwest that extends to the U.S. East Coast. Additionally, Fig. 4.6e presents the cyclone tracks for the 12 most positive CDF VRPC1 (Fig. 4.2a) months, superimposed on the same plot. This figure shows relatively many cyclone tracks around Iceland and upstream to its southwest, and relatively few cyclone tracks reaching southwest of Ireland into the central-eastern North Atlantic. This is further evidence of the above type 1+ regime and reflects a positive NAO/Arctic Oscillation (AO) environment. This result is consistent with previous studies (e.g., Rogers 1990; Hurrell 1995b; Serreze et al. 1997; Clark et al. 1999; McCabe et al. 2001) that used different methods and/or data sets to show there is a northward shift of the storm tracks across the central North Atlantic during the positive phase of the NAO/AO.

In contrast, for the month with the most negative CDF VRPC1 score (January 1966 with 55 cyclone systems, Fig. 4.2a), Fig. 4.6b shows that the raw cyclone tracks tended to occupy a very well-defined zone across the entire North Atlantic Basin that starts from the U.S. East Coast and reaches across to Western Europe. This cyclone track pattern ("type 1- regime") is predominately confined in the region between 35°-55°N,

with very few cyclone passages to the north or south. The raw cyclone track pattern for the second negative extreme month (February 1960, 66 cyclone systems) presented in Fig. 4.6d is very much like the most negative VRPC1 pattern. Note in particular that very few cyclones reached the Greenland/Iceland corridor and more cyclones attained southwest of Ireland. This type 1- regime is very consistent with the negative phase of the CDF VRPC1 mode (Fig. 4.1d), and reflects a negative NAO/AO environment. During a negative phase of the NAO/AO, there is a southward shift of the storm tracks across the central Atlantic. Such southward migration also is notable in the pattern for the 12 most negative extreme months (Fig. 4.6f).

b. VRPC2-based Raw Cyclone Track Pattern

The raw cyclone track pattern for the winter month with the most positive CDF VRPC2 score (December 1975 with 66 cyclone systems, Fig. 4.2b) is shown in Fig. 4.7a. The track is split into a well-defined northern branch reaching Iceland from Nova Scotia and a well-defined southern branch with storms reaching Morocco and the Iberian Peninsula from the southwest, with very few cyclones traversing the central North Atlantic region. The split occurs near Newfoundland. The northern cyclone track maximum may lead to occluded cyclones over Iceland and surrounding areas. This split track pattern ("type 2+ regime") also is visible in Fig. 4.7c for the second positive extreme month (October 1993, 64 cyclone systems) and Fig. 4.7e for the 12 most positive months.

In contrast, the raw cyclone track pattern for the most negative CDF VRPC2 month (February 1966 with 46 cyclone systems, Fig. 4.2b) depicted in Fig. 4.7b is characterized by a very well-defined west-east cyclone track originating from the U.S. and

Canadian East Coasts and reaching the British Isles, which may lead to a collection of occluded cyclones in the central-eastern North Atlantic region. This cyclone track pattern (type 2- regime) is more zonal across the North Atlantic, definitely occupying region between the two branches of the split track in Fig. 4.7a (type 2+ regime). The type 2- regime also is supported further by the patterns in Fig. 4.7d and Fig. 4.7f for the second (February 1990, 53 cyclone systems) and the 12 most negative months, respectively.

c. VRPC3-based Raw Cyclone Track Pattern

The raw cyclone track pattern for the month with the highest positive CDF VRPC3 score (December 1953 with 64 cyclone systems, Fig. 4.2c) (Fig. 4.8a) has a principal (secondary) track south of Greenland (central-southern part of the basin), with the ends of the tracks becoming rather diffuse towards the Iberian Peninsula and Morocco. These two cyclone branches of this "type 3+ regime" clearly reflect the positive phase of the CDF VRPC3 mode (Fig. 4.1f) that has a south-north dipole structure influencing the central North Atlantic. This type 3+ regime also is discernible in the raw cyclone track patterns for the second positive extreme month (November 1988, 57 cyclone systems) (Fig. 4.8c) and the 12 most positive months (Fig. 4.8e).

In contrast, for the negative VRPC3 counterpart (November 1966 with 69 cyclone systems, Fig. 4.2c) (Fig. 4.8b), there is a split track pattern in the northwest-southeast direction, with well-defined cyclone track maxima in the northeastern and southwestern parts of the basin, with relatively fewer cyclones traversing the central basin. The southern cyclone track maximum tends to produce occluded cyclones in the central-southern part of the basin. This "type 3- regime" reflects the negative phase of the CDF VRPC3 mode (Fig. 4.1f). The above split pattern also is apparent in the raw cyclone

track patterns for the second negative extreme month (December 1964, 56 cyclone systems) (Fig. 4.8d) and the 12 most negative months (Fig. 4.8f).

Therefore, the above analysis of the raw cyclone tracks for individual extreme months confirms the existence of periods when each of the CDF VRPC modes dominates, yielding a new classification of the North Atlantic winter cyclone behavior into three distinctly different regimes. Briefly, VRPC1 is essentially the well known NAO teleconnection mode, whereas the new CDF VRPC2 reflects southwest-northeast split pattern. As opposed to VRPC1 and VRPC2, the new CDF VRPC3 features diffuse pattern of cyclone activity from the southern tip of Greenland towards the Iberian Peninsula/Morocco.

Some of the present results are consistent with those obtained by Blender et al. (1997), who applied a Cluster Analysis to cyclone displacements (over a minimum of 3 days) for the short November-March 1990-94 period. They identified three cyclone track clusters differentiating between stationary cyclones and northeastward and zonally traveling systems (see their Fig. 3). The stationary cyclones are predominantly located around Greenland and in the Mediterranean Sea, approximately corresponding to the positive phase of the present CDF VRPC3. The northeastward and zonally traveling cyclones correspond qualitatively to the positive and negative phase of the above VRPC1 mode, respectively. Note that their Cluster Analysis led to three types of cyclone tracks whereas the present VRPC-based analysis yields three modes but six types of regimes corresponding to the positive and negative amplitude excursions of each of the first three rotated CDF VRPCs.

It should be noted that, to date, the central focal point of most climate investigations on North Atlantic/European sector has involved the NAO. Therefore, these unique CDF VRPC modes are used extensively in this Dissertation, across a broad range of time-scales, to give new insight into the cyclone track organization and behavior over the North Atlantic Basin during wintertime. Next subsection emphasizes other key differences between the CDF modes by examining associated atmospheric and oceanic circulation anomalies.

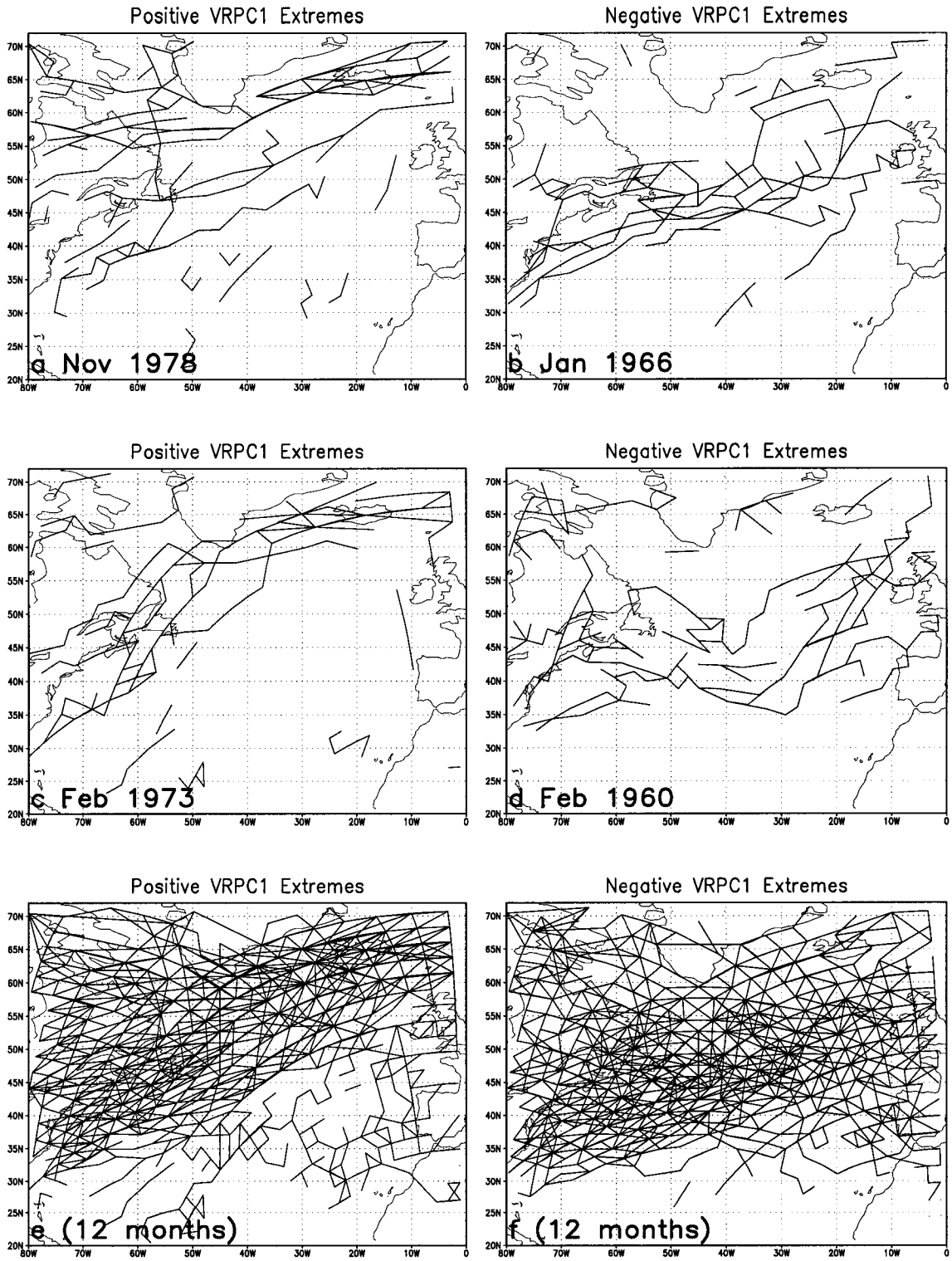


Fig. 4.6. Raw surface extratropical cyclone tracks over North Atlantic Ocean during 1948-99 for the winter semester (October-March) month with the most positive (a) and negative (b) CDF VRPC1 scores (Fig. 4.2a). Panels (c) and (d) are for the second most positive and negative extreme months, respectively. Panels (e) and (f) present the cyclone tracks for the 12 most positive and negative extreme months, respectively.

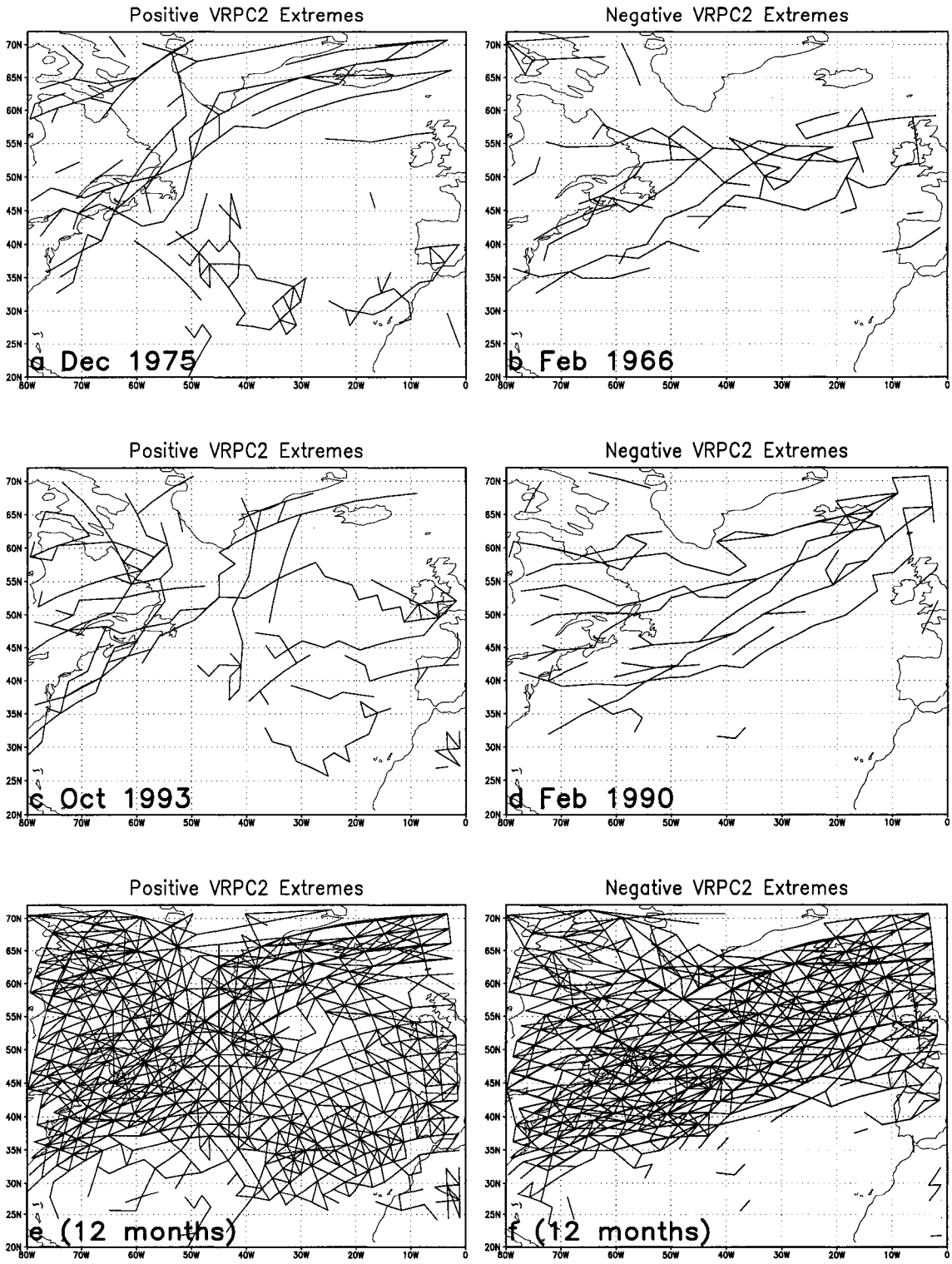


Fig. 4.7. As in Fig. 4.6 but for CDF VRPC2 mode.

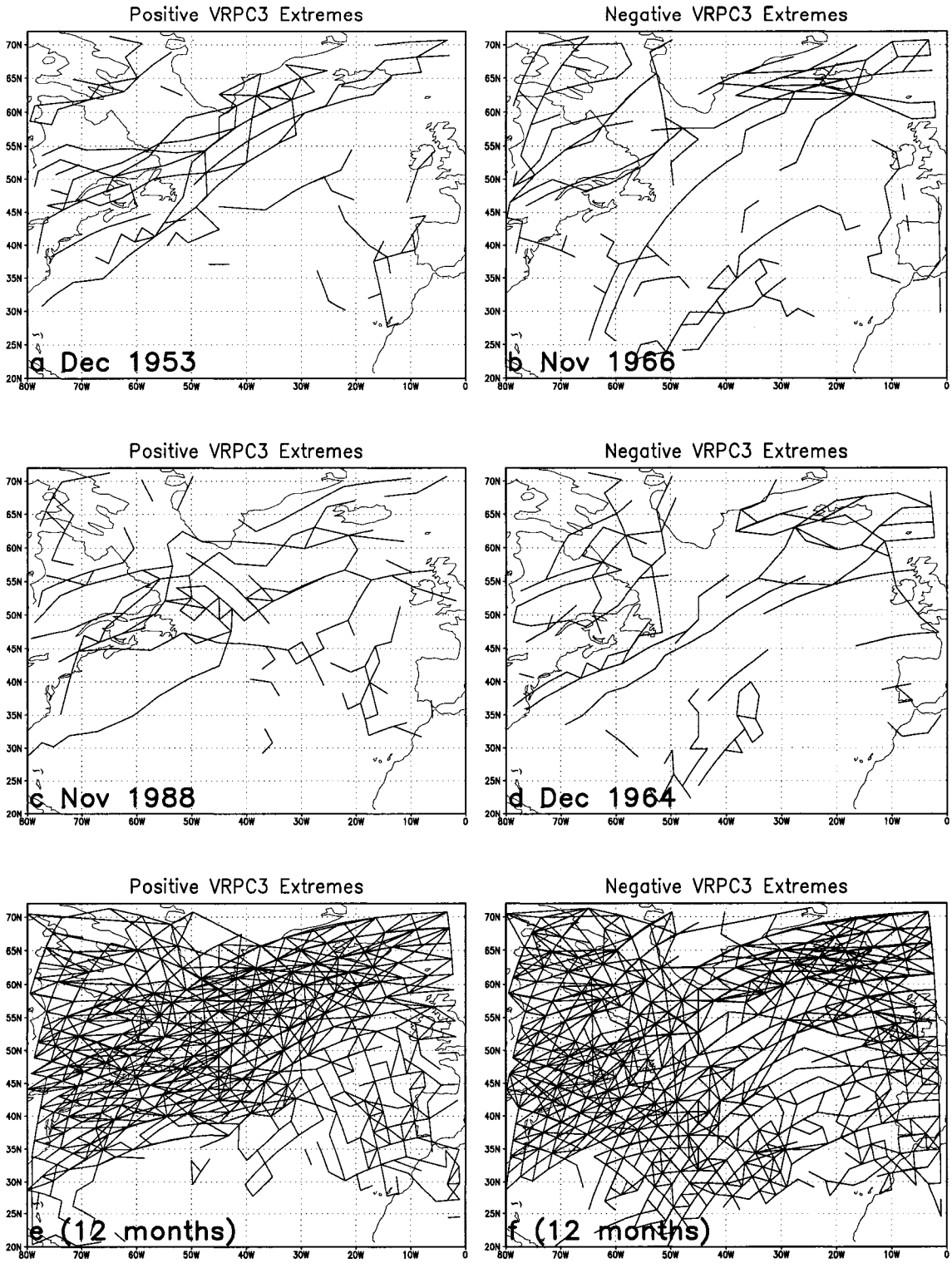


Fig. 4.8. As in Fig. 4.6 but for CDF VRPC3 mode.

4.4.4 Associated Atmospheric and Oceanic Circulation Anomalies

This subsection documents relationships of atmospheric and oceanic anomaly fields to the CDF VRPC modes. Using a VRPC cutoff score of ±1, as shown in Fig. 4.2, the months with the highest positive (≥ +1) and lowest negative (≤ -1) monthly scores are identified for each individual mode. These months provide the basis for high-minus-low composite anomaly difference fields for each CDF mode, that illustrate spatial patterns in atmospheric and oceanic anomalies associated with the CDF VRPC time series extremes. The above cutoff score of ±1 gave 53 and 59 monthly members in the high and low composites for VRPC1, 46 and 49 for VRPC2, and 45 and 41 for VRPC3 (Fig. 4.2). The difference fields of the high-minus-low ensembles essentially reflect the spatial patterns characteristic of the high scores. These differences were tested for statistical significance using a local two-sided Student's t-test that assumes the high and low composite population variances are unequal. Only areas with statistically significant results are discussed below.

Figs. 4.9-12 present CDF VRPC-based high-minus-low composite difference fields of the following anomalies: SLP and SST (Fig. 4.9), surface wind vector and wind speed (Fig. 4.10), surface air temperature and sensible plus latent heat net fluxes (Fig. 4.11), and precipitation rate and 500-hPa geopotential height (Fig. 4.12). Note that both sensible and latent heat net fluxes are defined positive when directed downward, which leads to warming of oceanic mixed layer. While displays in Figs. 4.9-12 reveal differences between the three CDF VRPC modes, the discussion below treats each mode individually so as to elucidate the different physical mechanisms associated with their positive (or negative) polarity.

The CDF VRPC1 high-minus-low SLP anomaly composite difference field in Fig. 4.9a is strongly reminiscent of the positive phase of the NAO, but with the dipole displaced north of its NAO counterpart (e.g., van Loon and Rogers 1978; Lamb and Peppler 1987; Hurrell 1995a). Also, the SLP anomaly composite is very consistent with the spatial loading pattern of the first CDF VRPC1 mode depicted in Fig. 4.1d. Note that the largest difference in SLP anomalies in Fig. 4.9a exceeds -16 hPa over the Greenland/Iceland corridor where the long-term mean of SLP field exhibits its strongest variability during the winter semester (not shown). Next, of immediate interest is the VRPC1-based high-minus-low SST anomaly composite difference field that has a dipole structure (Fig. 4.9d), with an extremum east of Newfoundland (~50°N) at the boundary between the subtropical and subpolar ocean gyres. A stronger extremum of opposite polarity is located off the eastern U.S. (~40°N) where the long-term mean of SST field exhibits its maximum variability during the winter semester (not shown). The dipole pattern depicted in Fig. 4.9d is similar to that reported in previous observational studies – e.g., the second EOF of North Atlantic SST anomalies (November-March, 1900-89) in Deser and Blackmon (1993, Fig. 1); a regression mapping of SST anomalies onto the NAO in Marshall et al. (2001, Fig. 2).

To investigate if the above VRPC1-based SST difference field is generated by atmospheric forcing, we now turn to the VRPC1-based high-minus-low composites of the surface wind vector and wind speed, surface air temperature, and sensible plus latent heat net fluxes in Figs. 4.10 and 4.11. Other variables, such as wind stress curl (to which Ekman pumping is proportional) and oceanic friction velocity cubed (which is a measure of oceanic mixing), could be considered as well for a more complete picture of the SST-related fluctuations in the atmosphere-ocean system in the North Atlantic at times when

the first mode of CDF dominates. The surface wind (Figs. 4.10a,d) and pressure (Fig. 4.9a) difference fields are consistent with the geostrophic relationship. The positive phase of the CDF VRPC1 mode is associated with an anomalous North Atlantic surface cyclone north of Iceland with axis between 65°-70°N, and an anomalous anticyclone in the midlatitudes centered at ~45°N (Fig. 4.10a). The easterly flow anomalies just south of the anticyclonic center oppose the local climatological westerlies between 30°-45°N (not shown), producing negative wind speed differences to the west of Iberian Peninsula that exceed -2 ms^{-1}) (Fig. 4.10d). Conversely, the band of westerly anomalies north of the anticyclonic feature spans the zone of the local climatological westerlies, hence leading to positive wind speed differences in the northern portion of the basin (exceeding +2 m/s). Similarly, the climatological easterly trade wind belt that dominates south of ~30°N (not shown) is enhanced south of ~25°N (Fig. 4.10d).

For the CDF VRPC1 mode, advection of warm maritime air masses by the easterly wind anomalies in the 30°-40°N belt results in positive surface air temperature differences (exceeding +2 °C) off the eastern U.S. seaboard (Fig. 4.11a). Further, anomalous southerly winds over the Greenland Sea are accompanied by positive air temperature differences, exceeding +3.5 °C. In contrast, substantial negative temperature differences are seen over the Labrador Sea that is under the influence of anomalous westerly/northwesterly/continental winds. Note that the variability of the long-term mean surface air temperature maximizes over the Labrador Sea between 65°-70°N (not shown), where the composite air temperature difference exceeds -8.5 °C (Fig. 4.11a). Furthermore, negative air temperature differences exceeding -0.5 °C off the Moroccan Atlantic coast coincide with anomalous northeasterly winds from the Iberian Peninsula/Morocco land-masses.

Inspection of Figs. 4.11a and 4.11d indicates that the CDF VRPC1 composite difference patterns of the surface air temperature and sensible plus latent heat net fluxes are closely related in a manner consistent with atmosphere-to-ocean forcing of SST anomalies. Interestingly, the largest negative heat flux difference over the Labrador Sea is slightly downstream (Fig. 4.11d) of the largest negative air temperature difference (Fig. 4.11a). The decreased wind speeds/positive surface air temperature differences off the eastern U.S. seaboard and over northeast of Iceland reduce the oceanic loss to the atmosphere through sensible and latent heat fluxes, thus leading to warming of the oceanic mixed layer (Fig. 4.11d). On the other hand, increased wind speeds and negative surface air temperature differences over the Labrador Sea and off the Atlantic coast of Morocco are conductive to oceanic cooling. Note that the variability of the long-term mean of sensible plus latent heat net fluxes peaks over the Labrador Sea in the 60°-65°N (not shown), where the composite difference of these heat net fluxes exceeds -180 W/m^2 (Fig. 4.11d).

Fig. 4.11d contains further evidence of the correspondence between the spatial patterns of composite differences in the heat fluxes and SST anomalies (Fig. 4.9d). Particularly prominent is the occurrence south of Greenland of the largest negative SST difference downstream (Fig. 4.10a) of the largest negative difference of the heat fluxes. Therefore, this indicates that the relationship between the surface wind and SST anomalies is essentially local: for instance, stronger than normal wind speeds are accompanied by cooler than normal temperatures and abnormally high ocean-to-atmosphere turbulent heat transfer, and vice-versa. This is consistent with previous observational studies (e.g., Deser and Blackmon 1993) and modeling work (e.g., Alexander 1990) that suggested that changes in the air-sea fluxes and wind-induced vertical mixing processes contribute to the

formation of the SST anomalies. For instance, above-normal wind speeds will cool the ocean mixed layer by enhancing the sensible and latent heat fluxes from the ocean surface and by accelerating the entrainment of cooler water from below (Deser and Blackmon 1993).

To complement the above results, Fig. 4.12a depicts the CDF VRPC1-based high-minus-low composite difference field of precipitation rate anomalies. This shows that the major precipitation rate increase (up to +3 $kg/m^2/s$) during positive VRPC1 conditions occurs in the high latitudes, north of about 50°N, contrasting with a notable precipitation rate decrease in the central-eastern part of the basin (30°-50°N belt). This reflects the changes in the North Atlantic storm track already described for this CDF mode. Since VRPC1 is highly correlated with NAO, this finding is consistent with previous studies. For instance, during positive NAO events, the axis of maximum moisture transport shifts to a more SW to NE orientation over the Atlantic and extends much farther to the north and east into northern Europe and Scandinavia (Hurrell 1995b; Hurrell and van Loon 1997).

Finally, the VRPC1-based high-minus-low composite of the 500-hPa geopotential height field (Fig. 4.12d) also reflects a simple dipole structure similar to that of SLP (Fig. 4.9a), reminiscent of the positive polarity of NAO. This is indicative of good agreement between the cyclone behavior and the 500-hPa flow, which represents a further verification of the first mode.

Note that high-minus-low composite differences of the normalized departures of SLP and SST based upon the three CDF VRPC modes also were examined. The results

are essentially the same (plots not shown).

While the present results for the CDF VRPC1 mode are consistent with previous studies that focussed mainly on the NAO, the basic goal accomplished here, however, is to document the relationships of atmospheric and oceanic circulation anomalies to VRPC1 (besides VRPC2 and VRPC3, see below) in a different and comprehensive way. For instance, to describe the low-frequency variability of the North Atlantic winter surface climate, Deser and Blackmon (1993) – perhaps the most often cited study in this context – performed an EOF analysis of four components of the climate system: SLP, SST, wind vector, and air temperature; whereas the present compositing analysis incorporated five additional components: wind speed, sensible and latent heat net fluxes, precipitation rate, and 500-hPa geopotential height (Figs. 4.9-12), so as to give a rich picture of the different physical mechanisms involved, especially by invoking the new VRPC2 and VRPC3 modes.

Physical considerations similar to the above can be used to interpret the spatial patterns of the same atmospheric and oceanic circulation anomalies associated with the second and third modes of CDF. Compared to the first mode, the patterns for the high-minus-low composites associated with the CDF VRPC2 mode are essentially very similar to those related to VRPC1 but shifted farther south with the opposite polarity, which is consistent with the spatial loading patterns of CDF anomalies (Figs. 4.1d,e). However, of particular interest is the predominantly monopole structure of SST (Fig. 4.9e) centered at 45°-50°N/40°W, with the same sign as the VRPC2 scores (Fig. 4.2b). That is, positive (negative) VRPC2 conditions are associated with positive (negative) SST anomalies in the midocean area east of Newfoundland at the boundary between the subtropical and

subpolar ocean gyres. For the VRPC2 mode, anomalous anticyclonic anomalies south of Iceland (Fig. 4.10b) are accompanied by warmer than normal SSTs in the midocean area east of Newfoundland, and vice-versa. SST pattern is generally consistent with a response of the upper-ocean to the associated atmospheric forcing, although oceanic processes may be involved in determining and/or modulating the SST pattern; e.g., temperature anomalies in the midocean area east of Newfoundland may be connected to changes in the interface between the subtropical and subpolar ocean gyres. Coupled ocean-atmosphere GCM modeling is required to assess this hypothesis.

Compared to the first mode, the patterns for the high-minus-low composites associated with VRPC3 also are essentially very similar to those related to VRPC1 but shifted farther southwest with the same polarity, which is consistent with the spatial loading patterns of CDF anomalies (Figs. 4.1d,f). However, Fig. 4.9f reveals that the SST pattern also is monopole featured for VRPC3, centered at 40°-45°N/50°W, with opposite polarity to the VRPC2-based SST monopole. Positive (negative) VRPC3 conditions are associated with negative (positive) SST anomalies in the midocean area southeast of Newfoundland along the Gulf Stream current. For the VRPC3 mode, anomalous anticyclonic anomalies south of Greenland (Fig. 4.10c) are accompanied by warmer than normal SSTs in the midocean area southeast of Newfoundland, and vice-versa. Note that the VRPC3-based SST monopole is much stronger in magnitude than the VRPC2 counterpart, and displaced farther southwest. Similarly, VRPC3-based SST pattern is generally consistent with a response of the upper-ocean to the associated atmospheric forcing, although oceanic processes may be involved in determining and/or modulating the SST pattern; e.g., temperature anomalies southeast of Newfoundland may be related to variations in the strength and/or position of the Gulf Stream current.

This hypothetical assumption is somewhat supported by Ciasto and Thompson (2004), who after examining wintertime ocean-atmosphere interaction on weekly time-scales over the North Atlantic sector (via lag-regression), found a spatially coherent and statistically significant pattern of SST anomalies over the Gulf Stream extension region that precedes changes in the leading mode of Northern Hemisphere atmospheric variability [the so-called Northern Hemisphere annular mode (NAM; also referred to as the NAO and Arctic Oscillation)] by ~2 weeks. Again, further research is needed (coupled GCM modeling) to assess and quantify the present possible assertion for VRPC3 – recall that the time series of VRPC3 scores and the NAO_l/NAO_h indices are very poorly correlated (Table 4.1). Note that for any hypothetical assumption, the physical mechanisms involved in the coupled ocean-atmosphere system will be different between the CDF VRPC2 and VRPC3 modes.

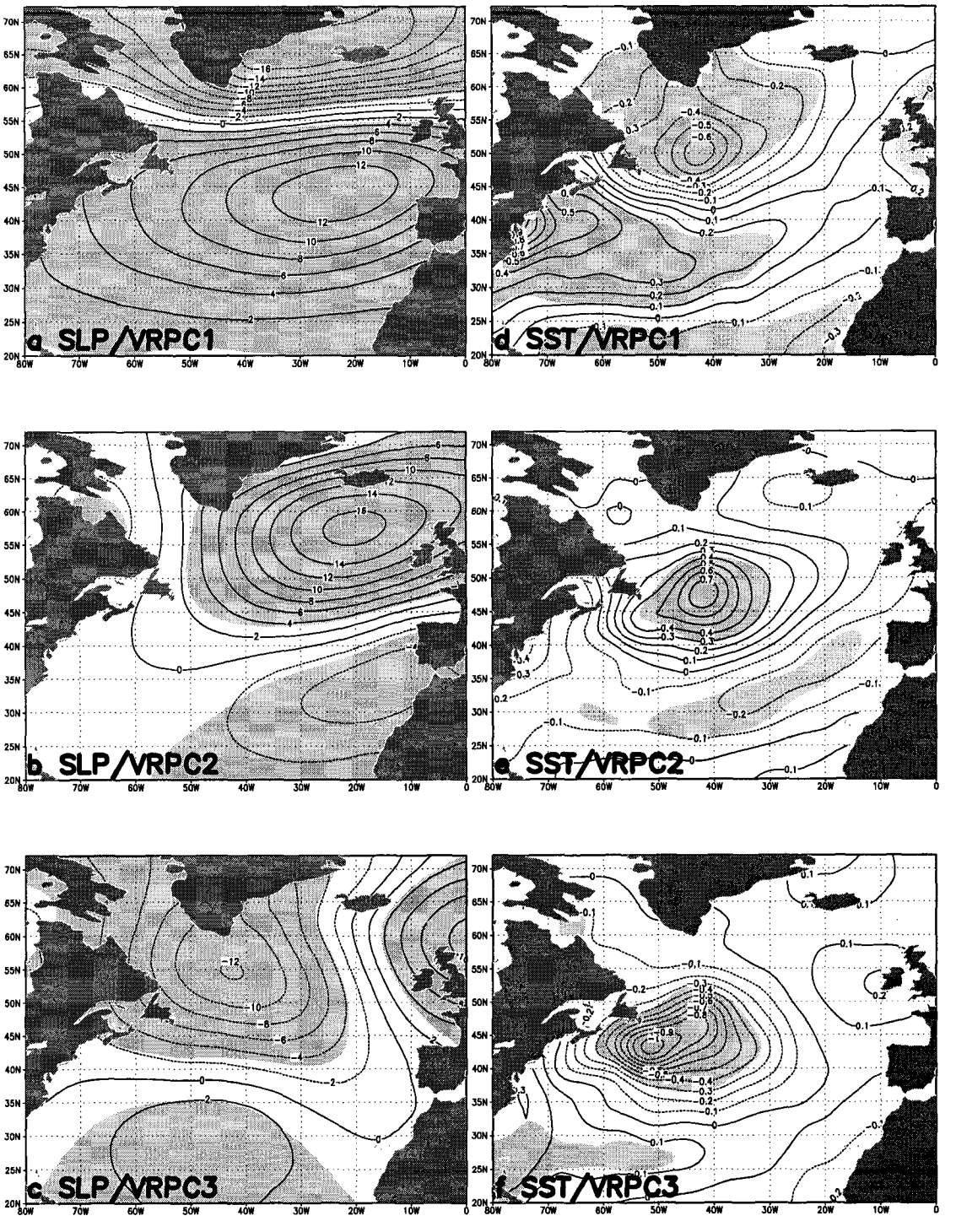


Fig. 4.9. High-minus-low composite difference fields of North Atlantic winter semester (October-March) SLP (hPa) anomalies for 1948-99, based upon (a) CDF VRPC1, (b) VRPC2, and (c) VRPC3. Panels (d-f): as in (a-c) but for SST (°C). Light shading covers areas where composite differences are statistically significant at the 99% level, according to a local two-sided Student's t-test assuming the high and low population variances are unequal.

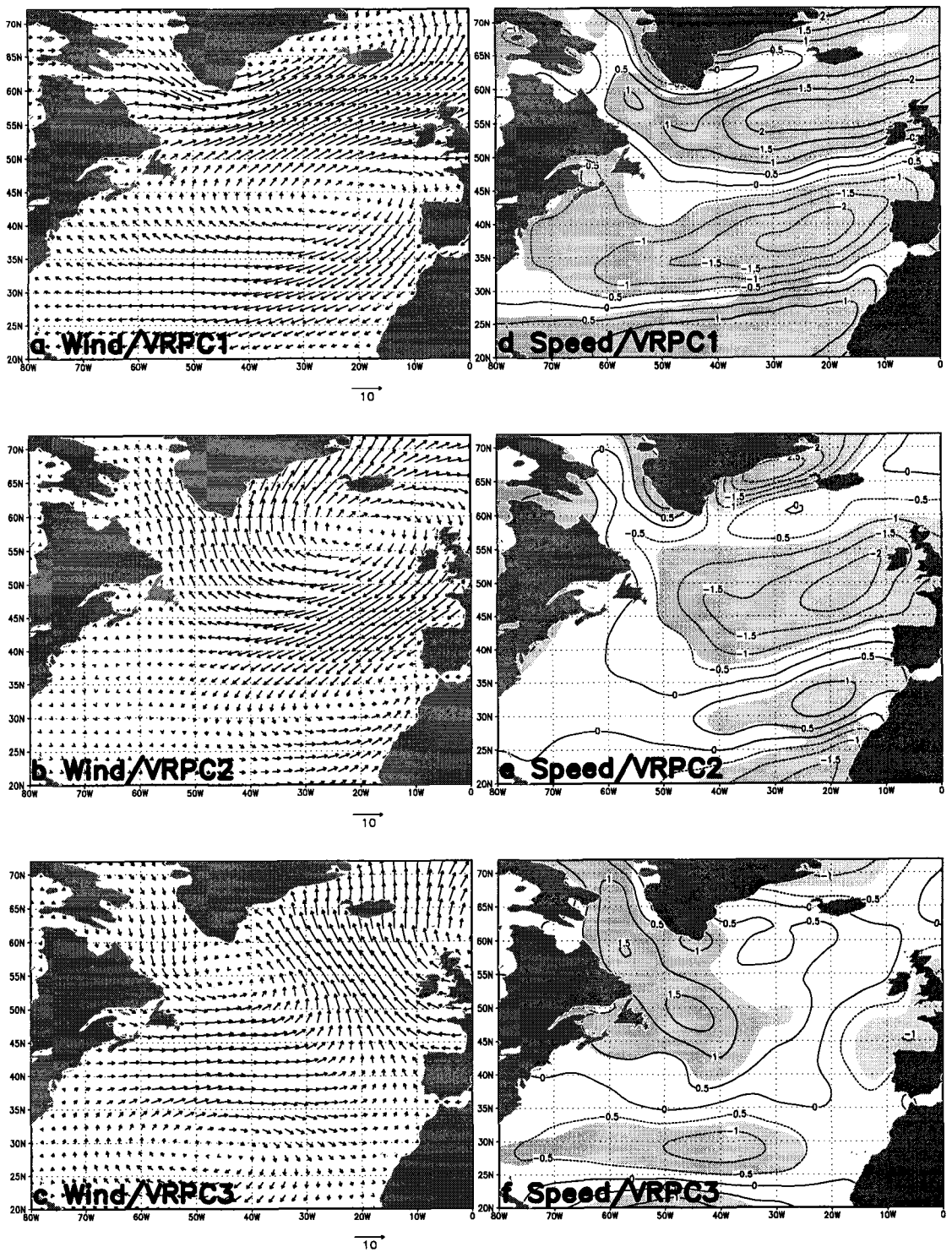


Fig. 4.10. As in Fig. 4.9 but for surface wind vector (arrows, see scale at bottom right of each wind vector panel) and wind speed (m/s).

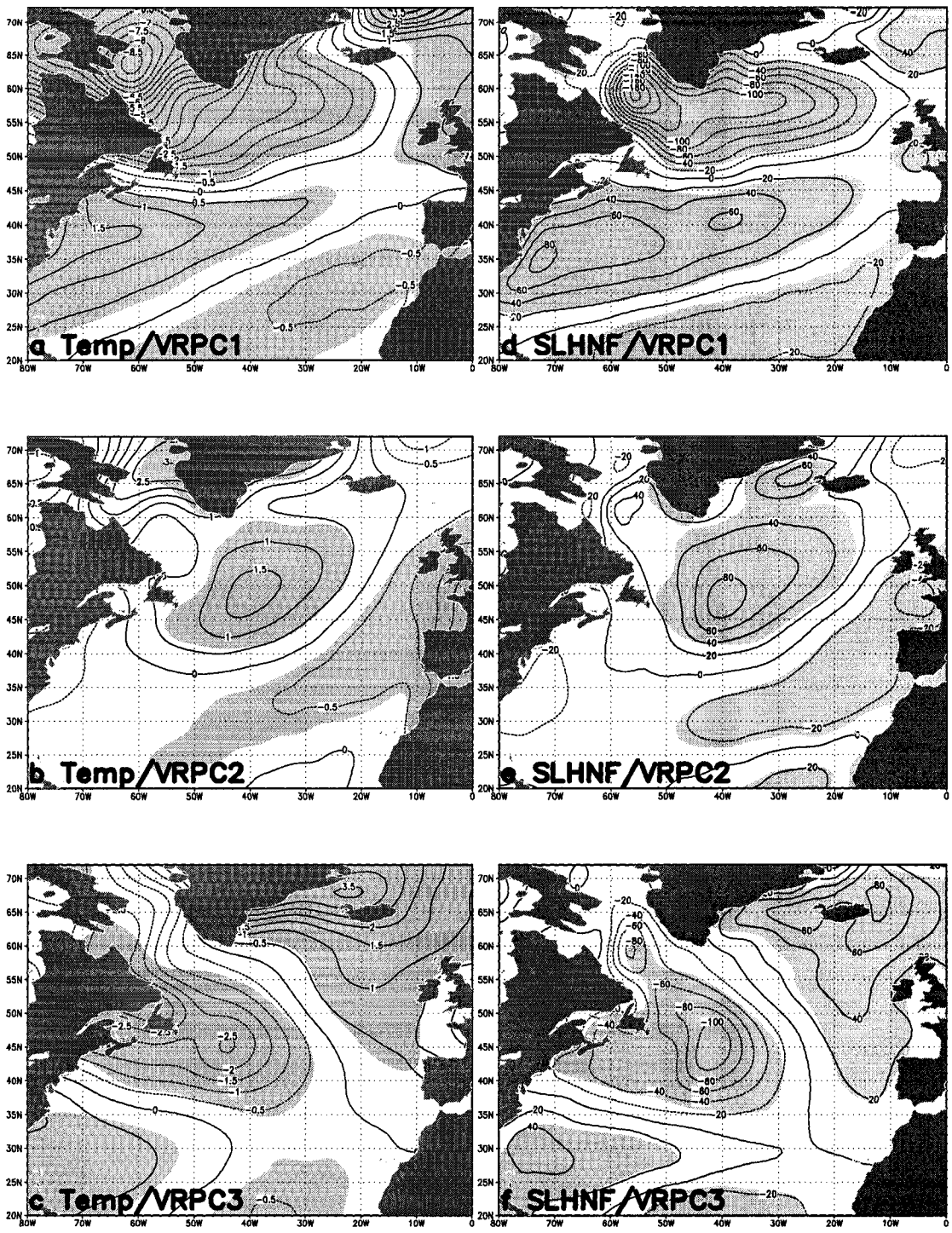


Fig. 4.11. As in Fig. 4.9 but for surface air temperature (°C) and sensible plus latent heat net fluxes (SLHNF, W/m^2). Both sensible and latent heat net fluxes are defined positive downward.

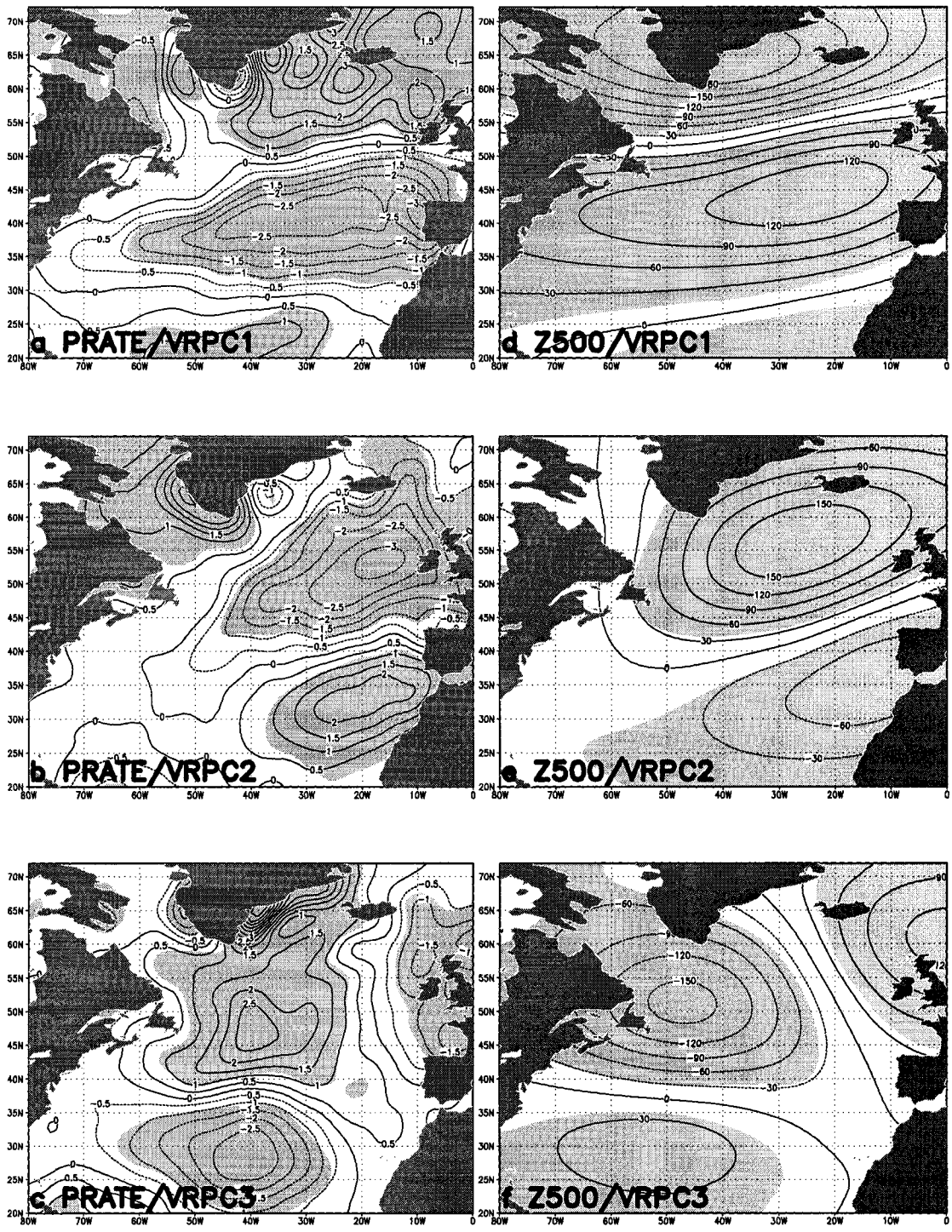


Fig. 4.12. As in Fig. 4.9 but for precipitation rate (PRATE, 10^5 kg/m^2/s) and 500-hPa geopotential height (Z500, gpm).

4.5 RELATIONSHIPS OF CYCLONE BEHAVIOR WITH OTHER VARIABLES

4.5.1 NAO Impact on Storm Characteristics

Based on traditional/proxy storm tracks, previous studies (e.g., Rogers 1990; Hurrell 1995b; Serreze et al. 1997; Clark et al. 1999; McCabe et al. 2001) showed that during a positive (negative) phase of the NAO/AO, there is a northward (southward) shift of the storm tracks across the central North Atlantic. The purpose of this subsection is to further document the relation of the NAO (Fig. 4.13a) with various cyclone characteristics. Specifically, Fig. 4.13b-d presents spatial distribution patterns of Hurrell's NAO-based high-minus-low composite differences of the following cyclone anomaly fields: CDF, intensity, and duration. The thresholds for Hurrell's NAO index were set to ±1.5, yielding 100 and 85 monthly members in the high and low composites, respectively.

During positive NAO events, the main cyclone track has a pronounced northeastward orientation across the North Atlantic (e.g., Rogers 1990), resulting in an absolute maximum of cyclone activity over the Greenland/Iceland corridor in terms of both CDF (Fig. 4.13b) and cyclone frequency (not shown), along with absolute maximum cyclone intensity (Fig. 4.13c) and absolute minimum central pressure (not shown) north of Iceland. However, intensification of cyclone deepening rate and moving speed maximize further upstream, to the northeast of Newfoundland (not shown). Cyclone duration tends to maximize over the Greenland Sea (Fig. 4.13d). In contrast, during negative NAO events, cyclones crossing the western Atlantic move eastward, tracking along latitude 45°N on average, in proximity to the Gulf Stream, resulting in the maximum of cyclone duration northwest of Portugal in Fig. 4.13d. This results in wet conditions over the northwestern Atlantic costal areas of Morocco (Section 4.6).

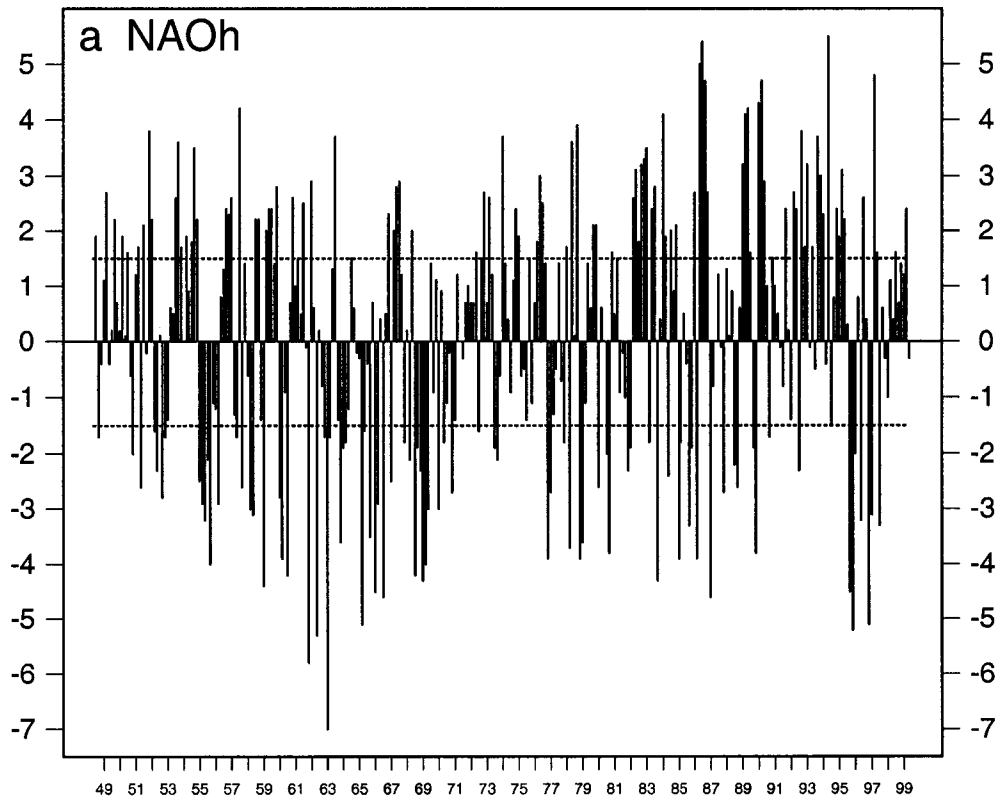


Fig. 4.13. Compositing Analysis. Panel (a) presents time series of Hurrell's NAO index (NAO_h) for the winter semester (October-March, 1948-99). The thresholds (broken lines) for NAO_h were set to ±1.5. The year (minus 1900) labeled on the horizontal axis corresponds to the year in which January occurs. Panels b-d: Hurrell's NAO-based high-minus-low composite difference fields of the following North Atlantic winter semester (October-March) anomalies for 1948-99: (b) cyclone track density function (CDF, cyclones/day/250 km x 250 km); (c) cyclone intensity (10^5 hPa/m^2); and (d) cyclone average lifetime (days). Light shading represents areas where high-minus-low composite differences are statistically significant at the 99% confidence level according to a local two-sided Student's t-test assuming the high and low population variances are unequal.

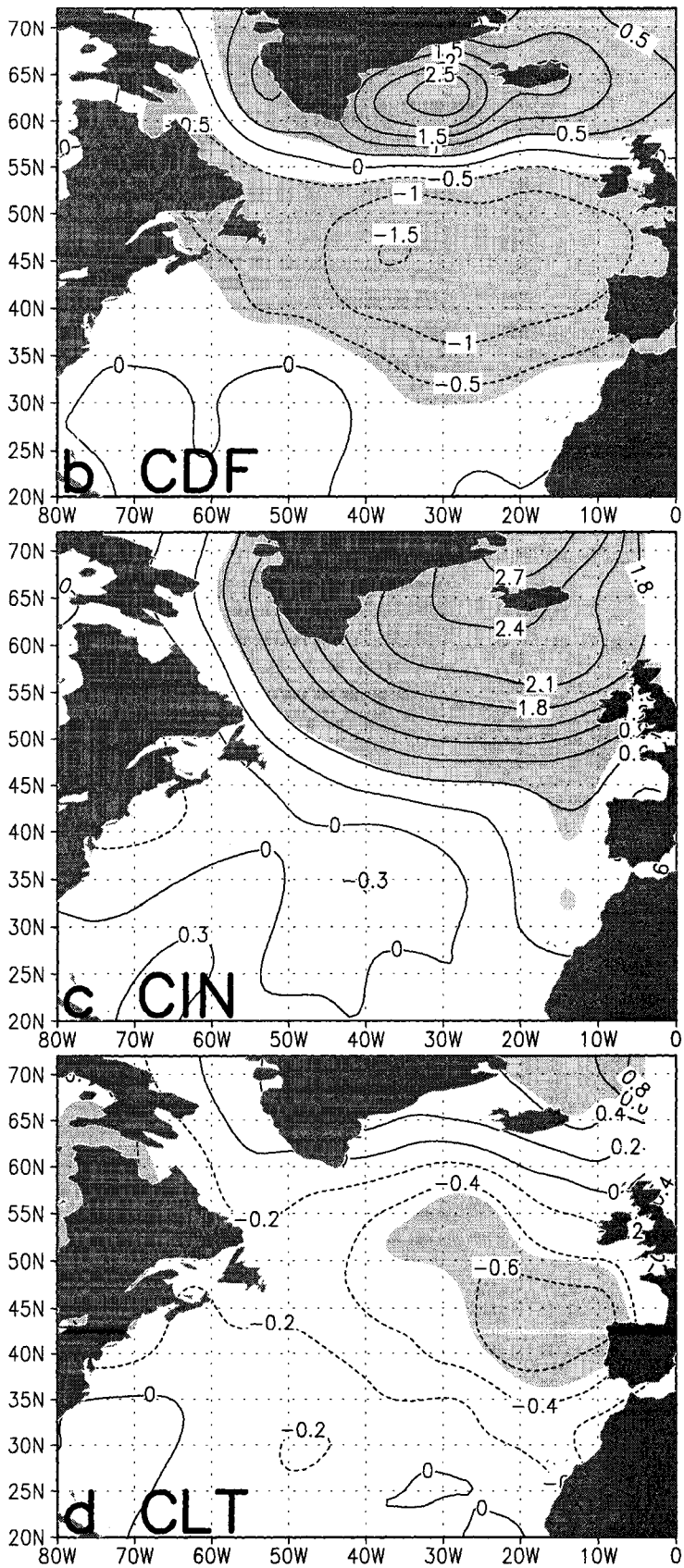


Fig. 4.13. (Continued).

4.5.2 ENSO Impact on Cyclone Tracks and Atmospheric/Oceanic Circulation

The ENSO phenomenon is recognized as a major source of global climate variability, especially in and around the Pacific Basin. However, the impact of ENSO on the North Atlantic cyclone tracks still is largely unknown. Thus, the aim of this subsection is to examine relationships of the ENSO with the North Atlantic CDF and atmospheric/oceanic circulation anomalies. Specifically, through the same composite difference technique as used above, characteristic North Atlantic winter cyclone track anomaly patterns were identified separately for warm and cold ENSO events. A range of ENSO indices – e.g., the standard SOI (Fig. 4.14a) and various SST indices including Montroy et al.'s (1998) tropical Pacific SST modes – were used, yielding very similar results. As an example, Fig.4.14b-d presents SOI-based high-minus-low composite differences of the following North Atlantic anomaly fields: CDF, SLP, and SST. The thresholds for SOI were set to ±1.5, yielding 32 and 40 monthly members in the high and low composites, respectively.

Fig. 4.14b suggests that, on interannual time-scales, North Atlantic storm tracks change in response to the ENSO cycle. It shows that the North Atlantic cyclone track shifts southward during El Niño years (SOI < -1.5), while La Niña events are associated with opposite shifts. In particular, pronounced below-normal cyclone activity off the U.S. East Coast tends to occur during cold ENSO events (SOI > 1.5), contrasting with above-normal storminess southeast of Greenland (though not statistically significant). Accompanying the significant below-normal cyclone activity off the U.S. East Coast is a marked tendency for positive SLP anomalies (Fig. 4.14c). Further, Fig. 4.14d shows that warm ENSO events are associated with above-normal SST along a zonally elongated belt in the band between 20°-30°N, and with below-normal temperature in the waters off

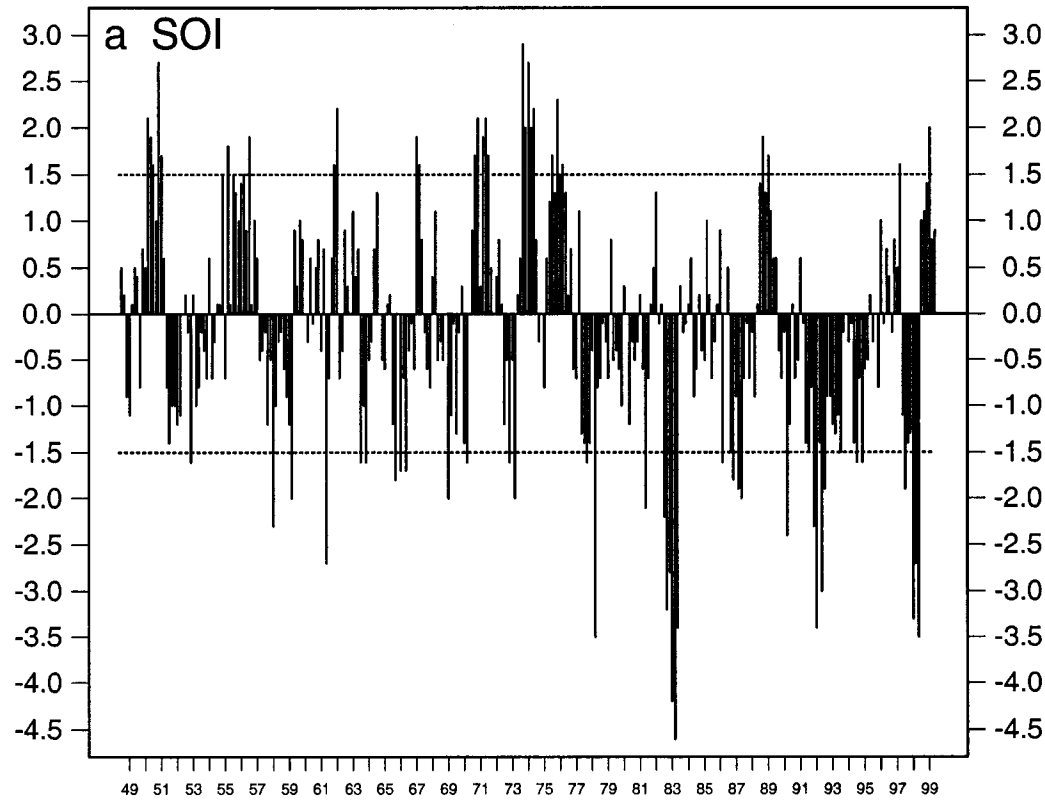


Fig. 4.14. Compositing Analysis. Panel (a) presents time series of the Southern Oscillation Index (SOI) for the winter semester (October-March, 1948-99). The thresholds (broken lines) for SOI were set to ±1.5. The year (minus 1900) labeled on the horizontal axis corresponds to the year in which January occurs. Panels b-d: SOI-based high-minus-low composite difference fields of the following North Atlantic winter semester (October-March) anomalies for 1948-99: (b) cyclone track density function (CDF, cyclones/day/250 km x 250 km); (c) SLP (hPa); and (d) SST (°C). Light shading represents areas where high-minus-low composite differences are statistically significant at the 99% confidence level according to a local two-sided Student's t-test assuming the high and low population variances are unequal.

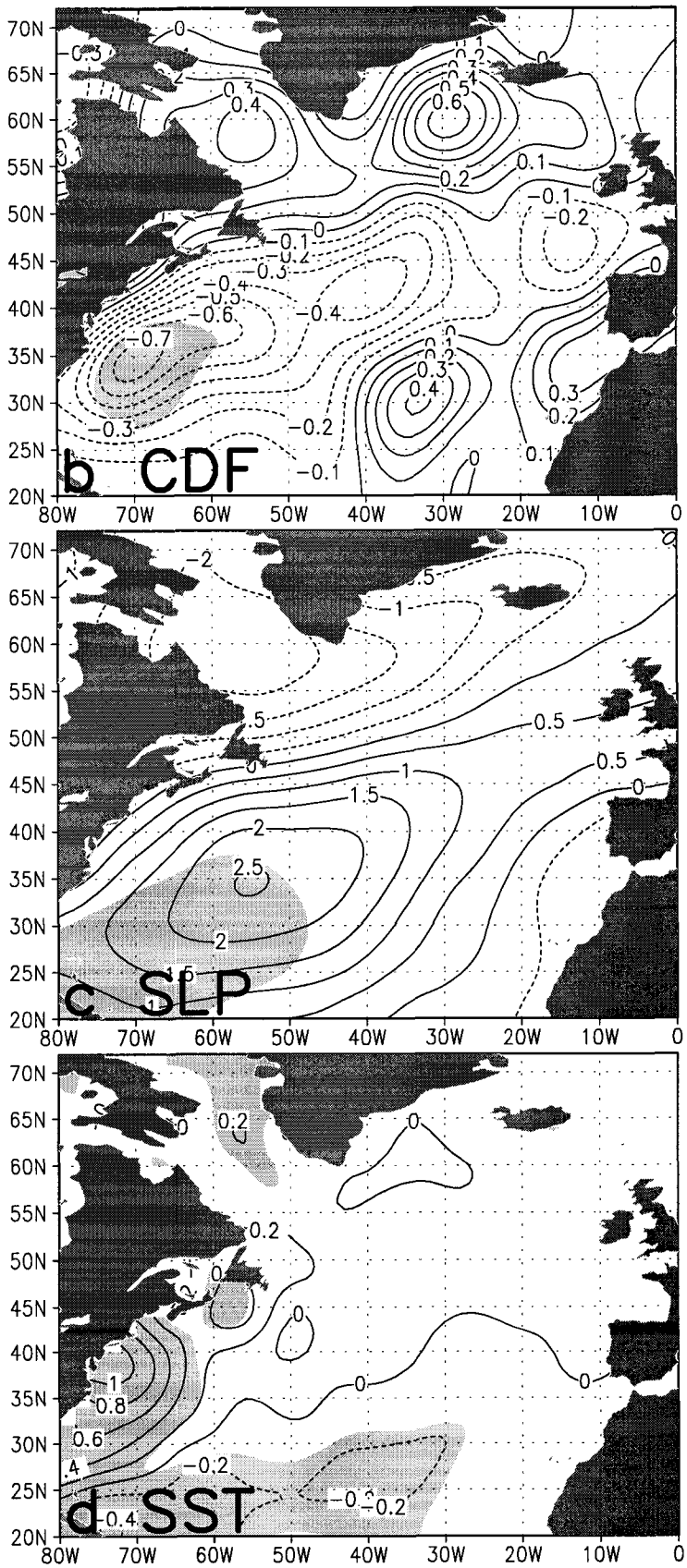


Fig. 4.14. (Continued).

the U.S. East Coast. The oceanic response is consistent with atmosphere-to-ocean forcing. In particular, analyses patterned after those in Subsection 4.4.4 (not shown) suggest SST is colder (warmer) than normal in areas where the anomalous wind comes from colder (warmer) regions during winter, the surface anomaly currents are southward (northward), and mechanical mixing is enhanced (reduced). Therefore, this present study presents evidence on teleconnections between ENSO forcing in the tropical Pacific and cyclone tracks/SST changes in the North Atlantic. Further, physical consistency was found between various atmospheric and oceanic anomalies: CDF, SLP, SST, surface wind vector and wind speed, surface air temperature, sensible plus latent heat net fluxes, precipitation rate, and 500-hPa flow (plots not reproduced here).

Merkel and Latif (2001), who conducted high-resolution atmospheric GCM experiments to assess the ENSO impact on the North Atlantic/European sector, also found a southward shift of the North Atlantic low-pressure systems in El Niño winters (DJF). Chang et al. (2002), by analysis of 300-hPa bandpass meridional velocity variance data (a cyclone track proxy), also found an ENSO response, though not discussed, along a narrow band off the U.S. East Coast centered at latitude ~35°N (see their Fig. 5).

To date, there is no consensus on how to interpret the sets of relationships between tropical ENSO phenomena and interannual variability of the ocean-atmosphere system in the temperate zone. For instance, Merkel and Latif (2001) indicated that it was not possible from their complex model simulations to formulate a causal chain describing explicitly how the tropical Pacific signal is transferred to the North Atlantic/European sector. On the other hand, Lau and Nath (2001), who also have reported that ENSO events are accompanied by marked changes in the midlatitude SST patterns in the North

Pacific and North Atlantic, invoked the concept of an "atmospheric bridge". However, Pozo-Vazquez et al. (2001) suggested an influence of the cold ENSO events on the atmospheric circulation of the North Atlantic region, indicating that possible mechanisms may involve an extension of the effects of the Pacific North American (PNA) pattern towards Europe and the influence of ENSO-related tropical Atlantic SST anomalies. Finally, Chang et al. (2002) stated that although the tropical Pacific SST-induced heating may be the ultimate driver behind these storm track shifts, attributing all of these storm track structural changes to the direct tropical forcing is improper. Nonlinear interactions among the tropical heating, storm track eddies, and the midlatitude stationary wave [because the storm track eddies are in turn organized by the stationary wave (Branstator 1995)] must be accounted for to make correct attributions of the storm track structural changes (Chang et al. 2002).

4.6 RELATION OF CDF & MOROCCAN PRECIPITATION PATTERNS WITH NAO

4.6.1 Background

It is now clear that climate can vary dramatically on interannual and decadal time-scales. In Africa, precipitation is a vital resource, so making the best possible use of monitoring and prediction technologies will make a strong contribution to sustainable development. An important first step was the identification of relatively homogeneous precipitation regions in Morocco, to form the basis for real-time monitoring and build the units for prediction (El Hamly et al. 1997a,b).

Standardized station precipitation anomalies were used because these measure the relative change in precipitation from year to year at each location. Various forms of

Unrotated and Rotated Principal Component Analysis (PCA) (e.g., Richman 1986) and Cluster Analysis (e.g., Gong and Richman 1995) were applied to a 17-station quality-controlled data set for 1932-95 (plus a supplementary 5-station data set for 1964-95) for each individual calendar month from October to April, and to the October-April totals (see Table 4.2 and Fig. 4.15 for key station information). It was found that the regions of coherent precipitation anomalies exhibit modest changes during the precipitation season, from early (October) to the heart of the season (December-February) to the late season (April). Thus, a regionalization for each month was defined, as well as a regionalization for the whole precipitation season (Fig. 4.15). Since VARIMAX orthogonally-rotated PCs, Harris-Kaiser obliquely-rotated PCs, and Hartigan's K-Means clustering algorithm (Hartigan and Wong 1979) generally gave consistent results, a human blend of the output from the techniques, along with analysis of inter-station correlations, was used to produce the final regionalization of Moroccan precipitation (El Hamly et al. 1997a).

The resulting regions depicted in Fig. 4.15 are as follows: Region I (Northwest), Region II (Southwest), Region III (Atlas Mountains), Region IV (South of Atlas Mountains), and Region V (Northeast). Various methods for describing the temporal variability of Moroccan precipitation were considered. Rotated PC scores were not felt to be ideal for this application, and time series of average standardized precipitation anomalies were used for each region, giving stability and ease of interpretation. The precipitation indices (i.e., average z-scores) for these regions show strong interannual variability and, especially since the middle of the 20th century, pronounced multi-decadal trends (El Hamly et al. 1997a). Details on climate variability in Northern Africa, including understanding droughts in the Maghreb, are given in Ward et al. (1999).

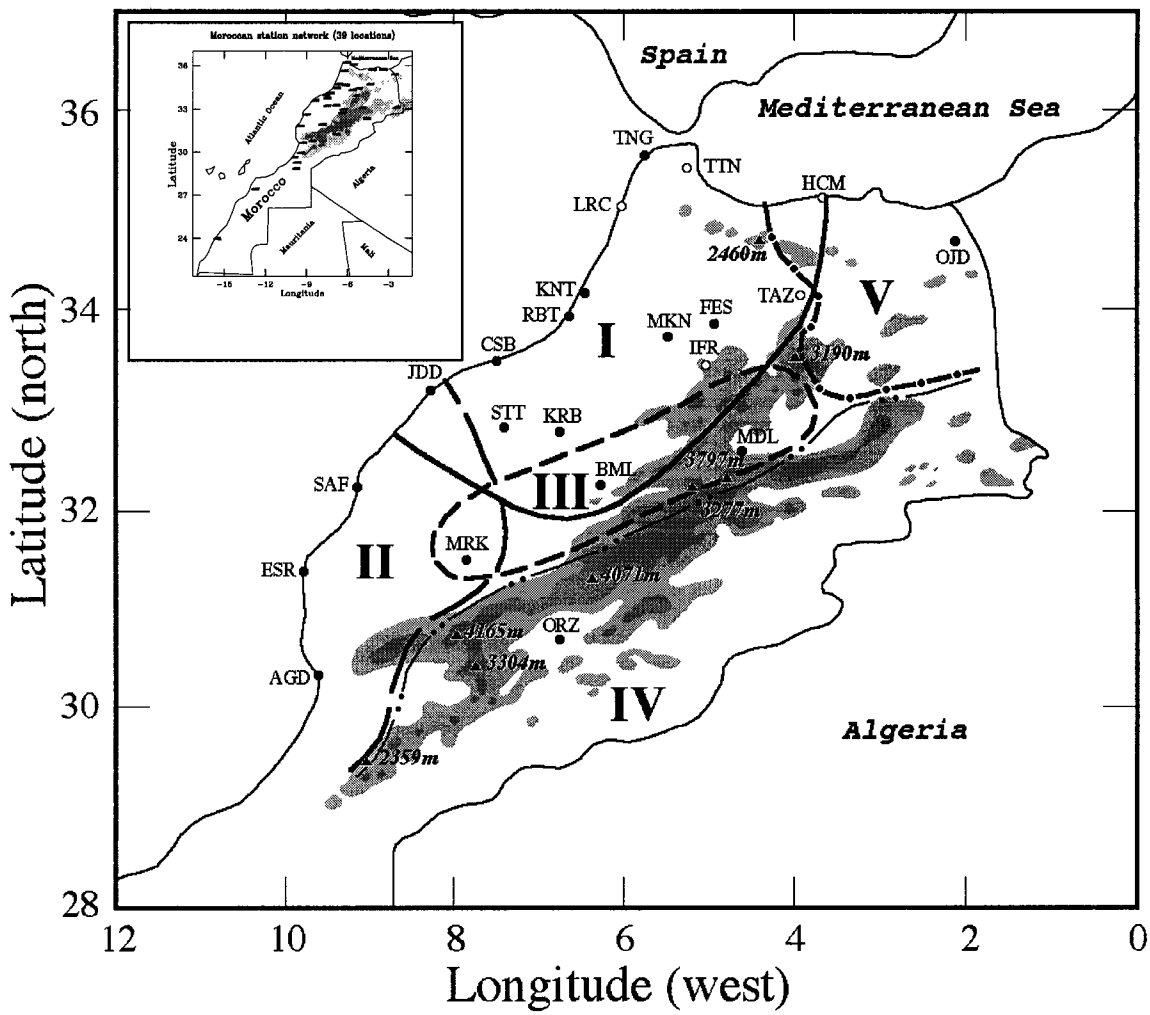


Fig. 4.15. Regionalization of October-April Moroccan precipitation for 1932-95, based on a synoptic station network of 17 locations (solid dots) and 5 additional stations for 1964-95 (open circles). Key station information is given in Table 4.2 below. This regionalization was based on combination of Unrotated/Rotated Principal Component Analysis and Cluster Analysis results. Note that a station may belong to more than one region. Shading indicates Moroccan topography: light shading for 1500-2000 m, dark shading for > 2000 m. The entire map of Morocco is shown in the insert at top left.

Table 4.2. Key information for stations on above map (Fig. 4.15). The first column refers to abbreviation of station names. The third column refers to the World Meteorological Organization (WMO) code for each synoptic station. The 17 first rows are for the long-term (1932-95) stations, whereas the 5 supplementary (1964-95) stations are shown in the last 5 rows.

Station Abbre.	Station Name	WMO #	Latitude (°N)	Longitude (°W)	Elevation (m)
STT	SETTAT	03658501	32.87	-7.58	375.0
TNG	TANGIERS	60101001	35.73	-5.92	15.4
OJD	OUJDA	60115001	34.78	-1.93	465.0
KNT	KENITRA	60120001	34.30	-6.60	5.0
RBT	RABAT	60135001	34.05	-6.77	75.3
FES	FES	60141001	33.97	-4.98	571.3
MKN	MEKNES	60150001	33.88	-5.53	549.0
CSB	CASABLANCA	60155001	33.57	-7.67	56.6
JDD	EL-JADIDA	60165001	33.23	-8.52	270.0
KRB	KHOURIBGA	60178001	32.88	-6.90	770.9
SAF	SAFI	60185001	32.28	-9.23	44.7
BML	BENI-MELLAL	60191001	32.37	-6.40	468.0
MDL	MIDELT	60195001	32.68	-4.73	1515.0
ESR	ESSAOUIRA	60220001	31.52	-9.78	7.1
MRK	MARRAKECH	60230001	31.62	-8.03	463.5
AGD	AGADIR	60250001	30.38	-9.57	23.0
ORZ	OUARZAZATE	60265001	30.93	-6.90	1136.0
LRC	LARACHE	60105001	35.18	-6.13	46.7
HCM	AL-HOUCEIMA	60107001	35.18	-3.85	12.1
TAZ	TAZA	60127001	34.22	-4.00	509.2
IFR	IFRANE	60160001	33.50	-5.17	1663.8
TTN	TETOUAN	60318001	35.58	-5.33	5.0

4.6.2 Relationship of CDF Patterns with Moroccan Precipitation

Previous work (e.g., Lamb and Peppler 1987, 1991) indicated a relatively strong relationship between Moroccan seasonal (November-April) precipitation and the NAO. The relationship affects much of the country in and to the west of the Atlas Mountains. The regions of strongest association are along and near the western and northwestern coast. Analyzing each month separately, Lamb et al. (1997a) showed that the precipitation relationship with the NAO increases progressively from October until February, and then decreases strongly through April. To illustrate further this relationship, Fig. 4.16 presents spatial correlation patterns between time series of North Atlantic winter semester (October-March) SLP anomalies and Moroccan regional precipitation indices (MRR) for Regions I-IV during 1948-99. This figure confirms that during the negative NAO phase, atmospheric blocking over North Atlantic and Northern Europe steers midlatitude disturbances south, bringing precipitation to Morocco (and the Iberian Peninsula). Fig. 4.16 also clearly reveals that the negative relationship of southeastern North Atlantic SLP with Moroccan precipitation anomalies decreases as we proceed from Region I to Region IV. Particularly prominent is the consistent counterclockwise displacement of the southern node of the correlation dipole (starting along the Moroccan Atlantic coast and moving southward) with the progression among the Regions I-III with precipitation that is most strongly linked to the SLP anomalies. These findings are confirmed further in Table 4.3 that displays correlations between the three NAO indices and MRR time series. Precipitation displays very similar dependence on the traditional NAO indices (NAO_r and NAO_h) based on fixed stations. In contrast, for Regions I-III, the relationship is markedly weaker for the seasonally and geographically varying "mobile" index of the North Atlantic Oscillation (NAO_m). Note that the seasonal correlation coefficients listed in Table 4.3 for Rogers' NAO index are

lower than those obtained previously for winter core (December-February) and individual calendar months in this core (Lamb et al. 1997a; El Hamly et al. 1997a).

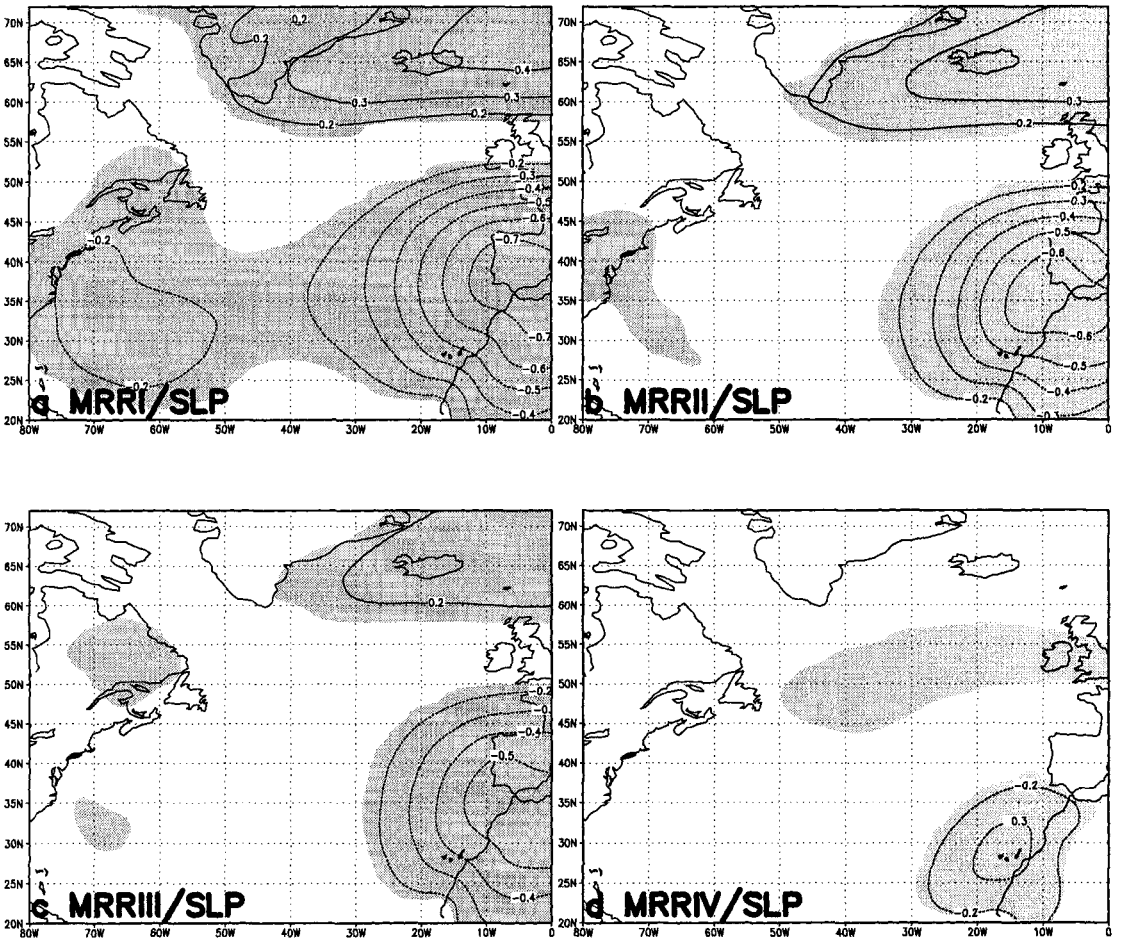


Fig. 4.16. Spatial correlation patterns between time series of North Atlantic winter semester (October-March) SLP anomalies during 1948-99 and Moroccan regional precipitation (MRR) indices (i.e., z-scores) for (a) Region I (Northwest area of Morocco); (b) Region II (Southwest area); (c) Region III (Atlas Mountains); and (d) Region IV (South of Atlas Mountains). These regions depicted in Fig. 4.15 were identified and defined in Al Moubarak Project (El Hamly et al. 1997a). Solid (dashed) contours indicate positive (negative) correlation coefficients. Light shading covers areas where correlation coefficients are statistically significant at the 99% confidence level according to a two-sided Student's t-test that factors in the effective sampling size of the time series at each grid point (Wilks 1995, p. 127). Only correlation coefficients greater than 0.2 in magnitude are contoured.

Table 4.3. Correlations between the three winter semester (October-March, 1948-99) NAO indices due to Rogers (1984) (NAO_r), Hurrell (1995a) (NAO_h), and Portis et al. (2001) (NAO_m) and the Moroccan regional precipitation indices (z-scores, MRR) for the 5 regions in Fig. 4.15. Total number of records in each individual NAO/precipitation time series is 306 months. Values next to the correlations indicate statistical significance levels (%) according to a two-sided Student's t-test that factors in the effective sampling size of the time series (Wilks 1995, p.127). Pairwise scatter plots of the above time series are given in Fig. 4.22.

	NAO_r	NAO_h	NAO_m
MRR I	-0.40 (99.99)	-0.40 (99.99)	-0.28 (99.99)
MRR II	-0.34 (99.99)	-0.34 (99.99)	-0.27 (99.99)
MRR III	-0.22 (99.96)	-0.23 (99.98)	-0.19 (99.76)
MRR IV	-0.02 (27.84)	-0.02 (29.41)	-0.10 (88.55)
MRR V	-0.01 (10.70)	-0.02 (28.08)	-0.04 (49.15)

Three avenues towards the seasonal prediction of Moroccan precipitation were considered: (a) behavior of NAO; (b) forcing from tropical SST; and (c) forcing from North Atlantic SST. Concerning the NAO behavior, some key findings to date are: (1) the empirical identification of a pronounced August-November-January NAO oscillation that produces the extreme positive January-February NAO values that induce moderate-to-severe Moroccan drought (El Hamly et al. 1998; Lamb et al. 2000); and (2) the replication of some of that August-January NAO evolution in a 34-year simulation by the ECHAM4 Global Climate Model (GCM) of the Max-Planck-Institut für Meteorologie (Ward et al. 1999). Furthermore, good evidence was found for a global (especially central and eastern tropical Pacific) SST-forced component of late season precipitation (March-April, and to a lesser extent, February) in sub-tropical northwestern Africa (Ward et al. 1999). Skill in ECHAM4 simulations with prescribed SST for this season and region was very promising and the result was supported by a Canonical Correlation Analysis (CCA) between November-January tropical Pacific SST and February-April precipitation for the five Moroccan regions in Fig. 4.15. For El Niño years, which are

characterized by warm tropical Pacific SST anomalies, late season precipitation in Regions I-III is likely to be poor; for La Niña years, with its cold SST anomalies, the late season precipitation is likely to be plentiful.

Besides SST forcing, from the standpoint of operational seasonal prediction, there is, however, also a compelling need to better understand that part of the variance *not* connected to the large-scale climate system behavior represented by the NAO. Thus, an additional avenue towards the seasonal prediction of Moroccan precipitation is through detailed analysis of the above CDF data set. As a first step in this direction, Fig. 4.17 depicts spatial correlation patterns between time series of gridded CDF anomalies and MRR time series for Regions I-IV. These patterns resemble strongly those for SLP (Fig. 4.16), with opposite polarity, though the southern extrema for CDF are shifted north of their SLP counterparts. This is consistent with the spatial loading patterns of the CDF VRPC1 mode (Fig. 4.1d) versus NAO. Further, note that the correlation patterns for CDF are somewhat more localized in space than those for SLP. As for the SLP correlation patterns in Fig. 4.16, the counterclockwise migration of the southern node of the CDF correlation dipole (starting along Portuguese Atlantic coast and moving southward) is consistent with the progression among the Regions I-III with precipitation that is most strongly linked to the CDF anomalies. In contrast, Regions I and II (III and IV) display similar correlations with CDF, exceeding +0.6 (+0.4). These findings are confirmed further by Table 4.4 that provides the correlations between the CDF VRPC score and MRR time series. VRPC1, like the NAO, is observed to covary negatively with Moroccan precipitation for Regions I-III. As opposed to the NAO, VRPC1 shows a statistically significant correlation with Region IV, though weak (r=+0.12). VRPC2, whose southern node is near the Atlantic coast of Morocco (Fig. 4.1e), stands out as the

only mode that is most closely (positively) related to Moroccan precipitation for all regions. In contrast, VRPC3 has no influence on Moroccan precipitation, which is consistent with its centers of action being farther west (Fig. 4.1f).

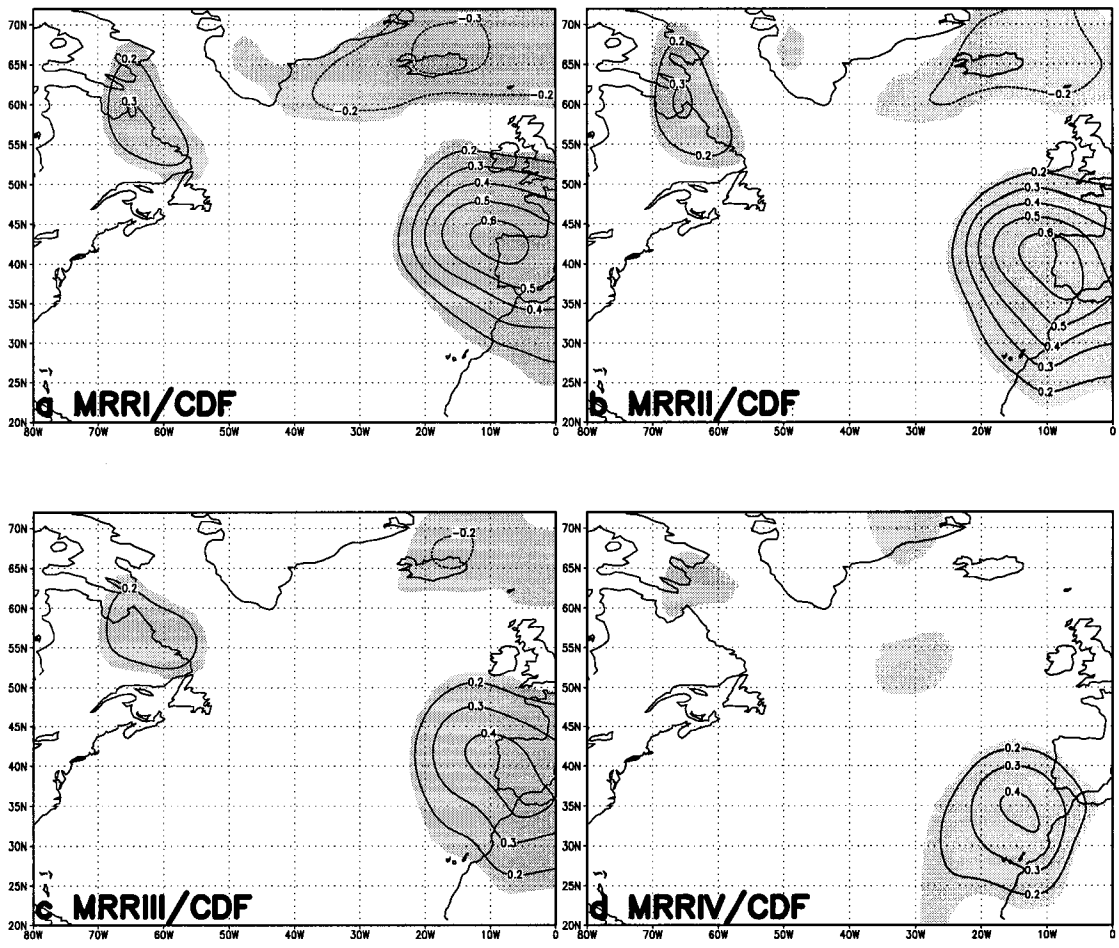


Fig. 4.17. As in Fig. 4.16 but for surface extratropical cyclone track density function (CDF) anomalies.

Table 4.4. Correlations between the three winter semester (October-March, 1948-99) CDF VRPC score time series and the Moroccan regional precipitation indices (z-scores, MRR) for the 5 regions in Fig. 4.15. Total number of records in each individual VRPC/precipitation time series is 306 months. Values next to the correlations indicate statistical significance levels (%) according to a two-sided Student's t-test that factors in the effective sampling size of the time series (Wilks 1995, p. 127). Pairwise scatter plots of the above time series are given in Fig. 4.22.

	$VRPC_1$	$VRPC_2$	$VRPC_3$
MRR I	-0.42 (99.99)	+0.31 (99.99)	-0.02 (28.16)
MRR II	-0.30 (99.99)	+0.43 (99.99)	0.00 (04.62)
MRR III	-0.23 (99.97)	+0.29 (99.99)	+0.03 (39.78)
MRR IV	+0.12 (93.43)	+0.30 (99.99)	+0.03 (37.34)
MRR V	-0.01 (16.06)	+0.13 (96.39)	-0.04 (40.99)

4.6.3 Relationship of Cyclone Tracks and Moroccan Precipitation with NAO

This subsection examines the relations of North Atlantic cyclone activity and Moroccan precipitation patterns to the NAO. The primary focus is to address the key issue of how much of the cyclone activity is NAO-related and how much is unrelated. Thus, the concern extends to explaining the "Rest of the (Moroccan Precipitation) Variance" that is *not* due to large-scale climate system control, in this case by the NAO.

a. Methodology

Selection of monthly cases for this investigation was designed to examine the NAO control versus non-NAO control of Moroccan precipitation documented in Table 4.3. The extreme cases were chosen using NAO and regional precipitation indices for the Moroccan Regions I-IV during the winter semester (October-March). For each individual region, monthly extremes of its MRR standardized anomaly index and Roger's NAO index (NAO_r) were binned according to the following four categories:

(I) Non-NAO Control:

(1) +NAO & +MRR (Category 1)

(2) -NAO & -MRR (Category 2); and

(II) NAO Control:

(3) -NAO & +MRR (Category 3) and

(4) +NAO & -MRR (Category 4).

where the "+" ("-") sign denotes "highly" positive (negative) values for the NAO and MRR time series. "Highly" is defined in the following paragraph.

The extreme months were chosen from scatter plots of NAO versus MRR for Regions I-IV. The best candidates for those extremes had extreme values for both precipitation *and* NAO. Large outliers and closest points to the least-squares regression line were identified. For each individual region, two additional constraints were applied to define the four above categories: $|NAO| > 1.0$ and $|MRR| > 0.5$. The extreme winter months were then determined objectively from the scatter plots (not shown) using Cook's distance distribution for each observation (Cook and Weisberg 1982). In this application, the total number of potential closest points/huge outliers to/from the regression line was set to 50% of total number of records (306 months). That is, the outliers (closest points) were defined as the top (bottom) 50% of Cook's distance distribution. The results are provided in Table 4.5 below. To visualize/track the cyclone systems during the above extreme months, an ImageMagick application was developed where we can see the animation of the month's daily SLP from the NCEP Reanalysis data.

Then, for a given Moroccan precipitation region and for each category, compositing analysis of North Atlantic winter semester (October-March, 1948-99) CDF

and SLP anomalies was performed based on the two variables (NAO and MRR). Next, Category 1-minus-Category 2 (featuring non-NAO control of precipitation) and Category 3-minus-Category 4 (characterizing NAO control) composite difference fields were derived. These differences were tested for statistical significance using a local two-sided Student's t-test assuming the Category 1 (Category 3) and Category 2 (Category 4) population variances are unequal. Only areas within the North Atlantic Basin with statistical significance greater than 99% level are presently taken into consideration.

Table 4.5. Total number of extreme months (out of 306) of relationship between Moroccan regional precipitation indices (z-scores, MRR) and Rogers' NAO time series (October-March, 1948-99) for Regions I-IV in Fig. 4.15. Categories 1-4 and additional constraints on NAO and MRR are defined in text. The outliers (closest points) to the least-squares regression line were defined as top (bottom) 50% of the Cook's distance distribution.

	Category 1	**Category 2**	**Category 3**	**Category 4**
Region I	8	16	13	23
Region II	11	17	5	23
Region III	15	27	5	10
Region IV	18	34	2	3

Interestingly, Table 4.5 shows that the total number of extreme cases increases/ decreases in the non-NAO/NAO control case (i.e., Categories 1-2/Categories 3-4) as we move from Region I to Region IV. Thus, of all regions, Region I has the lowest/highest total number of extreme cases (24/36) in the non-NAO/NAO control (Categories 1-2/3-4); the opposite being true for Region IV. Over all regions, Category 2 (non-NAO control) has the highest occurrence of extreme cases (94), whereas Category 3 (NAO control) has the lowest occurrence (25).

b. Results

Figs. 4.18-21 show the above {NAO and MRR}-based composite difference fields for each region separately. The patterns in the Category 3-minus-Category 4 (i.e., NAO control) SLP anomaly composites (panel b in each figure) essentially reflect a strong negative NAO environment. Consistent with Table 4.3, strongest SLP dipole is evident for Region I, whereas no statistical significance is apparent for Region IV. These extreme negative NAO events are accompanied by atmospheric blocking over the northern North Atlantic and Northern Europe (Fig. 4.16), which steers midlatitude disturbances south, resulting in wet conditions over Morocco (panel d in each figure). Note that the strongest negative NAO environment for Region I (Fig. 4.18b) is associated with strongest CDF dipole, resulting in statistically significant cyclone activity in this region (Fig. 4.18d). Weaker SLP dipoles for Regions II (Fig. 4.19b) and III (Fig. 4.20b) result in weaker CDF dipoles for the same regions (Fig. 4.19d and Fig. 4.20d, respectively). Similarly, nonsignificant CDF dipole for Region IV (Fig. 4.21d) is consistent with the SLP counterpart (Fig. 4.21b).

More prominent is the non-NAO control on precipitation, in which case the SLP patterns indicate a strong (and statistically significant for all Regions I-IV) positive NAO environment (panel a in each figure). In contrast, recall that Region I, for the above NAO control case, is the only region for which the SLP dipole is statistically significant. For the non-NAO control, the strong SLP dipole is accompanied by strong and statistically significant CDF dipole for each Region (panel c in each figure). Further, these extreme positive NAO events are seen to coincide with significant cyclone activity (characterized by CDF) over all the Moroccan regions. That is, this configuration (i.e., non-NAO control) brings significant precipitation to Morocco in all Regions I-IV (panels c) despite

the strong positive phase of the NAO (panels a). Recall that strong positive NAO phase would induce moderate-to-severe Moroccan drought (El Hamly et al. 1998; Lamb et al. 2000) in the total absence of CDF influence on Moroccan precipitation. However, by accounting for the additional CDF control of Moroccan precipitation (i.e., non-NAO control), all Regions I-IV still get precipitation (panels c) even though NAO is strongly positive (panels a). This indicates that CDF explains some of the rest of variance in Moroccan precipitation that is not due to the large-scale climate system control involving the NAO teleconnection pattern.

The simultaneous influence of both NAO and CDF on Moroccan precipitation patterns raises the question of how much of precipitation variance is explained by each component alone or both. This question is addressed through multivariate linear regression in next subsection. Furthermore, the fact that the cyclone activity is statistically significant for all regions in the non-NAO control case (panels c) and insignificant for Regions II-IV in the NAO control (panels d) suggests that CDF would explain more variance in Moroccan precipitation than NAO. This point also is assessed and quantified using the multiple regression method.

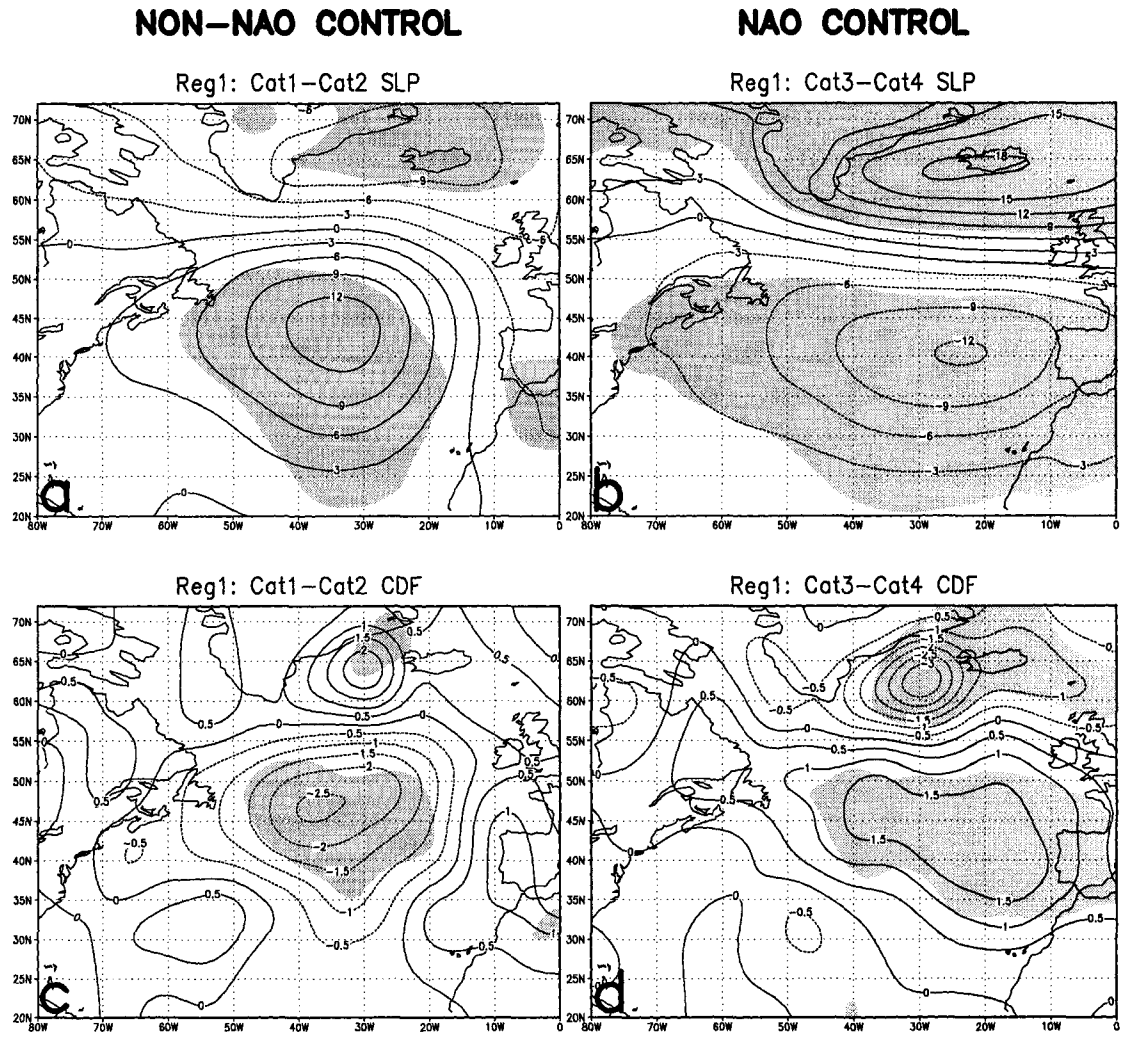


Fig. 4.18. NAO control versus non-NAO control of Moroccan precipitation in Region I (Northwest, Fig. 4.15). Panels (a) and (b) depict Category 1-minus-Category 2 (featuring non-NAO control of precipitation) and Category 3-minus-Category 4 (characterizing NAO control) composite difference fields of North Atlantic winter semester (October-March) SLP anomalies (hPa) for 1948-99, respectively. Panels (c)-(d): as in (a)-(b) but for surface extratropical cyclone track density function (CDF) anomalies (cyclones/day/250 km x 250 km). Rogers' NAO index was used to construct all panels. See text for computational details. Solid (dashed) contours indicate positive (negative) anomalies. Light shading represents areas where category composite differences are statistically significant at the 99% confidence level according to a local two-sided Student's t-test assuming the two category population variances are unequal.

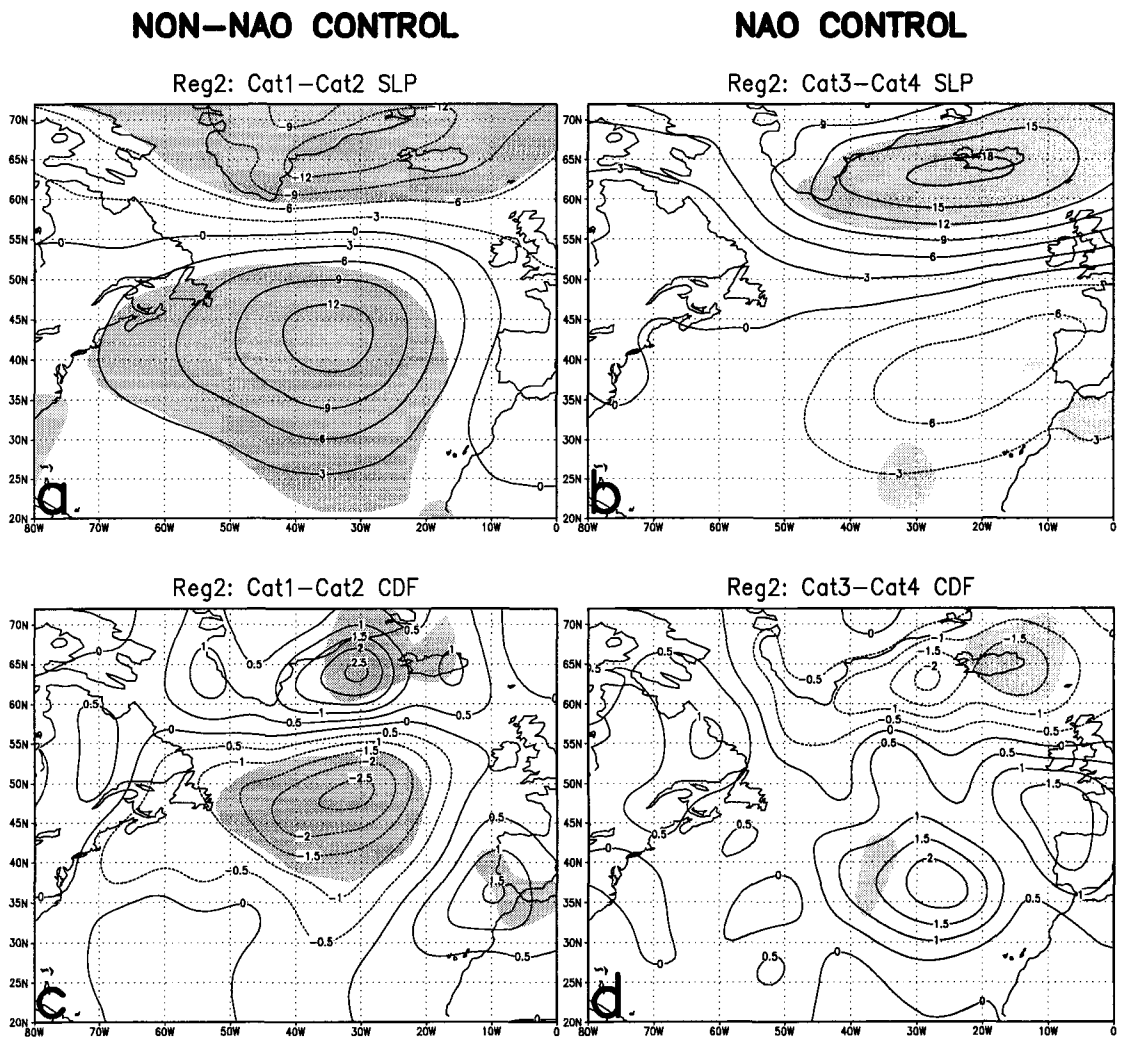


Fig. 4.19. As in Fig. 4.18 but for the Southwest region of Morocco (Region II, Fig. 4.15).

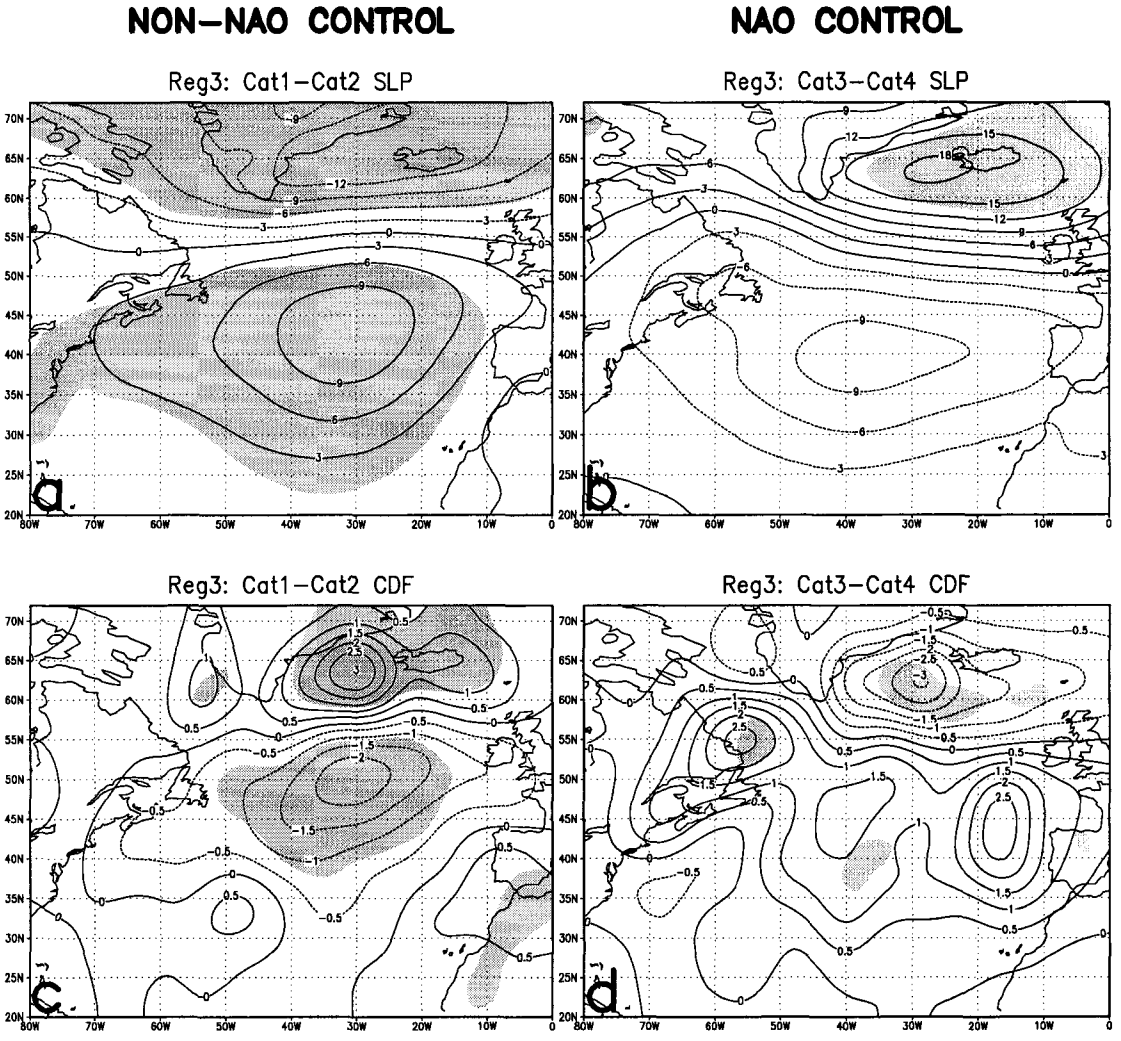


Fig. 4.20. As in Fig. 4.18 but for the Atlas Mountains (Region III, Fig. 4.15).

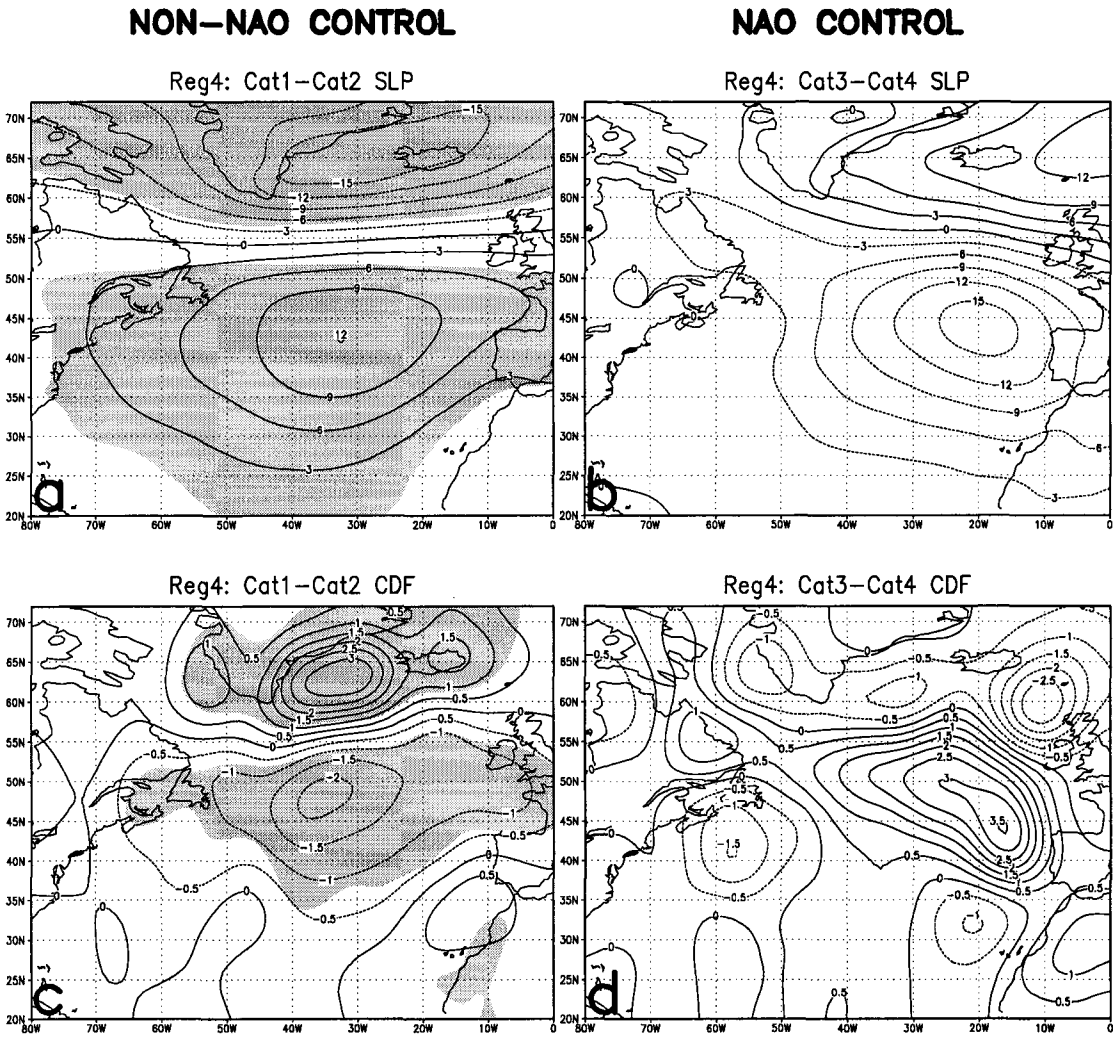


Fig. 4.21. As in Fig. 4.18 but for South of Atlas Mountains (Region IV, Fig. 4.15).

4.6.4 Predictability of Moroccan Regional Precipitation Index

The previous results have illustrated that the patterns of interannual Moroccan precipitation variability are related to changes in North Atlantic cyclone activity and atmospheric circulation as well. The purpose of this subsection is to quantify the relationships between the atmospheric circulation/cyclone activity over the North Atlantic and Moroccan precipitation anomalies during the winter semester. Specifically, this subsection revisits the predictability of Moroccan regional precipitation indices by accounting for the additional new monthly CDF VRPC score time series, besides the three NAO indices. Multiple regression models are constructed involving the following predictor time series: NAO_r, NAO_h, NAO_m, and CDF VRPC1, VRPC2, VRPC3. First, it is usually helpful to view mutivariate data (i.e., input predictors and the linear response MRR) as a whole using pairwise scatter plots. Thus, Fig. 4.22 contains all of the time series scatter plots of one variable against another. These plots feature linear relationships between some variables. Table 4.1 above already presented correlations between the CDF VRPC scores and the NAO indices, then linear relationships between the NAO and MRR were provided in Table 4.3, and finally, the linear dependence of MRR on VRPCs was given in Table 4.4. All these various interrelationships were already discussed.

Then, for each Moroccan region, the precipitation index was modeled as a linear function of the six potential predictors, exploiting the fact that multiple regression approach can be improved by adding and dropping terms from the linear model. Regression literature discusses many criteria for adding and dropping terms (e.g., Weisberg 1985), from which an appropriate criterion (i.e., C_p statistic) was selected for use in this application where the "Best Model" was chosen via "Stepwise Selection". If a term has a C_p statistic lower than that of the current model, then the term with the

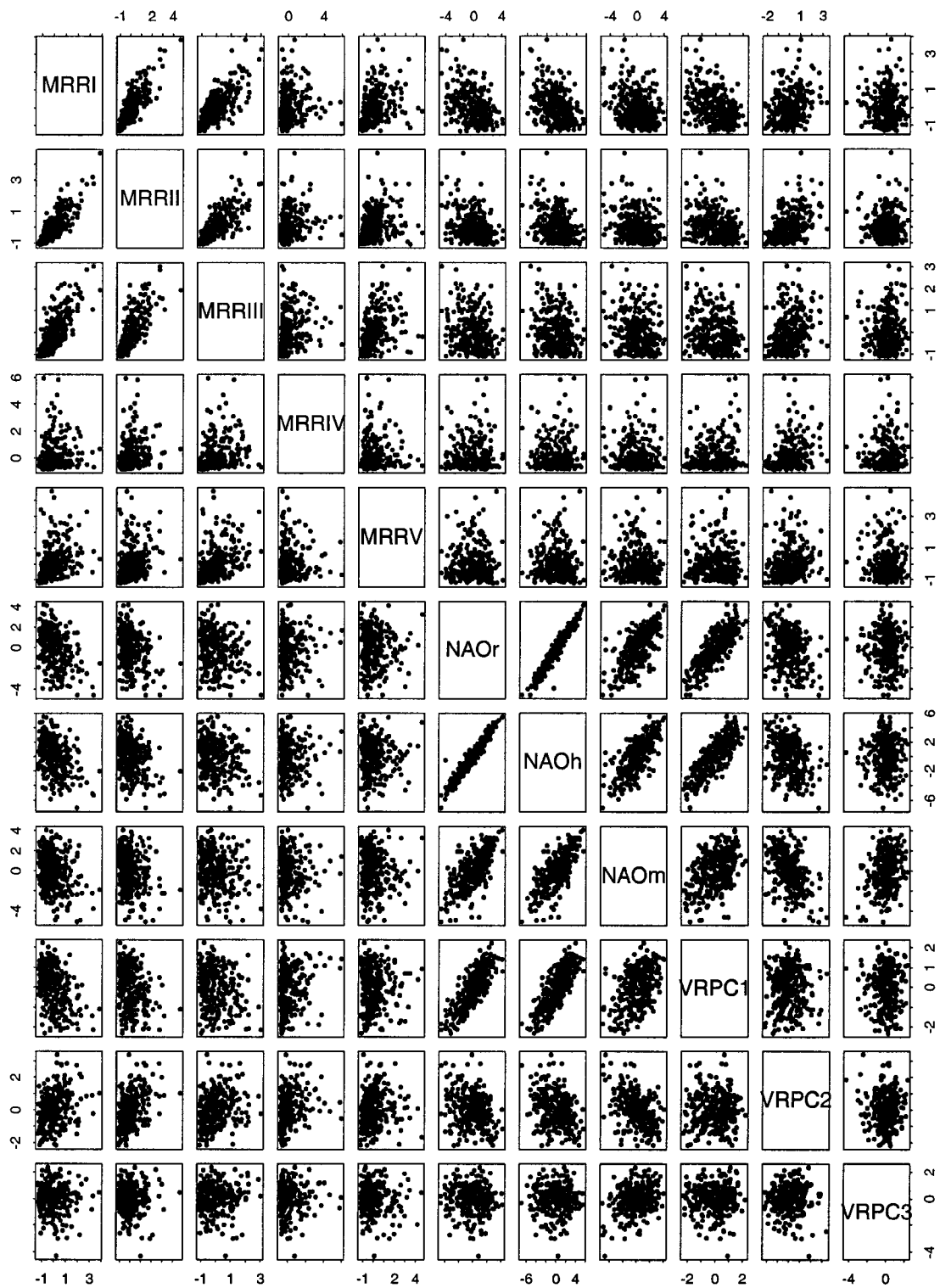


Fig. 4.22. Pairwise scatter plots of time series of one variable against another for October-March, 1948-99. The variables are: Moroccan Regional Precipitation indices (z-scores) for all regions (MRRI-V), Rogers' NAO index (NAO_r), Hurrell's NAO index (NAO_h), Mobile NAO index (NAO_m), and the three VARIMAX Rotated Principal Component score time series for North Atlantic CDF (VRPC1, VRPC2, VRPC3) (given in Fig. 4.2). Total number of records in each individual time series is 306 months.

lowest C_p is dropped. If the current model has the lowest C_p, the model is not improved by dropping any term. An automated procedure was used to conduct stepwise model selection. Essentially, this selection process calculates the C_p statistics for the current model, as well as those for all reduced and augmented models, and then adds or drops the term that reduces C_p the most. In other words, C_p is used to decide upon acceptance or rejection of terms in the linear model.

The output of this stepwise model selection is given below in Table 4.6. This table also presents three related measures of the "fit" of a regression. The first of these is the residual standard error. From the standpoint of forecasting, this is perhaps the most fundamental of the three measures, since it directly reflects the accuracy of the resulting forecasts (Wilks 1995, p. 166). The second usual measure of the fit of a regression is the coefficient of determination, or R^2. The third commonly used measure of the strength of the regression is the F-statistic defined as F=MSR/MSE, where MSR is the Mean-Squared Regression and MSE is the Mean-Squared Error (i.e., sample variance of the residuals). MSR is defined as MSR=SSR/df, where the regression df stands for degrees of freedom (df=1), and the term SSR denotes the regression sum of squares, or the sum of squared differences between the regression predictions and the sample mean of the time series (see Wilks 1995, p. 160 for more details). The ratio F increases with the strength of the regression, since a strong relationship will produce a large MSR and a small MSE. A literal interpretation of the MSE would indicate that a 95% confidence interval for Moroccan precipitation index around the regression line would be about $\pm 2\ (MSE)^{1/2}$.

Table 4.6. Summary statistics from multivariate linear regression modeling of Moroccan regional precipitation (MRR) as a function of: (1) the three NAO indices (October-March, 1948-99) due to Rogers (1984) (NAO_r), Hurrell (1995a) (NAO_h), and Portis et al. (2001) (NAO_m); and (2) the three North Atlantic winter semester (October-March, 1948-99) CDF VRPC score time series (given in Fig. 4.2). Total number of records in each individual NAO/VRPC/MRR time series is 306 months. Panels (a-e) pertain to Regions I-V in Fig. 4.15. For each region, three cases are examined where the predictors are NAOs only, VRPCs only, and NAOs and VRPCs. In each case, the "Best Model" was determined through "Stepwise Selection". See text for more details on the related measures of the "fit" of a multiple regression.

a. Region I

Predictors	Best Model	Residual Stand. Error	Multiple R^2 (%)	F-statistic
NAOs only	NAO_h	0.8153	16.26	59.03
VRPCs only	VRPC1+ VRPC2	0.7638	26.75	55.34
NAOs & VRPCs	VRPC1+ VRPC2+NAO_r	0.7603	27.66	38.49

b. Region II

Predictors	Best Model	Residual Stand. Error	Multiple R^2 (%)	F-statistic
NAOs only	NAO_r	0.8310	11.60	39.90
VRPCs only	VRPC2+ VRPC1	0.7536	27.54	57.59
NAOs & VRPCs	VRPC2+ VRPC1+NAO_h	0.7476	28.93	40.98

c. Region III

Predictors	Best Model	Residual Stand. Error	Multiple R^2 (%)	F-statistic
NAOs only	NAO_h	0.8071	05.51	17.73
VRPCs only	VRPC2+ VRPC1	0.7736	13.48	23.6
NAOs & VRPCs	VRPC2+ VRPC1+NAO_r	0.7674	15.14	17.97

Table 4.6. (Continued)

d. Region IV

Predictors	Best Model	Residual Stand. Error	Multiple R^2 (%)	F-statistic
NAOs only	NAO_m	1.075	01.03	03.16
VRPCs only	VRPC2+ VRPC1	1.025	10.31	17.42
NAOs & VRPCs	VRPC2+ VRPC1	1.025	10.31	17.42

e. Region V

Predictors	Best Model	Residual Stand. Error	Multiple R^2 (%)	F-statistic
NAOs only	1	1.0020	$3.463\ 10^{-30}$	NA
VRPCs only	VRPC2	0.9951	01.61	4.979
NAOs & VRPCs	VRPC2	0.9951	01.61	4.979

The key points of Table 4.6 are as follows. For all Regions I-V, the VRPC-based regression model outperforms the NAO-based model. This comparison is based on the multiple R^2 and residual standard error for Regions I-V and the F-statistic for Regions II-V. This result largely is consistent with a comparison of Tables 4.2 and 4.3. Owing to the relatively local nature of Moroccan precipitation patterns, this finding can be explained in part by the local influence of the cyclone tracks (represented by CDF) versus the large-scale climate system control involving the NAO teleconnection pattern. Further, for Regions I-III, the multiple regression model using both NAOs and CDF VRPCs as predictors is slightly better than those based on NAOs only or VRPCs only. That is, NAO adds little information in this case, largely due to the fact that NAO is essentially very similar to VRPC1. As for Regions IV-V, VRPCs-based and {NAOs & VRPCs}-

based models yield the same results since these two regions show no significant correlations with NAO (Table 4.3). In particular, note that the NAO and CDF have essentially no influence on Region V. This suggests that precipitation in this northeastern region of Morocco may be controlled by other factors (e.g., Mediterranean cyclogenesis).

For Region I, the leading predictor is VRPC1 (Fig. 4.23a); this may be explained in part by the fact that Region I is the closest region to its centers of action. In contrast, the leading predictor is VRPC2 for Regions II-V (Fig. 4.23b), which is consistent with its nodes being closer to the northwestern Atlantic coastal areas of Morocco (Fig. 4.1e). In contrast, VRPC3 has no influence on precipitation in any region, which agrees with its two extrema being farther west (Fig. 4.1f). Finally, a counterpart analysis for ENSO suggested that climate system mode has no statistically significant impact on Moroccan precipitation patterns (not shown).

The skill of the above multivariate linear regression modeling of Moroccan regional precipitation indices is assessed via temporal correlation between the predicted MRR and observed MRR, and corresponding root-mean-square root (RMSE). The training period was set to October 1948-March 1980, followed by the prediction period, October 1980-March 1999. Table 4.7 presents the results for the regions I-III and the three different models. This table reveals that, indeed, the VRPCs-based model outperforms the NAOs-based model, with higher (lower) correlation (RMSE) for the former model. Further, Table 4.7 also confirms that the {NAOs & VRPCs}-based model is slightly better than the VRPCs-based model in predicting Moroccan precipitation.

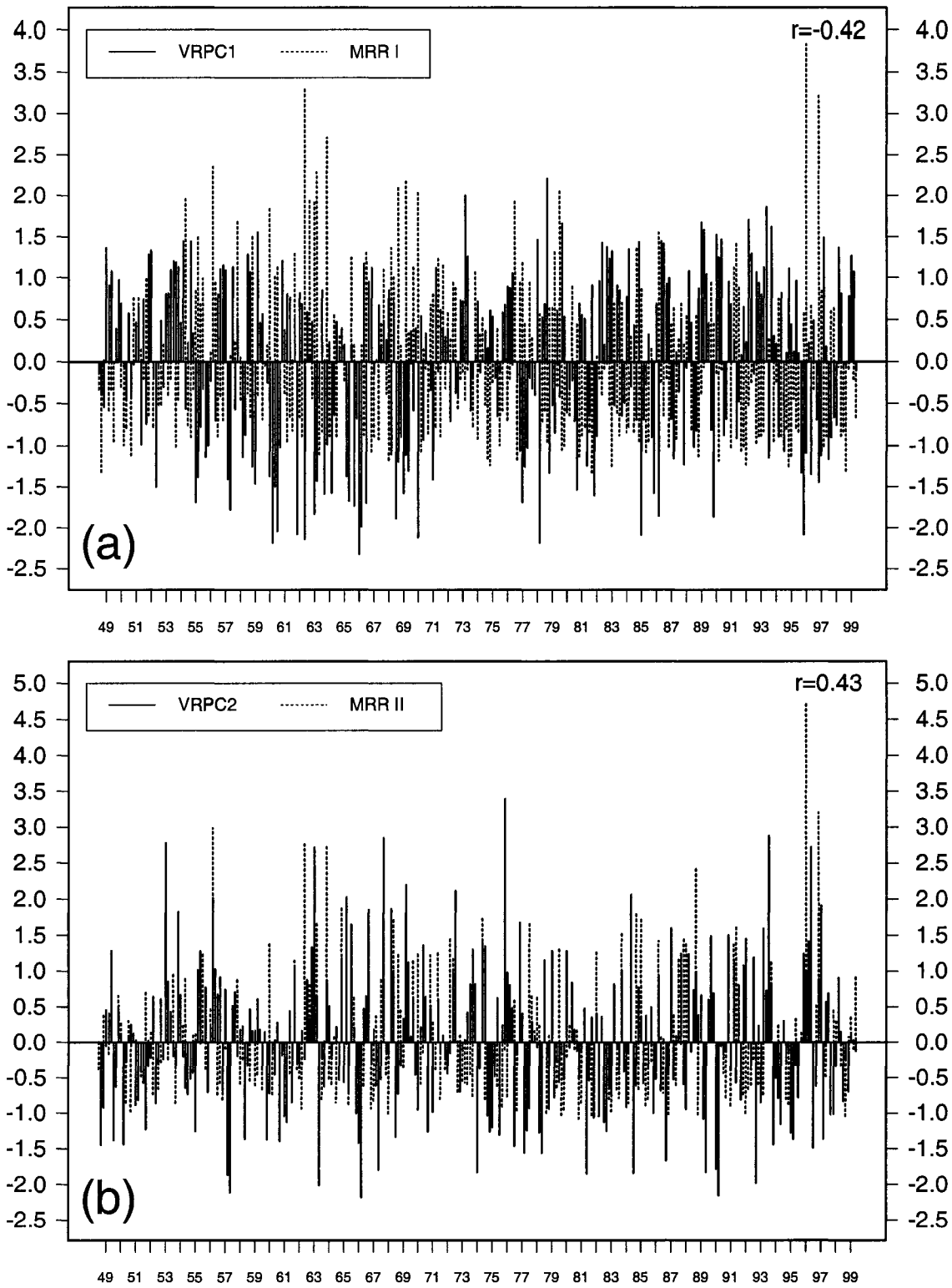


Fig. 4.23. Time series for the winter semester (October-March, 1948-99). Panel (a): CDF VRPC1 scores (solid bars) versus Moroccan regional precipitation index for Region I (MRR I) (broken bars). Panel (b): as in Panel (a) but for VRPC2 and MRR II. In each panel, r denotes the temporal correlation between the two time series.

Table 4.7. Skill of multivariate linear regression modeling of Moroccan regional precipitation indices (MRR) listed in Table 4.6. The models were fitted for the training period, October 1948-March 1980. For each individual region and a given model, r denotes the temporal correlation between the predicted MRR and observed MRR for the prediction period, October 1980-March 1999; RMSE is the corresponding root-mean-square error of the prediction.

a. Region I

Predictors	Best Model	r	RMSE
NAOs only	NAO_h	0.46	0.76
VRPCs only	VRPC1+ VRPC2	0.54	0.74
NAOs & VRPCs	VRPC1+ VRPC2+NAO_r	0.54	0.73

b. Region II

Predictors	Best Model	r	RMSE
NAOs only	NAO_r	0.50	0.87
VRPCs only	VRPC2+ VRPC1	0.57	0.80
NAOs & VRPCs	VRPC2+ VRPC1+NAO_h	0.58	0.79

c. Region III

Predictors	Best Model	r	RMSE
NAOs only	NAO_h	0.34	0.72
VRPCs only	VRPC2+ VRPC1	0.44	0.68
NAOs & VRPCs	VRPC2+ VRPC1+NAO_r	0.46	0.68

4.7 SUMMARY AND CONCLUSIONS

This chapter examined the interannual variability of North Atlantic winter cyclone activity and its associations with regional climate variations, including one sensitive bordering region (Morocco). Several analysis methods were applied to the CDF and other related cyclone attributes (e.g., intensity, moving speed, duration) to illuminate such variability.

First, the principal modes of North Atlantic winter surface extratropical cyclone track variability were identified from a VARIMAX Rotated Principal Component (VRPC) Analysis of CDF anomalies. It is found that the VARIMAX rotation has better isolated the patterns of variability. The three VRPCs (retained in this analysis) collectively account for ~26.4% of total CDF variance. Consistent with the design of the VARIMAX algorithm, each of these VRPCs explains similar fractions of the total variance. VRPC1 reflects predominant northward or southward migration of the primary storm track from its time-mean position. Further, VRPC1 pattern is strongly reminiscent of the positive phase of the NAO, but with the dipole shifted north of its NAO counterpart. VRPC2 (VRPC3) also has a dipole structure in eastern (mid-) North Atlantic. Relative to VRPC1, VRPC2 (VRPC3) has the opposite (same) polarity and nodes shifted farther south (southwest). Thus, VRPC2 is much less a NAO-like pattern than VRPC1; whereas VRPC3 has no relationship with the NAO.

Linear trends in the CDF VRPC score time series were found to be not statistically significant. Persistence of the VRPC scores, via 1-month lag autocorrelation function (ACF) and month-to-month correlation analyses, is generally weak. Both analyses show that, of all three modes, VRPC3 (affects mid-Atlantic) is the most persistent at 1-month

lag; whereas VRPC1 and VRPC2 (influence eastern North Atlantic) are less persistent.

Matching Pursuit Transform (MPT) was applied to each CDF VRPC score time series in order to best match the signal structures. The changing nature of the CDF signal is very well reflected in the MPT time-frequency decomposition that clearly reveals that each CDF mode displays different patterns of cyclone activity at a given point in time for a particular frequency band. Further, it is found that the MPT is very efficient in identifying singularities in both time and frequency. The three CDF modes exhibit different time-based singularity characters and they are of quite different frequency-based singularity nature. Therefore, the CDF signal is characterized by non-stationarity.

The analysis of the North Atlantic raw surface extratropical cyclone tracks for individual extreme months confirms the existence of periods when each of the CDF VRPC modes dominates, yielding a new classification of the North Atlantic winter cyclone behavior into three distinctly different regimes. Briefly, VRPC1 is essentially the NAO, whereas the new CDF VRPC2 reflects southwest-northeast split pattern. In contrast, the new CDF VRPC3 features diffuse pattern of cyclone activity from the southern tip of Greenland towards the Iberian Peninsula/Morocco. To date, the central focal point of most climate investigations on North Atlantic/European sector has involved the NAO. Therefore, these unique CDF VRPC modes are used extensively in this Dissertation to give new insight into the cyclone track organization and behavior.

Relationships of atmospheric and oceanic circulation anomalies to the CDF VRPC modes were documented in a different and comprehensive way. Consistent with previous results, the relationship between the surface wind and SST anomalies for VRPC1 is

essentially local: For instance, above-normal wind speeds will cool the ocean mixed layer by enhancing the sensible and latent heat fluxes from the ocean surface and by accelerating the entrainment of cooler water from below (Deser and Blackmon 1993). Compared to VRPC1, the patterns for the high-minus-low composites associated with VRPC2 (VRPC3) are essentially very similar to those related to VRPC1 but shifted farther south (southwest) with the opposite (same) polarity, which is consistent with the spatial VRPC loading patterns. However, the SST pattern is monopole featured for both VRPC2 and VRPC3, with the same (opposite) sign as VRPC2 (VRPC3) scores. The SST pattern for VRPC2 (VRPC3) is generally consistent with a response of the upper-ocean to the associated atmospheric forcing, although oceanic processes may be involved in determining and/or modulating the SST pattern. For VRPC2 (VRPC3), temperature anomalies in the midocean area east (southeast) of Newfoundland may be related to changes in the interface between the subtropical and subpolar ocean gyres (in the strength and/or position of the Gulf Stream current). Coupled ocean-atmosphere GCM modeling is required to assess the above hypotheses.

Short-term cyclone variability was related to global and regional teleconnection patterns (e.g., ENSO, NAO). The regional NAO impact on North Atlantic winter cyclone characteristics was documented. During positive NAO events, the main cyclone track has a pronounced northeastward orientation across the North Atlantic (e.g., Rogers 1990), resulting in an absolute maximum of cyclone activity over the Greenland/Iceland corridor in terms of both CDF and cyclone frequency, along with absolute maximum cyclone intensity and absolute minimum central pressure north of Iceland. However, intensification of cyclone deepening rate and moving speed maximize further upstream, to the northeast of Newfoundland. Cyclone duration tends to maximize over the

Greenland Sea. In contrast, during negative NAO events, cyclones crossing the western Atlantic move eastward, tracking along latitude 45°N on average, in proximity to the Gulf Stream, resulting in the maximum of cyclone duration northwest of Portugal.

Additionally, the possibility of a more remote ENSO influence on North Atlantic winter cyclone tracks and atmospheric/oceanic circulation was explored. The cyclone track shifts southward during El Niño years, while La Niña events are associated with opposite shifts. Accompanying the significant above (below)-normal cyclone activity off the U.S. East Coast is a marked tendency for negative (positive) SLP anomalies. Further, warm ENSO events are associated with above-normal SST along a zonally elongated belt in the band between 20°-30°N, and with below-normal temperature in the waters off the U.S. East Coast. The oceanic response is consistent with atmosphere-to-ocean forcing.

The relationship of CDF and Moroccan precipitation patterns to the NAO was examined. The key issues were how much of the cyclone activity is NAO-related, and how much is not, and the implications this has for the predictability of Moroccan precipitation (El Hamly et al. 1998; Ward et al. 1999). Thus, the concern extended to explaining the "Rest of the (Moroccan Precipitation) Variance" that is *not* due to large-scale climate system control by the NAO. Analysis of the {NAO and MRR}-based composite difference fields for each Moroccan region (Fig. 4.15) indicates that CDF explains some of the rest of variance in precipitation that is not due to NAO. The results illustrated that interannual Moroccan precipitation anomalies are the residual of strong regional patterns of change involving both NAO and CDF. Thus, the predictability of MRR indices by accounting for the additional new CDF VRPC scores, besides the three

NAO indices, was revisited via multiple regression, where the "Best Model" for each region was chosen via "Stepwise Selection" (C_p criterion). For all Regions I-V, the VRPC-based regression model outperforms the NAO-based model. Owing to the relatively local nature of Moroccan precipitation patterns, this finding can be explained in part by the local influence of the cyclone tracks (represented by CDF) versus the large-scale climate system control involving NAO. For Regions I-III, the {NAOs & VRPCs}-based model is slightly better than those based on NAOs only or VRPCs only; i.e., NAO adds little information in this case, largely due to its high correlation with VRPC1. As for Regions IV-V, VRPCs-based and {NAOs & VRPCs}-based models yield the same results since these two regions show no significant correlations with NAO; in particular, both NAO and CDF have essentially no influence on Region V. For Region I (II-V), the leading predictor is VRPC1 (VRPC2), which is consistent with their spatial loading patterns. VRPC3 has no influence on precipitation in any region, which agrees with its two centers of action being farther west. Finally, a counterpart analysis for ENSO suggested that climate system mode has no statistically significant impact on Moroccan precipitation patterns.

CHAPTER 5: DECADAL-TO-MULTIDECADAL VARIABILITY OF CYCLONE TRACKS INVOLVING OCEAN-ATMOSPHERE INTERACTIONS

5.1 BACKGROUND AND MOTIVATION

The Percentage Wavelet Energy Concentration Analysis (Section 3.5, Fig. 3.11) applied to anomaly fields of the North Atlantic winter semester (October-March) surface extratropical cyclone track density function (CDF) revealed a clear and fundamental distinction between two frequency bands in the cyclone behavior: high-frequency (HF) and low-frequency (LF), with a separation of ~5 years. This 5-year period corresponds to the coarsest-scale features of the CDF signal, as revealed by the Discrete Wavelet Transform (DWT). This differentiation first led to the documentation of the shorter-term variability of cyclone behavior in Chapter 4. Now, the present chapter considers the lower-frequency variability at decadal-to-multidecadal time-scales.

Climate variability on decadal and longer time-scales is a subject of increasing interest and relevance (e.g., Deser and Blackmon 1993). Concern over anthropogenic impacts on global climate is one strong catalyst to describe and understand the natural modes of longer-term climate system variability. It is now well known that the low-frequency component of the North Atlantic atmospheric circulation exhibits significant interdecadal variability (Hurrell 1995a; Portis et al. 2001; and many others). Consequently, the LF variability of the NAO – that is highly correlated with the leading mode of CDF anomalies on the monthly time-scale (Table 4.1) – has recently become one of the foci of climate research (CLIVAR 1998). This is partly due to the desire to

perform long-range predictions for the North Atlantic/European sector and Northwest Africa, where climate variability is strongly influenced by NAO. The research is being facilitated by two salient features to NAO. First, Hurrell's NAO index for instance, as well as proxy reconstructions (e.g., Appenzeller 2000), show a spectrum of variability that maximizes in the interannual, decadal, and even longer frequency bands (e.g., Hurrell and van Loon 1997). The second striking feature of NAO is that it has exhibited a notable trend over the last three decades towards predominance of the positive phase over the negative. The extreme positive values of NAO since the late 1980s may be unprecedented over the instrumental and proxy record (Stockton and Glueck 1999), though paleoclimate evidence suggests periods of prolonged phase preference have occurred in the past (e.g., Luterbacher et al. 1999).

Detection of trends in climatological time series has become central to the discussion of possible climate change due to the enhanced greenhouse effect (e.g., Karoly et al. 2003; Karl and Trenberth 2003). While it has been speculated that future global warming will change the frequency and intensity of extratropical storms in the Northern Hemisphere (e.g., Zhang et al. 2000 and references therein), there is considerable uncertainty as to what changes actually will occur (McCabe et al. 2001 and references therein). Very few published studies have examined recent trends in cyclone activity over the Northern Hemisphere/North Atlantic Basin (e.g., McCabe et al. 2001; Geng and Sugi 2001). Therefore, the first main component (Section 5.3) of this chapter examines the LF behavior of North Atlantic cyclone tracks (including trends) and their associations with other LF atmospheric and oceanic fields/indices (NAO, ENSO).

The second main component (Section 5.4) of this chapter expands on Section 5.3 by exploring whether a coupled ocean-atmosphere mode exists in the North Atlantic at decadal-to-multidecadal time-scales. Interaction between the oceans and overlying atmosphere is fundamental to the dynamical processes governing climate and its variability. While there has been substantial recent progress in understanding the role of the tropical Pacific Ocean in global ocean-atmosphere interactions, the role of the North Atlantic Ocean currently is much less well understood. There are basically three ways the atmosphere and ocean can interact in the extratropics. At one extreme, on sub-annual time-scales, the atmosphere's intrinsic variability forces an ocean response, while at the other extreme (centennial time-scales), there is evidence that oceanic variations drive the atmosphere. Between these two regimes, on decadal-to-multidecadal time-scales, there may or may not be a mutual interaction in which variability arises as a fundamentally coupled process (Goodman and Marshall 1999). Because the NAO appears to favor more than one time-scale and the shortness of the instrumental record, it has proven difficult to reveal a clear coupled mechanism in the North Atlantic climate system.

That not all of NAO variability can be attributed to intraseasonal stochastic atmospheric processes points to a role for external forcing (i.e., surface, stratospheric and anthropogenic processes) and, perhaps, a small but useful amount of predictability (Hurrell et al. 2003). Finding an ocean role in the NAO would increase the predictability of the phase and amplitude of this index (e.g., Rodwell et al. 1999). In contrast to the atmosphere, the ocean changes much slower and has a far greater thermal inertia ("memory"). However, as stated before, the role of the ocean in the NAO remains quite debatable, reflected in several different groups of hypotheses. At one extreme, a group of hypotheses claims that the LF variability of NAO can be explained stochastically with

no coupling with other components of the climate system (e.g., Wunsch 1999; Stephenson et al. 2000), while at the other extreme, a group of hypotheses proposes that external forcings (e.g., tropical origins) to the North Atlantic climate system drive the LF NAO (e.g., Graf et al. 1995; Hoerling et al. 2001). Between these two extremes, one possibility is the passive/active coupling of atmosphere/ocean within the North Atlantic climate system. On one hand (atmosphere-to-ocean forcing, with no active coupling), there is evidence that SST is responding to atmospheric forcing on weekly (Deser and Timlin 1997), monthly (Cayan 1992a,b), and interannual-to-decadal (Deser and Blackmon 1993; Kushnir 1994; Sutton and Allen 1997) time-scales. On the other hand (ocean-to-atmosphere forcing, with no active coupling), the nature of the atmospheric response to various idealized extratropical SST anomalies is not clear. The results from several model studies (Palmer and Sun 1985; Kushnir and Held 1996; Robinson 2000; Kushnir et al. 2002; Peng et al. 2003) are not consistent in all respects, but tend to suggest that the response is rather weak relative to internal variability; i.e., a signal-to-noise problem (Venzke et al. 1999). In contrast, another group of hypotheses are based on the *active* coupling of the atmosphere/ocean within the North Atlantic climate system. Specifically, these hypotheses involved oceanic gyres (Bjerknes 1964), oceanic advection (Sutton and Allen 1997), the existence of a "warm water transformation pipeline" as proposed by McCartney (Kerr 1997), the subtropical gyre and the NAO (Grötzner et al. 1998), the thermohaline circulation (Timmermann et al. 1998), and the formation of mode waters (Joyce et al. 2000). Recently, Marshall et al. (2001) stated that on decadal time-scales (?), there may be a mutual coupling between the two fluids in which ocean gyres and the thermohaline circulation can both play a role.

Subsection 5.4.1 reviews briefly the main studies that have dealt with this controversial but yet very pointed research question, suggesting the existence of coupled ocean-atmosphere modes in the North Atlantic. Confirmation of a mutual coupling could provide significant potential for dynamical climate prediction as exemplified by the most well-known coupled phenomenon, ENSO (Neelin et al 1994). However, the leading modes from the present studies do not agree on the exact periodicities, amplitudes, or physical mechanisms involved (Häkkinen 2000). The modes seem highly dependent on the data, coupled model, or technique used. The model-dependence of the coupled modes is a situation that should hopefully develop some convergence with future improvements in fully coupled model resolution and physical parametrizations. This stresses the need for further observational studies (Häkkinen 2000).

With this motivation, Subsection 5.4.2 employs a new Canonical Correlation Analysis (CCA)-based procedure to attempt further clarification of the role of the ocean in the North Atlantic decadal climate variability. The goal is to contribute to our understanding of how the North Atlantic atmospheric circulation could respond to ocean forcing on decadal time-scales, and to determine the extent to which SST anomalies feed back on the atmospheric circulation. Finally, Section 5.5 gives a summary and recapitulates the key points of this chapter.

5.2 DATA AND METHODOLOGY

The data/indices (with monthly resolution) used in this LF analysis are as follows:

- CDF (developed in Chapter 2).
- Atmospheric and oceanic variables: SLP, surface wind vector and wind speed, surface air temperature, sensible and latent heat net fluxes, precipitation rate, and 500-hPa

geopotential height from the NCEP/NCAR Reanalysis Project (Kalnay et al. 1996; Kistler et al. 2001); and NOAA extended reconstructed SST from the NOAA-CIRES CDC website (URL=http://www.cdc.noaa.gov/cdc/reanalysis/reanalysis.shtml) (Smith and Reynolds 2003).

- NAO indices: (1) Rogers' NAO (NAO_r) (Rogers 1984), (2) Hurrell's NAO (NAO_h) (Hurrell 1995a), and (3) the Mobile NAO (NAO_m) (Portis et al. 2001).
- ENSO: a range of ENSO indices – SOI; various standard SST indices such as Niño 3.4 (N34); the new Trans-Niño Index (TNI, Trenberth and Stepaniak 2001) which focuses particularly on decadal variability.

The above grid-cell fields (e.g., CDF, SLP, SST, etc...) were first prepared in the following manner:

- At each grid-point and for each individual winter month (from October to March), anomalies were computed with respect to the mean climatological values derived for the given calendar month (6 values/yr; 1948/49-1998/99), and then normalized by the temporal standard deviation of the calendar month (6 values/yr).
- At each grid-point, these normalized monthly departures were then averaged into seasonal anomalies (October-March) to form winter-mean departures from normal (1 value/yr; 1949-99).
- A 11-term low-pass Lanczos filter (Duchon 1979) was then applied to the gridded winter-mean standardized departures to retain only the lower-frequencies (LF, periods greater than 10 years). Use of the Lanczos filter involved setting the Lanczos sigma factor to 2 in order to maximize the frequency response function and reduce Gibbs oscillations (Duchon 1979). Fig. 5.1a depicts the frequency response function of this filter, and the corresponding weight sequence is shown in Fig. 5.1b. Note that the cutoff

frequency was set to 10 yrs instead of the 5 years suggested by the earlier DWT analysis (Fig. 3.11), in order to enhance the frequency response function. Such a response is about 20% and 70% for the 5-yr and 10-yr periodicities, respectively (Fig. 5.1a). To study decadal variability, it is often useful to filter climatic indices, separating the decadal variability (LF) from the sub-decadal (HF) variability (Ward et al. 1999). Note that they used the 10-yr period in their analysis to emphasize the decadal variability.

- Finally, anomalies of the above smoothed gridded fields were computed.

Thus, the result of the above process were time series anomalies of smoothed winter-mean standardized departures for each grid cell (1 value/yr; 1949-99).

Similarly, the aforementioned 1-D time series (e.g., NAO, SOI, etc...) also were prepared in the same manner as above for the gridded fields. First, their normalized monthly departures were averaged for each winter semester, and then those winter averages were smoothed using the same Lanczos filter procedure as in Ward et al. (1999).

5.3 LF BEHAVIOR OF CDF AND ASSOCIATIONS WITH OTHER ATMOSPHERIC & OCEANIC FIELDS/INDICES

5.3.1 Leading Mode (UPC1) of LF Cyclone Track Variability

A PCA was applied to the North Atlantic low-frequency winter CDF anomaly fields. The leading UPC mode of LF cyclone track variability accounts for 23.23% of total LF CDF variance. The spatial loading pattern for this mode is plotted in Fig. 5.2, and the associated UPC1 score time series is in Fig. 5.3. The UPC1 pattern mainly is characterized by a dipole structure, with the northern center of action being maximized over the Greenland Sea, and a contrasting southern center of action that maximizes over the central North Atlantic while extending from the U.S. East Coast to Western Europe.

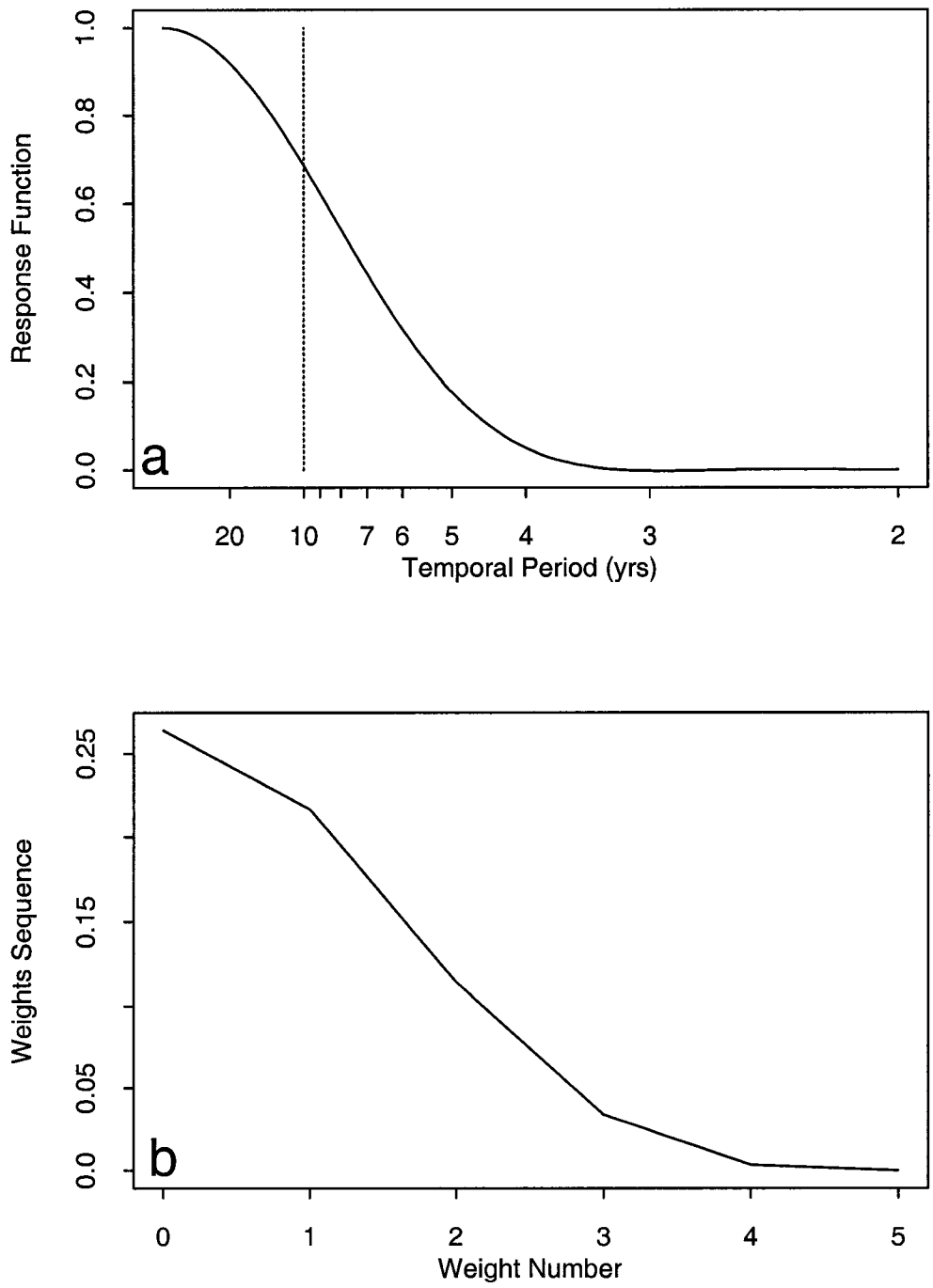


Fig. 5.1. Low-pass Lanczos filter characteristics (Duchon 1979). Panel (a) depicts the frequency response function (i.e., ratio of amplitude after filtering to before) as a function of temporal period (in years) (cutoff frequency is set to 10 years; Lanczos sigma factor is set to 2). Panel (b) shows the corresponding weight sequence, with a total number of weights set to 11.

Note the existence of a relatively weaker and more localized extremum in the southeast of the study domain. Thus, depending upon the sign of the UPC1 score time series, the UPC1 pattern reflects either predominant northeastward-traveling cyclones across the northern basin or zonal cyclones across the central basin. Note that the peak in the UPC1 pattern occurs downstream of the long-term climatological CDF maximum (Fig. 3.1a).

Of particular interest is the relatively weaker third extremum off Northwest Africa, which is in phase with the northern center of action. For instance, in its positive (negative) phase, the UPC1 mode is associated with above (below)-normal cyclone activity off Northwest Africa. The above-normal storminess over this region may be due in part to the possible intrusion of tropical disturbances from the south into the North Atlantic Basin, some of which may reach the Atlas Mountains over Morocco. Knippertz et al. (2003) documented three late summer/early autumn cases of tropical-extratropical interactions causing precipitation in Northwest Africa, with respect to the sources and the vertical and horizontal transports of moisture, as well as local factors for precipitation generation. In particular, they found that the dynamically forced ascent in connection with orographic lifting at the Atlas Mountains in the southerly flow and surface heating over the elevated terrain triggers convective rainfall that occurs preferably close to and downwind of the mountain chain.

The UPC1 and VRPC1 spatial loading patterns (not shown) bear strong resemblance and their associated score time series are highly correlated (r=+0.90). This shows that the LF CDF UPC1 mode is robust. The UPC1 mode is rather retained in this low-frequency analysis because it explains more variance than VRPC1 (23.23% versus 20.65% of total LF CDF variance).

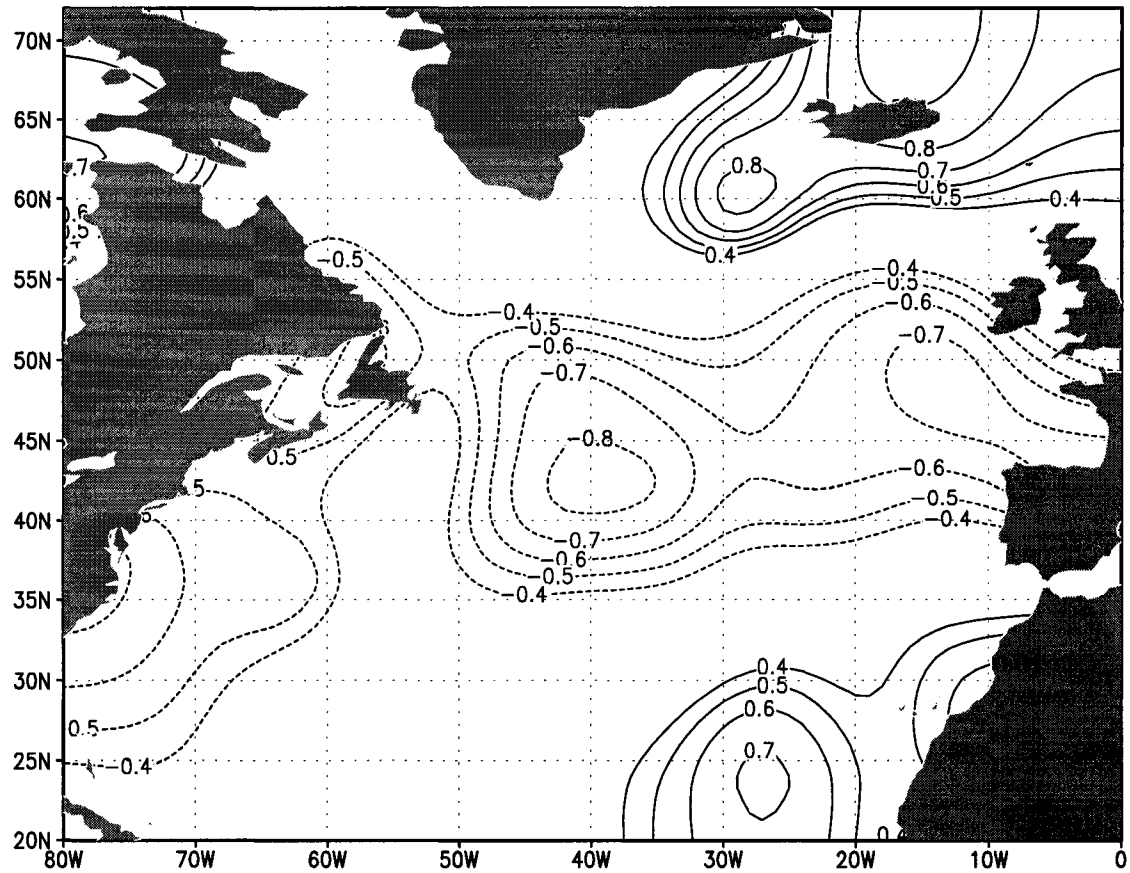


Fig. 5.2. Spatial loading pattern for the UPC1 mode of North Atlantic low-frequency winter CDF anomalies (1 value/yr; 1949-99).

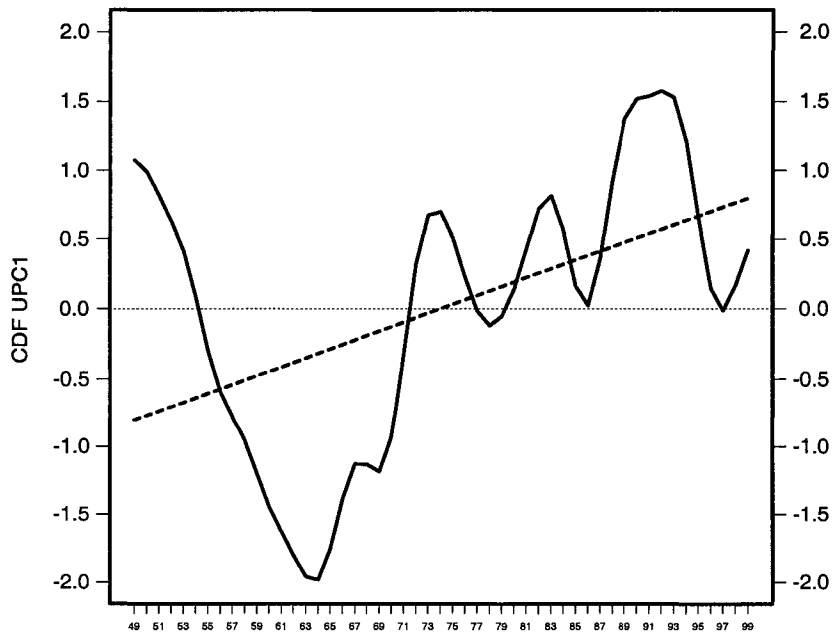


Fig. 5.3. Standardized score time series associated with the UPC1 mode of North Atlantic LF winter CDF anomalies (Fig. 5.2). Linear trend is indicated by broken line (least-squares regression line). The year (minus 1900) is labeled on the horizontal axis.

The UPC1 score time series in Fig. 5.3 displays pronounced low-frequency, decadal-scale variability, with a statistically significant (99.95%) upward trend of 1.62 std devs/51 yrs indicated by least-squares regression line. The trend is dominant after mid-1960s, before which it was preceded by a sharp downtrend. Further, examining the UPC1 score time series, we can identify a clear transition during the early 1970s, from an earlier period beginning in the early 1950s (with negative scores) when the main cyclone track was generally zonal across the central North Atlantic Basin, to the more recent era (with mainly positive scores) when the main cyclone track had a pronounced northeastward orientation, resulting in above-normal cyclone activity southeast of Greenland and over the Greenland Sea. The transition occurred in 1971/72, consistent with a singularity in time (January 1973) that was revealed by the Matching Pursuit Transform wavelet technique applied to the CDF VRPC1 scores (Fig. 4.5). Chang and Fu (2002), who examined upper-tropospheric eddy variance/covariance statistics over the Northern Hemisphere using NCEP/NCAR Reanalysis data (DJF, 1948/49-1998/99), also found a transition during the early 1970s from a weak storm track state prior to 1972/73 to a strong storm track state subsequently. They have chosen to denote storm track intensity primarily using high-pass-filtered 300-hPa meridional velocity variance. The leading EOF of their "proxy" variable corresponds to the simultaneous strengthening/weakening of both the Pacific and Atlantic storm tracks. They showed that the upper-tropospheric eddy activity has increased significantly – by up to 40% or more close to the cyclone track peaks, as noted in a subsequent paper (Chang and Fu 2003).

To highlight this 1971/72 transition in the LF CDF UPC1 functioning, Fig. 5.4 presents the LF winter CDF difference field between semesters with the highest and lowest average UPC1 score values. These periods compared were determined from the

UPC1 score time series (Fig. 5.3), and comprised the 10-year periods, when the 10-year average UPC1 scores were highest (1987-96), and lowest (1959-68). The difference pattern in Fig. 5.4 is very similar to the UPC1 loading pattern (Fig. 5.2), with an absolute maximum (minimum) over the Greenland Sea (central North Atlantic), which suggests that during 1987-96, the main cyclone track was shifted markedly northeast relative to its time-mean position during the 1960s. Further, the aforementioned secondary extremum off Northwest Africa (Fig. 5.2) also is replicated in the above UPC1-based CDF difference field, which indicates a statistically significant increase in the decadal cyclone activity off Northwest Africa and south of the Atlas Mountains (not shown). Further, there is a significant resemblance between the UPC1-based difference field (Fig. 5.4) and the linear trend in LF winter CDF anomalies over the entire 51-yr period, 1949-99 (Fig. 5.5), despite UPC1 explaining only 23.23% of total LF CDF variance. The trend in LF CDF anomalies is maximized southeast of Iceland and northeast of Scotland, whereas its minimum occurs over the central North Atlantic. These pronounced NAO-related signatures in the LF winter cyclone track variations will be further examined in Subsection 5.3.3. Further, Fig. 5.5 indicates a statistically significant upward trend in cyclone activity south of the Atlas Mountains at decadal time-scale, due in part to possible increase in the intrusion of tropical disturbances from the south into the North Atlantic Basin. In the interim, because the interdecadal variability of North Atlantic winter cyclone tracks is so well captured by the leading mode of LF winter CDF anomalies, this UPC1 mode will be used in next sections to examine the relationship between variations in LF cyclone tracks and LF (seasonal mean) atmospheric and oceanic circulation anomalies.

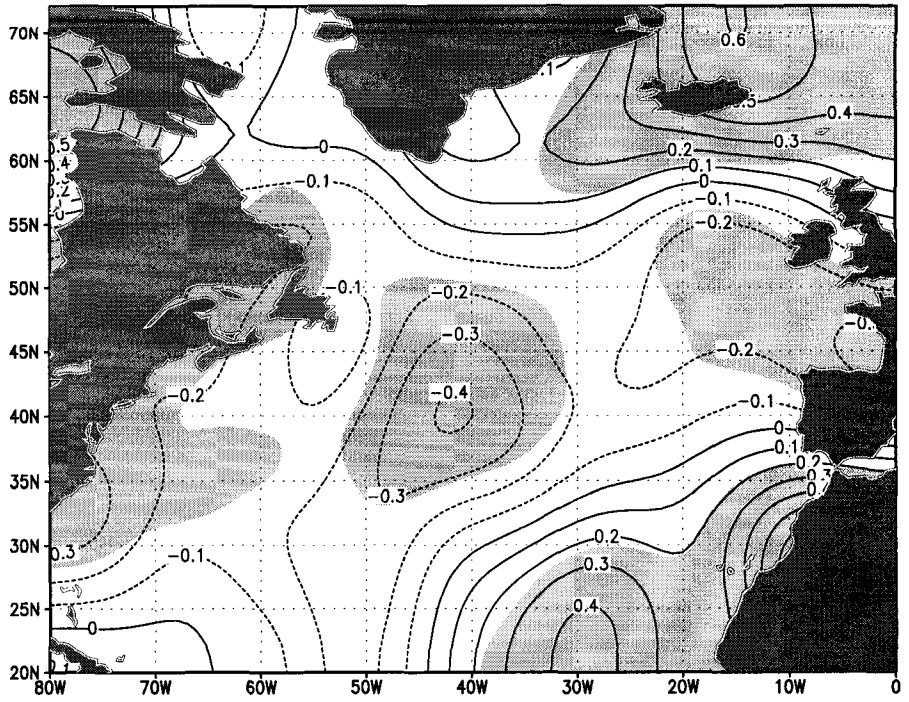


Fig. 5.4. The LF winter CDF difference field between the 10-yr periods when the 10-yr average UPC1 score was highest (1987-96), and lowest (1959-68). The CDF UPC1 score time series is depicted in Fig. 5.3. Light shading covers areas where composite differences are statistically significant at the 99% level, according to a local two-sided Student's t-test assuming the high and low population variances are unequal.

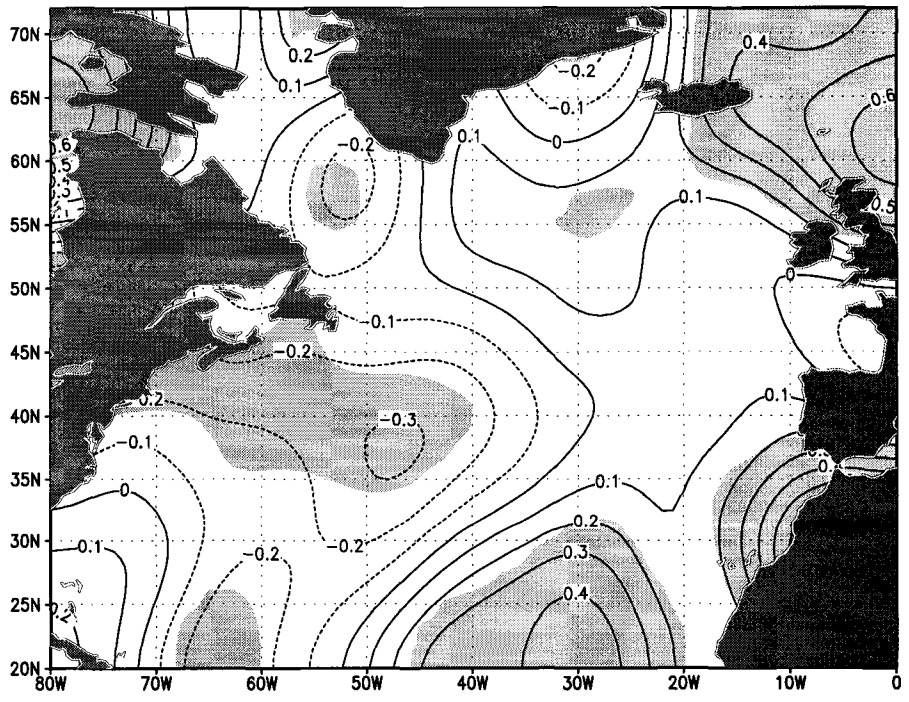


Fig. 5.5. Spatial distribution of time rate of change in North Atlantic LF winter CDF anomalies over the 51-yr period, 1949-99 (in units of std devs/51 yrs). Light shading represents areas where the linear trend is statistically significant at the 99% confidence level according to a local two-sided Student's t-test.

5.3.2 Relationship of LF CDF Behavior to LF Atmospheric/Oceanic Anomalies

The purpose of this subsection is to examine how the low-frequency winter cyclone track variations are related to low-frequency winter atmospheric and oceanic circulation anomalies. This was achieved via spatial regression analysis, in which grid cell values of various atmospheric and oceanic anomaly fields were regressed (as dependent variables) onto the CDF UPC1 score time series (depicted in Fig. 5.3). The resulting fields of regression slope coefficients then were isoplethed to yield spatial patterns, some of which are shown in Fig. 5.6. Hence, each panel in this figure gives the expected departure from the field mean (zero, since anomaly fields are considered) given a unit departure in UPC1. Usually, this regression technique is sensitive to the dimensions of the input variables; but it is not in this case since were are dealing with dimensionless variables. For statistical significance purposes, each panel indicates the areas over which the temporal correlation between the UPC1 score time series and the corresponding grid-cell anomaly field exceeds 0.5. Only areas with such statistical significance are considered here. Note that the spatial regression patterns of the fields shown in Fig. 5.6 bear some resemblance to their respective high-minus-low composite differences based upon the CDF VRPC1 mode (interannual time-scale) (Figs. 4.9-12; panels a and d).

Fig. 5.6a displays the spatial regression pattern for SLP, used here as background field. To see how well the LF SLP anomalies relate to the LF CDF variations, the spatial regression pattern shown in Fig 5.6a was projected back onto the original observed LF winter SLP anomalies. The resulting time series for SLP, shown in Fig. 5.7 (top right panel), was then correlated with the CDF UPC1 time series (reproduced in Fig. 5.7, top left panel, for comparison purposes). The correlation coefficient (r) is +0.79 for SLP,

indicating that the cyclone track pattern depicted in Fig. 5.2 and the SLP pattern shown in Fig. 5.6a do vary together closely. In comparison, the variations of the other variables shown in Fig. 5.7 are even more tightly connected to the LF cyclone track variations, with r exceeding +0.85 in all cases. All of the time series shown in Fig. 5.7 reveal very similar low-frequency variability to UPC1 scores, with the values being mainly positive during the late 1980s and 1990s, and negative during the late 1950s, 1960s, and early 1970s.

Further, the regression patterns for all the variables (Fig. 5.6a-f) are physically consistent with each other. The same physical considerations as described fully in Subsection 4.4.5 can be used here to interpret the regression patterns. The SLP pattern (Fig. 5.6a) – which reflects a strong positive NAO environment – and that of surface wind vector (not shown) are found to be consistent geostrophically. The 500-hPa geopotential height and SLP patterns show a strong barotropic component. The precipitation rate is maximized (minimized) mainly in the high-latitudes (midlatitudes). The patterns for surface air temperature and heat fluxes bear strong resemblance. The SST pattern in Fig. 5.6d will be discussed further in next subsection. The key result of this subsection is that the North Atlantic LF winter cyclone track variations and their associated seasonal mean atmospheric and oceanic circulation anomalies are highly correlated, with the explained variance (r^2) varying from 62% for SLP to 86% for precipitation rate. Next section examines relationship of LF winter CDF anomalies to other modes of decadal variability (i.e., NAO, SOI).

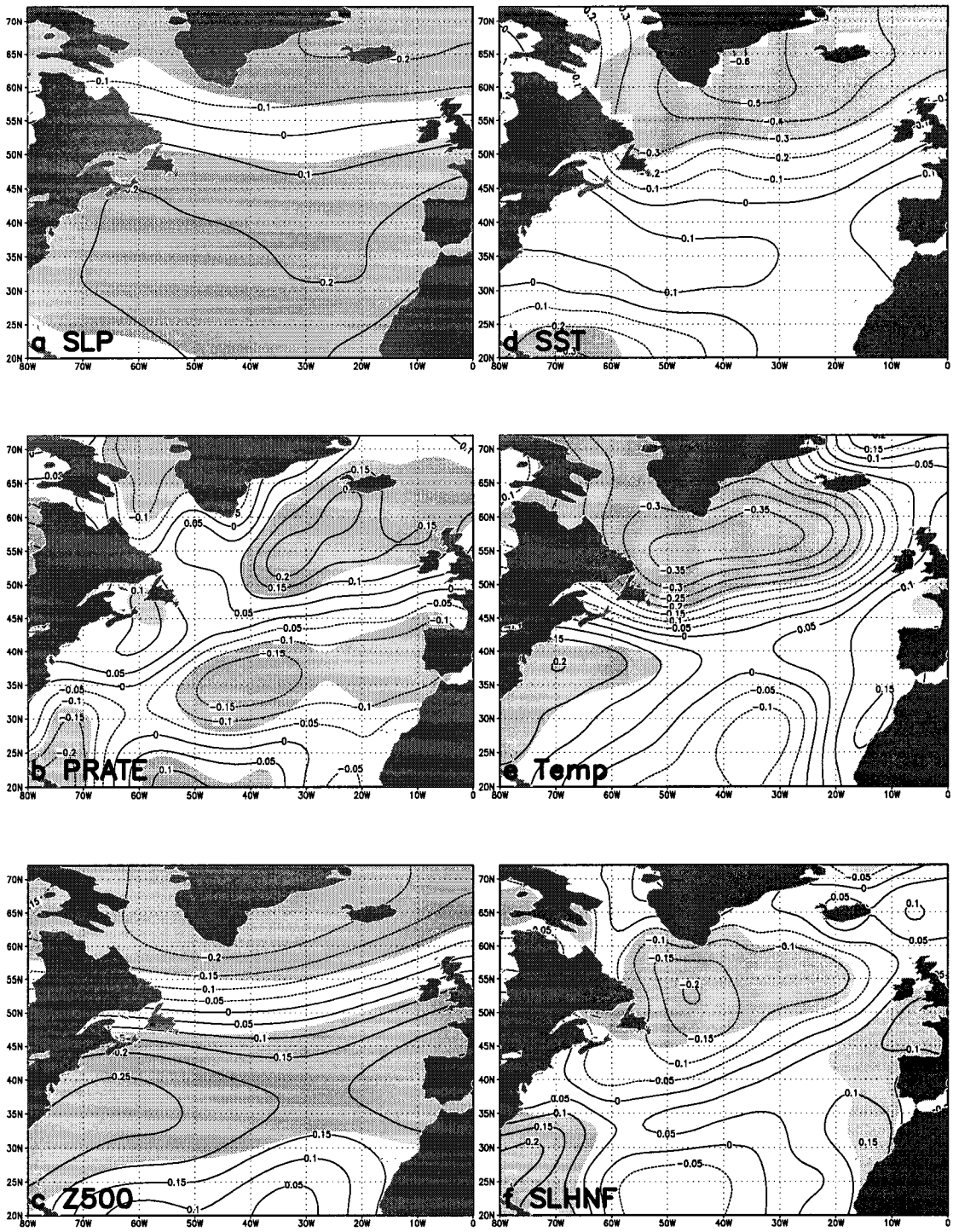


Fig. 5.6. Spatial regression patterns of North Atlantic low-frequency winter fields of atmospheric/oceanic anomalies on the CDF UPC1 score time series depicted in Fig. 5.3: (a) SLP; (b) precipitation rate (PRATE); (c) 500-hPa geopotential height (Z500); (d) SST; (e) surface air temperature (Temp); and (f) sensible plus latent heat net fluxes (SLHNF). All the variables are dimensionless. Shading indicates areas over which the temporal correlation of the UPC1 scores with the respective fields exceeds 0.5.

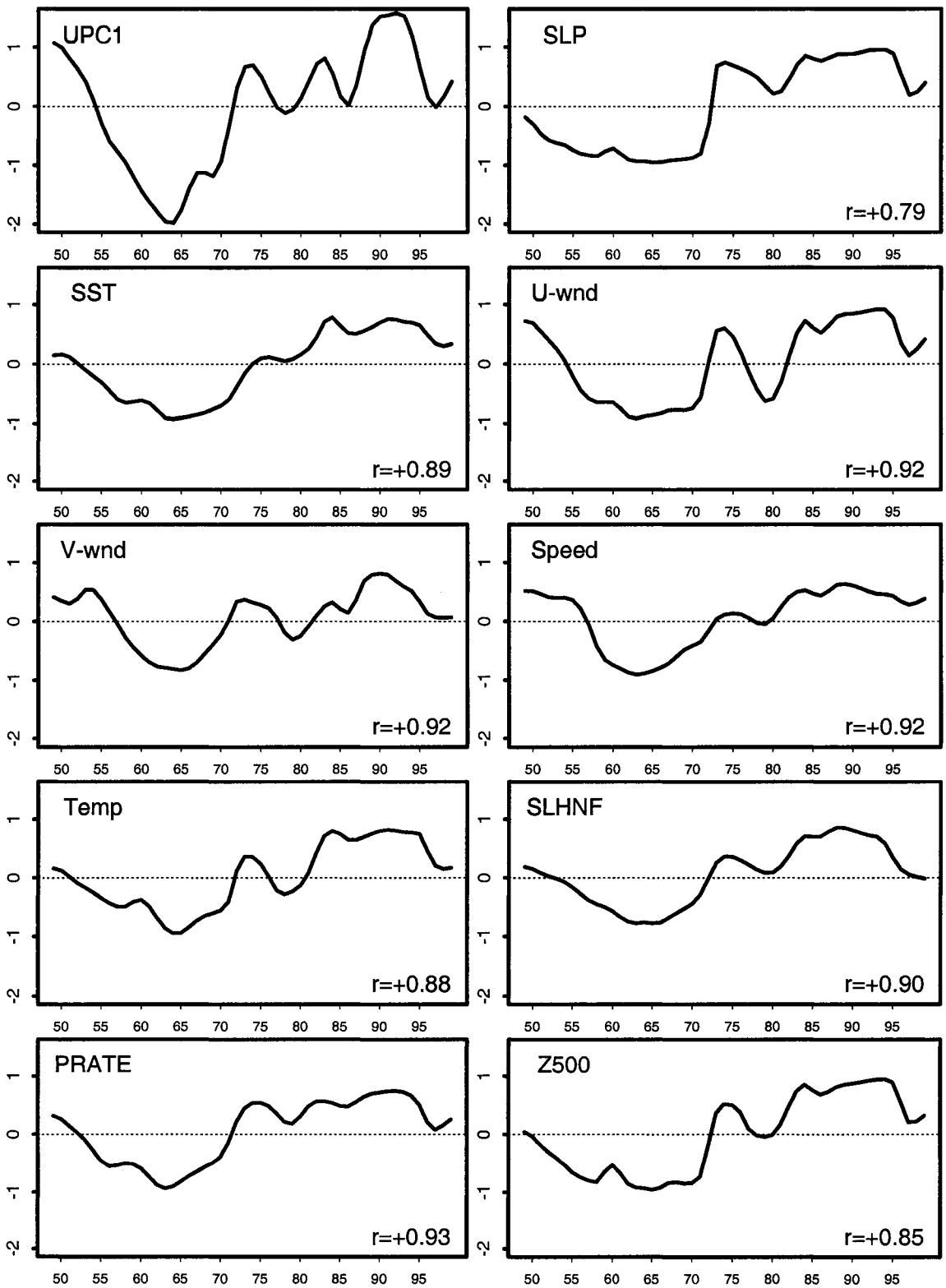


Fig. 5.7. LF CDF UPC1 (top left panel reproduced from Fig. 5.3) and time series obtained by projecting the spatial regression patterns shown in Fig. 5.6 onto their respective seasonal mean anomalies. Note the addition of three time series for the surface zonal wind (U-wind), surface meridional wind (V-wind), and wind speed (Speed). For each individual field, r denotes the temporal correlation between the UPC1 scores and the respective time series.

5.3.3 Removal of Linear Dependence of LF CDF on NAO/SOI

In Figs. 5.3 and Fig. 5.7, we saw that the leading UPC of North Atlantic low-frequency winter cyclone track variability displays a sharp transition during the early 1970s from negative to positive values, and is dominated by a statistically significant upward trend since the early 1960s. Several teleconnection modes of LF variability in the atmosphere and the coupled ocean-atmosphere system reported in the literature also show a trend or transition during the 1970s (or both), such as the NAO (e.g., Hurrell et al. 2003) and the ENSO-like interdecadal variability (Zhang et al. 1997; Chang and Fu 2002) that is significantly correlated with the Pacific Decadal Oscillation (PDO; Chang and Fu 2002).

Thus, it is of interest to examine whether the decadal-scale cyclone track variations in Fig. 5.7 are related to one or a combination of these two teleconnection modes. Several NAO and SO indices were used in this analysis because they relate to relatively well-understood circulation anomalies. In this regard, Trenberth and Stepaniak (2001) suggested that an optimal characterization of both the distinct character and the evolution of each El Niño or La Niña event requires at least two indices: (1) SST anomalies in the Niño-3.4 region (referred to as N3.4); and (2) a new index termed the Trans-Niño-Index (TNI), which is defined as the difference in normalized SST anomalies between the Niño-1+2 and Niño-4 regions. The N3.4 index can be thought of as the mean SST throughout the equatorial Pacific east of the date line and the TNI index is the SST gradient across the same region. For the NAO, the three indices listed in Section 5.2 are used here. All seven time series are plotted in Fig. 5.8, with the UPC1 score time series again reproduced in this figure for comparison purposes. The negative sign adopted for both SOI and TNI is for ease of comparison, since both indices correlate negatively with N3.4.

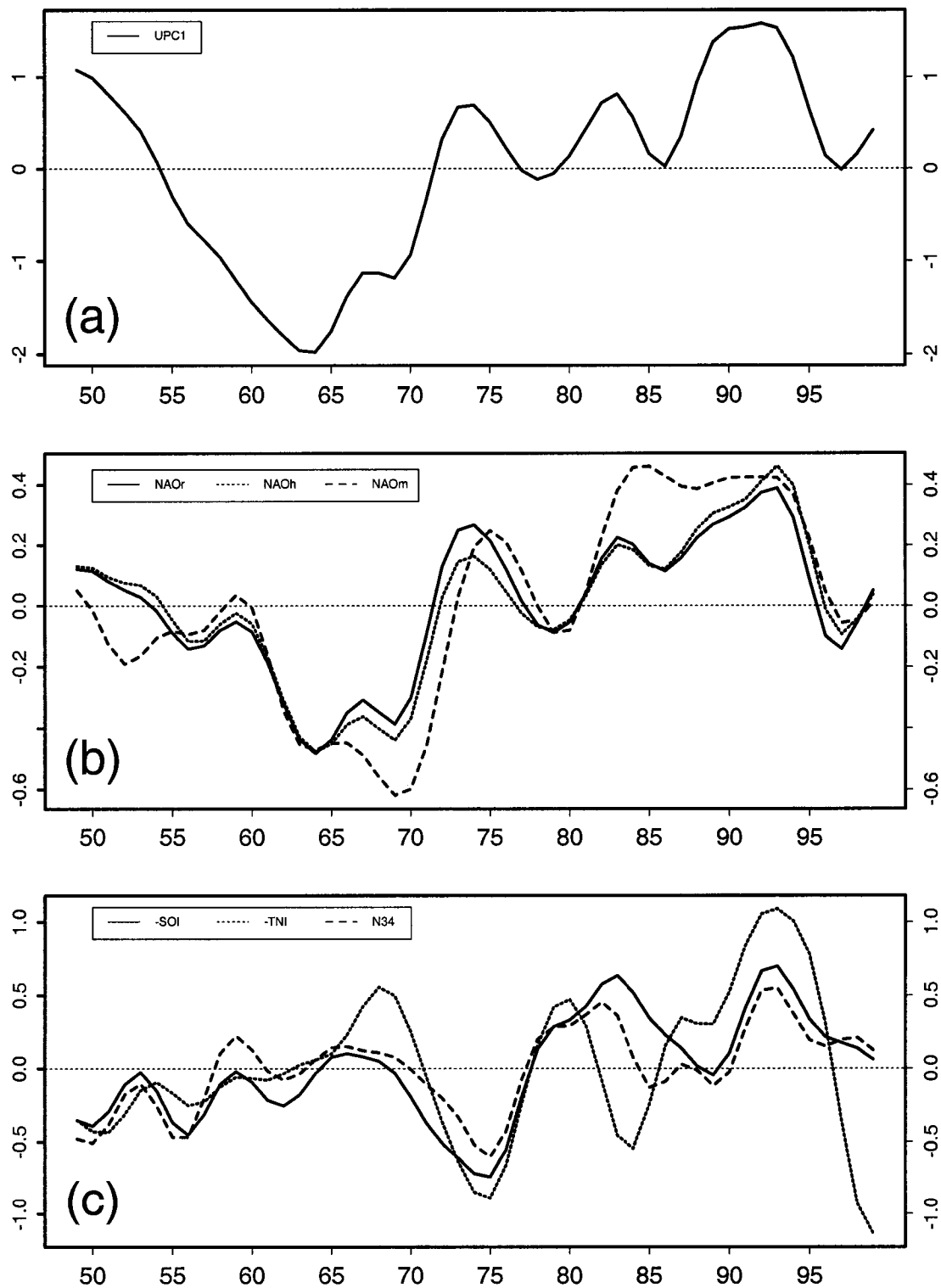


Fig. 5.8. Time series of low-frequency winter: (a) CDF UPC1 scores (as in Fig. 5.3); (b) NAO indices due to Rogers (1984, NAO_r), Hurrell (1995a, NAO_h), and Portis et al. (2001, NAO_m); and (c) ENSO indices (negative of SOI, negative of TNI, and N34). See Section 5.2 for details of Lanczos filtering involved.

In Fig. 5.8, the UPC1 is highly correlated with NAO, with r^2 (variance) equaling 85%, 84%, and 57% for NAO_r, NAO_h, and NAO_m, respectively. However, UPC1 is linked to the SOI only very weakly (r^2=7%), and is completely unrelated to the TNI and N3.4 (r^2=1% and 0%, respectively). Therefore, much (little) of the LF winter cyclone track variability is associated with LF winter NAO (SOI) anomalies.

To examine how much of the LF cyclone track variability is *unrelated* to these NAO and SO modes, further analysis was performed. The most important application of linear regression has been to remove the linear influence of an index from gridded time series. Some examples of previous applications of such approach are Jones (1994), Hurrell (1996), and Chang and Fu (2002). Following Chang and Fu (2002), first, the LF winter CDF anomalies were regressed onto both the HF and LF components of the SOI separately (where HF SOI=original SOI minus LF SOI). This approach was prompted by Zhang et al.'s (1997) suggestion that there may be two distinct modes of variability associated with SST variations in the tropical Pacific: a higher-frequency mode (interannual time-scale ENSO cycle) and a lower-frequency mode (ENSO-like interdecadal variability). They showed that the ENSO-like interdecadal variability can be retrieved simply by low-pass filtering of the SOI time series. Chang and Fu (2002) similarly defined this ENSO-like interdecadal mode by applying a 5-yr running mean to the interannual time series (51 winters from DJF of 1948/49-1998/99; 1 value/yr). In the present analysis, the LF SOI time series was defined as described in Section 5.2.

The above regression assumed that the HF and LF components of the SOI could be physically distinct (Zhang et al. 1997; Chang and Fu 2002 and references therein).

Also, the HF SOI and LF SOI are not significantly correlated, with r^2 equaling only 3%. In the next step of the analysis, the part of LF CDF anomalies that is linearly dependent upon the HF SOI and LF SOI was removed from the original LF winter CDF anomalies. The above decomposition of the SOI signal into HF and LF components, before removing the linear effect due to SOI, reduced the LF variability in the final residual data. These residual CDF data were then linearly regressed onto the NAO_r index, and the part that is linearly dependent upon the NAO_r was removed. NAO_r was chosen among the other NAO indices because of its highest correlation with UPC1 scores. In general, regression analysis is sensitive to the order of removal of a signal before another one from the input gridded anomalies. However, in this case, although the SOI signal was removed before the NAO_r signal, the order of operation is not important since; (1) currently it is not exactly clear what are the physical mechanisms that cause the LF variations and trends in the NAO and SOI and so they are treated as distinct mechanisms; and (2) these two signals show no statistical relationship (r^2=0.7%). Unlike the SOI, the NAO was not decomposed into HF and LF components, since at the present time there is no reason to believe that the dynamics of the NAO is different between the two different time-scales (Chang and Fu 2002).

Lastly, a PCA was performed on the final residual CDF data (referred to as CDF_b). The UPC1 (Fig. 5.2) counterpart obtained from this analysis (denoted UPC_b) is shown in Fig. 5.9. UPC_b accounts for 18.66% of total residual variance. Its associated score time series is depicted in Fig. 5.10. The northern center of action in the new loading pattern in Fig. 5.9 is somewhat weaker than its counterpart in Fig. 5.2, which is due to the removal of the NAO signal. The southern node also is weaker off the U.S. East Coast; this probably is due to the removal of the SOI signal (see Fig. 4.14a for a justification;

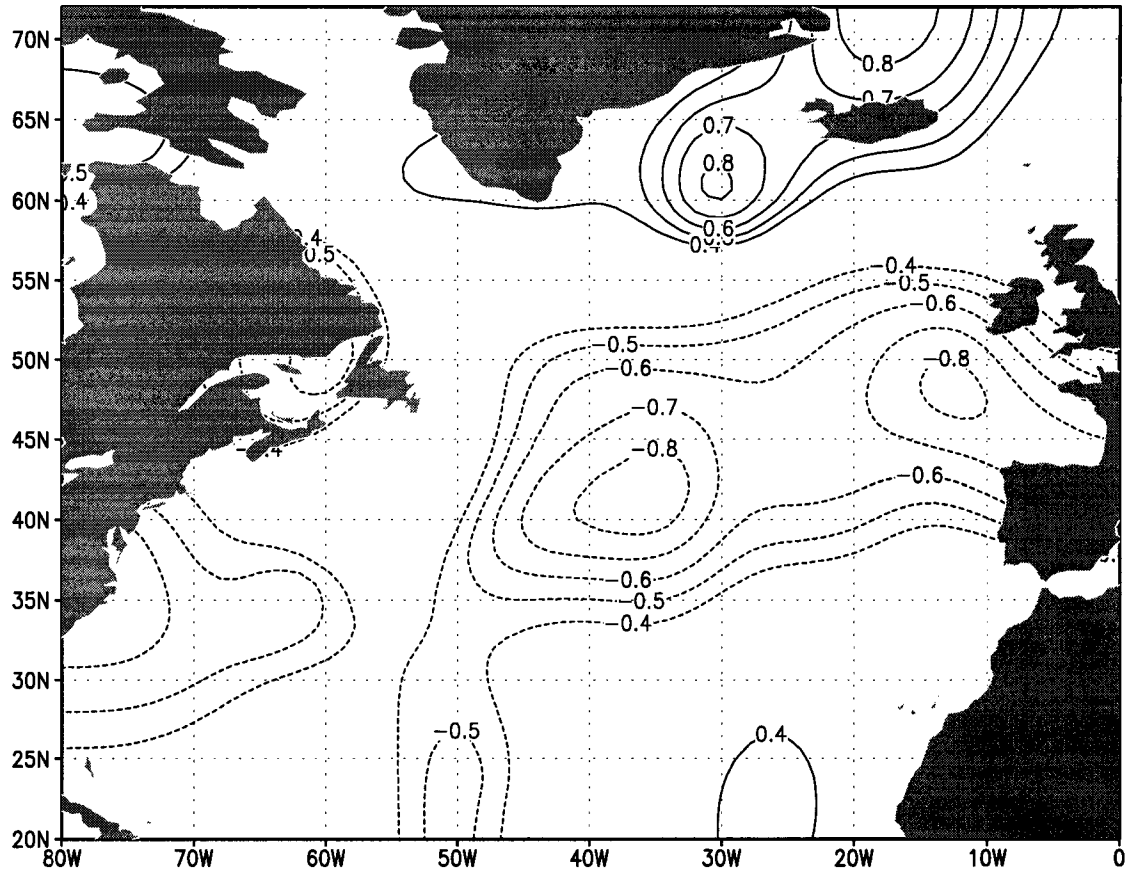


Fig. 5.9. Same as Fig. 5.2, except that PCA is performed after removal of the part linearly dependent upon the NAO and SOI signals from the North Atlantic LF winter CDF anomalies.

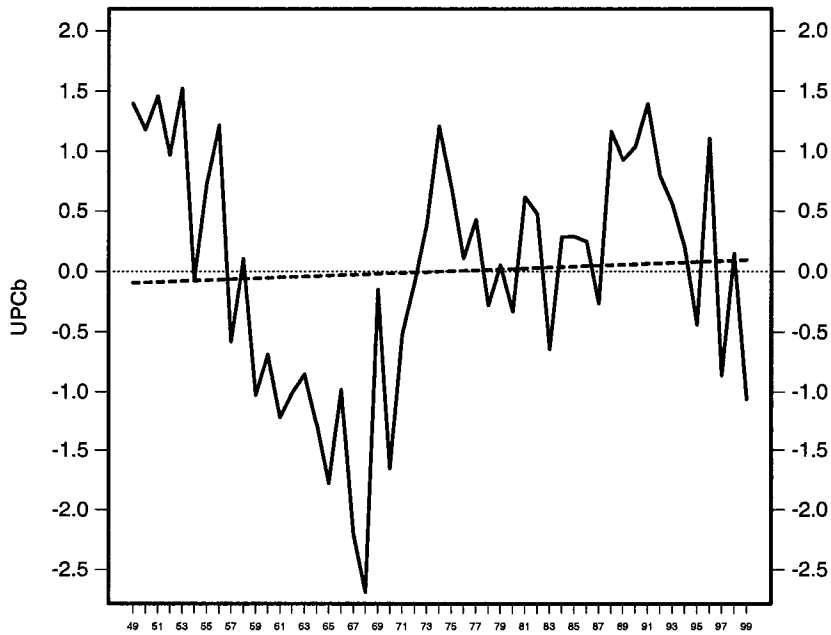


Fig. 5.10. Standardized score time series associated with the above spatial loading pattern (UPC_b). Linear trend is indicated by broken line (least-squares regression line). The year (minus 1900) is labeled on the horizontal axis.

the respective pattern at decadal time-scale, which is similar to that in Fig. 4.14a, is not shown). The most significant change in the loading pattern is the near disappearance of the third extremum in the southeast of the study domain, discussed in Subsection 5.3.1. The linear effect due to the NAO (SOI) signal alone was removed from the original LF winter CDF anomalies. The results reveal that most of the feature associated with that third extremum in the southeast of the study domain is due to the ENSO, although some of it is linked to the NAO pattern (plots not shown).

The UPC_b score time series clearly reveals that, even after the removal of the linear effect due to both the NAO and SOI signals, there is still substantial interdecadal variability in the CDF data. The residual cyclone track generally was zonal across the central part of the basin during the late 1950s and 1960s, and with a northeastward orientation afterward in the mid-1970s and late 1980s-early 1990s.

Further, the statistically significant upward trend in the UPC1 score time series (Fig. 5.3) is not a feature of the UPC_b scores (Fig. 5.10). The trend in UPC_b over the entire time period is only 0.19 std devs/51 yrs at a 30.3% significance level. This lack of significant upward trend in UPC_b is mainly due to the removal of the NAO signal since (1) the NAO index exhibits a considerable decadal variability that appears to be amplifying with time. In a record extending back to 1865, the NAO index evolved to its most persistent and extreme negative state in the 1960s, and thereafter to an equally extreme positive state in the late 1980s-early 1990s (Hurrell 1995a, updated by Dickson et al. 2000); (2) the UPC1 scores and the NAO are closely related, with (as mentioned above) r^2 equaling 85%, 84%, and 57% for NAO_r, NAO_h, and NAO_m, respectively; (3) the interdecadal variability of North Atlantic winter cyclone tracks is so well captured by

the LF CDF UPC1 mode (key result of Subsection 5.3.1); and (4) the trend in LF winter CDF anomalies reveals significant NAO-related signature (Fig. 5.5).

Fig. 5.11 presents the UPC_b-based regression patterns of the same atmospheric and oceanic circulation anomalies depicted in Fig. 5.6. These spatial patterns also were projected back onto their respective original data; the resulting time series are plotted in Fig. 5.12, which includes the corresponding correlations between UPC_b and the other time series presented. Comparison of Fig. 5.11 against Fig. 5.6 indicates a significant reduction in both nodes of the SLP dipole, resulting in a relatively weaker correlation r equaling +0.52 (Fig. 5.12) versus +0.79 (Fig. 5.7) in the first case. Thus, with the NAO and SOI removed, the LF SLP variations are not as tightly connected to the LF CDF variations. This change in the SLP pattern is mainly associated with the removal of the NAO signal (since obviously NAO is derived from SLP data), though some change in the SLP pattern can be attributable to SOI off the U.S. East Coast (see Fig. 4.14b for justification). It is reflected further in diminished correlations for both the zonal (r=+0.71 versus +0.92; Fig. 5.12 versus Fig. 5.7) and meridional (r=+0.80 versus +0.92) components of the surface wind vector, as well as for the wind speed (r=+0.78 versus +0.92). The 500-hPa geopotential height and SLP patterns show a strong barotropic component both before and after the removal of the NAO and SOI signals, with a decline in r from +0.85 to +0.62 for Z500. The precipitation rate pattern (in both cases) is consistent with the respective SLP pattern, with r decreasing from +0.93 to +0.75. Accompanying the reduction in the SLP pattern is the weakening of the dipole structure in both surface air temperature and sensible plus latent heat net fluxes, with r dropping from +0.88 and +0.90 to +0.75 and +0.76, respectively. Fig 5.6 and Fig. 5.11 suggest that the UPC1 and UPC_b patterns are effective in modulating the turbulent surface heat

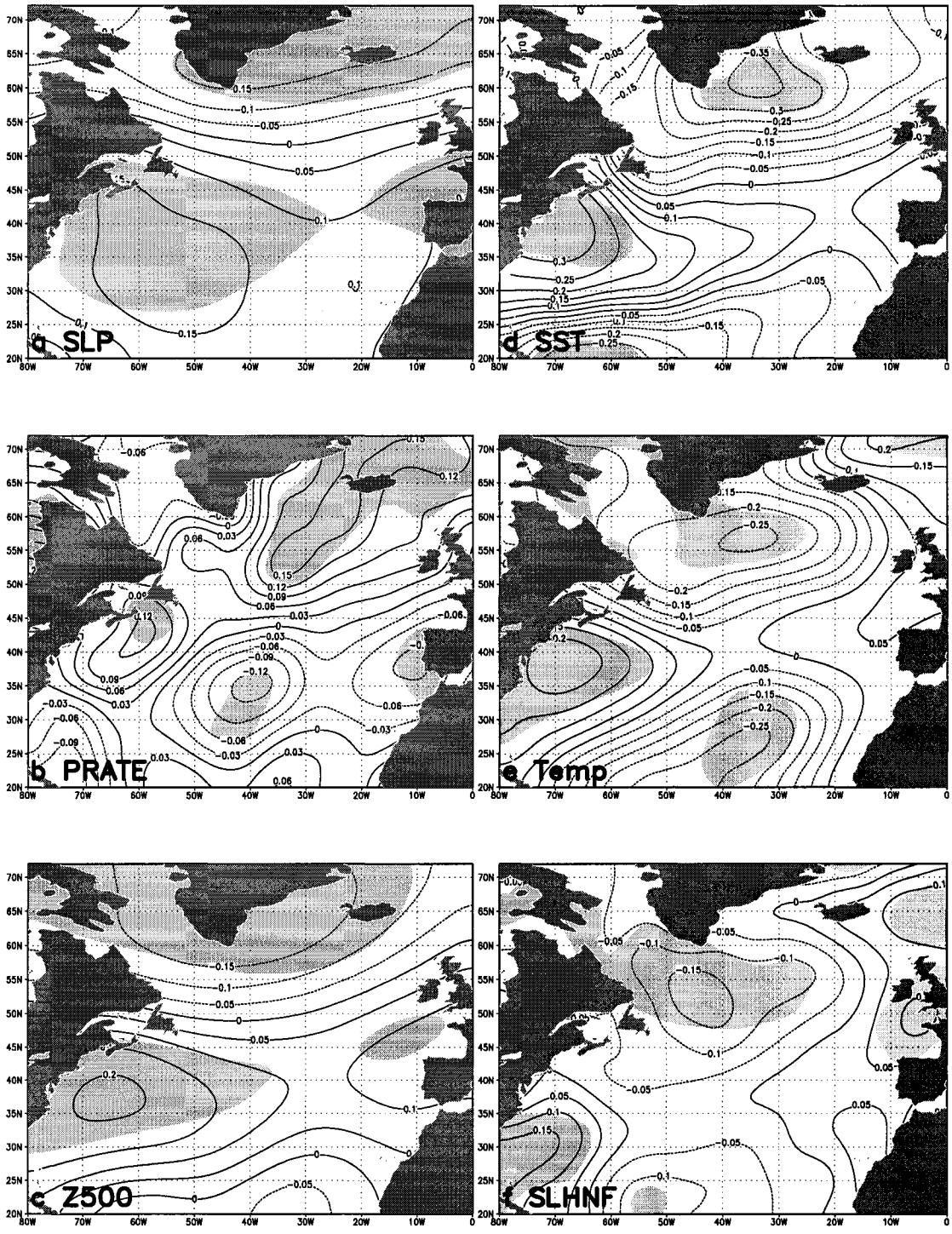


Fig. 5.11. Same as Fig. 5.6, except that the NAO and SOI signals have been removed from the original LF winter CDF anomalies.

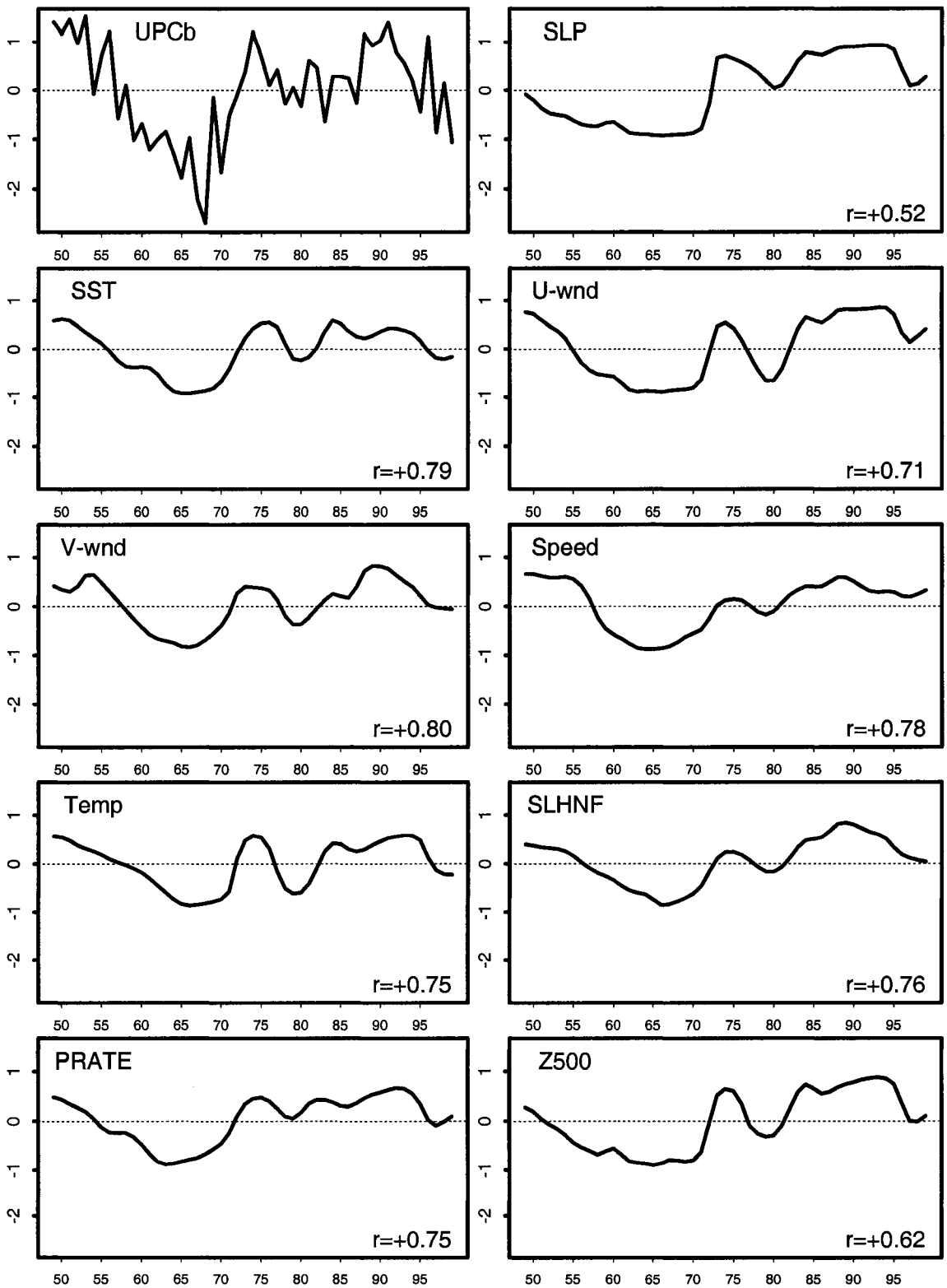


Fig. 5.12. Same as Fig. 5.7, except that the linear effects of the NAO and SOI have been removed.

fluxes and wind-driven vertical mixing and entrainment, through their influence upon surface wind speed (plots not shown). The most significant change in the SST pattern is the substantial decrease of the negative SST anomalies southeast of Greenland, and this change again is primarily associated with the removal of the NAO signal, with r falling from +0.89 to +0.79, since LF SST is closely related to SOI off the U.S. East Coast at decadal-scale (plot not shown, or see Fig. 4.14c for justification). The remaining SST anomaly signal is probably consistent with the SST being forced by the associated surface circulation (Fig. 5.11a). It is worth noting that, despite the weakening of the signals in the residual anomalies of atmospheric and oceanic fields (Fig. 5.11a-f), all of the associated time series clearly exhibit very similar low-frequency variability to UPC_b (Fig. 5.12).

Recall that in order to assess whether most of the North Atlantic low-frequency winter cyclone track variability can be explained by the NAO and the ENSO-like interdecadal mode, the part that is linearly dependent upon these two indices was removed above from the original CDF data. However, Fig. 5.12 shows that even after the removal of the NAO and SOI, the residual data still exhibit significant interdecadal variability in cyclone track activity and related atmospheric and oceanic anomalies. This suggests that much of the cyclone track variations are not linearly related to either the NAO or tropical SST anomalies. Therefore, it should be recognized (1) that the residual anomalies in the patterns associated with UPC_b (Fig. 5.11) probably reflect the exclusion of other teleconnection modes/indices (besides NAO and ENSO; discussed below) that may affect patterns of interdecadal cyclone track variability in the North Atlantic; and (2) that linear regression techniques do not account for feedback (nonlinear) effects. In particular, the atmosphere and the ocean may undergo a coupled interaction at decadal-to-multidecadal

time-scales, that was not identified by the above linear regression analysis. This important question is explored in next section.

Any other causes of the North Atlantic LF winter surface cyclone track variations? One source may the Tropics. Rajagopalan et al. (1998) hypothesized that tropical Atlantic ocean-atmosphere interaction is affecting North Atlantic climate variability. They found strong broad-band coherence between the NAO and the tropical Atlantic cross-intertropical convergence zone (ITCZ) SST difference in the 8-20 yr period band, suggesting a significant tropical-midlatitude interaction. Dima et al. (2001) used observational data to identify a 5- to 7-yr lag between the main modes of variability in the midlatitudes and in the tropics. They proposed a mechanism for quasi-decadal variability based on tropics-midlatitudes and ocean-atmosphere interaction. The memory of the coupled mode likely resides in the ocean. Other studies (e.g., Tourre et al. 1999) also pointed to a strong tropical-extratropical connection at decadal time-scales. They argued that a tropical SST dipole pattern is one of the characteristics of the quasi-decadal signal. Note that other external forcings (e.g., stratospheric and other anthropogenic processes) may also play a role, as was discussed in the introduction (Section 5.1). Very recently, Magnusdottir et al. (2004) addressed the question of whether the observed multidecadal trends in extratropical atmospheric flow (e.g., positive trend in the NAO) may be caused by observed trends in oceanic boundary forcing (SST and sea ice anomalies confined to the North Atlantic sector). They found that the wintertime response to both types of forcing resembles the NAO to first order. Therefore, regardless of the causes for the LF cyclone track variations and trends, the present analysis has provided evidence that, even after the removal of the NAO and SOI signals, the amplitudes of the North Atlantic winter cyclone tracks and related seasonal mean

atmospheric and oceanic circulation anomalies have undergone significant interdecadal variability during the last half century. Hence, this suggests that these substantial interdecadal variations that still remain (Fig. 5.12) are caused by other factors, as discussed above. However, this does not exclude feedback (nonlinear) effects in connection with the NAO and ENSO.

5.4 OCEAN-ATMOSPHERE INTERACTIONS

5.4.1 Literature Review

Low-frequency ocean-atmosphere interactions in the North Atlantic Basin recently have been the focus of considerable inquiry. Summaries of the most often cited studies dealing with such interactions are presented below, mainly in chronological order. The purpose of this review is to show that the leading modes from these various studies do not agree on the exact periodicities, amplitudes, or physical mechanisms involved. This will reveal that this topic indeed still is an actively debated question. Therefore, this stresses the need to carry out a new analysis (Subsection 5.4.2) to attempt further clarification of the role of the ocean in the North Atlantic decadal climate variability, especially by invoking the new CDF data set.

• Deser and Blackmon (1993) presented evidence from observations for a quasi-decadal cycle within the North Atlantic (November-March, 1900-89). This EOF-based mode has a structure similar to the interannual variability (Fig. 4.9d), with SST anomalies of one sign east of Newfoundland and anomalies of the opposite sign further southwest off the U.S. southeast coast. This mode exhibits a significant spectral peak at ~12 yrs in the postwar period. Before 1945, the decadal fluctuations were less regular with a dominating period of ~9 yrs. These findings were essentially confirmed by Levitus et al.

(1994) and Molinari et al. (1997) who analyzed subsurface data (for the postwar period) that are much less contaminated by high-frequency noise than surface data.

• Mann and Park (1996) isolated coherent spatial-temporal modes of climate variability based on a multivariate frequency domain Singular Value Decomposition (SVD) of nearly a century of monthly Northern Hemisphere SLP and surface temperature data. They reported that a quasi-decadal (10-11 yr time-scale) largely cold-season oscillatory behavior is more closely tied to the North Atlantic. Insight into the underlying physical processes associated with potential climate signals was obtained by examining the relationship between surface temperature and inferred atmospheric circulation patterns as they evolved over a typical cycle, taking potential seasonal distinctions into account.

• Sutton and Allen (1997) used shipboard observations for 1945-89 to document spreading of SST anomalies along the paths of the Gulf Stream and North Atlantic Current (NAC). Winter (November-April) SST anomalies born in the western subtropical gyre appear to propagate northeastward with a transit time of 12-14 yrs. Subsequently, this relatively slow propagating signal along the NAC pathway was essentially seen in the Hadley Centre coupled climate model (HadCM3) with a time-scale close to that of observed anomalies (Cooper and Gordon 2001). Other observational analyses indicate the importance of advection of SST anomalies by the mean gyre currents; e.g., Watanabe et al. (1999) reported that observed and modeled decadal variations have dominant periodicities around 12.3 and 9.9 yr, respectively.

• Using extended EOF analysis, Zorita and Frankignoul (1997) identified a coupled ocean-atmosphere mode of North Atlantic decadal variability with a period of ~10 yrs in a 325-

yr integration of the ECHAM1/LSG coupled ocean-atmosphere GCM. The oceanic changes reflect the direct forcing by the atmosphere through anomalous air-sea fluxes and Ekman pumping, which after some delay affects the intensity of the subtropical and subpolar gyres. SST also was strongly modulated by the gyre currents in this long-term simulation.

• Grötzner et al. (1998) identified a decadal climate cycle in the North Atlantic with periodicity of ~17 yrs from a 125-yr integration of the ECHAM3/HOPE coupled ocean-atmosphere GCM. This decadal mode is based on unstable air-sea interactions and must therefore be regarded as an inherently coupled mode. It involves the subtropical gyre and the NAO. The memory of the coupled system, however, resides in the ocean and is related to horizontal advection and to the oceanic adjustment to low-frequency wind stress curl variations. Recent development of other coupled ocean-atmosphere GCMs has made it possible to simulate decadal cycles similar to those identified in observational data (Watanabe et al. 1999). Selten et al. (1999) used a coupled atmosphere-ocean-sea-ice model of intermediate complexity (ECBILT) to study the mechanism of a climate oscillation in the North Atlantic Basin, characterized by 16-18 yr time-scale covariability of an NAO-like atmospheric anomaly pattern and a SST dipole. This mode bears a strong resemblance to the one in the GCM described in Grötzner et al. (1998) and the observed mode in Sutton and Allen (1997).

• A coupled air-sea mode in the Northern Hemisphere with a period of ~35 yrs was identified by Timmermann et al. (1998) from a 700-yr integration of the ECHAM3/LSG coupled ocean-atmosphere GCM. The authors focused on the physics of North Atlantic interdecadal variability. The mode involves interactions of the thermohaline circulation

with the atmosphere in the North Atlantic.

• Tourre et al. (1999) analyzed historical data during 1856-1991 to identify dominant spatial-temporal patterns of joint SST and SLP variability in the Atlantic Ocean, using a multivariate frequency domain analysis. A significant frequency band was isolated at the quasi-decadal scale(~11.4 yrs). The quasi-decadal frequency, along with other frequency bands, represent to some extent fluctuations of the NAO and are associated with tropical Atlantic Ocean warming (cooling) with different spatial evolution.

• A simple analytical midlatitude atmosphere-ocean model was formulated by Goodman and Marshall (1999). The simulations produced supported coupled modes in which oceanic baroclinic Rossby waves of decadal period grow through positive coupled feedback between the thermal forcing of the atmosphere induced by SST anomalies and the resulting wind stress forcing of the ocean. Subsequently, based on a shallow-water model (spherical hemisphere), Primeau and Cessi (2001) reported a coupled oscillation with a decadal period between wind-driven currents and midlatitude storm tracks.

• Häkkinen (2000) isolated a decadal cycle (12-14 yrs) in North Atlantic SST and tide gauge data. This decadal air-sea interaction then was investigated using an ocean model simulation. The main finding is that this 12-14 yr cycle, that has potential to be a coupled mode, can be constructed based on the leading mode of the surface heat flux, which involves the thermohaline circulation.

• Finally, in their review article on North Atlantic climate variability (phenomena, impacts and mechanisms), Marshall et al. (2001) stated that on decadal time-scales (?), there may

be a mutual coupling between the two fluids. Ocean gyres and thermohaline circulation can both play a role.

5.4.2 New Lead/lag CCA-Based Procedure

Thus, the leading modes of North Atlantic decadal-to-multidecadal ocean-atmosphere interactions proposed in the above studies do not agree about the exact temporal periodicities, amplitudes, and physical mechanisms involved. The modes seem somewhat dependent on data, model, or technique used. This situation motivated the application of a new CCA-based procedure in this subsection to investigate further whether the North Atlantic atmosphere and ocean undergo coupled interaction.

CCA is a multivariate statistical technique that explores the linear relationships between two sets of space-time-dependent variables (e.g., SST and SLP). Basically, CCA decomposes the original data into pairs of spatial patterns (CCA modes) in such a way that their time series are optimally correlated (e.g., Barnett and Preisendorfer 1987; Barnston and Ropelewski 1992; Livezey and Smith 1999; and many others). A Singular Value Decomposition (SVD) analysis also can be applied to similar problems (e.g., Bretherton et al. 1992; Newman and Sardeshmukh 1995; Cherry 1996, 1997; Hu 1997; and many others). SVD is a technique designed to find covarying patterns in two different fields (e.g., SST and SLP). SVD operates on the covariance matrix between the two fields and provides pairs of spatial patterns (SVD modes) whose temporal covariance is high.

Because the possible existence of a coupled ocean-atmosphere mode in the North Atlantic has been suggested by the above previous studies, the dominant decadal coupled

covariability mode will be identified here using a new CCA-based approach applied to atmospheric and oceanic gridded anomaly fields. First, CDF and SST anomalies are used as indicators of surface atmospheric and upper-ocean variability, respectively. Then, the same procedure will be applied to the SLP and SST anomalies for comparison and verification. Before applying the lead/lag CCA-based technique, the input data were prepared in the following manner. To avoid quasi-degeneracy of the autocovariance matrices, it is highly advisable to reduce the spatial degrees of freedom prior to CCA. This can be done, for example, by projecting the original data onto their UPCs and retaining only a limited number of them that explain most of the total variance (e.g., Zorita et al. 1992). This also serves as a data filtering procedure to eliminate noise, although it can exclude potentially useful information. Therefore, PCA of all the above LF winter fields (1 value/grid-cell/yr) was performed separately to capture the spatially coherent variability; the resulting spatial fields of UPC loadings and associated score time series are not shown here. Only few UPCs of these fields were retained as input for the lead/lag CCA-based procedure (described below) – 8 CDF, 4 SLP, and 5 SST UPCs that explain 89.66%, 90.47%, and 92.31% of total variance of their low-frequency winter fields, respectively.

a. First Application: CCA of LF CDF/SST

This CCA application involved the following steps:

(1) For each of k lags (in years), where k varies from -15 to +15, and incremented by 1, the 5 UPC time series of SST scores are then lagged for the given lag (k) and used as input for CCA analysis along with the unlagged CDF score time series. A positive lag (k) corresponds to SST leading CDF, whereas a negative lag (k) corresponds to CDF leading SST. Since we are interested in the degree of coupling between the atmosphere

and ocean at various time lags, CCA analysis provides a direct and objective method for assessing the strength of the relationship between the two fluids.

(2) The above CCA procedure yields 5 canonical modes (spatial loading patterns and associated canonical time series are not shown) that represent patterns of maximum correlation between the low-frequency winter CDF and SST anomalies for the given lag (k). Only the leading CCA mode (CCA1) is retained in this study. CCA1 maximizes the temporal correlation between the expansion coefficients of the patterns in the two fields. Computing the canonical correlation coefficient (R_c) as a function of lag (k) for the CCA1 mode [$R_c(k)$] quantifies the strength of the link between the two fluids at each individual time lag, k.

(3) For the SST field, at each starting lag=k, *spatial* correlation $S_r(k)$ was computed between consecutive spatial loadings for SST at lag=k and lag=k+1. The purpose of such a computation is to ensure the continuity of a potential propagating signal in the SST anomalies (e.g., Sutton and Allen 1997). Thus, the values of the spatial correlation between the respective spatial CCA patterns for all starting lags must be positive. If, at any given lag (k), $S_r(k)$ were negative, then the sign of the CCA pattern of SST at lag=k was changed along with its associated canonical time series. This was done for some lags; then the spatial canonical patterns for the entire range of lags were plotted (not shown) in attempt to identify a propagating signal à la "Sutton and Allen"-ienne.

(4) Next, $R_c(k) * S_r^0(k) = f(k)$ was computed to yield Fig. 5.13a. Here $S_r^0(k)$ denotes the spatial correlation between the SST loadings at lag=k and lag=0. This formulation

quantifies the persistence of decadal SST anomalies over years. Concerning the physical rationale for the above formulation, it is clear that the atmosphere cannot counteract the local thermal damping because of its small heat capacity. A possible scenario that may help the persistence of SST anomalies over years has been proposed by Alexander and Deser (1995) and Alexander and Penland (1996). Using the temperature data at ocean weather stations and a one-dimensional ocean model, they showed that a temperature anomaly created in winter penetrates below the mixed layer in spring and reappears in the following winter. This process was originally put forward by Namias and Born (1970). Further, Watanabe and Kimoto (2000) showed that the temporal evolution of observed decadal anomalies in the upper-ocean temperature appears consistent with the so-called Namias-Born hypothesis. They integrated a mixed-layer model for the North Atlantic in order to extend Alexander and Deser's (1995) results to basin-scale features on the decadal time-scale. Watanabe and Kimoto (2000) suggested that this reemergence mechanism of SST anomalies associated with the seasonal cycle of the mixed layer depth helps decadal SST anomalies to persist over years against the local thermal damping in the North Atlantic Ocean. The recurrence of SST anomalies was found in two centers of the decadal anomaly pattern, one off the U.S. East Coast and the second south of Greenland.

(5) The final analysis step computed the power spectrum of the above function f(k), the result of which appears in Fig. 5.13b. This function exhibits a statistically significant spectral maximum at 10-11 years. Thus, this analysis reveals a clear quasi-decadal coupled ocean-atmosphere mode in the North Atlantic when CDF and SST are used as indicators of surface atmospheric and upper-ocean variability, respectively.

b. Second Application: CCA of LF SLP/SST

However, the same lead/lag CCA-based procedure applied to the LF winter SLP and SST anomalies (Fig. 5.14), in which SLP is used instead of CDF, reveals no clear coupled cycle in the low-frequency data.

The above findings imply that use of CDF (rather SLP) seems to support the feedback of SST to the atmosphere under the hypothetical coupled ocean-atmosphere mode. In other words, the new CDF field did "a better job" than the traditional SLP parameter in identifying a decadal coupled mode in the North Atlantic Basin. The temporal periodicity of this mode agrees with those which previous authors have associated with a hypothetical couple ocean-atmosphere mode (Subsection 5.4.1). The physics of this coupled mode can be determined via coupled ocean-atmosphere GCM modeling. Nevertheless, the potential factors that may be involved in such physics are the NAO, oceanic gyres, oceanic advection (e.g., advection of SST anomalies by the mean gyre currents), the thermohaline circulation, and others (Subsection 5.4.1).

5.5 SUMMARY AND CONCLUSIONS

Climate variability on decadal and longer time-scales is a subject of increasing interest and relevance (e.g., Deser and Blackmon 1993). The present chapter considers the LF variability of CDF at decadal-to-multidecadal time-scales. Detection of trends in climatological time series has become central to the discussion of possible climate change due to the enhanced greenhouse effect (e.g., Karoly et al. 2003; Karl and Trenberth 2003). Very few published studies (e.g., McCabe et al. 2001; Geng and Sugi 2001) have examined recent trends in cyclone activity over the Northern Hemisphere/North Atlantic Basin. Therefore, the first main component of this chapter examined the LF behavior of

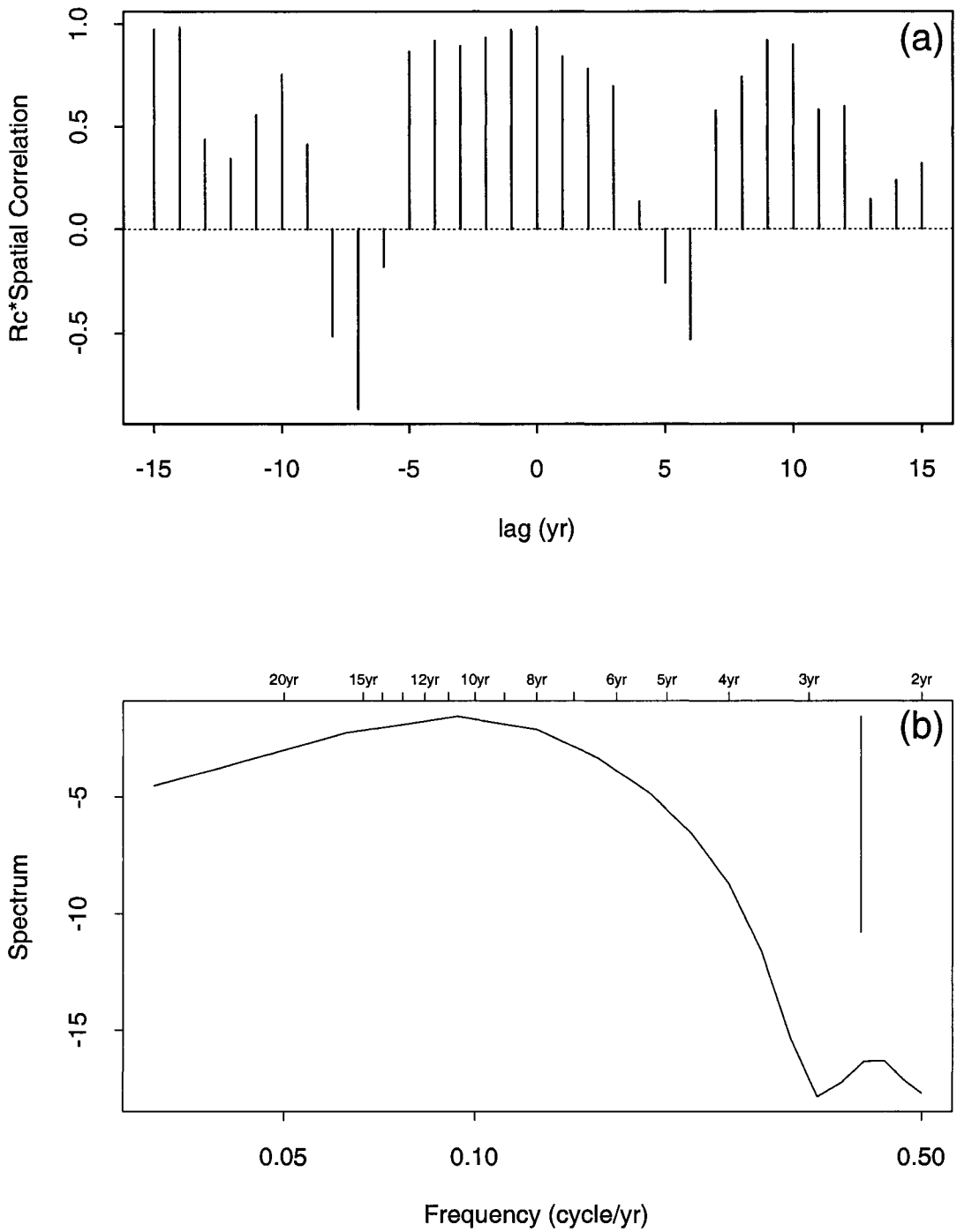


Fig. 5.13. Lead/lag Canonical Correlation Analysis (CCA) between components of dominant CDF and SST UPC modes. Panel (a) Canonical correlation, $R_c(k)$, times the spatial correlation, $S_r^0(k)$, between SST loadings at lag=k and lag=0 as a function of lag k (in years) for the first CCA mode (CCA1). (b) Power spectrum of the above function; i.e., $R_c(k)*S_r^0(k) = f(lag)$. The vertical line in the upper right corner indicates the 95% confidence interval for the spectrum (based on a chi-squared approximation).

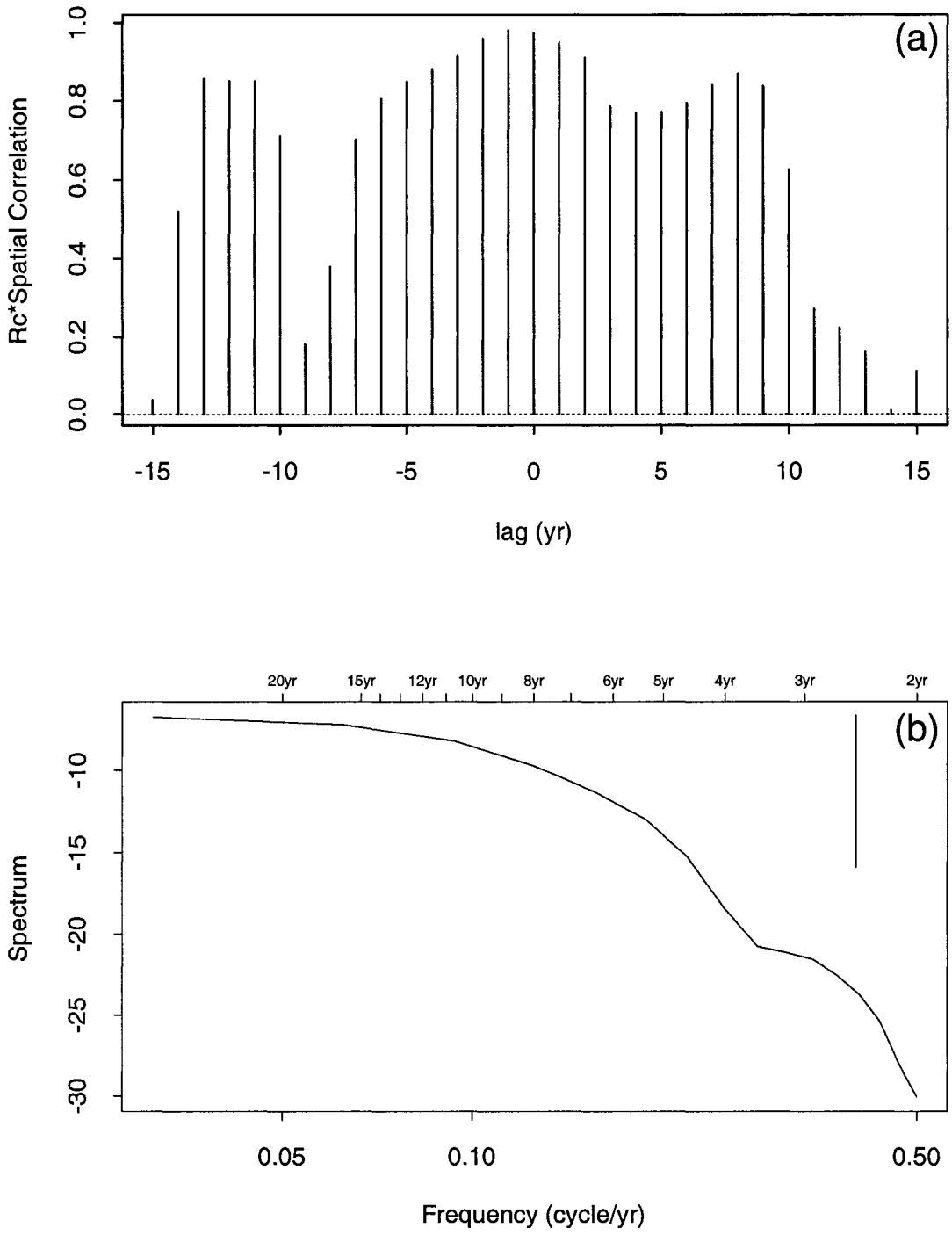


Fig. 5.14. As in Fig. 5.13 but for SST loadings derived from application of CCA between SLP (instead of CDF) and SST.

CDF (including trends) and associations with other LF atmospheric and oceanic fields/indices (NAO, ENSO).

A PCA was applied to the LF winter CDF anomaly fields. The leading UPC mode accounts for 23.23% of total LF CDF variance. The UPC1 pattern mainly is characterized by a dipole structure, with the northern center of action being maximized over the Greenland Sea, contrasting with a southern center of action that maximizes over the central North Atlantic while extending from the U.S. East Coast to Western Europe. Thus, depending upon the sign of the UPC1 score time series, the UPC1 pattern reflects either predominant northeastward-traveling cyclones across the northern basin or zonal cyclones across the central basin. The peak in the UPC1 pattern occurs downstream of the long-term climatological CDF maximum. Of particular interest is the relatively weaker third extremum off Northwest Africa, which is in phase with the northern center of action. In its positive (negative) phase, the UPC1 mode is associated with above (below)-normal cyclone activity off Northwest Africa. The above-normal storminess over this region may be due in part to the possible intrusion of tropical disturbances from the south into the North Atlantic Basin, some of which may reach the Atlas Mountains over Morocco.

The UPC1 score time series displays pronounced low-frequency, decadal-scale variability, with a statistically significant (99.95%) upward linear trend of 1.62 std devs/51 yrs. The trend is dominant after mid-1960s, before which it was preceded by a sharp downtrend. Further, a clear transition in the UPC1 scores was identified during the early 1970s, from an earlier period beginning in the early 1950s (with negative scores) when the main cyclone track was generally zonal across the central North Atlantic, to the more

recent era (with mainly positive scores) when the main cyclone track had a pronounced northeastward orientation, resulting in above-normal cyclone activity southeast of Greenland and over the Greenland Sea. The sharp transition occurred in 1971/72, consistent with the singularity in time (January 1973) revealed by the Matching Pursuit Transform wavelet technique applied to the CDF VRPC1 scores (Fig. 4.5).

To highlight this 1971/72 transition in the LF CDF UPC1 functioning, the LF winter CDF difference field between semesters with the highest and lowest average UPC1 score values was examined. The difference pattern is very similar to the UPC1 loading pattern. Further, there is a significant resemblance between the UPC1-based difference field and the linear trend in LF winter CDF anomalies over the entire 51-yr period, 1949-99, despite UPC1 explaining only 23.23% of total LF CDF variance. Therefore, the interdecadal variability of North Atlantic winter cyclone tracks is so well captured by the leading mode of LF winter CDF anomalies.

The LF winter cyclone track variations were related to LF winter atmospheric and oceanic circulation anomalies, via spatial regression analysis, in which various gridded fields were regressed onto the CDF UPC1 score time series. The resulting regression patterns bear some resemblance to their respective high-minus-low composite differences based upon the CDF VRPC1 mode (interannual time-scale, Chapter 4). The associated time series reveal very similar LF variability to UPC1 scores, with the values being mainly positive during the late 1980s and 1990s, and negative during the late 1950s, 1960s, and early 1970s. Further, the regression patterns for all the atmospheric and oceanic fields are physically consistent with each other, with the SLP pattern reflecting a strong positive NAO environment. The key result of this regression analysis is that the

North Atlantic LF winter cyclone track variations and their associated seasonal mean atmospheric and oceanic circulation anomalies are highly correlated, with the explained variance (r^2) varying from 62% for SLP to 86% for precipitation rate.

The decadal-scale cyclone track variations were related to ENSO and NAO. It was found that much (little) of the LF winter cyclone track variability is associated with LF winter NAO (SOI) anomalies. To assess whether most of the North Atlantic LF winter cyclone track variability can be explained by the NAO and the ENSO-like interdecadal mode, the part that is linearly dependent upon these two indices was removed from the original LF winter CDF anomalies. Then, a PCA was performed on the final residual CDF data. The resulting UPC_b mode accounts for 18.66% of total residual variance. The northern center of action in the UPC_b pattern is somewhat weaker than its counterpart in UPC1, which is due to the removal of the NAO signal. The southern node also is weaker off the U.S. East Coast; this probably is due to the removal of the SOI signal. The most significant change in the loading pattern is the near disappearance of the third extremum in the southeast of the study domain. The results reveal that most of this feature is due to the ENSO, although some of it is linked to the NAO.

The UPC_b score time series clearly reveals that, even after the removal of the linear effect due to both the NAO and SOI signals, there is still substantial interdecadal variability in the CDF data. The residual cyclone track generally was zonal across the central part of the basin during the late 1950s and 1960s, and with a northeastward orientation afterward in the mid-1970s and late 1980s-early 1990s. Further, the statistically significant upward trend in the UPC1 score time series is not a feature of the UPC_b scores. This lack of significant upward trend in UPC_b is mainly due to the removal

of the NAO signal.

The UPC_b-based regression patterns of the same atmospheric and oceanic circulation anomalies were examined. With the NAO and SOI removed, the LF SLP variations are not as tightly connected to the LF CDF variations. This change in the SLP pattern is mainly associated with the removal of the NAO signal, though some change in the SLP pattern can be attributable to SOI off the U.S. East Coast. The 500-hPa geopotential height and SLP patterns show a strong barotropic component both before and after the removal of the NAO and SOI signals. The precipitation rate pattern (in both cases) is consistent with the respective SLP pattern. Accompanying the reduction in the SLP pattern is the weakening of the dipole structure in both surface air temperature and sensible plus latent heat net fluxes. The results suggest that the UPC1 and UPC_b patterns are effective in modulating the turbulent surface heat fluxes and wind-driven vertical mixing and entrainment, through their influence upon surface wind speed. The most significant change in the SST pattern is the substantial decrease of the negative SST anomalies southeast of Greenland, and this change again is primarily associated with the removal of the NAO signal. The remaining SST anomaly signal probably is consistent with the SST being forced by the associated surface circulation.

Therefore, regardless of the causes for the LF cyclone track variations and trends, this analysis has provided evidence that, even after the removal of the NAO and SOI signals, the amplitudes of the North Atlantic winter cyclone tracks and related seasonal mean atmospheric and oceanic circulation anomalies have undergone significant interdecadal variability during the last half century. Hence, this suggests that these substantial interdecadal variations that still remain are caused by other factors (e.g.,

Tropics, oceanic boundary forcing, stratospheric and other anthropogenic processes). However, this does not exclude feedback (nonlinear) effects in connection with the NAO and ENSO. In particular, the atmosphere and the ocean may undergo a coupled interaction at decadal-to-multidecadal time-scales, that was not identified by the above linear regression analysis.

LF ocean-atmosphere interactions in the North Atlantic recently have been the focus of considerable inquiry. Interaction between the oceans and overlying atmosphere is fundamental to the dynamical processes governing climate and its variability. The most often cited studies dealing with such interactions were reviewed. However, the leading modes from these studies do not agree on the exact temporal periodicities, amplitudes, and physical mechanisms involved. The modes seem somewhat dependent on data, model, or technique used. This reveals that this topic indeed still is an actively debated question. Therefore, this stressed the need to carry out a new analysis to attempt further clarification of the role of the ocean in the North Atlantic decadal climate variability, especially by invoking the new CDF data set.

Because of the possible existence of a coupled ocean-atmosphere mode in the North Atlantic suggested by previous studies, the dominant decadal coupled covariability mode was identified here using a new lead/lag CCA-based approach applied to atmospheric and oceanic gridded anomaly fields. The goal is to contribute to our understanding of how the North Atlantic atmospheric circulation could respond to ocean forcing on decadal time-scales, and to determine the extent to which SST anomalies feed back on the atmospheric circulation. Confirmation of a mutual coupling could provide significant potential for dynamical climate prediction as exemplified by the most well-

known coupled phenomenon, ENSO (Neelin et al 1994).

First, LF winter CDF and SST anomalies were used as indicators of surface atmospheric and upper-ocean variability, respectively. This reveals a clear quasi-decadal (10-11 years) coupled ocean-atmosphere mode in the North Atlantic. This temporal periodicity agrees well with the previous ones. Then, the same procedure was applied to the SLP and SST anomalies for comparison and verification. This second application reveals no clear coupled cycle in the low-frequency data. This implies that use of CDF (rather SLP) appears to support the feedback of SST to the atmosphere under the hypothetical coupled ocean-atmosphere mode.

One may pose the question regarding the efficacy of CDF (along with SST) rather SLP in identifying that coupled mode. For any such coupled mode to exist, there must be a consistent atmospheric response to SST anomalies (Sutton and Allen 1997). As discussed in Section 5.1, how the atmosphere responds to midlatitude SST forcing is poorly understood (e.g., Kushnir and Held 1996). But, changes in the frequency, intensity, or spatial distribution of midlatitude storms are likely to be important (Palmer and Sun 1985; Kushnir and Held 1996; Sutton and Allen 1997). Therefore, this may provide further evidence that cyclone activity (i.e., CDF) is important in the context of coupled ocean-atmosphere interactions. Moreover, Subsection 4.4.4 suggested that oceanic processes may be involved in modulating the SST patterns for both CDF VRPC2 and VRPC3. Recall that VRPC2 (influencing eastern North Atlantic; Fig. 4.1e) is much less a NAO-like pattern and VRPC3 (affecting mid-Atlantic; Fig. 4.1f) departs significantly from the SLP-based NAO mode. This additional argument may explain in part the above different functioning of CDF vis-à-vis SLP in coupled interactions.

CHAPTER 6: ENSEMBLE SIMULATION OF LF NAO FOR 21st CENTURY CLIMATE CHANGES USING GLOBAL COUPLED OCEAN-ATMOSPHERE GCMs

6.1 INTRODUCTION

As stated earlier, low-frequency variability of the North Atlantic Oscillation (NAO) has recently become one of the major foci of decadal-scale climate research (CLIVAR 1998). This partly is due to the desire to perform long-range predictions for the North Atlantic/European sector and Northwest Africa, where climate variability is strongly influenced by NAO. The question of practical NAO predictability was addressed, for instance, by Rodwell et al. (1999) who used a set of runs with an atmospheric Global Climate Model (GCM) forced with prescribed SSTs. Their simulations indicated that much of the multiannual to multidecadal variability of the winter NAO over the second half of the 20th century can be reconstructed from North Atlantic SSTs. However, they suggested that further work was then required, which would involve using a fully coupled ocean-atmosphere model, in order to better understand the interannual and longer time-scale predictability of SST.

Accordingly, Chapter 6 deals with low-frequency (LF) NAO prediction. While this investigation complements the LF analysis of cyclone track activity (previous chapter), it involves also the further development of the central focus of this Dissertation on the North Atlantic winter cyclone track density function (CDF), since NAO was found to be quite highly correlated to the leading mode of CDF anomalies (Chapter 4, Table 4.1). Specifically, as a new contribution to climate change research, this present analysis

primarily aims at assessing the LF NAO behavior in long-term coupled GCM runs under different greenhouse gas forcing scenarios, with an emphasis put on trends in NAO and its nodes. The focus on fully coupled global models is driven by the potential importance of feedbacks inherent in the coupling of the atmosphere, ocean, and sea-ice components of the climate system (Walsh et al. 2002). Detection of trends in climatological time series has become central to the discussion of possible climate change due to the enhanced greenhouse effect (e.g., Karoly et al. 2003; Karl and Trenberth 2003). While it has been speculated that future global warming will change the frequency and severity of extratropical storms in the Northern Hemisphere (e.g., Zhang et al. 2000 and references therein), there is considerable uncertainty as to what changes actually will occur (McCabe et al. 2001 and references therein).

This chapter is structured as follows. Section 6.2 first describes the importance of using coupled models in climate change studies. A prerequisite for NAO predictions is the realistic simulation of the present NAO variability in coupled models; many recent studies already have explored this issue and shown that these coupled models in general do a reasonably good job. Data used in this present study, namely monthly simulated SLP for twenty-first century climate changes under different scenarios, are described in Section 6.3. These data were generated from a set of different coupled GCM runs; a brief description of these coupled systems is presented in Section 6.4. Then, Section 6.5 outlines a numerical recipe to compute different NAO indices (i.e., traditional NAO, mobile NAO, and PCA-based NAO) from those GCM SLP anomalies. Since there is no unique way to define the spatial structure of the NAO or thus its temporal evolution (Hurrell et al. 2003), the above different NAO definitions were adopted. Trends of simulated twenty-first century LF NAO were computed; various trends were then

compared and contrasted between different NAO indices, between coupled models, and between forcing scenarios. However, since ensemble averaging reduces the noise level in model-simulated climate changes (e.g., Dai et al. 2001), particularly on regional and smaller scales, this study performs ensemble averaging of NAO/SLP at its nodes under different forcing scenarios (Section 6.6). Finally, a summary and conclusions/discussion are provided in Section 6.7.

6.2 SIMULATIONS OF PRESENT NAO IN COUPLED GCMs

Coupled ocean-atmosphere GCMs have become a valuable tool for attempting to understand and predict climate change (Houghton et al. 1996). Although coupling the atmosphere to the ocean is technically challenging – because the ocean has a much longer time-scale of variability than the atmosphere – the methodology of this coupling now is receiving considerable attention. One of the critical deficiencies of these coupled systems has been the large climate drifts that occur when the models are used to simulate the present-day climate. In many coupled models, these problematic drifts have been alleviated by use of "artificial" flux adjustments of heat, salinity, and wind stress that link the atmospheric and oceanic components (e.g., Johns et al. 1997). Also, the paucity of data available limits the evaluation of the ability of coupled GCMs to simulate important aspects of past climate (U.S. National Research Council (NRC) 2001).

However, over the past few years a number of developments have been made to several global coupled models (e.g., NCAR-PCM; Hadley Centre global coupled model) that are used to investigate anthropogenic climate changes. Recent improvements to both atmospheric and oceanic models – especially new methods of "spinning up" the ocean model to equilibrium and thus reducing the "shock" the system components experience

upon coupling – have gone a long way towards reducing model climate drift, and thereby minimized or completely eliminated the requirement for such flux adjustments. Other models also have recently demonstrated the ability to produce stable climate simulations without flux adjustments (e.g., Barthelet et al. 1998; Boville and Gent 1998). Furthermore, GCMs continuously are being improved as their horizontal and vertical resolutions are being increased due to computing power increase, with many modeling groups taking advantage of the ability to split intensive calculations between multiple, parallel processors on a single computer ("multi-tasking"). Refinements in parameterizations of physical processes in all components of several coupled models also are being made (e.g., NCAR-PCM). Some examples are more sophisticated land surface schemes, improved representation of sub-grid-scale mixing in the oceans, improved treatment of clouds, convection, radiation and indirect effect of aerosols in the atmosphere, and the inclusion of sea-ice dynamics. Improvements of such coupled systems do need increased collaborative effort of a wide range of specialists in atmosphere, ocean, hydrology, biology, and other sciences (e.g., Lamb 2002). Coupled ocean-atmosphere GCMs being also are used to investigate the deficiencies of atmospheric general circulation model (AGCM) runs and to guide the design of AGCM climate variability analyses on longer time-scales, e.g., for identifying possible thermohaline circulation-related climate variations.

In contrast to many ENSO modeling studies, very few papers have assessed the skill of climate models to simulate NAO. First, as to simulations of the present (and past) NAO in atmosphere-only GCMs, Glowienka-Hense (1990) showed that the NAO was confidently reproduced, although not with its proper variance, by the ECMWF T21 model, using three runs in perpetual January mode. This suggested that atmospheric processes

are important for the NAO. Also, Davies et al. (1997) showed that Hadley Centre atmospheric climate model (HADAM1) forced by observed global sea-ice and SST for the period 1949-93 (using an ensemble of six integrations), reproduced with "considerable skill" the patterns of NAO.

Secondly, as noted before, coupled GCMs are preferred tools for understanding and predicting multidecadal climate variations. However, to gain confidence in these coupled models and to learn about their deficiencies, it is fundamental to carefully assess their skill at simulating major modes of natural climate variability. Several investigations already have shown that the NAO signal can be captured quite realistically by coupled ocean-atmosphere models (e.g., Pittalwala and Hameed 1991; Osborn et al. 1999; Christoph et al. 2000; Collins et al. 2000; Stephenson et al. 2003). Most importantly, Meehl et al. (2000) reported that many observed aspects of climate variability are simulated in global coupled models including NAO and its linkages to North Atlantic SSTs.

6.3 DATA

The objective of this chapter is made feasible by the recent availability of output from several coupled models archived at the Data Distribution Centre (DDC) of the Intergovernmental Panel on Climate Change (IPCC). These coupled models, described briefly in next section, represent the late 1990s state-of-the art of coupled global climate modeling. The choice of these models by IPCC for use in its Third Assessment Report (Houghton et al. 2001) was the reason their output was used in this present analysis.

IPCC published a Special Report on Emission Scenarios (SRES) in 2000 (URL=http://www.ipcc.ch/). This report describes the new set of emission scenarios used in the Third Assessment Report. IPCC facilitated the conversion of two of these emission scenarios, "A2" and "B2", – out of 40 different scenarios that are deemed "equally likely" – into concentration scenarios for use in climate simulations. Briefly, the A2 scenario predicts population growth to 15 billion by the year 2100 and rather slow economic and technological development. It projects slightly lower greenhouse gas (GHG) emissions than the previous IPCC IS92a scenario, but also slightly lower aerosol loadings, such that the warming response differs little from that of IS92a scenario. In contrast, the B2 scenario envisions slower population growth (10.4 billion by 2100) with a more rapidly evolving economy and more emphasis on protecting the environment. It therefore produces lower emissions and less future warming. Climate change results based on the A2 and B2 scenarios are discussed in the IPCC Third Assessment Report (Houghton et al. 2001).

The input data used in this study to examine LF NAO trends in coupled model simulations of climate change are monthly SLP fields derived from a set of global coupled ocean-atmosphere GCM runs based on the above newer IPCC-SRES A2 and B2 forcing scenarios. The simulation data for these scenarios were downloaded from the Data Distribution Centre of IPCC.

6.4 BRIEF DESCRIPTION OF COUPLED GCMs

The global coupled ocean-atmosphere GCMs that were used in this present study are listed below. Note that these coupled models were, at the time of this analysis, the only ones whose runs were available online at the IPCC/DDC website.

• **NCAR-PCM** (version 1): this is the National Center for Atmospheric Research Parallel Climate Model (Washington et al. 2000). Flux adjustments are not used in this coupled system. NCAR-PCM has atmospheric and land surface, ocean, sea-ice, and river transport components. The time period for the monthly SLP data derived from this model is January 1981-December 2099.

• **CGCM2**: this is the second generation (global) Coupled General Circulation Model of the Canadian Centre for Climate Modelling and Analysis (CCCma). A description of CGCM2 and a comparison, relative to CGCM1 (Flato et al. 2000), of its response to increasing greenhouse-gas forcing is in Flato and Boer (2001). Some technical modifications were made in the CGCM2 ocean spinup and flux adjustment procedure. The time period for the monthly SLP data outputted from this model is January 1900-December 2100.

• **HadCM3**: this is the third version of the Hadley Centre coupled atmosphere-ocean general circulation model (Gordon et al. 2000; Pope et al. 2000). The model requires no flux adjustments, needs no spinup procedure prior to coupling, and has a stable climate in the global mean (Collins et al. 2000). The time period for the monthly SLP data generated by this model is January 1950-December 2099.

• **CSIRO/Mk2**: this is Australia's Commonwealth Scientific and Industrial Research Organization Mark 2 global climate model with a slab ocean (also called CSIRO slab) (Hennessy 1998; Gordon and O'Farrell 1997). Adjusted heat fluxes are applied to this slab ocean to represent heat from the deep ocean and the effect of currents (Watterson et al. 1997). The time period for the monthly SLP data derived from this model is January

1961-December 2100.

6.5 NUMERICAL PROCEDURE USED TO COMPUTE NAO INDICES

This section outlines the numerical procedure used to compute different NAO indices from the monthly SLP data obtained from the above set of global coupled ocean-atmosphere GCM runs. For each model and each IPCC-SRES scenario (A2 and B2), the following actions were accomplished (by the author):

- Some diagnostics were performed on the input GRIB file (data inventory, checking the first and last records, checking the total number of records, checking the data unit).
- Then, the global GRIB file was converted into a binary/no-header file (Grid Analysis and Display System (GrADS) format) for the entire time period of the given coupled model. This step also requires the creation of two files: (1) a GrADS control file for the GRIB file, and (2) the corresponding "map" file (i.e., mapping index file) for using GRIB data in GrADS.
- From the global GRIB file, data were extracted for a larger North Atlantic (NAT) domain (90°W-30°E/10°-90°N) with a horizontal resolution of 2° latitude by 2° longitude. Note that the generated NAT grid is a uniform latitude/longitude whereas the input GRIB grid is Gaussian for most GCM models used in this study. This NAT domain was chosen to be larger than the final Domain Of Interest (DOI, see below) to minimize the "edge effect" problem resulting from the conversion of a non-uniform to uniform latitude-longitude grid via the Bessel function (Subsection 2.2.4d).
- From the NAT GCM file, final SLP data set was extracted for the present DOI. In this study, the DOI domain was defined as 80°W-20°E/20°-80°N, thus yielding a final 2° x 2° grid (covering North Atlantic Basin) of 51 x 31 grid cells.

• Long-term means and standard deviations of the resulting GCM SLP data for the DOI were computed and plotted (mainly for double checking purpose).

• For each individual month, SLP data at fixed NAO nodes (i.e., Ponta Delgada/Azores and Akureyri/Iceland) were obtained from a fine resolution (1° x 1°) version of the above data set over the same DOI for more accuracy. Monthly fixed NAO index (traditional NAO index; Rogers 1984), denoted NAO_f, was then computed from SLP data values at the two fixed nodes (12 values/year).

• Same as above was carried out for the mobile NAO_m index (Portis et al. 2001).

• For each grid-point and individual month, 2° x 2° SLP anomalies were computed with respect to the mean climatological values derived for the given calendar month (12 values/year).

• For each calendar month, a Principal Component Analysis (PCA) of the above SLP anomaly fields was performed in order to identify the major modes of variability (spatial patterns and associated score time series). A PCA-based NAO index, denoted NAO_p, was defined as the leading principal component (i.e., unrotated PC1 score time series).

• For each individual month, a 61-term low-pass Lanczos filter was applied to the resulting three NAO indices (i.e., NAO_f, NAO_m, NAO_p) to retain only the lower-frequencies (periods greater than 10 years); use of Lanczos filter involved setting Lanczos sigma factor to 2 in order to maximize the frequency response function and reduce Gibbs oscillation (Duchon 1979). To keep the filter stable at the ends of each NAO index, the NAO time series were extended at both ends with the average of the adjacent 30 values before applying the filter, as done in Ward et al. (1999).

• For each NAO index, monthly NAO time series were then averaged to form a seasonal mean (e.g., December-February) LF NAO index. Seasons are defined as 3-month running means. The study period is set to January 2002-December 2099.

6.6 RESULTS

First, as mentioned before, under each individual forcing scenario, ensemble averaging was performed over all coupled GCM runs and over the above three NAO indices, since it reduces the noise level in model-simulated climate changes. This yielded 21st century ensemble means of NAO in each season. Similarly, under A2 and B2, and for each given center of action of NAO, ensemble averaging was performed over all GCM runs and all SLP data (at fixed and mobile nodes) to generate ensemble means of SLP in each season. Then, trends in the LF NAO and its nodes are compared and contrasted for the A2 and B2 scenarios.

Under high emission and warming A2 scenario, there is a marked and statistically significant (99%) positive trend in LF NAO in all seasons especially in early spring (FMA, local maximum) and mid-summer (JJA, absolute maximum) (Fig. 6.1). Examination of the trends in the two NAO nodes under A2 (Fig. 6.2a versus Fig. 6.2b) shows that, for all seasons, most of this upward trend in the NAO comes from the contribution of the subpolar low that displays a considerable (significant at 99%) downward trend in all seasons, but most notably in mid-summer (Fig. 6.2a).

In contrast, under the lower emission and warming B2 scenario, there is a near-zero or negative trend in NAO in most seasons, with the negative trend being most pronounced in early spring (Fig. 6.1). The trend is statistically significant (exceeding 87%) only in the four seasons DJF-MAM. Most of this negative trend in the NAO comes from the contribution of the subtropical high that displays a significant negative trend in most seasons, most markedly in FMA (Fig. 6.2).

However, an important issue is the strength of the out-of-phase "signal" relative to the in-phase "noise" between the two centers of action. Following Trenberth (1984), who investigated the signal versus noise in the Southern Oscillation Index (SOI), the signal-to-noise ratio (SNR) for the NAO can be defined simply as SNR=Signal/Noise=$((1-r)/(1+r))^{0.5}$, where r is the simultaneous correlation between the two nodes of NAO. The noise in this case is a measure of all fluctuations (e.g., small-scale and transient meteorological phenomena not related to the NAO) where the two centers of action in the NAO are operating in phase and therefore are not part of the NAO. Fig. 6.3 shows this SNR assessed for the ensemble means of NAO under scenarios A2 and B2. This figure clearly reveals that more confidence may be given to the above findings in the winter core/early spring where there is a substantial increase in the signal-to-noise ratio under A2 versus B2. Note that the SNR in mid-summer (JJA) is almost equally the same under both scenarios, with values much lower than those in the winter core/early spring.

Therefore, such a marked and significant tendency for an upward trend in the NAO index, particularly in the winter core/early spring, would induce moderate-to-severe Moroccan drought (El Hamly et al. 1998; Lamb et al. 2000), in the total absence of CDF influence on Moroccan precipitation (Subsection 4.6.4). Recall that, owing to the relatively local nature of Moroccan precipitation patterns, CDF explains more variance in Moroccan precipitation than the NAO (Table 4.6). Thus, a more accurate analysis of 21st century LF Moroccan precipitation trends should consider at least the additional cyclone track (represented by CDF) influence on the precipitation patterns.

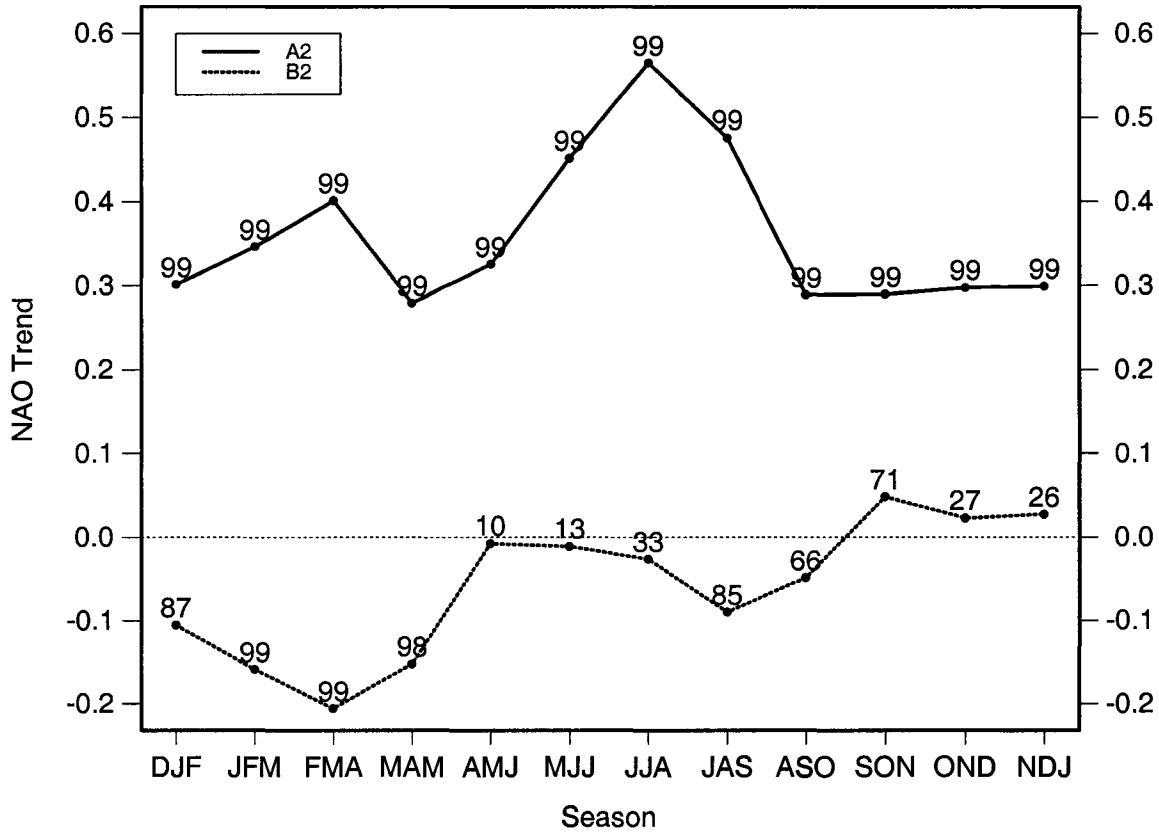


Fig. 6.1. Seasonal variations of predicted trends in ensemble mean of low-frequency NAO simulation for 21st century (2002-2099) climate changes from global coupled ocean-atmosphere GCMs. Ensemble averaging was performed over all GCM runs and over three NAO indices (traditional NAO, mobile NAO, and PCA-based NAO, as described in text). The trends are in units of std devs/98 yrs. The NAO indices were computed from the coupled GCM runs under IPCC forcing scenarios A2 (solid line) and B2 (dashed line). See text for more detail. Values on top of points indicate statistical significance level (in percent) of those LF NAO trends according to a two-sided Student's t-test.

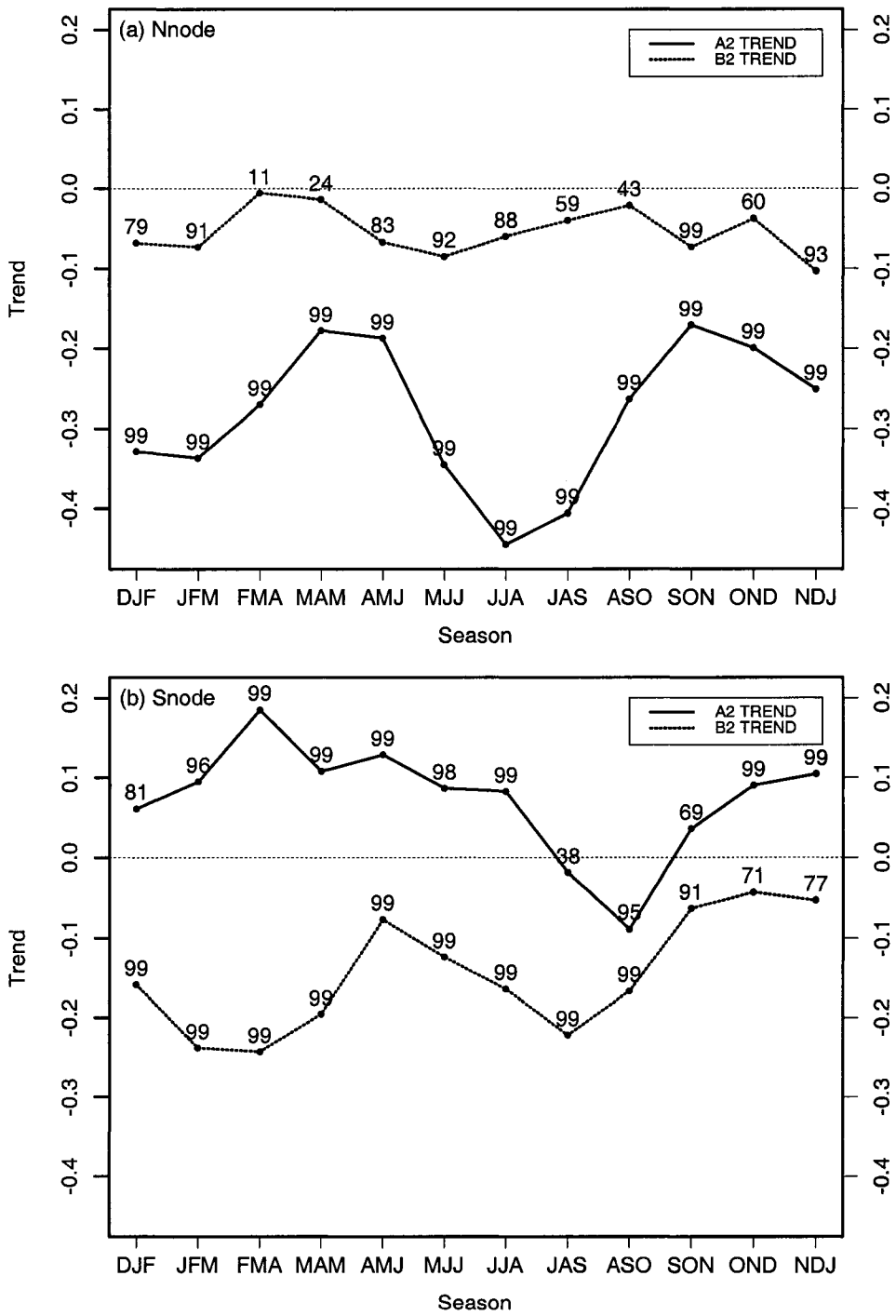


Fig. 6.2. As in Fig. 6.1 but for SLP at (a) northern node of NAO and (b) southern node. The ensemble averaging was taken here over all GCM runs and all SLP data (at fixed and mobile nodes).

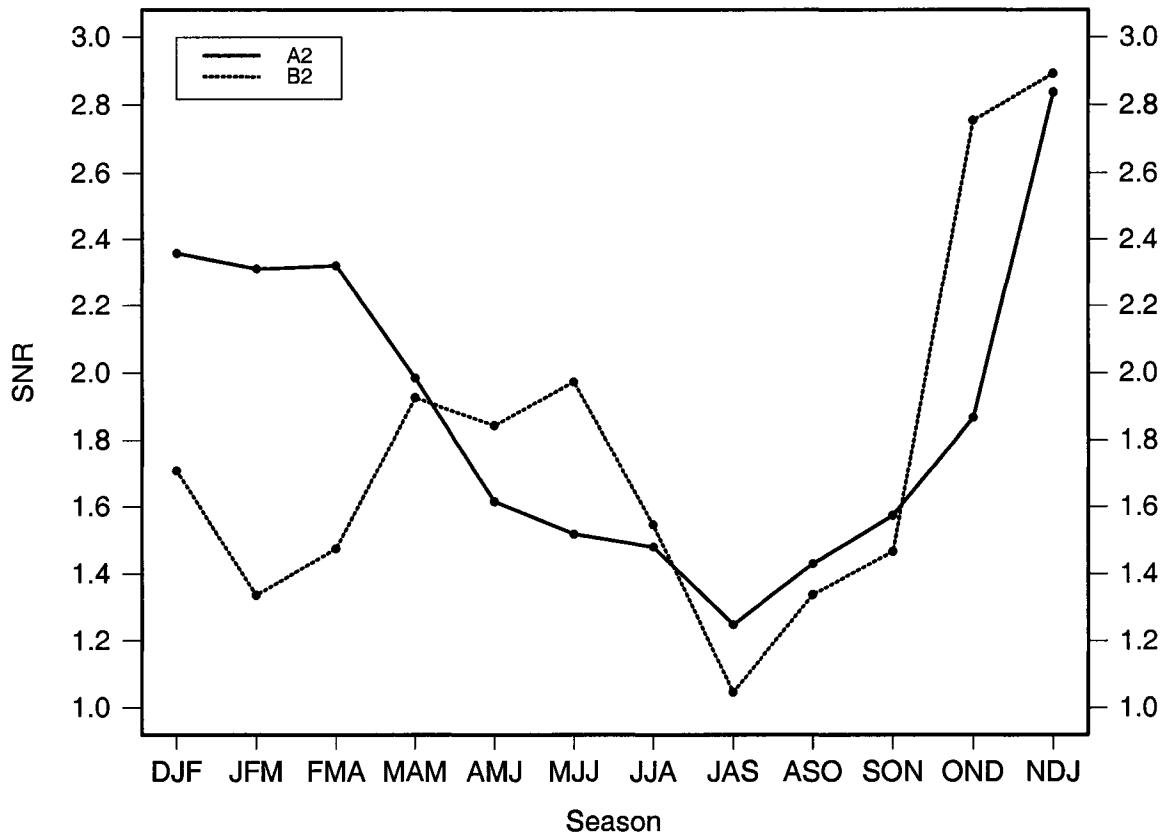


Fig. 6.3. Signal-to-noise ratio (SNR) for ensemble means of LF NAO under the IPCC A2 (solid line) and B2 (dashed line) forcing scenarios. The SNR in NAO was assessed from the simultaneous correlation between the northern (Fig. 6.2a) and southern (Fig. 6.2b) nodes of NAO in each season, as explained in the text.

6.7 SUMMARY AND CONCLUSIONS

The present study deals with the LF NAO prediction. While this investigation complements the previous analysis of LF cyclone track activity (Chapter 5), it involves also the further development of the central focus of this Dissertation on the CDF, since NAO was found to be quite highly correlated to the leading mode of CDF anomalies. As a new contribution to climate change research, this present analysis examined trends in LF NAO/nodes in long-term coupled GCM runs under different greenhouse gas forcing scenarios.

The focus on fully coupled GCMs is driven by the potential importance of feedbacks inherent in the coupling of the atmosphere, ocean, and sea-ice components of the climate system (Walsh et al. 2002). Coupled ocean-atmosphere GCMs are preferred tools for understanding and predicting multidecadal climate variations. However, to gain confidence in these coupled models and to learn about their deficiencies, it is fundamental to carefully assess their skill at simulating major modes of natural climate variability. Several investigations (e.g., Stephenson et al. 2003) already have shown that the NAO signal can be captured quite realistically by coupled models. Most importantly, Meehl et al. (2000) reported that many observed aspects of climate variability are simulated in global coupled models including NAO and its linkages to North Atlantic SSTs.

The objective of this analysis was made feasible by the recent availability of output from several coupled models (NCAR-PCM, CGCM2, HadCM3, CSIRO/Mk2) archived at the Data Distribution Centre of the IPCC. These models represent the late 1990s state-of-the art of coupled global climate modeling. The choice of these models by IPCC for use in its Third Assessment Report (Houghton et al. 2001) was the reason their output was used in this present study.

The input data used to examine LF NAO trends in coupled model simulations of climate change are monthly SLP fields derived from a set of global coupled ocean-atmosphere GCM runs based on the newer IPCC-SRES A2 and B2 forcing scenarios. Different NAO indices (i.e., traditional NAO, mobile NAO, and PCA-based NAO) were computed from those GCM SLP anomalies since there is no unique way to define the spatial structure of the NAO or thus its temporal evolution (Hurrell et al. 2003).

Under each individual forcing scenario, ensemble averaging was performed over all coupled GCM runs and over the above three NAO indices, since ensemble averaging reduces the noise level in model-simulated climate changes (e.g., Dai et al. 2001). This yielded 21st century ensemble means of NAO in each season. Similarly, under A2 and B2, and for each given center of action of NAO, ensemble averaging was performed over all GCM runs and all SLP data (at fixed and mobile nodes) to generate ensemble means of SLP in each season. Then, trends in the LF NAO and its nodes were compared and contrasted for the A2 and B2 scenarios.

Under high emission and warming A2 scenario, there is a marked and statistically significant (99%) positive trend in LF NAO in all seasons especially in early spring (FMA, local maximum) and mid-summer (JJA, absolute maximum). Examination of the trends in the two NAO nodes under A2 shows that, for all seasons, most of this upward trend in the NAO comes from the contribution of the subpolar low that displays a considerable (significant at 99%) downward trend in all seasons, but most notably in mid-summer.

In contrast, under the lower emission and warming B2 scenario, there is a near-zero or negative trend in NAO in most seasons, with the negative trend being most pronounced in early spring. The trend is statistically significant (exceeding 87%) only in the four seasons DJF-MAM. Most of this negative trend in the NAO comes from the contribution of the subtropical high that displays a significant negative trend in most seasons, most markedly in FMA.

However, an important issue is the strength of the out-of-phase "signal" relative to the in-phase "noise" between the two centers of action. Following Trenberth (1984), the signal-to-noise ratio (SNR) was assessed for the ensemble means of NAO under the scenarios A2 and B2. The results clearly reveal that more confidence may be given to the above findings in the winter core/early spring where there is a substantial increase in the SNR under A2 versus B2. The SNR in mid-summer (JJA) is almost equally the same under both scenarios, with values much lower than those in the winter core/early spring.

Therefore, the key result is that the response to enhanced greenhouse gas forcing is a marked and significant tendency for an upward trend in NAO index (i.e., strengthening of the westerlies), particularly in the winter core/early spring. If this is confirmed, this would induce moderate-to-severe Moroccan drought (El Hamly et al. 1998; Lamb et al. 2000), in the total absence of CDF influence on Moroccan precipitation (Subsection 4.6.4). However, recall that, owing to the relatively local nature of Moroccan precipitation patterns, CDF explains more variance in Moroccan precipitation than the NAO (Table 4.6). Thus, a more accurate analysis of 21st century LF Moroccan precipitation trends should consider at least the additional cyclone track (represented by CDF) influence on the precipitation patterns.

Furthermore, the above significant positive trend, if confirmed, will clearly have significant impact on the global climate trends since the NAO exerts a dominant influence on temperatures, precipitation and storms, fisheries and ecosystems of the Atlantic sector and surrounding continents (e.g., Hurrell et al. 2003). The NAO is the main factor controlling air-sea interactions over the Atlantic and, in particular, modulates the site and intensity of the sinking branch of the ocean's meridional overturning circulation (MOC).

In the North Atlantic, the MOC accounts for most of the oceanic heat transport and is a major player in maintaining the pole-equator temperature gradient (Marshall et al. 2001). An important feature of the coupled GCMs is the possibility of a significant weakening of the MOC under global warming scenarios. Even though this possibility remains litigious, Marshall et al. (2001) noted that "yet because of its large potential impact, the possibility that increased fresh-water input and atmospheric high-latitude temperature anomalies could suppress the MOC must be taken seriously" even if the chance of it happening were to be small.

However, the results of this present climate change study or others will still contain uncertainties resulting from coupled model deficiencies in simulating the climate response to any given forcing and from uncertainties in future emissions (under different scenarios). In addition, an accurate simulation of the present climate does not necessarily guarantee a realistic sensitivity to external (e.g., greenhouse gas) forcing.

CHAPTER 7: SUMMARY AND CONCLUSIONS/DISCUSSION

7.1 SUMMARY AND CONCLUSIONS

7.1.1 Introduction

The aim of this research was to give new insight into the North Atlantic winter surface extratropical cyclone track organization and behavior, including climatological features of cyclone activity and variability on different time-scales. To achieve this goal, state-of-the-art techniques, models, and data sets have been used.

7.1.2 CDF and Related Cyclone Characteristics

The construction of the hybrid space- and time-smoothed cyclone track density function (CDF) over the North Atlantic for the winter semesters (October-March) of 1948-99 provided the foundation for this Dissertation. The NCEP/NCAR reanalyses employed to develop the CDF fields are regarded as one of the best representations of the Northern Hemisphere atmosphere (e.g., Simmonds and Keay 2000a); use of these reanalyses at short (6-hourly) intervals means that uncertainties with identifying and tracking individual cyclones are greatly reduced. Additionally, the reanalysis SLP used in this present study to identify and track cyclones is in the most reliable class of reanalysis variables (Kalnay et al. 1996). The aim of this unique CDF approach was to give new insight into storm track organization and behavior over the North Atlantic. These CDF fields were used extensively in previous chapters – for a new and comprehensive long-term climatological description of North Atlantic winter surface extratropical cyclone activity (Chapter 3); for a new classification of North Atlantic

cyclone behavior into major modes of variability on interannual time-scale and associations with regional climate variations (Chapter 4), which provides better understanding of the dynamics of the atmosphere; for analyzing the decadal-to-multidecadal variability of cyclone activity, involving ocean-atmosphere interactions (Chapter 5); as well as for possible projections of 21st century cyclone behavior under increasing atmospheric greenhouse gases, and their implications for regional and local weather conditions (i.e., Morocco) (Chapter 6).

The Akima (1978) scheme was performed to quantify cyclone characteristics (e.g., intensity, moving speed, duration). Development of such fields is enlightening because of the additional physical insight provided; they also demonstrate the physical consistency among the different variables (e.g., CDF versus cyclone intensity). Additionally, the CDF and related Akima-based cyclone attributes were used to yield a rich picture of cyclone climatological features and variability.

7.1.3 Long-Term Climatological Features of Cyclone Activity

The key results obtained from the compilation of the long-term (1948-99) climatology of North Atlantic winter semester (October-March) surface extratropical cyclone activity and characteristics are as follows:

- Although the cyclone characteristics display different spatial patterns of variability, the spatial patterns of the long-term mean of CDF, deepening rate, moving speed, and intensity are physically consistent with each other, with absolute maxima in the CDF and intensity southeast of Greenland, whereas cyclone deepening rate and moving speed maximize upstream near Nova Scotia and Newfoundland. This is consistent with the fact that cyclones usually reach their maximum intensity a little downstream areas of

maximum cyclone deepening rate and moving speed (e.g., Geng and Sugi 2001).

- The spatial patterns of CDF mean and standard deviation both exhibit strong intraseasonal variability.
- Month-to-month persistence of cyclone activity is generally weak, with significant spatial and intraseasonal variability. Further, the 1-month lag autocorrelation function (ACF1) of the cyclone parameters is, in general, also weak, though the ACF1 fields are physically consistent with each other. This weakness in cyclone persistence may be explained in part by the considerable spatial and intraseasonal variability of CDF.
- Both cyclone pressure tendency and moving speed are very weakly dependent on the contemporary CDF over most of the basin. In contrast, CDF is more closely related to the cyclone intensity southeast of Greenland. Over the central-western North Atlantic, there is a marked tendency for cyclone systems to move faster as they deepen, with this effect greater for intense systems.

The significance of the above work lies in number of factors. First, the North Atlantic cyclone climatology has been derived from 51 years (1948/49-1998/99) of data, a period longer than any considered heretofore. For the CDF and other related cyclone parameters, different aspects of cyclone activity were examined and their interrelations and hence the robustness of the results were assessed. Also, this climatology has been compiled using the CDF, one of the most reliable automated methods of analysis of surface cyclone activity available to date. Hence, this climatology of North Atlantic winter cyclone activity is arguably the most accurate and representative yet produced. Finally, use of the unique Percentage Wavelet Energy Concentration (PEC) Analysis of CDF anomalies supported (1) separation of the high-frequency (HF, treated in Chapter 4) and low-frequency (LF, Chapter 5) components of cyclone activity; and (2) use of full 2-

dimensional grid analyses that document the spatial heterogeneity of cyclone behavior, rather than zonal or other area-averaging approaches. The PEC Analysis of CDF anomalies was based on the Discrete Wavelet Transform (DWT).

7.1.4 Interannual Variability of Cyclone Tracks & Associations with Regional Climate Variations

Chapter 4 examined the interannual variability of North Atlantic winter cyclone activity and its associations with regional climate variations, including one sensitive bordering region (Morocco). Several analysis methods were applied to the CDF and other related cyclone attributes (e.g., intensity) to illuminate such variability.

First, the principal modes of cyclone track variability were identified from a VARIMAX Rotated Principal Component (VRPC) Analysis of CDF anomalies. It is found that the VARIMAX rotation has better isolated the patterns of variability. The three VRPCs collectively account for ~26.4% of total CDF variance. Consistent with the design of the VARIMAX algorithm, each of these VRPCs explains similar fractions of the total variance. VRPC1 reflects predominant northward or southward migration of the primary storm track from its time-mean position. Further, VRPC1 pattern is strongly reminiscent of the positive phase of the NAO, but with the dipole shifted north of its NAO counterpart. VRPC2 (VRPC3) also has a dipole structure in eastern (mid-) North Atlantic. Relative to VRPC1, VRPC2 (VRPC3) has the opposite (same) polarity and nodes shifted farther south (southwest). Thus, VRPC2 is much less a NAO-like pattern than VRPC1; whereas VRPC3 has no relationship with the NAO. Linear trends in the CDF VRPC score time series are insignificant. Persistence of the VRPC scores, via ACF1 and month-to-month correlation analyses, is generally weak. Both analyses show

that, of all three modes, VRPC3 (affects mid-Atlantic) is the most persistent at 1-month lag; whereas VRPC1 and VRPC2 (influence eastern North Atlantic) are less persistent.

The Matching Pursuit Transform (MPT) wavelet technique was applied to each CDF VRPC score time series in order to best match the signal structures. The changing nature of the CDF signal is very well reflected in the MPT time-frequency decomposition that clearly reveals that each CDF mode displays different patterns of cyclone activity at a given point in time for a particular frequency band. Further, the MPT is very efficient in identifying singularities in both time and frequency. The three CDF modes exhibit different time-based singularity characters and they are of quite different frequency-based singularity nature. Therefore, the CDF signal is characterized by non-stationarity.

The analysis of the North Atlantic raw surface extratropical cyclone tracks for individual extreme months confirms the existence of periods when each of the CDF VRPC modes dominates, yielding a new classification of the North Atlantic winter cyclone behavior into three distinctly different regimes. Briefly, VRPC1 is essentially the NAO, whereas the new VRPC2 reflects southwest-northeast split pattern. In contrast, the new VRPC3 features diffuse pattern of cyclone activity from the southern tip of Greenland towards the Iberian Peninsula/Morocco. To date, the central focal point of most climate investigations on North Atlantic/European sector has involved the NAO. Therefore, these unique CDF VRPC modes were used extensively in this Dissertation to give new insight into the cyclone track organization and behavior.

Relationships of atmospheric and oceanic circulation anomalies to the CDF VRPC modes were documented in a different and comprehensive way. Consistent with previous

results, the relationship between the surface wind and SST anomalies for VRPC1 is essentially local: For instance, above-normal wind speeds will cool the ocean mixed layer by enhancing the sensible and latent heat fluxes from the ocean surface and by accelerating the entrainment of cooler water from below (Deser and Blackmon 1993). Compared to VRPC1, the patterns for the high-minus-low composites associated with VRPC2 (VRPC3) are essentially very similar to those related to VRPC1 but shifted farther south (southwest) with the opposite (same) polarity, which is consistent with the spatial VRPC loading patterns. However, the SST pattern is monopole featured for both VRPC2 and VRPC3, with the same (opposite) sign as VRPC2 (VRPC3) scores. The SST pattern for VRPC2 (VRPC3) is generally consistent with a response of the upper-ocean to the associated atmospheric forcing, although oceanic processes may be involved in determining and/or modulating the SST pattern. For VRPC2 (VRPC3), temperature anomalies in the midocean area east (southeast) of Newfoundland may be related to changes in the interface between the subtropical and subpolar ocean gyres (in the strength and/or position of the Gulf Stream current). Coupled ocean-atmosphere GCM modeling is required to assess these hypotheses.

Short-term cyclone variability was related to global and regional teleconnection patterns (e.g., ENSO, NAO). The regional NAO impact on North Atlantic winter cyclone characteristics was documented. During positive NAO events, the main cyclone track has a pronounced northeastward orientation across the North Atlantic (e.g., Rogers 1990), resulting in an absolute maximum of cyclone activity over the Greenland/Iceland corridor in terms of both CDF and cyclone frequency, along with absolute maximum cyclone intensity and absolute minimum central pressure north of Iceland. However, intensification of cyclone deepening rate and moving speed maximize further upstream,

to the northeast of Newfoundland. Cyclone duration tends to maximize over the Greenland Sea. In contrast, during negative NAO events, cyclones crossing the western Atlantic move eastward, tracking along latitude 45°N on average, in proximity to the Gulf Stream (e.g., Rogers 1990), resulting in the maximum of cyclone duration northwest of Portugal.

Additionally, the possibility of a more remote ENSO influence on North Atlantic winter cyclone tracks and atmospheric/oceanic circulation was explored. The cyclone track shifts southward during El Niño years, while La Niña events are associated with opposite shifts. Accompanying the significant above (below)-normal cyclone activity off the U.S. East Coast is a marked tendency for negative (positive) SLP anomalies. Further, warm ENSO events are associated with above-normal SST along a zonally elongated belt in the band between 20°-30°N, and with below-normal temperature in the waters off the U.S. East Coast. The oceanic response is consistent with atmosphere-to-ocean forcing.

The relationship of CDF and Moroccan precipitation (MRR) patterns to the NAO was examined. The key issues were how much of the cyclone activity is NAO-related, and how much is not, and the implications this has for the predictability of Moroccan precipitation (El Hamly et al. 1998; Ward et al. 1999). Analysis of the {NAO and MRR}-based composite difference fields for each Moroccan region indicates that CDF explains some of the rest of variance in precipitation that is not due to NAO. The results illustrated that interannual Moroccan precipitation anomalies are the residual of strong regional patterns of change involving both NAO and CDF. Thus, the predictability of MRR indices by accounting for the additional new CDF VRPC scores, besides the three

NAO indices, was revisited via multiple regression, where the "Best Model" for each region was chosen via "Stepwise Selection" (C_p criterion). For all Regions I-V, the VRPC-based regression model outperforms the NAO-based model. Owing to the relatively local nature of Moroccan precipitation patterns, this finding can be explained in part by the local influence of the cyclone tracks (represented by CDF) versus the large-scale climate system control involving NAO. For Regions I-III, the {NAOs & VRPCs}-based model is slightly better than those based on NAOs only or VRPCs only; i.e., NAO adds little information in this case, largely due to its high correlation with VRPC1. As for Regions IV-V, VRPCs-based and {NAOs & VRPCs}-based models yielded the same results since these two regions show no significant correlations with NAO; in particular, both NAO and CDF have essentially no influence on Region V. For Region I (II-V), the leading predictor is VRPC1 (VRPC2), which is consistent with their spatial loading patterns. VRPC3 has no influence on precipitation in any region, which agrees with its two centers of action being farther west. Finally, a counterpart analysis for ENSO suggested that climate system mode has no statistically significant impact on Moroccan precipitation patterns.

7.1.5 Decadal-to-Multidecadal Variability of CDF Involving Ocean-Atmosphere Interactions

Chapter 5 first examined the LF behavior of CDF (including trends) and associations with other LF atmospheric and oceanic fields/indices (NAO, ENSO). A PCA was applied to the LF winter CDF anomaly fields. The leading UPC mode accounts for 23.23% of total LF CDF variance. The UPC1 pattern mainly is characterized by a dipole structure, with the northern center of action being maximized over the Greenland Sea, contrasting with a southern center of action that maximizes over the central North Atlantic

while extending from the U.S. East Coast to Western Europe. Of particular interest is the relatively weaker third extremum off Northwest Africa, which is in phase with the northern center of action. Above-normal storminess over this region may be due in part to the possible intrusion of tropical disturbances from the south into the North Atlantic Basin, some of which may reach the Atlas Mountains over Morocco.

The UPC1 score time series displays pronounced low-frequency, decadal-scale variability, with a statistically significant (99.95%) upward linear trend of 1.62 std devs/51 yrs. The trend is dominant after mid-1960s, before which it was preceded by a sharp downtrend. Further, a clear transition in the UPC1 scores was identified during the early 1970s, from an earlier period beginning in the early 1950s (with negative scores) when the main cyclone track was generally zonal across the central North Atlantic, to the more recent era (with mainly positive scores) when the main cyclone track had a pronounced northeastward orientation, resulting in above-normal cyclone activity southeast of Greenland and over the Greenland Sea. The sharp transition occurred in 1971/72, consistent with the singularity in time (January 1973) revealed by the Matching Pursuit Transform applied to the CDF VRPC1 scores.

To highlight this 1971/72 transition in the LF CDF UPC1 functioning, the LF winter CDF difference field between semesters with the highest and lowest 10-yr average UPC1 score values was examined. The difference pattern is very similar to the UPC1 loading pattern. Further, there is a significant resemblance between the UPC1-based difference field and the linear trend in LF winter CDF anomalies over the entire 51-yr period, 1949-99, despite UPC1 explaining only 23.23% of total LF CDF variance. Therefore, the interdecadal variability of North Atlantic winter cyclone tracks is so well

captured by the leading mode of LF winter CDF anomalies.

The LF winter cyclone track variations were related to LF winter atmospheric and oceanic circulation anomalies, via spatial regression analysis, in which various gridded fields were regressed onto the UPC1 time series. The resulting regression patterns bear some resemblance to their respective high-minus-low composite differences based upon the CDF VRPC1 mode. The regression patterns for all the atmospheric and oceanic fields are physically consistent with each other, with the SLP pattern reflecting a strong positive NAO environment. One key result is that the LF winter cyclone track variations and their associated seasonal mean atmospheric and oceanic circulation anomalies are highly correlated (with the values being mainly positive during the late 1980s and 1990s, and negative during the late 1950s, 1960s, and early 1970s), and the explained variance (r^2) varying from 62% for SLP to 86% for precipitation rate.

The decadal-scale cyclone track variations were related to ENSO and NAO. Much (little) of the LF winter cyclone track variability is associated with LF winter NAO (SOI) anomalies. To assess whether most of the LF CDF variability can be explained by the NAO and the ENSO-like interdecadal mode, the part that is linearly dependent upon these two indices was removed from the original LF winter CDF anomalies. Then, a PCA was performed on the final residual CDF data. The resulting UPC_b mode accounts for 18.66% of total residual variance. The northern center of action in the UPC_b pattern is somewhat weaker than its counterpart in UPC1, which is due to the removal of the NAO signal. The southern node also is weaker off the U.S. East Coast; this probably is due to the removal of the SOI signal. The most significant change in the loading pattern is the near

disappearance of the aforementioned third extremum off Northwest Africa. The results revealed that most of this feature is due to the ENSO, although some of it is linked to the NAO.

The UPC_b score time series (with insignificant trend) clearly reveals that, even after the removal of the linear effect due to both the NAO and SOI signals, there is still substantial interdecadal variability in the CDF data. The residual cyclone track generally was zonal across the central part of the basin during the late 1950s and 1960s, and with a northeastward orientation afterward in the mid-1970s and late 1980s-early 1990s. The UPC_b-based regression patterns of the same atmospheric and oceanic circulation anomalies were examined. The most significant change in the SST pattern is the substantial decrease of the negative SST anomalies southeast of Greenland, and this change is primarily associated with the removal of the NAO signal. The remaining SST anomaly signal probably is consistent with the SST being forced by the associated surface circulation. Therefore, regardless of the causes for the LF cyclone track variations and trends, this analysis has provided evidence that, even after the removal of the NAO and SOI signals, the amplitudes of the North Atlantic winter cyclone tracks and related seasonal mean atmospheric and oceanic circulation anomalies have undergone significant interdecadal variability during the last half century. Hence, this suggests that these substantial interdecadal variations that still remain are caused by other factors (e.g., Tropics, oceanic boundary forcing, stratospheric and other anthropogenic processes). However, this does not exclude feedback (nonlinear) effects in connection with the NAO and ENSO. In particular, the atmosphere and the ocean may undergo a coupled interaction at decadal-to-multidecadal time-scales, that was not identified by the above

linear regression analysis.

LF ocean-atmosphere interactions in the North Atlantic recently have been the focus of considerable inquiry. The leading modes from these studies do not agree on the exact temporal periodicities, amplitudes, and physical mechanisms involved. The modes seem somewhat dependent on data, model, or technique used. This reveals that this topic indeed still is an actively debated question. Therefore, this stressed the need to carry out a new analysis to attempt further clarification of the role of the ocean in the North Atlantic decadal climate variability, especially by invoking the new CDF data set. Because of the possible existence of a coupled ocean-atmosphere mode in the North Atlantic suggested by previous studies, a new lead/lag CCA-based approach was applied to atmospheric and oceanic gridded anomalies.

First, LF winter CDF and SST anomalies were used as indicators of surface atmospheric and upper-ocean variability, respectively. This revealed a clear quasi-decadal (10-11 years) coupled ocean-atmosphere mode in the North Atlantic. This temporal periodicity agrees well with those published. Then, the same procedure was applied to the SLP and SST anomalies, which revealed no clear coupled cycle in the low-frequency data. This implies that use of CDF (rather SLP) appears to support the feedback of SST to the atmosphere under the hypothetical coupled ocean-atmosphere mode.

One may pose the question regarding the efficacy of CDF (along with SST) rather SLP in identifying that coupled mode. For any such coupled mode to exist, there must be a consistent atmospheric response to SST anomalies (Sutton and Allen 1997). As discussed in Section 5.1, how the atmosphere responds to midlatitude SST forcing is

poorly understood (e.g., Kushnir and Held 1996). But, changes in the frequency, intensity, or spatial distribution of midlatitude storms are likely to be important (Palmer and Sun 1985; Kushnir and Held 1996; Sutton and Allen 1997). Therefore, this may provide further evidence that cyclone activity (i.e., CDF) is important in the context of coupled ocean-atmosphere interactions. Moreover, Subsection 4.4.4 suggested that oceanic processes may be involved in modulating the SST patterns for both CDF VRPC2 and VRPC3. Recall that VRPC2 is much less a NAO-like pattern and VRPC3 departs significantly from the SLP-based NAO mode. Hence, this additional argument may explain in part the above different functioning of CDF versus SLP in coupled interactions.

7.1.6 Ensemble Simulation of LF NAO for 21st Century Climate Changes Using Global Coupled Ocean-Atmosphere GCMs

As a new contribution to climate change research, Chapter 6 examined trends in LF NAO/nodes in long-term coupled ocean-atmosphere GCM (NCAR-PCM, CGCM2, HadCM3, CSIRO/Mk2) runs under the newer IPCC-SRES A2 and B2 forcing scenarios. Different NAO indices (i.e., traditional NAO, mobile NAO, and PCA-based NAO) were computed from monthly GCM SLP anomalies since there is no unique way to define the spatial structure of the NAO or thus its temporal evolution (Hurrell et al. 2003). Under each individual forcing scenario, ensemble averaging was performed over all coupled GCM runs and over the above three NAO indices, since ensemble averaging reduces the noise level in model-simulated climate changes (e.g., Dai et al. 2001). This yielded 21st century ensemble means of NAO in each season.

Under high emission and warming A2 scenario, there is a marked and statistically significant (99%) positive trend in LF NAO in all seasons especially in early spring

(FMA, local maximum) and mid-summer (JJA, absolute maximum). Examination of the trends in the two NAO nodes under A2 shows that, for all seasons, most of this upward trend in the NAO comes from the contribution of the subpolar low that displays a considerable (significant at 99%) downward trend in all seasons, but most notably in mid-summer.

In contrast, under the lower emission and warming B2 scenario, there is a near-zero or negative trend in LF NAO in most seasons, with the negative trend being most pronounced in early spring. The trend is statistically significant (exceeding 87%) only in the four seasons DJF-MAM. Most of this negative trend in the NAO comes from the contribution of the subtropical high that displays a significant negative trend in most seasons, most markedly in FMA.

Therefore, the key result is that the response to enhanced greenhouse gas forcing is a marked and significant tendency for an upward trend in NAO index (i.e., strengthening of the westerlies), particularly in the winter core/early spring where there is a substantial increase in the signal-to-noise ratio under A2 versus B2. If this is confirmed, this would induce moderate-to-severe Moroccan drought (El Hamly et al. 1998; Lamb et al. 2000), in the total absence of CDF influence on Moroccan precipitation (Subsection 4.6.4). However, recall that, owing to the relatively local nature of Moroccan precipitation patterns, CDF explains more variance in Moroccan precipitation than the NAO (Table 4.6). Thus, a more accurate analysis of 21st century LF Moroccan precipitation trends should consider at least the additional cyclone track (represented by CDF) influence on the precipitation patterns.

Furthermore, the above significant positive trend, if confirmed, will clearly have significant impact on the global climate trends since the NAO exerts a dominant influence on temperatures, precipitation and storms, fisheries and ecosystems of the Atlantic sector and surrounding continents (e.g., Hurrell et al. 2003). The NAO is the main factor controlling air-sea interactions over the Atlantic and, in particular, modulates the site and intensity of the sinking branch of the ocean's meridional overturning circulation (MOC). In the North Atlantic, the MOC accounts for most of the oceanic heat transport and is a major player in maintaining the pole-equator temperature gradient (Marshall et al. 2001). An important feature of the coupled GCMs is the possibility of a significant weakening of the MOC under global warming scenarios. Even though this possibility remains litigious, Marshall et al. (2001) noted that "yet because of its large potential impact, the possibility that increased fresh-water input and atmospheric high-latitude temperature anomalies could suppress the MOC must be taken seriously" even if the chance of it happening were to be small.

However, the results of this present climate change study or others will still contain uncertainties resulting from coupled model deficiencies in simulating the climate response to any given forcing and from uncertainties in future emissions (under different scenarios). In addition, an accurate simulation of the present climate does not necessarily guarantee a realistic sensitivity to external (e.g., greenhouse gas) forcing.

7.2 NEW CONTRIBUTIONS

The new contributions of this Dissertation to research in the field of climate dynamics are as follows:

1. CDF yields the first ever *objectively analyzed* winter semester (October-March) surface extratropical cyclone track data set over the North Atlantic Ocean for 1948/49-1998/99 on a 2° latitude x 2° longitude grid with 1-day time resolution (constructed in Chapter 2).

2. Development of other related cyclone characteristics (e.g., intensity, moving speed, duration) (in Chapter 2) using the Akima (1978) interpolation scheme.

3. Comprehensive 2-D climatology of cyclone attributes on a seasonal and monthly basis (Chapter 3).

4. 2-D Persistence (via month-to-month correlation analysis and autocorrelation function at different lag months) patterns of cyclone activity (Chapter 3) and 2-D trend (Chapter 5).

5. Discrete Wavelet Transform-based Percentage Energy Concentration analysis of CDF anomalies (Chapter 3).

6. VRPC-based regime classification of cyclone behavior into three distinctly different modes (i.e., CDF VRPC modes) (Chapter 4).

7. Matching Pursuit Transform time-frequency decomposition of the three CDF VRPC score time series (Chapter 4).

8. Compositing analysis of a field (e.g., CDF) based upon two time series (i.e., NAO and Moroccan precipitation indices) with additional constraints on the two time series (Chapter 4).

9. A lead/lag CCA-based procedure used to explore ocean-atmosphere interactions at decadal time-scale (Chapter 5).

10. Ensemble simulation of LF NAO for 21st century climate changes using global coupled ocean-atmosphere GCMs (Chapter 6).

7.3 FUTURE WORK

The following lines of investigation can be conducted in future work:

- *Ensemble Simulation of LF NAO for 21st Century Climate Changes Using Global Coupled Ocean-atmosphere GCMs*

Outputs under the A2 and B2 forcing scenarios from other coupled models are now available online at the IPCC/DDC website. These models are: (1) Max Planck Institute für Meteorologie (MPIfM) ECHAM4/OPYC3, (2) Geophysical Fluid Dynamics Laboratory (GFDL) R30, and (3) Center for Climate Research Studies (CCRS)/National Institute for Environmental Studies (NIES) AGCM/OGCM. These additional models can be incorporated in a new analysis to assess the robustness of the results obtained in Chapter 6, using the same ensemble framework.

- *Kalman Filtering*

The development of the present cyclone track data set was based on the CDF objective analysis scheme. However, this data set may be enhanced by applying advanced data assimilation methods such as Kalman filtering. This requires high-performance computing capability. In this analysis, first, one will have to learn about Kalman-based model errors (e.g., bias, empirical parameters) from cyclone "observations" and covariances. Then, these model errors can be used as a tool to improve cyclone analysis. Note that this Kalman filtering-based cyclone analysis requires tremendous research work.

- *Atlantic Cyclone Tracks*

Once the new cyclone track fields are created from Kalman filtering approach, redo the present analysis for the North Atlantic Basin.

• *Pacific-Atlantic Relationship*

As above, but for the Pacific Ocean and the entire Northern Hemisphere. The purpose here is to explore the relationship between the Pacific and Atlantic cyclone tracks at different time-scales.

• *Hydrologic Design of dams*

The key result of Chapter 6 is that the response to enhanced greenhouse gas forcing is a marked and significant tendency for an upward trend in NAO index, particularly in winter. Drier-than-normal conditions occur during high NAO index winters over Morocco (Lamb and Peppler 1987). Thus, Moroccan regional precipitation indices (MRR) can be projected into the 21st century using the NAO-MRR-CDF relationship (Chapter 4) for regions I-III. Signals in eastern North American precipitation and runoff also show a relation to the NAO (Perreault et al. 1999), which could impact the development of water management rules in water resource systems (Marshall et al. 2001). During the last 20 years use of climate data and information in agriculture and water resources has increased dramatically (Changnon and Kunkel 1999). The use of climate information and forecasts to reduce the uncertainty inherent in managing large systems for diverse needs bears significant promise (Pulwarty and Redmond 1997). Therefore, a new action of research is to incorporate the predicted MRR for the 21st century into a hydrologic design (Chow et al. 1988, p. 416) of Moroccan dams (small, intermediate, large). Further, coupled regional climate and macroscale hydrologic simulations of the NAO hydroclimate signals in a Moroccan river basin can also be performed as in Leung et al. (1999) who simulated the ENSO hydroclimate signals in the Pacific Northwest Columbia river basin. They reported that such simulations demonstrated the prospect for generating and utilizing seasonal climate forecasts for managing reservoirs.

APPENDIX

Matching Pursuit Transform

1. Background (Literature Review)

Matching Pursuit Transform (MPT) was originally introduced in the signal-processing and wavelets community as an algorithm "that decomposes any signal into a linear expansion of waveforms that are selected from a redundant dictionary of functions." (Mallat and Zhang 1993). These waveforms are chosen in order to best match the signal structures. Matching pursuit algorithm is a general, greedy (that locally optimizes the decomposition of the signal), sparse function approximation scheme with the squared error loss, which iteratively adds new basis functions to the linear expansion. Mallat and Zhang (1993) showed that matching pursuits provide extremely flexible signal representations since the choice of waveform dictionaries is not limited. They demonstrated that time-frequency dictionaries (e.g., dictionary of Gabor functions) yield adaptive decompositions where signal structures are represented by atoms that match their time-frequency signature. More details on adaptive greedy approximations (and behavior of approximation errors) from matching pursuits are given in Davis et al. (1997). Time-frequency dictionaries include vectors that are spread between Fourier and Dirac bases. They are regularly distributed of the unit sphere of the signal space and are thus well adapted to decompose signals over which we have little prior information (Mallat and Zhang 1993). An orthonormal decomposition is a particular case of matching pursuit transform where the dictionary is the orthonormal bases. Besides the dictionary of Gabor functions, other interesting types of dictionaries for matching pursuit are wavelet packets (Coifman et al. 1990; Coifman and Meyer 1991; Coifman and Wickerhauser 1992;

Coifman et al. 1992) and cosine packets (Coifman and Meyer 1991).

As mentioned earlier, matching pursuit and its variants were developed primarily in the signal-processing and wavelets community. Previous work consisted of a very few but interesting applications of this algorithm in other scientific communities. For instance, in the machine learning community, Vincent and Bengio (2002) showed how matching pursuit provides an interesting and flexible framework to build kernel-based solutions to machine learning problems, while keeping control of the sparsity of the solution. In general, the sparsity of representation is an important issue, essentially for computational efficiency of the resulting representation.

As an oceanographic application, Walden and Cristan (1998) described how to formulate a matching pursuit algorithm that successively approximates a periodic nonstationary time series with orthogonal projections onto elements of a suitable dictionary (constructed from undecimated Discrete Wavelet Transform (Shensa 1992)). They analyzed a time series of subtidal sea levels from Crescent City, California. The matching pursuit shows in an iterative fashion how localized dictionary elements (scale and position) account for residual variation, and in particular emphasizes differences in construction for varying parts of the time series. That is, the matching pursuit technique gives insight into the "physical construction" of the time series, as evidenced, for example, by the way that differences in the winter-spring transitions of water level from year to year become evident through the step-by-step choice of basis sequence building blocks.

Matching pursuit algorithm was also used in biological cybernetics. Movement-Related Potentials (MRPs) recorded from the brain are thought to vary during learning of a motor task. However, since MRPs are recorded at a very low signal-to-noise ratio, it is difficult to measure these variations. Yom-Tov et al. (2001) attempted to remove most of the accompanying noise thus enabling the tracking of transient phenomena in MRPs recorded during learning of a motor task. They used a modified version of the matching pursuit algorithm in order to remove a significant portion of the electroencephalographic noise overlapping the MRPs recorded in the experiment (subjects performed a simple motor task that required learning).

In the climate community, Wang and Wang (1996) applied both Morlet wavelet transform and Gabor waveform transform approaches to display time-frequency characteristics of SST variations in the equatorial eastern and central Pacific and Darwin SLP variance since 1872. The purpose of their paper was to reveal temporal structure of the Southern Oscillation.

In Chapter 4, a matching pursuit transform was applied to examine the changing nature and singularities in both time and frequency of North Atlantic winter CDF signal. Wavelet packets have been used as basis sequence building blocks (i.e., dictionary) for this matching pursuit. The properties of the CDF signal components are explicitly given by the scale, frequency, time and phase indices of the selected atoms. The author will show that the matching pursuit transform is very efficient in identifying singularities in both time and frequency. At the same time, a fundamental question concerning CDF will also be addressed: is CDF a nonstationary time series?

In this matching pursuit application, CDF time period was restrained to October 1951-March 1999, yielding a sampling size, n, of 288. The total number of scale levels, J (i.e., the total number of multi-resolution components), is set to 5 ($n/2^J = 9$ must be an integer). The total number of wavelet atoms, N, is set to 50.

2. Methodology

The original idea of matching pursuit technique as set out initially in Mallat and Zhang (1993) and Davis et al. (1994) is the successive approximation of functions with orthogonal projections onto elements of a collection of waveforms that Mallat and Zhang called "dictionaries". An adaptive time-frequency decomposition of a signal f(t) from a Hilbert space **H** is obtained by expanding f(t) into linear combinations of elements from a large collection $\mathbf{D}=\{ W_\gamma(t):\gamma \in \Gamma \}$ of waveforms with $\|W_\gamma\|^2=\int W_\gamma^2(t)dt=1$ (unit norm), called a waveform dictionary. Three examples of waveform dictionaries are Gabor functions (which are the product of a window or taper function and a complex exponential function), wavelet packets, and cosine packets. In contrast to the discrete wavelet transform and best basis transforms (Coifman and Wickerhauser 1992), matching pursuit decompositions are not orthogonal. The methodology outlined below is based on material in Mallat and Zhang (1993), Bruce and Gao (1996), and Vincent and Bengio (2002).

As elements of the "waveform" dictionary in the present matching pursuit analysis, we choose basis sequences arising from "wavelet packets". That is, a decomposition of a signal f(t) (e.g., CDF VRPC score time series) is given by:

$$f(t) = \sum_{j=1}^{J} \sum_{b=0}^{2^j-1} \sum_{k=1}^{n/2^j} w_{j,b,k}\, W_{j,b,k}(t) + R_N(t) \qquad \text{(Eq. 1)}$$

where:

- the index j corresponds to the scale level (or resolution level) (as in DWT, see Section 3.4 for more details); j=1,2,....,J.

- the index k corresponds to the translation shift (as in DWT); k=1,2,...,$n/2^j$ (n is the sampling size).

- b is the oscillation parameter; b=0,1,...,2^j-1

Eq. 1 defines the matching pursuit approximation of f(t) as a sum of N atomic packet waveforms $W_{j,b,k}(t)$.

Wavelet packet approximations are based on translated and scaled wavelet packet functions $W_{j,b,k}(t)$ that are generated from the base functions W_b as follows:

$$W_{j,b,k}(t) = W_b(t/2^j - k) / 2^{j/2} \qquad \text{(Eq. 2)}$$

The wavelet packet $W_{j,b,k}$ has scale 2^j (the scale factor 2^j is also called dilation factor) and location 2^j k (also called translation parameter). The wavelet packet base functions $W_b(t)$ are parameterized by an *oscillation* or frequency index b. A father (mother) wavelet $\phi(t)$ ($\psi(t)$) corresponds to b=0 (b=1), hence $\phi(t) \equiv W_0(t)$ ($\psi(t) \equiv W_1(t)$). Larger values of b correspond to wavelet packets with more oscillations and higher frequency. In Eq. 1 above, the $w_{j,b,k}$ are the matching pursuit coefficients and $R_N(t)$ is the residual term resulting from the approximation of the signal f(t) after N iterations. The localizations of the waveforms in time and frequency match those of the different signal structures; γ is thus a vector of parameters (j,b,k) (such as location, scale, and frequency modulation) that define the exact form of $W_\gamma(t) \in \mathbf{D}$. The smallest possible dictionary **D** is a basis for the Hilbert space, but a dictionary used in practice is typically a very redundant set; such redundance is of great importance as it allows increased freedom in constructing function

expansions well matched to the signal structure. In the present case, the dictionary may be constructed by translating, scaling, and modulating the wavelet packet base functions W_b (Eq. 2).

The matching pursuit algorithm proceeds by successively finding and removing atomic waveforms, $W_\gamma(t)$, from the signal f(t). An approximation of f(t) with N atoms is obtained iteratively as follows:

- Step 1. Initialization step: initialize the residual $R_0(t) \equiv f(t)$ and the iteration number i=1.

- Step 2. For all atomic packet waveforms W_γ (elements of the dictionary **D**), $\gamma \in \Gamma$, compute the orthogonal projections

$$c_{\gamma,i} = \langle R_{i-1}, W_\gamma \rangle = \int R_{i-1}(t) W_\gamma(t) dt \qquad \text{(Eq. 3)}$$

where $\langle h_1, h_2 \rangle$ denotes the dot product between two vectors h_1 and h_2. Note that the coefficients $c_{\gamma,i}$ depend upon the iteration number i.

- Step 3. Find the index i of the atomic packet waveform γ_i to minimize the approximation error $\|R_{i-1}(t) - c_{\gamma,i} W_\gamma(t)\|^2$. That is,

$$\gamma_i = \arg \min_{\gamma \in \Gamma} \{ \|R_{i-1}(t) - c_{\gamma,i} W_\gamma(t)\|^2 \} \qquad \text{(Eq. 4)}$$

Proof of Eq. 4: For any $W_\gamma \in \mathbf{D}$, the $c_{\gamma,i}$ that minimizes the residual error $\|R_{i-1}(t) - c_{\gamma,i} W_\gamma(t)\|^2$ is given by

$$\partial \|R_{i-1}(t) - c_{\gamma,i} W_\gamma(t)\|^2 / \partial c_{\gamma,i} = 0$$

$$\Leftrightarrow -2 \langle R_{i-1}, W_\gamma \rangle + 2 c_{\gamma,i} = 0 \text{ (since } \|W\gamma\|=1 \text{ for all } \gamma \in \Gamma)$$

$$\Leftrightarrow c_{\gamma,i} = \langle R_{i-1}, W_\gamma \rangle \text{ (which is Eq. 3)}$$

For this optimal value of $c_{\gamma,i}$, we have

$$\begin{aligned}\|R_{i-1}(t) - c_{\gamma,i} W_\gamma(t)\|^2 &= \|R_{i-1}(t) - \langle R_{i-1}, W_\gamma \rangle W_\gamma(t)\|^2 \\ &= \|R_{i-1}(t)\|^2 - 2\langle R_{i-1}, W_\gamma \rangle^2 + \langle R_{i-1}, W_\gamma \rangle^2 \\ &= \|R_{i-1}(t)\|^2 - \langle R_{i-1}, W_\gamma \rangle^2 \qquad \text{(Eq. 5)}\end{aligned}$$

Thus, the $W_\gamma \in \mathbf{D}$ that minimizes Eq. 4 is the one that minimizes Eq. 5, which corresponds to maximizing $|\langle R_{i-1}, W_\gamma \rangle|$. In other words, Eq. 4 is mathematically equivalent to find the index i so that to maximize the absolute value of the projection, $|c_{\gamma,i}|$. Formally,

$$\gamma_i = \arg\max_{\gamma \in \Gamma} \{ |c_{\gamma,i}| \} \qquad \text{(Eq. 6)}$$

Note we showed that a least-square problem is mathematically equivalent to a projection problem in a Hilbert space. The i^{th} matching pursuit atom is given by $W_{\gamma i}$. The corresponding i^{th} matching pursuit coefficient w_i is the optimal value of $c_{\gamma,i}$ (hence $w_i = \langle R_{i-1}, W_{\gamma i} \rangle$).

- Step 4. Compute the i^{th} residual $R_i(t)$ as

$$R_i(t) = R_{i-1}(t) - w_i W_{\gamma i}(t) \qquad \text{(Eq. 7)}$$

Note that $W_{\gamma i}(t)$ is orthogonal to the residual $R_i(t)$. In fact,

$$\begin{aligned}\langle W_{\gamma i}(t), R_i(t) \rangle &= \langle W_{\gamma i}(t), R_{i-1}(t) - w_i W_{\gamma i}(t) \rangle \text{ (using Eq. 7)} \\ &= \langle W_{\gamma i}(t), R_{i-1}(t) \rangle - w_i \langle W_{\gamma i}(t), W_{\gamma i}(t) \rangle \\ &= \langle W_{\gamma i}(t), R_{i-1}(t) \rangle - w_i \|W_{\gamma i}(t)\|^2 \\ &= \langle W_{\gamma i}(t), R_{i-1}(t) \rangle - w_i \quad (\text{since } \|W\gamma\| = 1 \text{ for all } \gamma \in \Gamma) \\ &= 0 \text{ (by definition of } w_i \text{ in the previous step)}\end{aligned}$$

• Step 5. Increment the iteration index i (i=i+1). If $i \leq N$, then go to step 2 to compute the orthogonal projections $c_{\gamma,i}$ for all atomic packet waveforms.

• Step 6. After N iterations, perform the back-fitting (also called back-projection) step. Let P_N the orthogonal projector onto the N atomic packet waveforms, $W_{\gamma i}(t)$, i=1,2,...,N. Compute

$$P_N R_N(t) = \sum_{i=1}^{N} x_i W_{\gamma i}(t)$$

The matching pursuit coefficients, w_i, are finally given by

$$w_i = c_{\gamma i,i} + x_i$$

Let us show that

$$\|R_{i-1}(t)\|^2 = w_i^2 + \|R_i(t)\|^2 \qquad \text{(Eq. 8)}$$

$$\|R_{i-1}(t)\|^2 = \|R_i(t) + w_i W_{\gamma i}(t)\|^2 \text{ (from Eq. 7)}$$

$$= \|R_i(t)\|^2 + w_i^2 \|W_{\gamma i}(t)\|^2 + 2 \text{ wi } \langle R_i(t), W_{\gamma i}(t)\rangle$$

$$= \|R_i(t)\|^2 + w_i^2 \|W_{\gamma i}(t)\|^2 \text{ (since } W_{\gamma i} \text{ is orthogonal to the residual } R_i(t) \text{ from step 4)}$$

Since $\|W\gamma\|=1$ for all $\gamma \in \Gamma$, the result follows.

The previous equation leads to the energy conservation equation (using the equality $R_0(t) \equiv f(t)$):

$$\|f(t)\|^2 = \sum_{i=1}^{N} w_i^2 + \|R_N(t)\|^2 \qquad \text{(Eq. 9)}$$

even though the atomic waveforms W_γ may not be orthogonal. Eq. 9 may also be written as

$$\|f(t)\|^2 = \sum_{j=1}^{J} \sum_{b=0}^{2^j-1} \sum_{k=1}^{n/2^j} w_{j,b,k}^2 + \|R_N(t)\|^2 \qquad \text{(Eq. 10)}$$

where the scale level j=1,2,...,J; the oscillation parameter $b=0,1,...,2^j-1$; and the translation shift $k=1,2,...,n/2^j$ (n is the sampling size; N is the number of atomic waveforms).

Although a matching pursuit is nonlinear, like an orthogonal expansion, it maintains an energy conservation (e.g., Eq. 10) which guarantees its convergence.

3. Time-Frequency Plane Plot

In the time-frequency plane plot (Fig. 4.5) each wavelet coefficient occupies a box having a constant area. The height of the box depends on the scale level, j, for the wavelet packet. Fine scale (lower values of j) coefficients occupy tall thin boxes and coarse scale (higher values of j) coefficients occupy flat wide boxes. In this figure, the color of each box corresponds to the absolute value of a wavelet packet coefficient $w_{j,b,k}$ (plotting out the square root of $|w_{j,b,k}|$ yields exactly the same time-frequency patterns but with different labels for the color bar). The horizontal and vertical center of a box is located roughly at the time and frequency center of the associated wavelet packet function. The width and height of the box is given by the time and frequency bandwidth. For a signal sampled at times $t_0, t_0+\Delta t, \ldots, t_0+(n-1)\Delta t$ where Δt is the sampling interval, the center of the box for coefficient $w_{j,b,k}$ is given by

$$x = t_0 + (2^j (k-.5)+.5)\ \Delta t \quad \text{and} \quad y = (b+.5)/2^j$$

Thus, the x-center of the box depends on both j (resolution level) and k (translation shift). The frequency y-center increases with increasing oscillations, b (for a fixed j), and decreases with increasing scale level, j (for a fixed b).

In time-frequency plots, the tradeoff between time and frequency is given by:

time bandwidth * frequency bandwidth ≥ constant.

This relationship is a version of the known "*Heisenberg uncertainty principle*". It says that a signal cannot be simultaneously concentrated in arbitrarily small time and frequency

regions. For example, if a signal is very highly concentrated in a coarse scale region, then it must be spread out in time. In terms of the time-frequency plane plot, the Heisenberg uncertainty principle means that each wavelet coefficient occupies a box having a constant area. In fact, the width and height of the box, for a given resolution level, j, are given by:

$$\Delta x = x(j, k+1) - x(j, k)$$

$$= t_0 + (2^j (k+1-.5)+.5)\ \Delta t - [t_0 + (2^j (k-.5)+.5)\ \Delta t]$$

$$= 2^j (k+.5-k+.5)\ \Delta t$$

$$= 2^j\ \Delta t$$

$$\Delta y = y(j, b+1) - y(j, b)$$

$$= (b+1+.5)/2^j - (b+.5)/2^j$$

$$= 1/2^j$$

Hence, the area of each box is $\Delta x\ \Delta y = (2^j\ \Delta t)\ (1/2^j) = \Delta t$ = constant. These boxes are sometimes called Heisenberg uncertainty boxes.

Fig. 4.5 displays only those Heisenberg uncertainty boxes that exhibit relatively powerful features (a power greater than an arbitrary threshold of 0.5 (dimensionless)). CDF is thus a nonstationary time series as evidenced by the significant "activity" at both fine and coarse wavelet scales.

a. Singularities in time

The "jumps" in the f(t) signal appear as fine-scale features (tall thin vertical boxes). These fine-scale features are well localized in time, but poorly localized in frequency. We define the singularities of f(t) in time by the tallest (thus most thin) vertical boxes; that is, by minimizing the time interval, Δx (recall that $\Delta x = 2^j\ \Delta t$),

which yields j=0 (i.e., the finest scale resembling a Dirac signal). The resolution level index j=0 corresponds to $\Delta x=\Delta t=1$ month. Hence, using the area equality $\Delta x\ \Delta y=\Delta t$, the frequency width is then given by $\Delta y=\Delta t/\Delta x=1$ which shows that the time singularity boxes must span the whole frequency spectrum.

b. Singularities in frequency

In contrast, the "smooth" part of the f(t) signal appears as coarse-scale features (relatively flat wide boxes) which are poorly localized in time. However, these coarse-scale features are generally well localized in frequency. We define singularities of f(t) in frequency by minimizing the frequency width, Δy(recall that $\Delta y=1/2^j$); that is by maximizing the wavelet scale (resolution) level, j, which yields j=J=5 (i.e., the coarsest scale). Hence, $\Delta y=1/2^J=0.03125$.

References

Aberson, S., 1998: Five-day tropical cyclone track forecasts in the North Atlantic Basin. *Wea. Forecasting*, **13**, 1005-1015.

Aberson, S. D., 2001: The ensemble of tropical cyclone track forecasting models in the North Atlantic Basin (1976-2000). *Bull. Amer. Meteor. Soc.*, **82**, 1895-1904.

Agee, E. M., 1991: Trends in cyclone and anticyclone frequency and comparison with periods of warming and cooling over the Northern Hemisphere. *J. Climate*, **4**, 263-268.

Akima, H., 1978: A method of bivariate interpolation and smooth surface fitting for irregularly distributed data points. *ACM Transactions on Mathematical Software*, **4**, 148-164.

Alexander, M. A., 1990: Simulation of the response of the North Pacific Ocean to the anomalous atmospheric circulation associated with El Niño. *Climate Dyn.*, **5**, 53-65.

Alexander, M. A., and C. Deser, 1995: A mechanism for the recurrence of wintertime midlatitude SST anomalies. *J. Phys. Oceanogr.*, **25**, 122-137.

Alexander, M. A., and C. Penland, 1996: Variability in a mixed layer ocean model driven by stochastic atmospheric forcing. *J. Climate*, **9**, 2424-2442.

Alexandersson, H., T. Schmith, K. Iden, and H. Tuomenvirta, 1998: Long-term variations of the storm climate over NW Europe. *Global Ocean Atmos. Syst.*, **6**, 97-120.

Alpert, P., B. U. Neeman, and Y. Shay-El, 1990: Intermonthly variability of cyclone tracks in the Mediterranean. *J. Climate*, **3**, 1474-1478.

Ambaum, M. H. P., B. J. Hoskins, and D. B. Stephenson, 2001: Arctic Oscillation or North Atlantic Oscillation? *J. Climate*, **14**, 3495-3507.

Anctil, F., and P. Coulibaly, 2004: Wavelet analysis of the interannual variability in southern Québec streamflow. *J. Climate*, **17**, 163-173.

Anderson, D., K. I. Hodges, and B. J. Hoskins, 2003: Sensitivity of feature-based analysis methods of storm tracks to the form of background field removal. *Mon. Wea. Rev.*, **131**, 565-573.

Anderson, J. R., and J. R. Gyakum, 1989: A diagnostic study of Pacific basin circulation regimes as determined from extratropical cyclone tracks. *Mon. Wea. Rev.*, **117**, 2672-2686.

Appenzeller, C., T. F. Stocker, and M. Anklin, 1998: North Atlantic Oscillation dynamics recorded in Greenland ice cores. *Science*, **282**, 446-449.

Appenzeller, C., A. K. Weiss, and J. Staehelin, 2000: North Atlantic oscillation modulates total ozone winter trends. *Geophys. Res. Lett.*, **8**, 1131-1134.

Araneo, D. C., and R. H. Compagnucci, 2004: Removal of systematic biases in S-mode principal components arising from unequal grid spacing. *J. Climate*, **17**, 394-400.

Arbic, B. K., and W. B. Owens, 2001: Climatic warming of Atlantic intermediate waters. *J. Climate*, **14**, 4091-4108.

Armstrong, R. L., and M. J. Brodzik, 1995: An earth-gridded SSM/I data set for cryospheric studies and global change monitoring. *Adv. Space. Res.*, **16**(10), 155-163.

Ballenzweig, E. M., 1959: A practical equal-area grid. *J. Geophys. Res.*, **64**, 647-651.

Barnett, T. P., M. Latif, N. Graham, M. Flugel, S. Pazan, and W. White, 1993: ENSO and ENSO-related predictability. Part I: Prediction of equatorial Pacific sea surface temperature with a hybrid coupled ocean-atmosphere model. *J. climate*, **6**, 1545-1566.

Barnett, T. P., D. W. Pierre, and R. Schnur, 2001: Detection of anthropogenic climate change in the world's oceans. *Science*, **292**, 270-274.

Barnett, T. P., and R. Preisendorfer, 1987: Origins and levels of monthly forecast skill for the United States surface air temperatures determined by canonical correlation analysis. *Mon. Wea. Rev.*, **115**, 756-773.

Barnston, A. G., and R. E. Livezey, 1987: Classification, seasonality, and persistence of low-frequency atmospheric circulation patterns. *Mon. Wea. Rev.*, **115**, 1083-1126.

Barnston, A. G., and C. F. Ropelewski, 1992: Prediction of ENSO episodes using Canonical Correlation Analysis. *J. Climate*, **5**, 1316-1345.

Barthelet, P., L. Terray, and S. Valcke, 1998: Transient CO_2 experiment using the ARPEGE/OPAICE non flux corrected coupled model. *Geophys. Res. Lett.*, **25**, 2277-2280.

Bell, G. D., and L. F. Bosart, 1989: A 15-year climatology of Northern Hemisphere 500 mb closed cyclone and anticyclone centers. *Mon. Wea. Rev.*, **117**, 2142-2164.

Berbery, E. H., and C. S. Vera, 1996: Characteristics of the Southern Hemisphere winter storm track with filtered and unfiltered data. *J. Atmos. Sci.*, **53**, 468-481.

Bjerknes, J., 1964: Atlantic air-sea interaction. *Advances in Geophysics*. Vol. **10**, Academic Press, 1-82.

Blackmon, M. L., 1976: A climatological spectral study of the 500 mb geopotential height of the Northern Hemisphere. *J. Atmos. Sci.*, **33**, 1607-1623.

Blackmon, M. L., Y. Lee, and J. Wallace, 1984: Horizontal structure of 500-mb height fluctuations with long, intermediate, and short time scales. *J. Atmos. Sci.*, **41**, 961-979.

Bladé, I., 1999: The influence of midlatitude ocean-atmosphere coupling on the low-frequency variability of a GCM. Part II: Interannual variability induced by tropical SST forcing. *J. Climate*, **12**, 21-45.

Blender, R., K. Fraedrich, and F. Lunkeit, 1997: Identification of cyclone track regimes in North Atlantic. *Quart. J. Roy. Meteor. Soc.*, **123**, 727-741.

Blender, R., and M. Shubert, 2000: Cyclone tracking in different spatial and temporal resolutions. *Mon. Wea. Rev.*, **128**, 377-384.

Boville, B. A, and P. R. Gent, 1998: The NCAR climate system model, version one. *J. Climate*, **11**, 1115-1130.

Branstator, G., 1995: Organization of storm track anomalies by recurring low-frequency circulation anomalies. *J. Atmos. Sci.*, **52**, 207-226.

Brennan, F. E., and P. J. Smith, 1978: The climatology of cyclones and anticyclones in the upper Mississippi and Ohio River Valleys and Great Lakes Region, 1950-74. *Proc. Indiana Acad. Sci.*, **87**, 391-402.

Bretherton, C. S., C. Smith, and J. M. Wallace, 1992: An intercomparison of methods for finding coupled patterns in climate data. *J. Climate*, **5**, 541-560.

Briggs, W., and R. A. Levine, 1997: Wavelets and field forecast verification. *Mon. Wea. Rev.*, **125**, 1329-1341.

Brinkmann, W. A. R., 1976: Surface temperature trend for the Northern Hemisphere-Updated. *Quat. Res.*, **6**, 355-358.

Bruce A., and H.-Y. Gao, 1996: *Applied Wavelet Analysis with S-PLUS*. Springer, 338 pp.

Budyko, M. I., 1982: *The Earth's Climate Past and Future*. Academic Press, 307 pp.

Businger, S., D. I. Knapp, and G. F. Watson, 1990: Storm following climatology of precipitation associated with winter cyclones originating over the Gulf of Mexico. *Wea. Forecasting*, **5**, 378-403.

Cai, M., and H. M. Van den Dool, 1991: Low-frequency waves and traveling storm tracks. Part I: Barotropic component. *J. Atmos. Sci.*, **48**, 1420-1444.

Carleton, A. M., 1981: Monthly variability of satellite-derived cyclonic activity for the Southern Hemisphere winter. *J. Climatol.*, **1**, 21-38.

Carleton, A. M., 1988: Meridional transport of eddy sensible heat in winters marked by extremes of the North Atlantic Oscillation, 1948/49-1979/80. *J. Climate*, **1**, 212-223.

Carnell, R. E., C. A. Senior, and J. F. B. Mitchell, 1996: An assessment of measures of storminess: Simulated changes in Northern Hemisphere winter due to increasing CO_2. *Climate Dyn.*, **12**, 467-476.

Casey, K. S., and P. Cornillon, 2001: Global and regional sea surface temperature trends. *J. Climate*, **14**, 3801-3818.

Cayan, D. R., 1992a: Latent and sensible heat flux anomalies over the northern oceans: The connection to monthly atmospheric circulation. *J. Climate*, **5**, 354-369.

Cayan, D. R., 1992b: Latent and sensible heat flux anomalies over the northern oceans: Driving the sea surface temperature. *J. Phys. Oceanogr.*, **22**, 859-881.

Chang, J. C. L., 2000: Tropical cyclone activity over the western North Pacific associated with El Niño and La Niña events. *J. Climate*, **13**, 2960-2972.

Chang, E. K. M., 2001: GCM and observational diagnoses of the seasonal and interannual variations of the Pacific storm track during the cool season. *J. Atmos. Sci.*, **58**, 1784-1800.

Chang, E. K. M., and Y. Fu, 2002: Interdecadal variations in Northern Hemisphere winter storm track intensity. *J. Climate*, **15**, 642-658.

Chang, E. K. M., and Y. Fu, 2003: Using mean flow change as a proxy to infer interdecadal storm track variability. *J. Climate*, **16**, 2178-2196.

Chang, E. K. M., S. Lee, and K. L. Swanson, 2002: Storm track dynamics. *J. Climate*, **15**, 2163-2183.

Chang, E. K. M., and I. Orlanski, 1993: On the dynamics of a storm track. *J. Atmos. Sci.*, **50**, 999-1015.

Changnon, D., J. J. Noel, and L. H. Maze, 1995: Determining cyclone frequencies using equal-area circles. *Mon. Wea. Rev.*, **123**, 2285-2294.

Changnon, S. A., and K. E. Kunkel, 1999: Rapidly expanding uses of climate data and information in agriculture and water resources: Causes and characteristics of new applications. *Bull. Amer. Meteor. Soc.*, **80**, 821-830.

Cherry, S., 1996: Singular Value Decomposition analysis and Canonical Correlation Analysis. *J. Climate*, **9**, 2003-2009.

Cherry, S., 1997: Some comments on Singular Value Decomposition analysis. *J. Climate*, **10**, 1759-1767.

Chow, V. T., D. R. Maidment, and L. W. Mays, 1988: *Applied Hydrology*. McGraw-Hill, Inc., 572 pp.

Christoph, M., U. Ulbrich, J. M. Oberhuber, and E. Roeckner, 2000: The role of ocean dynamics for low-frequency fluctuations of the NAO in a coupled ocean-atmosphere GCM. *J. Climate*, **13**, 2536-2549.

Christoph, M., U. Ulbrich, and P. Speth, 1997: Midwinter suppression of Northern Hemisphere storm track activity in the real atmosphere and in GCM experiments. *J. Atmos. Sci.*, **54**, 1589-1599.

Ciasto, L. M., and D. W. J. Thompson, 2004: North Atlantic atmosphere-ocean interaction on intraseasonal time scales. *J. Climate*, **17**, 1617-1621.

Clark, M. P., M. C. Serreze, and D. A. Robinson, 1999: Atmospheric controls on Eurasian snow extent. *Int. J. Climatol.*, **19**, 27-40.

Climatological Data, National Summary, 1950-1977. NOAA/EDIS, U.S. Dept. of Commerce, Washington, D.C.

CLIVAR, 1998: World Climate Research Programme Report No. 103, WMO/TD No. 869, 314 pp. [Available from International CLIVAR Project Office, Southampton Oceanography Centre, Empress Dock, Southampton SO14 3ZH, United Kingdom.]

Coifman, R., and Y. Meyer, 1991: Remarques sur l'analyse de Fourrier à fenêtre. *C. R. Acad. Sci.* Paris, **312**, 259-261.

Coifman, R., and V. Wickerhauser, 1992: Entropy-based algorithms for best basis selection. *IEEE Transactions on Information Theory*, **38**(2), 713-718.

Collins, M., S. F. B. Tett, and C. Cooper, 2000: The internal climate variability of HadCM3, a version of the Hadley Centre coupled model without flux adjustments. *Climate Dyn.*, **17**, 61-81.

Colucci, S. J., 1976: Winter cyclone frequencies over the eastern United States and adjacent western Atlantic, 1964-1973. *Bull. Amer. Meteor. Soc.*, **57**, 548-553.

Cook, R. D., and S. Weisberg, 1982: *Residuals and Influence in Regression.* Chapman and Hall, New York.

Cooper, C., and C. Gordon, 2001: North Atlantic oceanic decadal variability in the Hadley Centre coupled model. *J. Climate*, **15**, 45-72.

Cox, P., R. Betts, C. Bunton, R. Essery, P. R. Rowntree, and J. Smith, 1999: The impact of new land surface physics on the GCM simulation of climate and climate sensitivity. *Climate Dyn.*, **15**, 183-203.

Cressman, G. P., 1959: An operational objective analysis system. *Mon. Wea. Rev.*, **87**, 367-374.

Dai, A., G. A. Meehl, W. M. Washington, T. M. L. Wigley, and J. M. Arblaster, 2001: Ensemble simulation of twenty-first century climate changes: Business-as-usual versus CO_2 stabilization. *Bull. Amer. Meteor. Soc.*, **82**, 2377-2388.

Daily Series, Northern Hemisphere Sea Level Charts, 1958-1971: NOAA/EDIS, U.S. Dept. of Commerce, Washington, D.C.

Daley, R., 1991: *Atmospheric Data Analysis*. Cambridge University Press, 457 pp.

Daubechies, 1990: The wavelet transform, time-frequency localization and signal analysis. *IEEE Trans. Informat. Theory*, **36**, 961-1005.

Daubechies, 1992: *Ten Lectures on Wavelets*. CBMS-NSF Series in Applied Mathematics, No 61, Philadelphia, SIAM.

Davies, J. R., D. P. Rowell, and C. K. Folland, 1997: North Atlantic and European seasonal predictability using an ensemble of multidecadal atmospheric GCM simulations. *Int. J. Climatol.*, **17**, 1263-1284.

Davis, G., S. Mallat, and M. Avellaneda, 1997: Adaptive greedy approximations. *Constr. Approx.*, **13**, 57-98.

Davis, R., 1976: Predictability of sea surface temperature and sea surface pressure anomalies over the North Pacific Ocean. *J. Phys. Oceanogr.*, **6**, 249-266.

Delworth, T. L., 1996: North Atlantic interannual variability in a coupled ocean-atmosphere model. *J. Climate*, **9**, 2356-2375.

Delworth, T. L., and K. W. Dixon, 2000: Implications of the recent trend in the Arctic/North Atlantic Oscillation for the North Atlantic thermohaline circulation. *J. Climate*, **13**, 3721-3727.

Delworth, T. L., and R. J. Greatbatch, 2000: Multidecadal thermohaline circulation variability driven by atmospheric surface flux forcing. *J. Climate*, **13**, 1481-1495.

Delworth, T. L., S. Manabe, and R. Stouffer, 1993: Interdecadal variability of the thermohaline circulation in a coupled ocean-atmosphere model. *J. Climate*, **6**, 1993-2011.

Deser, C., 2000: On the teleconnectivity of the "Arctic Oscillation". *Geophys. Res. Lett.*, **27**, 779-782.

Deser, C., and M. L. Blackmon, 1993: Surface climate variations over the North Atlantic Ocean during winter: 1900-1989. *J. Climate*, **6**, 1743-1753.

Deser, C., and M. S. Timlin, 1997: Atmosphere-ocean interaction on weekly time scales in the North Atlantic and Pacific. *J. Climate*, **10**, 393-408.

Deser, C., J. E. Walsh, and M. E. Timlin, 2000: Arctic sea ice variability in the context of recent atmospheric circulation trends. *J. Climate*, **13**, 617-633.

DeWeaver, E., and S. Nigam, 2000: Zonal-eddy dynamics of the North Atlantic Oscillation. *J. Climate,* **13**, 3893-3914.

Dickson, R. R., 1996: Physical and biological effects of the North Atlantic Oscillation. ICES 1996 open lecture. CEFAS, Lowestoft, U.K.

Dickson, R., Lazier J., Meincke J., Rhines P., and Swift J., 1996: Long-term co-ordinated changes in the convective activity of the North Atlantic. *Progress in Oceanography*, **38**, 241-295.

Dickson, R., and J. Namias, 1976: North American influences on the circulation and climate of the North Atlantic sector. *Mon. Wea. Rev.*, **104**, 1255-1265.

Dickson, R. R., T. J. Osborn, J. W. Hurrell, J. Meincke, J. Blindheim, B. Adlandsvik, T. Vinje, G. Alekseev, and W. Maslowski, 2000: The Arctic Ocean response to the North Atlantic Oscillation. *J. Climate*, **13**, 2671-2696.

Dima, M., N. Rimbu, S. Stefan, and I. Dima, 2001: Quasi-decadal variability in the Atlantic basin involving Tropics-Midlatitudes and ocean-atmosphere interactions. *J. Climate*, **14**, 823-832.

Dolan, R., B. Hayden, C. Rea, and J. Heywood, 1979: Shoreline erosion rates along the middle Atlantic coast of the United States. *Geology*, **7**, 602-606.

Donoho, D. L., and I. M. Johnstone, 1995: Adapting to unknown smoothness via wavelet shrinkage. *Journal of the American Statistical Association*, **90**(432), 1200-1224.

Duchon, C. E., 1979: Lanczos filtering in one and two dimensions. *J. Appl. Meteor.*, **18**, 1016-1022.

Eden, C., and T. Jung, 2001: North Atlantic interdecadal variability: Oceanic response to the North Atlantic Oscillation (1865-1997). *J. Climate*, **14**, 676-691.

Ekstrom, P. A., and J. M. Hales, 2000: A wavelet-based approach for atmospheric pollution modeling: algorithm development. *Mon. Wea. Rev.*, **128**, 3169-3186.

El Hamly, M., P. J. Lamb, and D. H. Portis, 2001a: North Atlantic winter storm track variability and associations with monthly regional climate variations. *Proc. of the U.S. CLIVAR Atlantic Conference*, Boulder, CO, USA, June 12-14, U.S. CLIVAR Program, Washington, D. C., 54-57.

El Hamly, M., P. J. Lamb, and D. H. Portis, 2001b: Decadal variability in the North Atlantic Ocean involving ocean-atmosphere interactions. *Eos. Trans. AGU*, **82**(47), Fall Meet. Suppl., Abstract A32A-0031.

El Hamly, M., A. Mokssit, S. El Khatri, R. Sebbari, and F. Driouech, 1997: *La Prévision À Longue Écheance Au Maroc.* DMN Technical Report, 38 pp.

El Hamly, M., and R. Sebbari, 1997: Régionalisation de l'état pluviométrique au Maroc. *Info-Met*, **12**, 46-47.

El Hamly, M., R. Sebbari, S. El Khatri, D. H. Portis, M. N. Ward, and P. J. Lamb, 1997: On the North Atlantic Oscillation and the seasonal prediction of Moroccan precipitation. *Proc. of the AGU Fall Meeting*, San Francisco, CA, USA, OS08, Dec 8-12, F393-F394.

El Hamly, M., R. Sebbari, P. J. Lamb, M. N. Ward, and D. H. Portis, 1996: Prédiction des Précipitations au Maroc. *Info-Met* (Journal for the 5th WMO Technical Conference on the Management for the Development of the Meteorological Services in Africa, Casablanca, Morocco, November 19-23), 63-68.

El Hamly, M., R. Sebbari, P. J. Lamb, M. N. Ward, and D. H. Portis, 1998: Towards the seasonal prediction of Moroccan precipitation and its implications for water resources management. *Water Resources Variability in Africa during the XXth Century* (E. Servat, D. Hughes, J. M. Fritsch, and M. Hulme, Eds.) IAHS Publ. **252**, 79-87.

El Hamly, M., R. Sebbari, D. H. Portis, P. J. Lamb, and M. N. Ward, 2000: Temporal and time-scale behavior of North Atlantic Oscillation. *AGU Chapman Conference on the North Atlantic Oscillation*, Orense, Galicia, Spain, Nov 28-Dec 01.

El Hamly, M., R. Sebbari, D. H. Portis, M. N., Ward, and P. J. Lamb, 1997a: Regionalization of Moroccan precipitation for monitoring and prediction. *Proc. of the 7th Conference on Climate Variations of the Amer. Meteor. Soc.*, Long Beach, CA, USA, Feb 2-7, 354-357.

El Hamly, M., R. Sebbari, D. H. Portis, M. N. Ward, and P. J. Lamb, 1997b: Developing the relationship between Moroccan precipitation and the climate system. *Proc. of the 7th Conference on Climate Variations of the Amer. Meteor. Soc.*, Long Beach, CA, USA, Feb 2-7, 358.

Feldstein, S. B., 2002: The recent trend and variance increase of the Annular Mode. *J. Climate*, **15**, 88-94.

Flato, G. M., and G. J. Boer, 2001: Warming asymmetry in climate change simulations. *Geophys. Res. Lett.*, **28**, 195-198.

Flato, G. M., G. J. Boer, W. G. Lee, N. A. McFarlane, D. Ramsden, M. C. Reade, and A. J. Weaver, 2000: The Canadian Centre for Climate Modelling and Analysis Global Coupled Model and its Climate. *Climate Dyn.*, **16**, 451-467.

Flato, G. M., and Hibler, W. D. III, 1992: Modelling pack ice as a cavitating fluid. *J. Phys. Oceanogr.*, **22**, 626-651.

Folland, C. K., D. E. Parker, and F. E. Kates, 1984: Worldwide marine temperature fluctuations 1856-1981. *Nature*, **310**, 670-673.

Fournier, A., 2000: Introduction to orthonormal wavelet analysis with shift invariance: Application to observed atmospheric blocking spatial structure. *J. Atmos. Sci.*, **57**, 3856-3880.

Fournier, A., 2003: Atmospheric energetics in the wavelet domain. Part II: Time-averaged observed atmospheric blocking. *J. Atmos. Sci.*, **60**, 319-338.

Fraedrich, K., 1994: An ENSO impact on Europe? A review. *Tellus*, **46**, 541-552.

Fraedrich, K., and K. Muller, 1992: Climate anomalies in Europe associated with ENSO extremes. *Int. J. Climatol.*, **12**, 25-31.

Frankignoul, C., 1985: Sea surface temperature anomalies, planetary waves and air-sea feedback in the middle latitudes. *Rev. Geophys.*, **23**, 357-390.

Frankignoul, C., and K. Hasselmann, 1977: Stochastic climate models. Part II: Application to sea-surface temperature anomalies and thermocline variability. *Tellus*, **29**, 289-305.

Frankignoul, C., P. Müller, and E. Zorita, 1997: A simple model of the decadal response of the ocean to stochastic wind forcing. *J. Phys. Oceanogr.*, **27**, 1533-1546.

Gannabathula, S. S. D., W. Castro Jr, L. D. A. Sa, and K. P. R. V. Murty, 2000: Wavelet analysis of coherent structures above and within the Amazon rain forest. *Amer. Meteor. Soc., 15th Conference on Hydrology*, Long Beach, CA, USA, 9-14 January, 375-377.

Geng, Q., and M. Sugi, 2001: Variability of the North Atlantic cyclone activity in winter analyzed from NCEP-NCAR reanalysis data. *J. Climate*, **14**, 3863-3873.

Gent, P. R., and J. C. McWilliams, 1990: Isopycnal mixing in ocean circulation models. *J. Phys. Oceanogr.*, **20**, 150-155.

Giannini, A., M. A. Cane, and Y. Kushnir, 2001: Interdecadal changes in the ENSO teleconnection to the Caribbean region and the North Atlantic Oscillation. *J. Climate*, **14**, 2867-2879.

Gill, A. E., 1982: *Atmosphere-Ocean Dynamics*. Academic Press, 662 pp.

Glowienka-Hense, R., 1990: The North Atlantic Oscillation in the Atlantic-European SLP. *Tellus*, **42A**, 497-507.

Gong, X., and M. Richman, 1995: On the application of cluster analysis to growing season precipitation data in North America east of the Rockies. *J. Climate*, **8**, 897-931.

Gonzalez-Rouco, J. F., H. Heyen, E. Zorita, and F. Valero, 2000: Agreement between observed rainfall trends and climate change simulations in the Southwest of Europe. *J.*

climate, **13**, 3057-3065.

Goodman, J., and J. Marshall, 1999: A model of decadal middle-latitude atmosphere-ocean coupled modes. *J. Climate*, **12**, 621-641.

Gordon, C., C. Cooper, C. A. Senior, H. Banks, J. M. Gregory, T. C. Johns, J. F. B. Mitchell, and R. A. Wood, 2000: The simulation of SST, sea ice extents and ocean heat transports in a version of the Hadley Centre coupled model without flux adjustments. *Climate Dyn.*, **16**, 147-168.

Gordon, H. B., and S. P. O'Farrell, 1997: Transcient climate change in the CSIRO coupled model with dynamic sea ice. *Mon. Wea. Rev.*, **125**, 875-907.

Graf, H.-F., J. Perlwitz, I. Kirchner, and I. Schult, 1995: Recent northern winter climate trends, ozone changes and increased greenhouse gas forcing. *Contr. Atmos. Phys.*, **68**, 233-248.

Graham, N. E., T. P. Barnett, R. Wilde, M. Ponater, and S. Schubert, 1994: On the roles of tropical and midlatitude SSTs in forcing interannual to interdecadal variability in the winter Northern Hemisphere circulation. *J. Climate*, **7**, 1416-1448.

Gregory, D., G. J. Shutts, and J. R. Mitchell, 1998: A new gravity wave drag scheme incorporating anisotropic orography and low level wave breaking: Impact upon the climate of the UK Meteorological Office Unified Model. *Quart. J. Roy. Meteor. Soc.*, **124**, 463-493.

Grimm, A. M., V. R. Barros, and M. E. Doyle, 2000: Climate variability in Southern South America associated with El Niño and La Niña events. *J. Climate*, **13**, 35-58.

Grimm, A. M., S. E. T. Ferraz, and J. Gomes, 1998: Precipitation anomalies in Southern Brazil associated with El Niño and La Niña events. *J. Climate*, **11**, 2863-2880.

Grötzner, A., M. Latif, and T. P. Barnett, 1998: A decadal climate cycle in the North Atlantic Ocean as simulated by the ECHO coupled GCM. *J. Climate*, **11**, 831-847.

Gyakum, J. R., J. R. Anderson, R. H. Grumm, and E. L. Gruner, 1989: North Pacific cold-season surface cyclone activity: 1975-1983. *Mon. Wea. Rev.*, **117**, 1141-1155.

Hacker, J. P., E. S. Krayenhoff, and R. B. Stull, 2003: Ensemble experiments on numerical weather prediction error and uncertainty for a North Pacific forecast failure. *Wea. Forecasting*, **18**, 12-31.

Häkkinen, S., 2000: Decadal air-sea interaction in the North Atlantic based on observations and modeling results. *J. Climate*, **13**, 1195-1219.

Hall, N. M. J., B. J. Hoskins, P. Valdes, and C. A. Senior, 1994: Storm tracks in a high-resolution GCM with doubled carbon dioxide. *Quart. J. Roy. Meteor. Soc.*, **120**, 1209-1230.

Halliwell Jr, G. R., 1997: Decadal and multidecadal North Atlantic SST anomalies driven by standing and propagating basin-scale atmospheric anomalies. *J. Climate*, **10**, 2405-2411.

Hansen, D. V., and H. F. Bezdek, 1996: On the nature of decadal anomalies in North Atlantic sea surface temperature. *J. Geophys. Res.*, **101**, 8749-8758.

Harnik, N., and E. K. M. Chang, 2003: Storm track variations as seen in radiosonde observations and reanalysis data. *J. Climate*, **16**, 480-495.

Harr, P., and R. L. Elsberry, 1991: Tropical cyclone track characteristics as a function of large-scale circulation anomalies. *Mon. Wea. Rev.*, **119**, 1448-1468.

Hartigan, J. A., and M. A. Wong, 1979: A k-means clustering algorithm. *Applied Statistics*, **28**, 100-108.

Hasselmann, K., 1976: Stochastic climate models. Part I: Theory. *Tellus*, **28**, 473-485.

Hastenrath, S., and L. Greischar, 2001: The North Atlantic Oscillation in the NCEP-NCAR reanalysis. *J. Climate*, **14**, 2404-2413.

Hayden, B. P., 1981a: Secular variation in Atlantic coast extratropical cyclones. *Mon. Wea. Rev.*, **109**, 159-167.

Hayden, B. P., 1981b: Cyclone occurrence mapping-equal area or raw frequencies? *Mon. Wea. Rev.*, **109**, 168-172.

Hayden, B., R. Dolan, and W. Fedler, 1979: Spatial and temporal analyses of shoreline variations. *Coastal Eng*, **2**, 351-361.

Hayden, B. P., and W. Smith, 1982: Season-to-season cyclone frequency prediction. *Mon. Wea. Rev.*, **110**, 239-253.

Hennessy, K. J., 1998: Climate change output. CSIRO Atmospheric research Technical Paper No 37.

Hense, A., R. G. Hense, H. von Storch, and U. Stahler, 1990: Northern Hemisphere atmospheric response to changes of Atlantic Ocean SST on decadal timescales: A GCM experiment. *Climate Dyn.*, **4**, 157-174.

Hense, R. G., 1990: The North Atlantic Oscillation in the Atlantic-European SLP. *Tellus*, **42A**, 497-507.

Herrera, R. G., D. G. Puyol, E. H. Martin, L. G. Presa, and P. R. Rodriguez, 2001: Influence of the North Atlantic Oscillation on the Canary Islands precipitation. *J. Climate*, **14**, 3889-3903.

Hirsch, M. E., A. T. DeGaetano, and S. J. Colucci, 2001: An East Coast winter storm climatology. *J. Climate,* **14**, 882-899.

Hodges, K. I., 1994: A general method for tracking analysis and its implication to meteorological data. *Mon. Wea. Rev.*, **122**, 2573-2586.

Hoerling, M. P., J. W. Hurrell, and T. Xu, 2001: Tropical origins for recent North Atlantic climate change. *Science*, **292**, 90-92.

Hoskins, B. J., and K. I. Hodges, 2002: New perspectives on the Northern Hemisphere winter storm tracks. *J. Atmos. Sci.*, **59**, 1041-1061.

Hoskins, B. J., and P. D. Sardeshmukh, 1987: Transcient eddies and the seasonal mean rotational flow. *J. Atmos. Sci.*, **44**, 328-338.

Hoskins, B. J., and P. J. Valdes, 1990: On the existence of storm tracks. *J. Atmos. Sci.*, **47**, 1854-1864.

Hosler, C. L., and L. A. Gamage, 1956: Cyclone frequencies in the United States for the period 1905-1954. *Mon. Wea. Rev.*, **84**, 388-390.

Houghton, R. W., 1996: Subsurface quasi-decadal fluctuations in the North Atlantic. *J. Climate*, **9**, 1363-1373.

Houghton, J. T., Y. Ding, D. J. Griggs, M. Noguer, P. J. van der Linden, D. Xiaosu, K. Maskell, and C. A. Johnson, Eds., 2001: *Climate Change 2001: The Scientific Basis. Third Assessment Report of the Intergovernmental Panel on Climate Change*. Cambridge University Press, 944 pp.

Houghton, J. T., L. G. Meira Filho, B. A. Callander, N. Harris, A. Kattenberg, and K. Maskell K, 1996: *Climate Change 1995: The Science of Climate Change*. Cambridge University Press.

Hu, Q., 1997: On the uniqueness of the Singular Value Decomposition in meteorological applications. *J. Climate*, **10**, 1762-1766.

Hunke, E. C., and J. K. Dukowicz, 1997: An elastic-viscous-plastic model for sea ice dynamics. *J. Phys. Oceanogr.*, **27**, 1849-1867.

Hurrell, J. W., 1995a: Decadal trends in the North Atlantic Oscillation: Regional temperatures and precipitation. *Science*, **269**, 676-679.

Hurrell, J. W., 1995b: Transcient eddy forcing of the rotational flow during northern winter. *J. Atmos. Sci.*, **52**, 2286-2301.

Hurrell, J. W., 1996: Influence of variations in extratropical wintertime teleconnections on Northern Hemisphere temperature. *Geophys. Res. Lett.*, **23**, 665-668.

Hurrell, J. W., Y. Kushnir, G. Ottersen, and M. Visbeck, Eds., 2003: *The North Atlantic Oscillation: Climate Significance and Environmental Impact.* Geophysical Monograph Series, **134**, 279 pp.

Hurrell, J. W., Y. Kushnir, and M. Visbeck, 2001: The North Atlantic Oscillation. *Science*, **291**, 603-605.

Hurrell, J. W., and H. van Loon, 1997: Decadal variations in climate associated with the North Atlantic Oscillation. *Climatic Change*, **36**, 301-326.

James, I. N., and P. M. James, 1989: Ultralow-frequency variability in a simple circulation model. *Nature*, **342**, 53-55.

Johns, T. C., R. E. Carnell, J. F. Crossley, J. M. Gregory, J. F. B Mitchell, C. A. Senior, S. F. B. Tett, and R. A. Wood, 1997: The second Hadley Centre coupled ocean-atmosphere GCM: Model description, spinup and validation. *Climate Dyn.*, **13**, 103-134.

Joly, A., and Coauthors, 1997: The fronts and Atlantic storm-track experiment (FASTEX): Scientific objectives and experimental design. *Bull. Amer. Meteor. Soc.*, **78**, 1917-1940.

Jones, P. D., 1994: Recent warming in global temperature series, *Geophys. Res. Lett.*, **21**, 1149-1152.

Jones, R. H., 1975: Estimating the variance of time averages. *J. Appl. Meteor.*, **14**, 159-163.

Jordan, J. R., R. J. Lataitis, and D. A. Carter, 1997: Removing ground and intermittent clutter contamination from wind profiler signals using wavelet transforms. *J. Atmos. Oceanic Tech.*, **14**, 1280-1297.

Joyce, T. M., C. Deser, and M. A. Spall, 2000: The relation between decadal variability of the subtropical mode water and the North Atlantic Oscillation. *J. Climate*, **13**, 2550-2569.

Kageyama, M., P. J. Valdes, G. Ramstein, C. Hewitt, and U. Wyputta, 1999: Northern Hemisphere storm tracks in present day and last glacial maximum climate simulations: A comparison of the European PMIP models. *J. Climate*, **12**, 742-760.

Kalnay, E., and Coauthors, 1996: The NCEP/NCAR 40-Year Reanalysis Project. *Bull. Amer. Meteor. Soc.*, **77**, 437-471.

Karas, S., and A. Zangvil, 1999: A preliminary analysis of disturbance tracks over the Mediterranean Basin. *Theor. Appl. Climatol.*, **64**, 239-248.

Karl, T. R., A. J. Koscielny, and H. F. Diaz, 1982: Potential errors in the application of Principal Component (Eigenvector) analysis to geophysical data. *J. Appl. Meteor.*, **21**, 1183-1186.

Karl, T. R., and K. E. Trenberth, 2003: Modern global climate change. *Science*, **302**, 1719-1723.

Karoly, D. J., K. Braganza, P. A. Stott, J. M. Arblaster, G. A. Meehl, A. J. Broccoli, and K. W. Dixon, 2003: Detection of a human influence on North American climate. *Science*, **302**, 1200-1203.

Keegan, T. J., 1958: Arctic synoptic activity in winter. *J. Meteor.*, **15**, 513-521.

Kerr, R., 1997: A new driver for the Atlantic's moods and Europe's weather? *Science*, **275**, 754-755.

Key, J. R., and A. C. K. Chan, 1999: Multidecadal global and regional trends in 1000 mb and 500 mb cyclone frequencies. *Geophys. Res. Lett.*, **26**, 2053-2056.

Kharin, V. V., 1995: The relationship between sea surface temperature anomalies and the atmospheric circulation in GCM experiments. *Climate Dyn.*, **11**, 359-375.

Kim, K., and Q. Wu, 1999: A comparison study of EOF techniques: Analysis of nonstationary data with periodic statistics. *J. Climate*, **12**, 185-199.

Kistler, R., and Co-authors, 2001: The NCEP-NCAR 50-year reanalysis: monthly means CD-ROM and documentation. *Bull. Amer. Meteor. Soc.*, **82**, 247-268.

Klein, W. H., 1957: Principal tracks and mean frequencies of cyclones and anticyclones in the Northern Hemisphere. *Research Paper No. 40*, U.S. Weather Bureau, Washington, D.C., 60 pp.

Klein, W. H., 1958: The frequency of cyclones and anticyclones in relation to the mean circulation. *J. Meteor.*, **15**, 98-102.

Knippertz, P., A. H. Fink, A. Reiner, and P. Speth, 2003: Three late summer/early autumn cases of tropical-extratropical interactions causing precipitation in Northwest Africa. *Mon. Wea. Rev.*, **131**, 116-135.

König, W., R. Sausen, and F. Sielmann, 1993: Objective identification of cyclones in GCM simulations. *J. Climate*, **6**, 2217-2231.

Kovacevic, J., and I. Daubechies, 1996: Special issue on wavelets. *Proc. IEEE*, **84**, 507-688.

Kowalczyk, E. A., J. G. Garratt, and P. B. Krummel, 1994: Implementation of a soil-canopy scheme into the CSIRO GCM - regional aspects of the model response. *Technical Paper* 32, CSIRO Division of Atmospheric Research.

Kraus, E. B., and J. S. Turner, 1967: A one dimensional model of the seasonal thermocline II. The general theory and its consequences. *Tellus*, **19**, 98-105.

Kushnir, Y., 1994: Interdecadal variations in the North Atlantic sea surface temperature and associated atmospheric conditions. *J. Climate*, **7**, 141-157.

Kushnir, Y., 2001: The interaction between the NAO and North Atlantic SST: Evidence of feedback? *Eos Trans. AGU*, **82**(47), Fall Meet. Suppl., Abstract A31A-05.

Kushnir, Y., V. Cardone, J. Greenwood, and M. Cane, 1997: The recent increase in North Atlantic wave heights. *J. Climate*, **10**, 2107-2113.

Kushnir, Y., and I. M. Held, 1996: Equilibrium atmospheric response to North Atlantic SST anomalies. *J. Climate*, **9**, 1208-1220.

Kushnir, Y., W. A. Robinson, I. Blade, N. M. J. Hall, S. Peng, and R. Sutton, 2002: Atmospheric GCM response to extratropical SST anomalies: Synthesis and evaluation. *J. Climate*, **15**, 2233-2256.

Kutzbach, J. E., 1970: Large-scale features of monthly mean Northern Hemisphere anomaly maps of sea-level pressure. *Mon. Wea. Rev.*, **98**, 708-716.

Lab Sea Group, 1998: The Labrador Sea Deep Convection Experiment. *Bull. Amer. Meteor. Soc.*, **79**, 2033-2058.

Lamb, P. J., 1994: Cooperative Research on "Al Moubarak" and Moroccan Precipitation. *Proposal to USAID/Morocco and DMN*, April 1994. CIMMS, The University of Oklahoma, Norman, OK, 49 pp.

Lamb, P. J., 1997: Cooperative Research on "Al Moubarak" and Moroccan Precipitation. *Proposal to DMN* (Department of Public Works, Kingdom of Morocco), September 1997. CIMMS, The University of Oklahoma, Norman, OK, 9 pp.

Lamb, P. J., 2002: The climate revolution: a perspective (an Editorial Essay). *Climatic Change*, **54**, 1-9.

Lamb, P. J., M. El Hamly, and D. H. Portis, 1997a: North Atlantic Oscillation. *Geo Observateur*, **7**, 103-113.

Lamb, P. J., M. El Hamly, R. Sebbari, D. H. Portis, and M. N. Ward, 2000: Application of North Atlantic Oscillation for seasonal prediction of Moroccan precipitation. *AGU Chapman Conference on the North Atlantic Oscillation*, Orense, Galicia, Spain, Nov 28-Dec 01.

Lamb, P. J., M. El Hamly, M. N. Ward, R. Sebbari, and D. H. Portis, 1997b: Towards the seasonal prediction of Moroccan precipitation. *Proc. of the 22nd Annual Climate Diagnostics and Prediction Workshop*, Berkeley, CA, USA, October 6-10, 57-60.

Lamb, P. J., and R. A. Peppler, 1987: North Atlantic Oscillation: Concept and application. *Bull. Amer. Meteor. Soc.*, **68**, 1218-1225.

Lamb, P. J., and R. A. Peppler, 1991: West Africa. Chapter 5 in *Teleconnections Linking Worldwide Climate Anomalies: Scientific Basis and Societal Impact* (M. H. Glantz, R. W. Katz, and N. Nicholls, Eds.), Cambridge University Press, 121-189.

Lamb, P. J., and M. B. Richman, 1990: Use of cooperative weather station data in contemporary climate research. *Transactions of the Illinois State Academy of Science*, **83**, 70-81.

Lambert, S. J., 1988: A cyclone climatology of the Canadian Climate Centre General Circulation Model. *J. Climate*, **1**, 109-115.

Lambert, S. J., 1995: The effect of enhanced greenhouse warming on winter cyclone frequencies and strengths. *J. Climate*, **8**, 1447-1452.

Lambert, S. J., 1996: Intense extratropical Northern Hemisphere winter cyclone events: 1899-1991. *J. Geophys. Res.*, **101** (D16), 21319-21325.

Lang, M., H. Guo, J. E. Odegard, C. S. Burrus, and R. O. Wells, 1995: Nonlinear processing of a shift invariant DWT for noise reduction. In *Wavelet Applications II*, **2491**, 640-651. SPIE.

Latif, M., K. Arpe, and E. Roeckner, 2000: Oceanic control of decadal North Atlantic sea level pressure variability in winter. *Geophys. Res. Lett.*, **27**, 727-730.

Latif, M., and T. P. Barnett, 1994: Causes of decadal variability over the North Pacific and North America. *Science*, **266**, 634-637.

Latif, M., T. Stockdale, J. Wolff, G. Burgers, E. Maier-Reimer, and M. M. Junge, 1994: Climatology and variability in the ECHO coupled GCM. *Tellus*, **46**, 351-366.

Lau, K. M., and H. Weng, 1995: Climate signal detection using wavelet transform: How to make a time series sing. *Bull. Amer. Meteor. Soc.*, **76**, 2391-2402.

Lau, N.-C., 1988: Variability of the observed midlatitude storm tracks in relation to low-frequency changes in the circulation pattern. *J. Atmos. Sci.*, **45**, 2718-2743.

Lau, N.-C., and M. J. Nath, 1990: A general circulation model study of the atmospheric response to observed extratropical SST anomalies in 1950-79. *J. Climate*, **3**, 965-989.

Lau, N.-C, and M. J. Nath, 2001: Impact of ENSO on SST variability in the North Pacific and North Atlantic: Seasonal dependence and role of extratropical sea-air coupling. *J. Climate*, **14**, 2846-2866.

Leith, C. E., 1973: The standard error of time-average estimates of climatic means. *J. Appl. Meteor.*, **12**, 1066-1069.

Leung, L. R., A. F. Hamlet, D. P. Lettenmaier, and A. Kumar, 1999: Simulations of the ENSO hydroclimate signals in the Pacific Northwest Columbia River Basin. *Bull. Amer.*

Meteor. Soc., **80**, 2313-2329.

Levitus, S., J. I. Antonov, and T. P. Boyer, 1994: Interannual variability of temperature at a depth of 125 m in the North Atlantic Ocean. *Science*, **266**, 96-99.

Levitus, S., and T. P. Boyer, 1994: *World Ocean Atlas 1994*, Volume **4**: Temperature. NOAA/NESDIS E/OC21, US Department of Commerce, Washington, DC, 117 pp.

Levitus, S., R. Burgett, and T. P. Boyer, 1995: *World Ocean Atlas 1994*, Volume **3**: Salinity. NOAA/NESDIS E/OC21, US Department of Commerce, Washington, DC, 99 pp.

Lindsay, R. W., 1998: Temporal variability of the energy balance of thick Arctic pack ice. *J. Climate*, **3**, 313-333.

Lindzen, R. S., and B. J. Farrell, 1980: A simple approximate result for the maximum growth rate of baroclinic instabilities. *J. Atmos. Sci.*, **37**, 1648-1654.

Livezey, R. E., and T. M. Smith, 1999: Considerations for use of the Barnett and Preisendorfer (1987) algorithm for Canonical Correlation Analysis of climate variations. *J. Climate*, **12**, 303-305.

Lorenz, E. N., 1950: Seasonal and irregular variations of the Northern Hemisphere sea-level pressure profile. *J. Meteor.*, **8**, 52-59.

Luksch, U., 1996: Simulation of North Atlantic low-frequency SST variability. *J. Climate*, **9**, 2083-2092.

Luksch, U., H. von Storch, and E. Maier-Reimer, 1990: Modeling North Pacific SST anomalies as a response to anomalous atmospheric forcing. *J. Mar. Sys.*, **1**, 155-168.

Luterbacher, J., C. Schmutz, D. Gyalistras, E. Xoplaki, and H. Wanner, 1999: Reconstruction of monthly NAO and EU indices back to AD 1675. *Geophys. Res. Lett.*, **26**, 2745-2748.

Luterbacher, J., E. Xoplaki, D. Dietrich, P. D. Jones, T. D. Davies, D. Portis, J. F. Gonzalez-Rouco, H. von Storch, D. Gyalistras, C. Casty, and H. Wanner, 2002: Extending North Atlantic Oscillation reconstructions back to 1500. *Atmos. Sci. Lett.*, doi:**10.1006**/asle.2001.0044.

Madden, R., and W. Sadeh, 1975: Empirical estimates of the standard error of time-averaged climatic means. *J. Appl. Meteor.*, **14**, 164-169.

Magnusdottir, G., C. Deser, and R. Saravanan, 2004: The effects of North Atlantic SST and sea ice anomalies on the winter circulation in CCM3. Part I: Main features and storm track characteristics of the response. *J. Climate*, **17**, 857-876.

Mak, M., 1995: Orthogonal wavelet analysis: Interannual variability in the sea surface temperature. *Bull. Amer. Meteor. Soc.*, **76**, 2179-2186.

Mallat, S. G., 1999: *A Wavelet Tour of Signal Processing*. 2nd ed. Academic Press, 637 pp.

Mallat, S., and Z. Zhang, 1993: Matching pursuits with time-frequency dictionaries. *IEEE Transactions on Signal Processing*, **41**(12), 3397-3415.

Malmgren, B. A., A. Winter, and D. Chen, 1998: El Niño-Southern Oscillation and North Atlantic Oscillation control of climate in Puerto Rico. *J. Climate*, **11**, 2713-2718.

Mann, M. E., and J. Park, 1996: Joint spatio-temporal modes of surface temperature and sea level pressure variability in the Northern Hemisphere during the last century. *J. Climate*, **9**, 2137-2162.

Mariners Weather Log, 1958-1977: NOAA/EDIS, U.S. Dept. of Commerce, Washington, D.C.

Marshall, J., H. Johnson, and J. Goodman, 2001: A study of the interaction of the North Atlantic Oscillation with ocean circulation. *J. Climate*, **14**, 1399-1421.

Marshall, J., Y. Kushnir, D. Battisti, P. Chang, A. Czaja, R. Dickson, J. Hurrell, M. McCartney, R. Saravann, and M. Visbeck, 2001: North Atlantic climate variability: Phenomena, impacts and mechanisms. *Int. J. Climatol.*, **21**, 1863-1898.

Marshall, J., Y. Kushnir, D. Battisti, P. Chang, J. Hurrell, M. McCartney, and M. Visbeck, 1997: Atlantic climate variability. A white paper.

McCabe, G. J., M. P. Clark, and M. C. Serreze, 2001: Trends in Northern Hemisphere surface cyclone frequency and intensity. *J. Climate*, **14**, 2763-2768.

McCartney, M. S., R. G. Curry, and H. F. Bezdek, 1996: North Atlantic's transformation pipeline chills and redistributes subtropical water. *Oceanus*, **39**, 19-23.

McFarlane, N. A., G. J. Boer, J.-P. Blanchet, and M. Lazare, 1992: The Canadian Climate Centre Second-Generation General Circulation Model and its equilibrium climate. *J. Climate*, **5**, 1013-1044.

McGregor, J. L., 1993: Economical determination of departure points for semi-Lagrangian models. *Mon. Wea. Rev.*, **121**, 221-230.

McGregor, J. L., K. J. Walsh, and J. J. Katzfey, 1993: Nested modelling for regional climate studies. In: A. J. Jakeman, M. B. Beck and M. J. McAleer (Eds.), *Modelling Change in Environmental Systems*, J. Wiley and Sons, 367-386.

Meehl, G. A., 1995: Global coupled general circulation models. *Bull. Amer. Meteor. Soc.*, **76**, 951-957.

Meehl, G. A., G. J. Boer, C. Covey, M. Latif, and R. J. Stouffer, 2000: The Coupled Model Intercomparison Project (CMIP). *Bull. Amer. Meteor. Soc.*, **81**, 313-318.

Merkel, U., and M. Latif, 2001: A high-resolution AGCM study of the El Niño impact on the North Atlantic/European sector. Max-Planck-Institut für Meteorologie. Report No. 325, 13 pp.

Mikolajewicz, U., and E. Maier-Reimer, 1990: Internal secular variability in an ocean general circulation model. *Climate Dyn.*, **4**, 145-156.

Milton, S. F., and C. A. Wilson, 1996: The impact of parametrized sub-grid scale orographic forcing on systematic errors in a global NWP model. *Mon. Wea. Rev.*, **124**, 2023-2045.

Molinari, R. L., D. A. Mayer, J. F. Festa, and H. F. Bezdek, 1997: Multi-year variability in the near-surface temperature structure of the midlatitude western North Atlantic Ocean. *J. Geophys. Res.*, **102** (C2), 3267-3278.

Monahan, A. H., L. Pandolfo, and J. C. Fyfe, 2001: The preferred structure of variability of the Northern Hemisphere atmospheric circulation. *Geophys. Res. Lett.*, **28**, 1019-1022.

Montroy, D. L., 1997: Linear relationship of central and eastern North American precipitation to tropical Pacific sea surface temperature anomalies, *J. Climate*, **10**, 541-558.

Montroy, D. L., M. B. Richman, and P. J. Lamb, 1998: Observed nonlinearities of monthly teleconnections between tropical Pacific sea surface temperature anomalies and central and eastern North American precipitation. *J. Climate*, **11**, 1812-1835.

Murray, R. J., and I. Simmonds, 1991a: A numerical scheme for tracking cyclone centers from digital data. Part I: Development and operation of the scheme. *Aust. Meteor. Mag.*, **39**, 155-166.

Murray, R. J., and I. Simmonds, 1991b: A numerical scheme for tracking cyclone centers from digital data. Part II: Application to January and July general circulation model simulations. *Aust. Meteor. Mag.*, **39**, 167-180.

Nagata and Coauthors, 2001: Meeting summary: Third COMPARE workshop: A model intercomparison experiment of tropical cyclone intensity and track prediction. *Bull. Amer. Meteor. Soc.*, **82**, 2007-2020.

Nakamura, H., 1992: Midwinter suppression of baroclinic wave activity in the Pacific. *J. Atmos. Sci.*, **49**, 1629-1642.

Namias, J., and R. M. Born, 1970: Temporal coherence in North Pacific sea-surface temperature patterns. *J. Geophys. Res.*, **75**, 5952-5955.

National Research Council, 2001: *Climate Change Science: an Analysis of Some Key Questions*. National Academy Press, Washington, D.C., 29 pp.

Neelin, J. D., M. Latif, and F. F. Jin, 1994: Dynamics of coupled ocean-atmosphere models: The tropical problem. *Annu. Rev. Fluid. Mech.*, **26**, 617-659.

Neumann, C. J., and J. M. Pellissier, 1981: Models for the prediction of tropical cyclone motion over the North Atlantic: An operational evaluation. *Mon. Wea. Rev.*, **109**, 522-538.

Newman, M., and P. D. Sardeshmukh, 1995: A caveat concerning Singular Value Decomposition. *J. Climate*, **8**, 352-360.

Nielsen, J. W., and R. M. Dole, 1992: A survey of extratropical cyclone characteristics during GALE. *Mon. Wea. Rev.*, **120**, 1156-1167.

NOAA, 1964-1973: *North American Surface Charts*, January 1964-December 1973.

O'Farrell, S. P., 1998: Investigation of the dynamic sea-ice component of a coupled atmosphere sea-ice general circulation model. *J. Geophys. Res.*, **103**, 15751-15782.

Orlanski, I., and B. Gross, 2000: The life cycle of baroclinic eddies in a storm track environment. *J. Atmos. Sci.*, **57**, 3498-3513.

Osborn, T. J., K. R. Briffa, S. F. B. Tett, P. D. Jones, and R. M. Trigo, 1999: Evaluation of the North Atlantic Oscillation as simulated by a coupled climate model. *Climate Dyn.*, **15**, 685-702.

Ostermeier, G. M., and J. M. Wallace, 2003: Trends in the North Atlantic Oscillation-Northern Hemisphere annular mode during the twentieth century. *J. Climate*, **16**, 336-341.

Ouergli, A., 2002: Hilbert transform from wavelet analysis to extract the envelope of an atmospheric mode: Examples. *J. Atmos. Oceanic Tech.*, **19**, 1082-1086.

Overland, J. E., and C. H. Pease, 1982: Cyclone climatology of the Bering Sea and its relation to sea ice extent. *Mon. Wea. Rev.*, **110**, 5-13.

Overland, J. E., and R. W. Preisendorfer, 1982: A significance test for principal components applied to a cyclone climatology. *Mon. Wea. Rev.*, **110**, 1-4.

Paciorek, C. J., J. S. Risbey, V. Ventura, and R. D. Rosen, 2002: Multiple indices of Northern Hemisphere cyclone activity, winters 1949-99. *J. climate*, **15**, 1573-1590.

Paeth, H., A. Hense, R. Glowienka-Hense, S. Voss, and U. Cubasch, 1999: The North Atlantic Oscillation as an indicator for greenhouse-gas induced regional climate change. *Climate Dyn.*, **15**, 953-960.

Palmer, T. N., and Z. Sun, 1985: A modelling and observational study of the relationship between sea surface temperatures in the northwest Atlantic and the atmospheric general

circulation. *Quart. J. Roy. Meteor. Soc.*, **111**, 947-975.

Palutikof, J. P., C. M. Goodess, S. J. Watkins, and T. Holt, 2002: Generalizing rainfall and temperature scenarios at multiple sites: Examples from the Mediterranean. *J. Climate*, **15**, 3529-3548.

Palutikof, J. P., J. A. Winkler, C. M. Goodess, and J. A. Andersen, 1997: The simulation of daily temperature time series from GCM output. Part I: Comparison of model data with observations. *J. Climate*, **10**, 2497-2513.

Parker, S. S., J. T. Hawes, S. J. Colucci, and B. P. Hayden: 1989: Climatology of 500-mb cyclones and anticyclones, 1950-85. *Mon. Wea. Rev.*, **3**, 558-571.

Peng, S., and J. Fyfe, 1996: The coupled patterns between sea level pressure and sea surface temperature in the midlatitude North Atlantic. *J. Climate*, **9**, 1824-1839.

Peng, S., L. A. Mysak, J. Derome, H. Ritchie, and B. Dugas, 1995: The differences between early and midwinter atmospheric responses to sea surface temperature anomalies in the northwest Atlantic. *J. Climate*, **8**, 137-157.

Peng, S., and W. A. Robinson, 2001: Relationships between atmospheric internal variability and the responses to an extratropical SST anomaly. *J. Climate*, **14**, 2943-2959.

Peng, S., W. A. Robinson, and S. Li, 2003: Mechanisms for the NAO responses to the North Atlantic SST triple. *J. Climate*, **16**, 1987-2004.

Peng, S., and J. S. Whitaker, 1999: Mechanisms determining the atmospheric response to midlatitude SST anomalies. *J. Climate*, **12**, 1393-1408.

Perreault, L., M. Ache, M. Slivitzky, and B. Bobee, 1999: Detection of changes in precipitation and runoff over eastern Canada and US using a Bayesian approach. *Stochastic Environmental Research and Risk Assessment*, **13**, 201-216.

Peterssen, S., 1950: Some aspects of the general circulation of the atmosphere. In *Centenary Proc. of the Roy. Meteor. Soc.*, London, Royal Meteorological Society, 120-155.

Peterssen, S., 1956: *Weather Analysis and Forecasting*, Vol. I, *Motion and Motion Systems*, Second Edition. New York, McGraw-Hill Book Co., 428 pp.

Piera, J., E. Roget, and J. Catalan, 2002: Turbulent patch identification in microstructure profiles: A method based on wavelet denoising and Thorpe displacement analysis. *J. Atmos. Oceanic Tech.*, **19**, 1390-1402.

Pittalwala, I. I., and S. Hammed, 1991: Simulation of the North Atlantic Oscillation in a General Circulation Model. *Geophys. Res. Lett.*, **18**, 841-844.

Pope, V. D., M. L. Gallani, P. R. Rowntree, and R. A. Stratton, 2000: The impact of new physical parametrizations in the Hadley Centre climate model – HadAM3. *Climate Dyn.*, **16**, 123-146.

Portis, D. H., J. E. Walsh, M. El Hamly, and P. J. Lamb, 2001: Seasonality of the North Atlantic Oscillation. *J. Climate*, **14**, 2069-2078.

Pozo-Vazquez, D., M. J. Esteban-Parra, F. S. Rodrigo, and Y. Castro-Diez, 2001: The association between ENSO and winter atmospheric circulation and temperature in the North Atlantic region. *J. Climate*, **14**, 3408-3420.

Preisendorfer, R. H., 1988: *Principal Component Analysis in Meteorology and Oceanography*. Elsevier, 425 pp.

Primeau, F., and P. Cessi, 2001: Coupling between wind-driven currents and midlatitude storm tracks. *J. Climate*, **14**, 1243-1261.

Pulwarty, R. S., and K. T. Redmond, 1997: Climate and Salmon restoration in the Columbia River Basin: The role and usability of seasonal forecasts. *Bull. Amer. Meteor. Soc.*, **78**, 381-397.

Raga, G. B., R. E. Stewart, and J. W. Strapp, 1994: Mesoscale structure of precipitation bands in a North Atlantic winter storm. *Mon. Wea. Rev.*, **122**, 2039-2051.

Rajagopalan, B., Y. Kushnir, and Y. M. Tourre, 1998: Observed decadal midlatitude and tropical Atlantic climate variability. *Geophys. Res. Lett.*, **25**, 3967-3970.

Ratcliffe, R., and R. Murray, 1970: New lag associations between North Atlantic sea surface temperature and European pressure applied to long-range weather forecasting. *Quart. J. Roy. Meteor. Soc.*, **96**, 226-246.

Redi, M. H, 1982: Oceanic isopycnal mixing by coordinate rotation. *J. Phys. Oceanogr.*, **12**, 1154 -1158.

Reed, R. J., and B. A. Kunkel, 1960: The Arctic circulation in summer. *J. Meteor.*, **17**, 489-506.

Reed, R. J., and A. J. Simmons, 1991: Numerical simulations of an explosively deepening cyclone over the North Atlantic that was unaffected by concurrent surface energy fluxes. *Wea. Forecasting*, **6**, 117-122.

Reitan, C. H., 1974: Frequencies of cyclones and cyclogenesis for North America, 1951-1970. *Mon. Wea. Rev.*, **102**, 861-868.

Reitan, C. H., 1979: Trends in the frequencies of cyclone activity over North America. *Mon. Wea. Rev.*, **107**, 1684-1688.

Resio, D., and B. Hayden, 1975: Recent secular variations in mid-Atlantic winter extratropical storm climate. *J. Appl. Meteor.*, **14**, 1223-1234.

Reynolds, R. W., and T. M. Smith, 1994: Improved global sea surface temperature analysis using optimum interpolation. *J. Climate*, **7**, 929-948.

Reynolds, R. W., and T. M. Smith, 1995: A high-resolution global sea surface temperature climatology. *J. Climate*, **8**, 1571-1583.

Richman, M. B., 1986: Rotation of Principal Components. *J. Climatol.*, **6**, 293-333.

Richman, M. B., 1987: Rotation of Principal Components: A reply. *J. Climatol.*, **7**, 511-520.

Richman, M. B., J. R. Angel, and X. Gong, 1992a: Determination of dimensionality in eigenanalysis. *Proc. Fifth Int. Meeting on Statistical Climatology*, Toronto, ON, Canada, Environment Canada, 229-235.

Richman, M. B., and X. Gong, 1999: Relationships between the definition of the hyperplane width to the fidelity of principal component loading patterns. *J. Climate*, **12**, 1557-1576.

Richman, M. B., and P. J. Lamb, 1985: Climatic pattern analysis of three- and seven-day summer rainfall in the central United States: Some methodological considerations and a regionalization. *J. Climate Appl. Meteor.*, **24**, 1325-1343.

Richman, M. B., and P. J. Lamb, 1987: Pattern analysis of growing season precipitation in southern Canada. *Atmos-Ocean*, **25**, 137-158.

Richman, M. B., P. J. Lamb, and J. R. Angel, 1991: Relationships between monthly precipitation over central and eastern North America and the Southern Oscillation. Preprints, *Fifth Conf. on Climate Variations*, Denver, CO, Amer. Meteor. Soc., 151-158.

Richman, M. B., P. J. Lamb, A. Zangvil, and J. R. Angel, 1992b: Multivariate statistical analysis of precipitation associated with North American storm tracks. Preprints, *12th Conf. on Probability and Statistics in the Atmospheric Sciences*, Toronto, ON, Canada, Amer. Meteor. Soc., 277-283.

Roberts, M. J., R. Marsh, A. L. New, and R. A. Wood, 1996: An intercomparison of a Bryan-Cox type ocean model and an isopycnic ocean model. Part I: The subpolar gyre and high latitude processes. *J. Phys. Oceanogr.*, **26**, 1495-1527.

Robertson, A. W., 1996: Interdecadal variability over the North Pacific in a multi-century climate simulation. *Climate Dyn.*, **12**, 227-241.

Robertson, A. W., C. R. Mechoso, and Y.-J. Kim, 2000: The influence of Atlantic seas surface temperature anomalies on the North Atlantic Oscillation. *J. Climate*, **13**, 122-138.

Robinson, W. A., 2000: Review of WETS- the workshop on extratropical SST anomalies. *Bull. Amer. Meteor. Soc.*, **81**, 567-577.

Rodwell, M. J., D. P. Rowell, and C. K. Folland, 1999: Oceanic forcing of the wintertime North Atlantic Oscillation and European climate. *Nature*, **398**, 320-323.

Roebber, P. J., 1984: Statistical analysis and updated climatology of explosive cyclones. *Mon. Wea. Rev.*, **112**, 1577-1589.

Roebber, P. J., 1989: On the statistical analysis of cyclone deepening rates. *Mon. Wea. Rev.*, **117**, 2293-2298.

Rogers, J. C., 1984: The association between the North Atlantic Oscillation and the Southern Oscillation in the Northern Hemisphere. *Mon. Wea. Rev.*, **112**, 1999-2015.

Rogers, J. C., 1990: Patterns of low-frequency monthly sea level pressure variability (1899-1986) and associated wave cyclone frequencies. *J. Climate*, **3**, 1364-1379.

Rogers, J. C., 1994: Atlantic storm track variability and the North Atlantic Oscillation. *Proc. Atlantic Climate Change Program: PI's Meeting*, Princeton, NJ, NOAA, 20-24.

Rogers, J. C., 1997: North Atlantic storm track variability and its association to the North Atlantic Oscillation and climate variability of Northern Europe. *J. Climate*, **10**, 1635-1647.

Rogers, J. C., 2001: Is the NAO inseparable from the Arctic Oscillation? *Eos Trans. AGU*, **82**(47), Fall Meet. Suppl., Abstract A21C-03.

Rogers, J. C., and E. Mosley-Thompson, 1995: Atlantic Arctic cyclones and the mild Siberian winters of the 1980s. *Geophys. Res. Lett.*, **22**, 799-802.

Rogers J. C., and H. van Loon, 1979: The seesaw in winter temperatures between Greenland and Northern Europe. Part II: Some oceanic and atmospheric effects in middle and high latitudes. *Mon. Wea. Rev.*, **107**, 509-519.

Schols, J. L., J. A. Weinman, G. D. Alexander, R. E. Stewart, L. J. Angus, and A. C. L. Lee, 1999: Microwave properties of frozen precipitation around a North Atlantic cyclone. *J. Appl. Meteor.*, **38**, 29-43.

Seager, R., Y. Kushnir, P. Chang, N. Naik, J. Miller, and W. Hazeleger, 2001: Looking for the role of the ocean in tropical Atlantic decadal climate variability. *J. Climate*, **14**, 638-655.

Seager, R., Y. Kushnir, M. Visbeck, N. Naik, J. Miller, G. Krahmann, and H. Cullen, 2000: Causes of Atlantic Ocean climate variability between 1958 and 1998. *J. Climate*, **13**, 2845-2862.

Selten, F. M., R. J. Haarsma, and J. D. Opsteegh, 1999: On the mechanism of North Atlantic decadal variability. *J. Climate*, **12**, 1956-1973.

Serrano, A., J. A. Garcia, V. L. Mateos, M. L. Cancillo, and J. Garrido, 1999: Monthly modes of variation of precipitation over the Iberian Peninsula. *J. Climate*, **12**, 2894-2919.

Serreze, M. C., 1995: Climatological aspects of cyclone development and decay in the Arctic. *Atmos.-Ocean*, **33**, 1-23.

Serreze, M. C., J. E. Box, R. G. Barry, and J. E. Walsh, 1993: Characteristics of Arctic synoptic activity, 1952-1989. *Meteor. Atmos. Phys.*, **51**, 147-164.

Serreze, M. C., F. Carse, R. G. Barry, and J. C. Rogers, 1997: Icelandic low cyclone activity: Climatological features, linkages with the NAO and relationships with recent changes in the Northern Hemisphere circulation. *J. Climate*, **10**, 453-464.

Serreze, M. C., J. E. Walsh, F. S. Chapin III, T. Osterkamp, M. Dyurgerov, V. Romanovsky, W. C. Oechel, J. Morison, T. Zhang, and R. G. Barry, 2000: Observational evidence of recent change in the Northern high-latitude environment. *Climatic Change*, **46**, 159-207.

Shensa, M. J., 1992: The discrete wavelet transform: Wedding the à trous and Mallat algorithms. *IEEE Transactions on Signal Processing*, **40**(10), 2464-2482.

Shindell, D. T., R. L. Miller, G. A. Schmidt, and L. Pandolfo, 1999: Simulation of recent northern winter climate trends by greenhouse-gas forcing. *Nature*, **399**, 452-455.

Simmonds, I., and K. Keay, 2000a: Mean Southern Hemisphere extratropical cyclone behavior in the 40-year NCEP-NCAR reanalysis. *J. Climate*, **13**, 873-885.

Simmonds, I., and K. Keay, 2000b: Variability of Southern Hemisphere extratropical cyclone behavior. *J. Climate*, **13**, 550-561.

Sinclair, M. R., 1994: An objective cyclone climatology for the Southern Hemisphere. *Mon. Wea. Rev.*, **122**, 2239-2256.

Sinclair, M. R., 1997: Objective identification of cyclones and their circulation intensity, and climatology. *Wea. Forecasting*, **12**, 595-612.

Smith, R. N. B, 1990: A scheme for predicting layer clouds and their water content in a general circulation model. *Quart. J. Roy. Meteor. Soc.*, **116**, 435-460.

Smith, R. B., 1992: Deuterium in North Atlantic storm tops. *J. Atmos. Sci.*, **49**, 2041-2057.

Smith, R. N. B., 1993: Experience and developments with the layer cloud and boundary layer mixing schemes in the UK Meteorological Office Unified Model. *Proc. of the ECMWF/GCSS workshop on parameterisation of the cloud-topped boundary layer*, 8-11 June, 1993. ECMWF, Reading, England.

Smith, T. M., and R. W. Reynolds, 2003: Extended reconstruction of global sea surface temperatures based on COADS data (1854-1997). *J. Climate*, **16**, 1495-1510.

Smith, T. M., R. W. Reynolds, R. E. Livezey, and D. C. Stokes 1996: Reconstruction of historical sea surface temperatures using Empirical Orthogonal Functions. *J. Climate*, **9**, 1403-1420.

Smith, T. M., R. W. Reynolds, and C. F. Ropelewski, 1994: Optimal averaging of seasonal sea surface temperatures and associated confidence intervals (1860-1989). *J. Climate*, **7**, 949-964.

Stephenson, D. B., and I. M. Held, 1993: GCM response of Northern winter stationary waves and storm tracks to increasing amounts of carbone dioxide. *J. Climate*, **6**, 1859-1870.

Stephenson, D. B., V. Pavan, and R. Bojariu, 2000: Is the North Atlantic Oscillation a random walk. *Inter. J. Climatol.*, **20**, 1-18.

Stephenson, D. B., and V. Pavan, 2003: The North Atlantic Oscillation in coupled climate models: A CMIP1 evaluation. *Climate Dyn.*, **19**, 381-399.

Stockton, C. W., and M. F. Glueck, 1999: Long-term variability of the North Atlantic oscillation (NAO). *Proc. Amer. Meteor. Soc.* Tenth Symp. Global Changes Studies, 11-15 January, 1999, Dallas, TX, 290-293.

Stommel, H., 1961: Thermohaline convection with two stable regimes of flow. *Tellus*, **13**, 224-230.

Sutton, R. T., and M. R. Allen, 1997: Decadal predictability of North Atlantic sea surface temperature and climate. *Nature*, **388**, 563-567.

Taylor, K. E., 1986: An analysis of the biases in traditional cyclone frequency maps. *Mon. Wea. Rev.*, **114**, 1481-1490.

Thompson, D. W. J., and J. M. Wallace, 1998: The Arctic Oscillation signature in the wintertime geopotential height and temperature fields. *Geophys. Res. Lett.*, **25**, 1297-1300.

Thompson, D. W. J., and J. M. Wallace, 2000a: Annular modes in the extratropical circulation. Part I: Month-to-month variability. *J. Climate*, **13**, 1000-1016.

Thompson, D. W. J., J. M. Wallace, and G. C. Hegerl, 2000b: Annular modes in the extratropical circulation. Part II: Trends. *J. Climate*, **13**, 1018-1036.

Thorncroft, C. D., and H. A. Flocas, 1997: A case study of Saharan cyclogenesis. *Mon. Wea. Rev.*, **125**, 1147-1165.

Timmermann, A., M. Latif, R. Voss, and A. Grötzner, 1998: Northern hemispheric interdecadal variability: A coupled air-sea mode. *J. Climate*, **11**, 1906-1931.

Ting, M., 1991: The stationary wave response to a midlatitude SST anomaly in an idealized GCM. *J. Atmos. Sci.*, **48**, 1249-1275.

Torrence, C., and G. P. Compo, 1998: A practical guide to wavelet analysis. *Bull. Amer. Meteor. Soc.*, **79**, 61-78.

Tourre, Y. M., B. Rajagopalan, and Y. Kushnir, 1999: Dominant patterns of climate variability in the Atlantic Ocean during the last 136 years. *J. Climate*, **12**, 2285-2299.

Trenberth, K. E., 1976: Spatial and temporal variations of the Southern Oscillation. *Quart. J. Roy. Meteor. Soc.*, **102**, 639-653.

Trenberth, K. E., 1984: Signal versus noise in the Southern Oscillation. *Mon. Wea. Rev.*, **112**, 326-332.

Trenberth, K. E., 1991: Storm tracks in the Southern Hemisphere. *J. Atmos. Sci.*, **48**, 2159-2178.

Trenberth, K. E., G. W. Branstator, D. Karoly, A. Kumar, N.-C. Lau, and C. F. Ropelewski, 1998: Progress during TOGA in understanding and modeling global teleconnections associated with tropical sea surface temperatures. *J. Geophys. Res.*, **103**, 14291-14324.

Trenberth, K. E., and T. J. Hoar, 1996: The 1990-1995 El Niño-Southern Oscillation event: Longest on record. *Geophys. Res. Lett.*, **23**, 57-60.

Trenberth, K. E., and J. W. Hurrell, 1994: Decadal atmosphere-ocean variations in the Pacific. *Climate Dyn.*, **9**, 303-319.

Trenberth, K. E., and J. G. Olson, 1988: An evaluation and intercomparison of global analyses from the National Meteorological Center and the European Centre for Medium Range Weather Forecasts. *Bull. Amer. Meteor. Soc.*, **69**, 1047-1057.

Trenberth, K. E., and D. P. Stepaniak, 2001: Indices of El Niño evolution. *J. Climate*, **14**, 1697-1701.

Trigo, I. F. and T. D. Davies, and G. R. Bigg, 1999: Objective climatology of cyclones in the Mediterranean region. *J. Climate*, **12**, 1685-1696.

Trigo, R. M., and C. C. DaCamara, 2000: Circulation weather types and their influence on the precipitation regime in Portugal. *Int. J. Climatol.*, **20**, 1559-1581.

Tung, W. W., and M. Yanai, 2002: Convective momentum transport observed during the TOGA COARE IOP. Part II: Case studies. *J. Atmos. Sci.*, **59**, 2535-2549.

Uccellini, L. W., 1990: Processes contributing to the rapid development of extratropical cyclones. Chap. 6 in: *Extratropical cyclones, The Erik Palmen Memorial Volume*, Amer. Meteor. Soc., Boston, Mass., 81-105.

U.K. Meteorological Office, 1964: *Weather in Home Fleet Waters. Vol. 1- The Northern Seas, Part 1.* Her Majesty's Stationery Office, London, 265 pp.

Ulbrich, U., and M. Christoph, 1999: A shift of the NAO and increasing storm track activity over Europe due to anthropogenic greenhouse gas forcing. *Climate Dyn.*, **15**, 551-559.

Uppenbrink, J., 1999: The North Atlantic Oscillation. *Science*, **283**, 948-949.

van Loon, H., and J. C. Rogers, 1978: The seesaw in winter temperatures between Greenland and northern Europe. Part I: General description. *Mon. Wea. Rev.*, **106**, 296-310.

van Loon, H., and J. Williams, 1976a: The connection between trends of mean temperature and circulation at the surface: Part I. Winter. *Mon. Wea. Rev.*, **104**, 365-380.

van Loon, H., and J. Williams, 1976b: The connection between trends of mean temperature and circulation at the surface: Part II. Summer. *Mon. Wea. Rev.*, **104**, 1003-1011.

van Loon, H., and J. Williams, 1977: The connection between trends of mean temperature and circulation at the surface: Part IV. Comparison of the surface changes in the Northern Hemisphere with the upper air and with the Antarctic in winter. *Mon. Wea. Rev.*, **105**, 636-647.

van Oldenborgh, G. J., G. Burgers, and A. K. Tank, 1999: On the El Niño teleconnection to spring precipitation in Europe. *KNMI*, de Bilt, Netherlands, 1-14.

Venables, W. N., and B. D. Ripley, 1994: *Modern Applied Statistics with S-Plus.* Springer-Verlag, 462 pp.

Venzke, S., M. R. Allen, R. T. Sutton, and D. P. Rowell, 1999: The atmospheric response over the North Atlantic to decadal changes in sea surface temperature. *J. Climate*, **12**, 2562-2584.

Vincent, P., and Y. Bengio, 2002: Kernel matching pursuit. *Machine Learning*, **48**, 165-187.

Visbeck, M., J. Marshall, T. Haine, and M. Spall, 1997: On the specification of eddy transfer coefficients in coarse resolution ocean circulation models. *J. Phys. Oceanogr.*, **27**, 381-402.

Walden, A. T., and A. C. Cristan, 1998: Matching pursuit by undecimated discrete wavelet transform for non-stationary time series of arbitrary length. *Statistics and Computing*, **8**, 205-219.

Walker, G. T., 1923: Correlation in seasonal variations of weather, VIII: A preliminary study of world weather. *Mem. Ind. Meteor. Dept.* (Poona), **24**, 275-332.

Walker, G. T., and E. W. Bliss, 1932: World weather. *V. Mem. Roy. Meteor. Soc.*, **103**, 29-64.

Wallace, J. M., 2000: North Atlantic Oscillation/annular mode: Two paradigms-one phenomenon. *Quart. J. Roy. Meteor. Soc.*, **126**, 791-805.

Wallace, J. M., and D. S. Gutzler, 1981: Teleconnections in the geopotential height field during Northern Hemisphere winter. *Mon. Wea. Rev.*, **109**, 784-812.

Wallace, J. M., G.-H. Lim, and M. L. Blackmon, 1988: Relationship between cyclone tracks, anticyclone tracks and baroclinic waveguides. *J. Atmos. Sci.*, **45**, 439-462.

Wallace, J. M., C. Smith, and Q. Jiang, 1990: Spatial patterns of atmosphere-ocean interaction in the northern winter. *J. Climate*, **3**, 990-998.

Wallace, J. M., and D. W. J. Thompson, 2002: Annular modes and climate prediction. *Physics Today*, 28-33.

Walsh, J. E., V. M. Kattsov, W. L. Chapman, V. Govorkova, and T. Pavlova, 2002: Comparison of Arctic climate simulations by uncoupled and coupled global models. *J. Climate*, **15**, 1429-1446.

Walsh, J. E., and D. H. Portis, 1999: Variations of precipitation and evaporation over the North Atlantic Ocean, 1958-1997. *J. Geophys. Res.*, **104**, 16613-16631.

Walsh, K., and I. G. Watterson, 1997: Tropical cyclone-like vortices in a limited area model: Comparison with observed climatology. *J. Climate*, **10**, 2240-2259.

Walter, K., U. Luksch, and K. Fraedrich, 2001: A response climatology of idealized midlatitude thermal forcing experiments with and without a storm track. *J. Climate*, **14**, 467-484.

Wang, B., and Y. Wang, 1996: Temporal structure of the Southern Oscillation as revealed by waveform and wavelet analysis. *J. Climate*, **9**, 1586-1598.

Wang, C.-C., and J. C. Rogers, 2001: A composite study of explosive cyclogenesis in different sectors of the North Atlantic. Part I: Cyclone structure and evolution. *Mon. Wea. Rev.*, **129**, 1481-1499.

Ward, M. N., P. J. Lamb & D. H. Portis, and M. El Hamly & R. Sebbari, 1999: Climate Variability in Northern Africa: Understanding Droughts in the Sahel and the Maghreb. Chapter 6 (pp 119-140) in the book "*Beyond El Niño: Decadal and Interdecadal Climate Variability*", Ed. Antonio Navarra, Springer Verlag, 375 pp.

Washington, and Coauthors, 2000: Parallel climate model (PCM) control and transient simulations. *Climate Dyn.*, **16**, 755-774.

Watanabe, M., M. Kimono, and T. Nitta, and M. Kachi, 1999: A comparison of decadal climate oscillations in the North Atlantic detected in observations and a coupled GCM. *J. Climate*, **12**, 2920-2940.

Watanabe, M., and M. Kimoto, 2000: On the persistence of decadal SST anomalies in the North Atlantic. *J. Climate*, **13**, 3017-3028.

Watterson, I. G., S. P. O'Farrell, and M. R. Dix, 1997: Energy transport in climates simulated by a GCM which includes dynamic sea-ice. *J. Geophys. Res.*, **102** (D10), 11027-11037.

Weatherly, J. W., and C. M. Bitz, 2001: Natural and anthropogenic climate change in the Arctic. *12th Symposium on Global Change and Climate Variations*, 15-18 Jan 2001, Albuquerque, Amer. Meteor. Soc., Boston.

Weatherly, J. W., and Y. Zhang, 2001: The response of the polar regions to increased CO_2 in a global climate model with elastic-viscous-plastic sea ice. *J. Climate*, **14**, 268-283.

Weaver, C. P., 1999: The interactions among cyclone dynamics, vertical thermodynamic structure, and cloud radiative forcing in the North Atlantic summertime storm track. *J. Climate*, **12**, 2625-2642.

Weaver, A. J., and E. S. Sarachik, 1991: Evidence for decadal variability in an Ocean General Circulation Model: An advective mechanism. *Atmos.-Ocean*, **29**, 197-231.

Weisberg, S., 1985: *Applied Linear Regression.* 2nd Edition. Wiley, New York.

Weisse, R., U. Mikolajewicz, and E. Maier-Reimer, 1994: Decadal variability of the North Atlantic in an Ocean General Circulation Model. *J. Geophys. Res.*, **99**, 12411-12421.

Whitaker, J. S., and R. M. Dole, 1995: Organization of storm tracks in zonally varying flows. *J. Atmos. Sci.*, **52**, 1178-1191.

Whittaker, L. M., and L. H. Horn, 1981: Geographical and seasonal distribution of North American cyclogenesis, 1958-1977. *Mon. Wea. Rev.*, **109**, 2312-2322.

Whittaker, L. M., and L. H. Horn, 1982: *Atlas of Northern Hemisphere Extratropical Cyclone Activity, 1958-1977.* Dept. of Meteorology, Univ. of Wisconsin-Madison, 67 pp.

Whittaker, L. M., and L. H. Horn, 1984: Northern Hemisphere extratropical cyclone activity for four mid-season months. *Journal of Climatology*, **4**, 297-310.

Wilby, R. L., G. O'Hare, and N. Barnsley, 1997: The North Atlantic Oscillation and British Isles climate variability. *Weather*, **52**, 266-276.

Wilks, D. S., 1995: *Statistical Methods in the Atmospheric Sciences.* Academic Press, 467 pp.

Winkler, J. A., J. P. Palutikof, J. A. Andersen, and C. M. Goodess, 1997: The simulation of daily temperature time series from GCM output. Part II: Sensitivity analysis of an empirical transfer function methodology. *J. Climate*, **10**, 2514-2532.

Wolter, K., and M. S. Timlin, 1993: Monitoring ENSO in COADS with a seasonally adjusted principal component index. *Proc. of the 17th Climate Diagnostics Workshop*, Norman, OK, NOAA/N MC/CAC, NSSL, Oklahoma Clim. Survey, CIMMS and the School of Meteor., Univ. of Oklahoma, 52-57.

Wolter, K., and M. S. Timlin, 1998: Measuring the strength of ENSO - how does 1997/98 rank? *Weather*, **53**, 315-324.

Wunsch, C., 1999: The interpretation of short climate records, with comments on the North Atlantic and Southern Oscillations. *Bull. Amer. Meteor. Soc.*, **80**, 245-255.

Yom-Tov, E., A. Grossman, and G. F. Inbar, 2001: Movement-related potentials during the performance of a motor task II: Cerebral areas activated during learning of the task. *Biological Cybernetics*, **85**, 387-394.

Zhang, K., B. C. Douglas, and S. P. Leatherman, 2000: Twentieth-century storm activity along the U.S. East Coast. *J. Climate*, **13**, 1748-1761.

Zhang, Y., J. M. Wallace, and D. S. Battisti, 1997: ENSO-like interdecadal variability: 1900-93. *J. Climate*, **10**, 1004-1020.

Zhang, Y., and W.-C. Wang, 1997: Model-simulated Northern winter cyclone and anticyclone activity under a greenhouse warming scenario. *J. Climate*, **10**, 1616-1634.

Zishka, K. M., and P. J. Smith, 1980: The climatology of cyclones and anticyclones over North America and surrounding ocean environs for January and July, 1950-77. *Mon. Wea. Rev.*, **108**, 387-401.

Zishka, K. M., and P. J. Smith, 1981: Reply. *Mon. Wea. Rev.*, **109**, 1358.

Zorita, E., and C. Frankignoul, 1997: Modes of North Atlantic decadal variability in the ECHAM1/LSG coupled ocean-atmosphere model. *J. Climate*, **10**, 183-200.

Zorita, E., V. Kharin, and H. von Storch, 1992: The atmospheric circulation and sea-surface temperature in the North Atlantic area in winter: Their interaction and relevance for Iberian precipitation. *J. Climate*, **5**, 1097-1108.